Fermilab

FERMILAB-THESIS-1996-79

# Partial Wave Analysis of the Process

$$p\ p \ \rightarrow \ p_s\ (K^0_s K^0_s)\ p_f$$

## at 800 GeV/c

**Tesis**
que submite el

**M. en C. Marco A. Reyes Santos**

al Departamento de Física
del Centro de Investigación y Estudios Avanzados del IPN
como requisito parcial para obtener el grado de

**Doctor en Ciencias**

México, D.F., Octubre de 1996

# Partial Wave Analysis of the Process

# $p\ p \ \rightarrow \ p_s\ (K^0_s K^0_s)\ p_f$

# at 800 GeV/c

M. en C. Marco A. Reyes

*Departamento de Física*

*Centro de Investigación y Estudios Avanzados del IPN*

*Apdo. Postal 14-740, México D.F. 07000, México*

**Abstract**

The partial wave analysis of the $K^0_s K^0_s$ system at $800 GeV/c$ is presented. We make emphasis on the region of the $f_0(1520)$ and the $f_J(1710)$, which are the two candidates for the lowest lying glueball. Our analysis shows a clear peak in $S$–wave in the region of the $f_0(1520)$, and $S$–wave dominance in the region of the $f_J(1710)$.

**A Victoria Santos Quiterio**

**A Caty y Laura**

**A Marisela**

## AGRADECIMIENTOS

Ha sido un placer trabajar con la gente de la Colaboración del Experimento E690. En particular, quisiera agradecer a los Doctores Dave Christian, Bruce Knapp, Mike Kreisler, Ed Hartouni, Erik Gottschalk, Alan Wehmann y Modesto Sosa, y a Kyriacos Markianos y Mike Wang, por sus consejos y apoyo desde el comienzo de mi participación en esta Colaboración. Indudablemente, la paciencia y la ayuda siempre atenta de mis asesores, Dr. Gastón Gutiérrez y Dr. Gerardo Moreno, hicieron posible conseguir una meta, y dejar puertas abiertas para trabajos posteriores.

Nada es más agradable para uno que contar con el apoyo de su propia familia. A mis padres, Victoria y Mariano, y a mis hermanos, Mariano, Gaspar, Leonardo, Laura, Caty, Eva, Hilda y Angélica, muchas gracias por los ánimos y el apoyo que siempre me han brindado.

También quiero agradecer la amistad de la gente del Departamento de Física del Centro de Investigación y Estudios Avanzados, y la cálida hospitalidad en el Instituto de Física de la Universidad de Guanajuato. Demasiados amigos para nombrarlos a todos.

Finalmente, este trabajo no hubiera sido posible sin el apoyo financiero de CONACyT, México, y de la Academia de la Investigación Científica, México, y la Fundación México–Estados Unidos para la Ciencia.

## ACKNOWLEDGEMENTS

It has been a pleasure working with people in the E690 Collaboration. In particular, I want to thank Drs. Dave Christian, , Bruce Knapp, Mike Kreisler, Ed Hartouni, Erik Gottschalk, Alan Wehmann and Modesto Sosa, together with Kyriacos Markianos and Mike Wang, for their advices and support since the very beginning of my participation in the E690 Collaboration. Of course, the patience and willingness of my advisors to help, Dr. Gaston Gutierrez and Dr. Gerardo Moreno, made it possible to achieve a goal, and to leave open doors for future work.

Nothing is as pleasant as having the support of your own family. To my parents, Victoria and Mariano, and brothers, Mariano, Gaspar, Leonardo, Laura, Caty, Eva, Hilda and Angelica, thanks a lot for all their cheering and supporting.

I also want to thank the friendship of people in the Departamento de Física del Centro de Investigación y Estudios Avanzados, and the warm hospitality at Instituto de Física de la Universidad de Guanajuato. Too many friends to cite.

Finally, this work could not have been possible without the financial support of CONACyT, Mexico, and of the Academia de la Investigación Científica, Mexico, and the Mexico–United States Foundation for Science.

# Contents

# List of Figures

# List of Tables

# 1 INTRODUCTION

The present knowledge of strong interactions is that they are described by Quantum Chromodynamics (QCD). This non-Abelian field theory not only describes how quarks and antiquarks interact, but also predicts that the gluons (which are the quanta of the field) will themselves interact to form mesons. If the object formed is composed entirely of valence gluons ($gg$ or $ggg$) the meson is called a glueball. However, if it is composed of a mixture of valence quarks, antiquarks and gluons (i.e. $q\bar{q}g$) it is called a hybrid. In addition, $q\bar{q}q\bar{q}$ states are also predicted. An unambiguous confirmation of these states would be an important test of QCD.

## 1.1 The $q\bar{q}$ Spectrum

The study of the $q\bar{q}$ system is by itself an important and interesting task. In order to locate and identify glueballs and hybrids states it is necessary to understand the "ordinary" mesons in detail. This means that each state in the $q\bar{q}$ nonets must be identified unambiguously and that all its properties have to be well measured. Of special importance is the light meson region (below 2.5 $GeV/c^2$), which is not yet completely understood, and where the lightest glueballs and hybrids may appear. Since the perturbative approach cannot, in fact, be easily extended to the low energy regime, the light hadron spectrum cannot be reliably calculated, and it is even more difficult to predict dynamical properties, such as decay widths. The spectroscopy of low mass states can however be accounted for, to a large degree, by QCD-inspired models. The most complete of these, built by S. Godfrey and N. Isgur in 1985 [1], is able to describe with sufficient accuracy the $q\bar{q}$ meson spectrum from the pion to the upsilon. This model is therefore often used in order to test whether a new discovered resonance belongs or not to one of the $q\bar{q}$ multiplets.

| $N\ ^{2S+1}L_J$ | $J^{PC}$ | $ud, u\bar{u}, dd$ $I=1$ | $u\bar{u}, dd, s\bar{s}$ $I=0$ | $c\bar{c}$ $I=0$ | $b\bar{b}$ $I=0$ | $\bar{s}u, \bar{s}d$ $I=1/2$ |
|---|---|---|---|---|---|---|
| $1\ ^1S_0$ | $0^{-+}$ | $\pi$ | $\eta,\ \eta'$ | $\eta_c$ | | $K$ |
| $1\ ^3S_1$ | $1^{--}$ | $\rho$ | $\omega,\ \phi$ | $J/\psi(1S)$ | $\Upsilon(1S)$ | $K^*(892)$ |
| $1\ ^1P_1$ | $1^{+-}$ | $b_1(1235)$ | $h_1(1170), h_1'(1380)$ | $h_c(1P)$ | | $K_{1B}$ |
| $1\ ^3P_0$ | $0^{++}$ | * | * | $\chi_{c0}(1P)$ | $\chi_{b0}(1P)$ | $K_0^*(1430)$ |
| $1\ ^3P_1$ | $1^{++}$ | $a_1(1260)$ | $f_1(1285), f_1(1510)$ | $\chi_{c1}(1P)$ | $\chi_{b1}(1P)$ | $K_{1A}$ |
| $1\ ^3P_2$ | $2^{++}$ | $a_2(1320)$ | $f_2(1270), f_2'(1525)$ | $\chi_{c2}(1P)$ | $\chi_{b2}(1P)$ | $K_2^*(1430)$ |
| $1\ ^1D_2$ | $2^{-+}$ | $\pi_2(1670)$ | | | | $K_2(1770)$ |
| $1\ ^3D_1$ | $1^{--}$ | $\rho(1700)$ | $\omega(1600)$ | $\psi(3770)$ | | $K^*(1680)$ |
| $1\ ^3D_2$ | $2^{--}$ | | | | | $K_2(1820)$ |
| $1\ ^3D_3$ | $3^{--}$ | $\rho_3(1690)$ | $\omega_3(1670), \phi_3(1850)$ | | | $K_3^*(1780)$ |
| $1\ ^3F_4$ | $4^{++}$ | $a_4(2040)$ | $f_4(2050), f_4(2220)$ | | | $K_4^*(2045)$ |
| $2\ ^1S_0$ | $0^{-+}$ | $\pi(1300)$ | $\eta(1295)$ | $\eta_c(2S)$ | | $K(1460)$ |
| $2\ ^3S_1$ | $1^{--}$ | $\rho(1450)$ | $\omega(1420), \phi(1680)$ | $\psi(2S)$ | $\Upsilon(2S)$ | $K^*(1410)$ |
| $2\ ^3P_2$ | $2^{++}$ | | $f_2(1810), f_2(2010)$ | | $\chi_{b2}(2P)$ | $K_2^*(1980)$ |
| $3\ ^1S_0$ | $0^{-+}$ | $\pi(1770)$ | $\eta(1760)$ | | | $K(1830)$ |

Table 1: Suggested $q\bar{q}$ quark-model assignments for most of the known light quark, $c\bar{c}$, and $b\bar{b}$ mesons. Some assignments, especially for the $0^{++}$ multiplet and for some of the higher multiplets are controversial. Within the $q\bar{q}$ model, it is hard to find a place for the $f_1(1420),\ f_0(1520)$ and $f_J(1710)$, and for one of the two peaks in the $\eta(1440)$. The candidates for the $I=1$ states are $a_0(980)$ and $a_0(1450)$, while for $I=0$ they are: $f_0(400-1200),\ f_0(980)$ and $f_0(1370)$. The light scalars are problematic, since there may be two poles for one $q\bar{q}$ state, and $a_0(980),\ f_0(980)$ may be $K\bar{K}$ bound states.

After decades of study, the $q\bar{q}$ system is still not perfectly understood. Table 1 summarizes the current status of the $q\bar{q}$ quark-model assignments[1]. The individual boxes represent the $I=1$, the four $I=0$ ($u\bar{u}+d\bar{d}$, $s\bar{s}$, $c\bar{c}$ and $b\bar{b}$) and the $I=1/2$ members of each multiplet. They correspond to the established mesons, as reported by the Particle Data Group [3]. When considering only light quarks ($u, d$ and $s$), we can see that only four nonets (of the ground states, N=1), are unambiguously filled: the $0^{-+}$, $1^{--}$, $2^{++}$ and $3^{--}$ nonets. Four other nonets have all positions filled with possible candidates. If the $h_1'(1380)$ is confirmed, the $1^{+-}$ nonet will also be complete. In the $0^{++}$, questions remain about $a_0(980)$, $f_0(400-1200)$, $f_0(980)$, $f_0(1370)$, $f_0(1520)$ and the $f_J(1710)$. In the $1^{++}$ nonet, the

[1]We omit in this table mesons corresponding to the $\{c\bar{u}, c\bar{d}\}$, $\{c\bar{s}\}$, $\{\bar{b}u, \bar{b}d\}$ and $\{\bar{b}s\}$ assignments, correpsonding to $D$ and $B$ mesons.

interpretation of the $f_1(1420)$ is unclear. In the $4^{++}$ nonet, the $a_4(2040)$ and $f_4'(2300)$ have to be confirmed, too. In the first radial excitations of the $0^{-+}$ nonet the $K(1830)$ and the radially excited $\eta'$ need to be established. The remaining nonets are in worse shape, since many candidates are missing and most of those shown need confirmation.

## 1.2 Glueballs and Hybrids

One of the most important expectations of QCD is the existence of particles having gluon constituents, like glueballs or hybrid states. Glueballs are bound states of two or three gluons in a color singlet. The $gg$ states have even $C$–parity, while for $ggg$ states both even and odd $C$ parities are allowed [2]. In the $gg$ sector, the lowest states are $0^{++}$ and $2^{++}$, where the scalar glueball is the ground state. In the $ggg$ sector, the lowest allowed states are $0^{-+}$, $1^{--}$ and $3^{--}$. However, the $gg$ states are expected to be at lower masses than the $ggg$ states. In the $gg$ sector, the first oddball, a $1^{-+}$ state, occurs with $L = 1$. Oddballs are glueballs with quantum numbers that do not exist in the $q\bar{q}$ sector, like $0^{--}$, $1^{-+}$, $3^{-+}, \ldots$, $0^{+-}, 2^{+-}, \ldots$. However, if gluons inside glueballs are in fact massless, $J$=*odd* states are forbidden in the $gg$ sector by Yang's theorem[4], although they may exist in the $ggg$ sector.

The mesonic decay of glueballs is determined by their flavor SU(3) singlet nature; ignoring phase space factors, glueballs are naively expected to couple equally to all flavors, while arguments from perturbation theory [5] favor a stronger coupling to strange, rather than $u$- or $d$-quarks. As yet the definite identification of such states has not been achieved, one of the biggest difficulties being the complexity of the $q\bar{q}$ meson spectrum in the 1–2 $GeV/c^2$ region, where $q\bar{q}$, $gg$, $q\bar{q}g$, four quark states and radial excitations may overlap in mass and mix. The search for gluonic states has been carried out using several production mechanisms which are thought to have a high gluonic content, e.g. $J/\psi$ radiative and hadronic decays, $p\bar{p}$ anihilations, high $p_T$ direct production, OZI violating processes and central production.

Since the $J/\psi$ decays dominantly through gluons into hadrons, one expects to be able to learn about the quark–gluon coupling and other gluon properties by studying its decays. It is

an excellent laboratory to perform these studies for various reasons: it is a narrow resonance with huge production cross section in $e^+e^-$, the non–resonant background is very small, it is produced at rest, the initial state is devoid of light quarks, etc. However, the big problem here is that in order to produce a $K\bar{K}$ system, for example, $J/\psi$ must decay to this system plus something else, a $\gamma$ or $\phi$, and these decays have very poor statistics.

OZI violating processes could shed light on glueball states, since it is likely that the produced mesons are not excited by quark exchange, and are therefore assumed to be gluon rich. The way to proceed is to analyze OZI allowed and OZI forbidden processes, and to compare the branching ratios obtained. Working in this direction, Lindenbaum *et al.*[6] have identified three $2^{++}$ states which are high enough in energy to decay into $\phi\phi$, by measuring the reaction $\pi^- p \to \phi\phi n$. Since this is an OZI suppressed channel, these states are glueball candidates.

The central system is assumed to be produced by double exchange processes. At high center–of–mass energies these double exchange processes are believed to be dominated by Double Pomeron Exchange (DPE), where the Pomeron is thought to have a large gluonic component, leading to the conclusion that Pomeron-Pomeron scattering could be a rich source for the production of gluonic states.

Several candidates have been reported for glueballs and exotic mesons in previous experiments[7, 8, 9, 10, 11]. Most of these states lie in the 1.0–2.5 $GeV/c^2$ mass region, where they can be easily confused with conventional $q\bar{q}$ states. To help settle the nature of these candidates, it is very important to make a full map of $q\bar{q}$ mesonic states, exploring the spectrum of excitations, as well as to search for exotic states which are directly produced in the hadronic processes. Since light quark spectroscopy has been studied for a long time, an experiment is required to have both good sensitivity and high acceptance in a wide variety of physics channels to make significant progress.

With respect to the theoretical point of view, it can be proven[12] that the lowest ly-

ing glueball must be scalar, with quantum numbers $0^{++}$. Two groups working on lattice calculations favor two different mesons to be the lowest mass scalar glueball. The UKQCD lattice group favors the $f_0(1520)$ [13], and the IBM group favors the $f_J(1710)$ [14], in which case the spin should be $J = 0$. Recently[15], the IBM group has been working on probing the possibility that the $f_0(1520)$ and $f_J(1710)$ are mixed states of a scalar meson and a scalar glueball. They conclude that $f_J(1710)$ is mostly glueball, and $f_0(1520)$ is a mostly quarkonium state, corresponding to the $s\bar{s}$ member of the scalar nonet.

The mesons $f_0(1520)$ and $f_J(1710)$ have been observed by various experiments. The Crystal Barrel Collaboration has observed an isoscalar $J^{PC} = 0^{++}$ resonance decaying to $\eta\eta$ in the process $p\bar{p} \to \eta\eta\pi^0$, compatible with the spin–0 resonance found by the GAMS Collaboration[10]. Initially, they assigned a mass of $1560 \pm 25\ MeV/c^2$ and a width of $245 \pm 50\ MeV/c^2$ to this resonance[16], but in a recent publication[17] they performed a simultaneous fit to the $\pi^0\pi^0\pi^0$ and $\eta\eta\pi^0$ channels, and changed their mass assignment to $1520 \pm 25\ MeV/c^2$. There is still the possibility that the $f_0(1520)$ and $f_0(1590)$ seen by the GAMS Collaboration, be mixed states of a glueball and the ninth member of the $q\bar{q}$ nonet.

## 1.3 The $K_s^0K_s^0$ System

The $K_s^0K_s^0$ system has been studied in many previous experiments, due to the several advantages this system has over other channels, such as $K^+K^-$, because: 1) the requirement that both neutral particles in the secondary vertices have definite masses, and decay visibly, makes the events readily distinguishable, 2) fits making use of kinematic constraints at the primary and secondary vertices result in a data sample which has little contamination and good resolution, and 3) no further particle identification information is required, so no holes in the acceptance of the spectrometer are created. In addition, due to Bose statistics, the $K_s^0K_s^0$ system has even $C$–parity and, consequently, even angular momentum and parity. Therefore, only meson states with $J^{PC}$ in the series $0^{++}$, $2^{++}$, $4^{++}$,..., are produced. A summary of the results obtained in previous experiments in the $K_s^0K_s^0$ system is given below.

Evidence for $f_J(1710)$ and $X(2220)$ in reactions like $K^-p \to K^0_s K^0_s \Lambda$ would be of great significance, since their production via hypercharge exchange in this kind of reactions would cast doubt on their status as candidate glueball states. Using the MSS ITEP spectrometer at Serpukhov the reaction $K^-p \to K^0_s K^0_s Y^*$ was studied[18]. This experiment found dominant production of $f'_2(1525)$, without a statistically significant peak in the $\Theta(1690)$ region. In a later work[19], they performed a partial wave analysis on the reaction $\pi^-p \to K^0_s K^0_s n$, and reported the observation of three $D^{++}$ resonances, additional to the $f(1270)$ and $f'(1525)$ states: $\Theta(1700)$, $f''(1980)$ and $\xi(2230)$. They also reported the observation of a $G_0$ wave, the $h(2030)$, an $s\bar{s}$ partner of the $h'(2160)$ meson, and $S$–wave resonances $\epsilon'(1440)$ and $S^*(1720)$. No signature of $g_s(1240)$ was found.

The LASS Collaboration at SLAC[20, 21], using a 11 $GeV/c$ $K^-$ beam, reported a single strong peak in the $f'_2(1525)$ region, and no apparent $f_J(1710)$ signal, suggesting that it is unlikely to be a conventional $s\bar{s}$ state. This observations are compatible with the results of Barreiro *et al.*[22]. They also report some excess events clustered right above the $K^0_s K^0_s$ threshold, the $a_0(980)$, $f_0(980)$ region, and some structure in the $X(2220)$ region, with angular distributions indicating $J = 2$ in this region. In addition, this experiment reports the observation of a $0^{++}$ state, the $f'_0$, approximately degenerate in mass and width with $f'_2(1525)$. Later, a partial wave analysis of the reaction $k^-p \to K^0_s K^{\pm}\pi^{\mp}\Lambda$ in the same experiment, confirmed the existence of the $1^{++}$ $f'_1(1525)$ claimed in earlier analysis[23], suggesting that the $0^{++}$ state they observed, together with $f'_1$, $f'_2$, would form the mainly $s\bar{s}$ triplet of isoscalar states expected in the quark model. If this is truth, then the $S^*/f_0(980)$ and $a_0(980)$ would have to be removed from the $0^{++}$ nonet and might be explained as $K\bar{K}$ molecules, as in the model of Weinstein and Isgur[24].

Radiative decays of the $J/\psi$ are of great interest because these decays are expected to be a copious source of glueball states. The Mark III Collaboration[11] performed studies on $K^+K^-$ and $K^0_s K^0_s$ final states. They reported the observation of a narrow signal, named $\xi(2230)$, and a $J = 2$ state, $f_2(1720)$. However, in 1991 [25] they performed further studies,

and found a large spin-0 component for $f_J(1720)$. The DM2 Collaboration[26], studying the processes $J/\psi \to \gamma K^+K^-$ and $\gamma K_s^0 K_s^0$, observed clean and well-separated signals of $f_2'(1525)$ and $f_J(1710)$ in both channels, but no signal of the narrow $\xi(2230)$ in either channel. Instead, they observed a very broad structure in the region between 2 and 2.5 $GeV/c^2$ with a width 8 times larger than the quoted for $\xi(2230)$.

The first measurements of the $K\bar{K}$ system in $\gamma\gamma$ collisions were done by the Tasso Collaboration[27]. This experiment found exclusive $f_2'(1525)$ production, and $f_2(1270) - a_2(1320) - f_2'(1525)$ constructive(destructive) interference for the $K^+K^-(K_s^0K_s^0)$ system. This confirms the QCD prediction[28] that $f_2$ and $a_2$ are expected to interfere constructively in the reaction $\gamma\gamma \to K^+K^-$, and destructively in the reaction $\gamma\gamma \to K_s^0K_s^0$. Later, PLUTO [29] and Cello [30] Collaborations corroborated these results.

At CERN, experiment WA76[31, 32] studied the reaction $pp \to p_s(K\bar{K})p_f$, at 85 and 300 $GeV/c$ beam momentum, where subindices $s$ and $f$ denote the slow and fast protons of the interaction. These processes are identical to the ones we want to study at experiment E690, except for the beam momenta. The corresponding center–of–mass energies for WA76 are of $\sqrt{s} = 12.7$ and 23.8 $GeV$, respectively. It is interesting then to compare their results with the ones we obtain (we leave that comparison for Section 4.1). The main interest of experiment WA76 in the study of $K^+K^-$ and $K_s^0K_s^0$ channels[31, 32] is to identify the spin $J$ of the $\Theta/f_J(1720)$, by the observation of the angular distributions in the $f_2'(1525)$ (1.45–1.59 $GeV/c^2$) and $\Theta/f_J(1720)$ (1.59–1.83 $GeV/c^2$) regions. Owing to the angular distributions in these regions (see fig.1), for the process $pp \to p_s(K^+K^-)p_f$, they conclude that the $f_2'(1525)$ and the $\Theta/f_J(1720)$ are both compatible with having $J^{PC} = 2^{++}$. The angular distributions in the $K_s^0K_s^0$ channel were not studied due to lack of statistics.

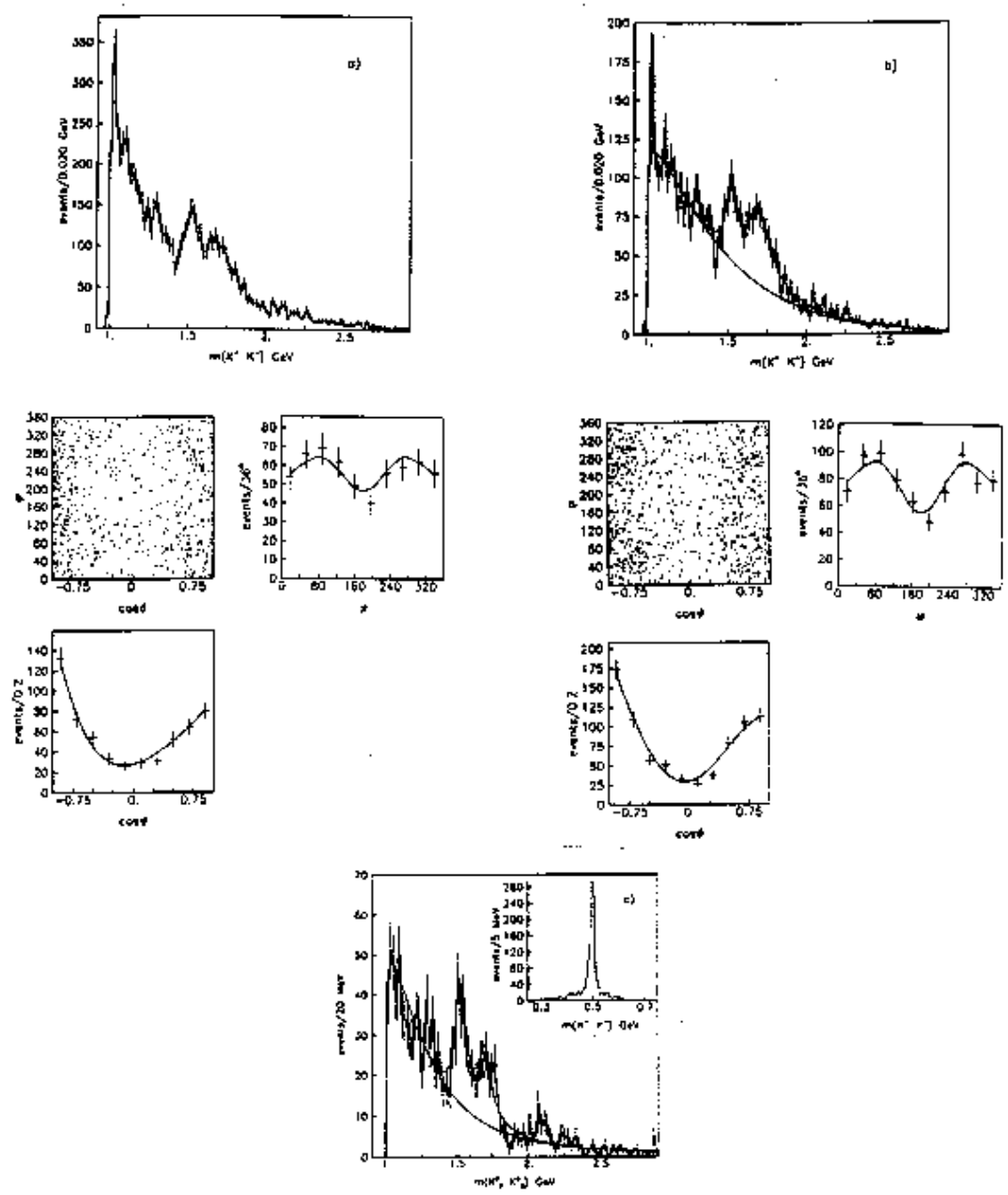

Figure 1: $K^+K^-$ invariant mass distributions from experiment WA76, at $\sqrt{s} = 12.7$ and 23.8 $GeV$, respectively (two upper plots). The six central plots show the angular distributions in the $f_2'(1525)$ (left) and $f_J(1710)$ (right) regions, respectively, for data at both CMS energies summed. Also shown, the $K_s^0 K_s^0$ invariant mass spectrum (lower plot).

Recently, the BES Collaboration[33] reported their studies on $J/\psi$ radiative decays. The channels $J/\psi \to \gamma\xi$, with $\xi$ subsequently decaying into a $\pi^+\pi^-$, $K^+K^-$, $K_s^0K_s^0$ or $p\bar{p}$ pairs, show a resonance of mass around 2232 $MeV/c^2$, with the following characteristics: (1) flavor–symmetric decays to $\pi\pi$ and $K\bar{K}$, (2) narrow width and (3) large production rate in $J/\psi$ decays. These properties make difficult to interpret the $\xi(2230)$ as a $q\bar{q}$ meson, or a multiquark state.

## 1.4 Light Meson Spectroscopy at Experiment E690

Because of its diffractive type trigger, very good track reconstruction, and very high statistics in light quark meson events, experiment E690 at Fermilab is an excellent place to look for non-$q\bar{q}$ mesons.

In this experiment, two samples of exclusive events have been selected in software for the light meson spectroscopy studies: 1) events in which all particles are reconstructed in the spectrometer, and 2) events in which there is a missing particle, which has to be reconstructed using energy-momentum conservation. The first group correspond to events of the type $pp \to p_{slow}(X)p_{fast}$. The E690 spectrometer acceptance for this kind of events is better in the region $x_F < -0.2$. The second group corresponds to events of the form $pp \to p_{missing}(X)p_{fast}$. There is better acceptance for these events in the region $-0.2 < x_F < 0$.

Two excellent works on light meson spectroscopy have already been done in the experiment. One is the study of the process $pp \to p_{missing}(K_s^0K^{\pm}\pi^{\mp})p_{fast}$, related to the $E/\iota$ puzzle. The $K_s^0K\pi$ invariant mass is plot in fig.2, and the work can be found in ref.[34]. The other study was done on the process $pp \to p_{missing}(\pi^+\pi^-)p_{fast}$, where the experiment has very high statistics[35]. The $\pi^+\pi^-$ invariant mass is shown in fig.3. Among others, processes of interest that can also be studied in the experiment are: $pp \to p(\phi\phi)p$, $pp \to p(K^*\bar{K}^*)p$, $pp \to p(K^+K^-)p$, and $pp \to p(\pi\pi\pi\pi)p$, The process of interest in the present thesis is $pp \to p_{missing}(K_s^0K_s^0)p_{fast}$.

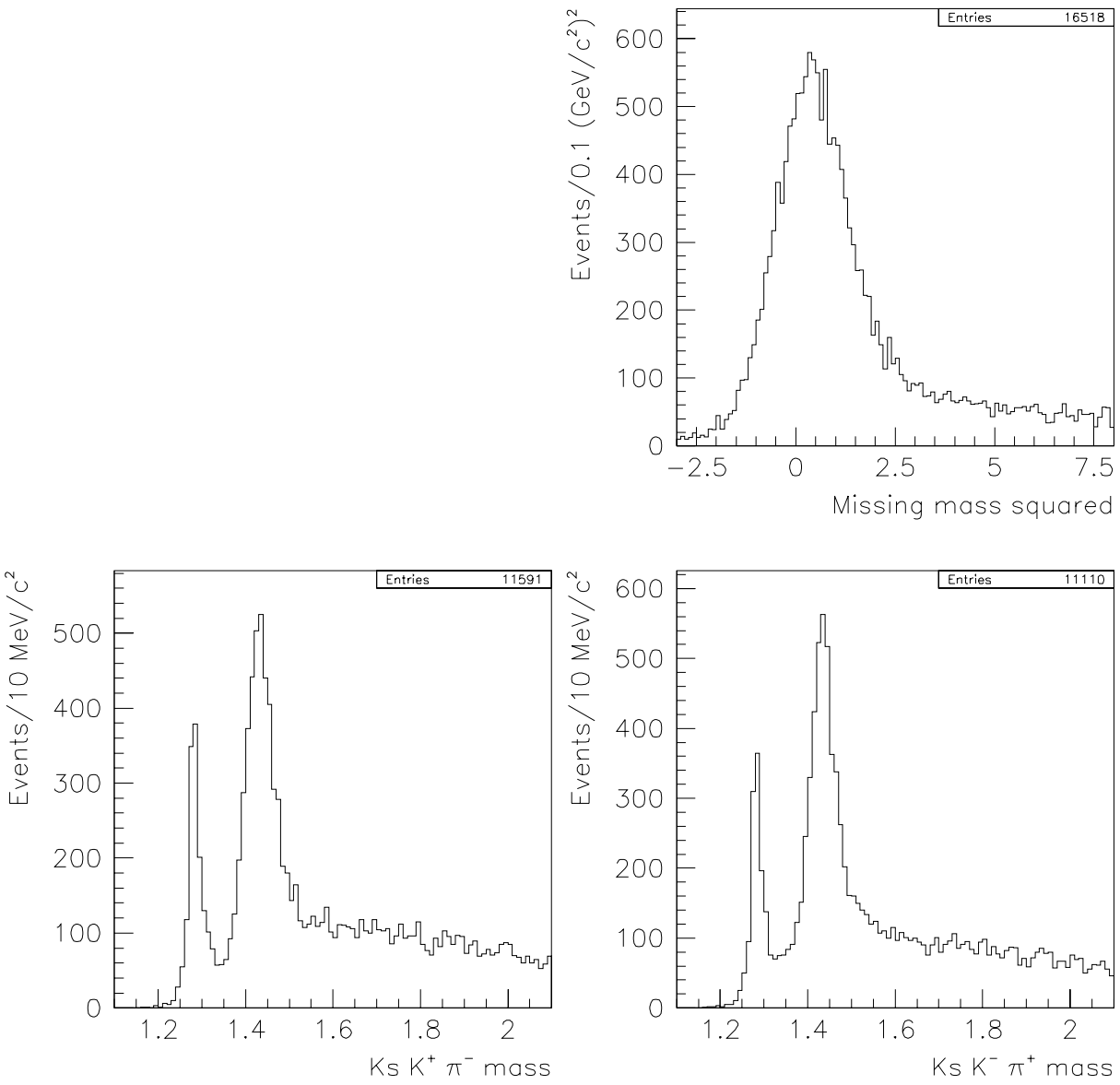


Figure 2: $K_s^0 K^{\pm}\pi^{\mp}$ mass spectrum in experiment E690. The upper plot shows the missing mass squared in the region of more interest (the two peaks in the lower plots), and the lower plots show the invariant mass for the two charge assignments, for 10% of the total data sample.

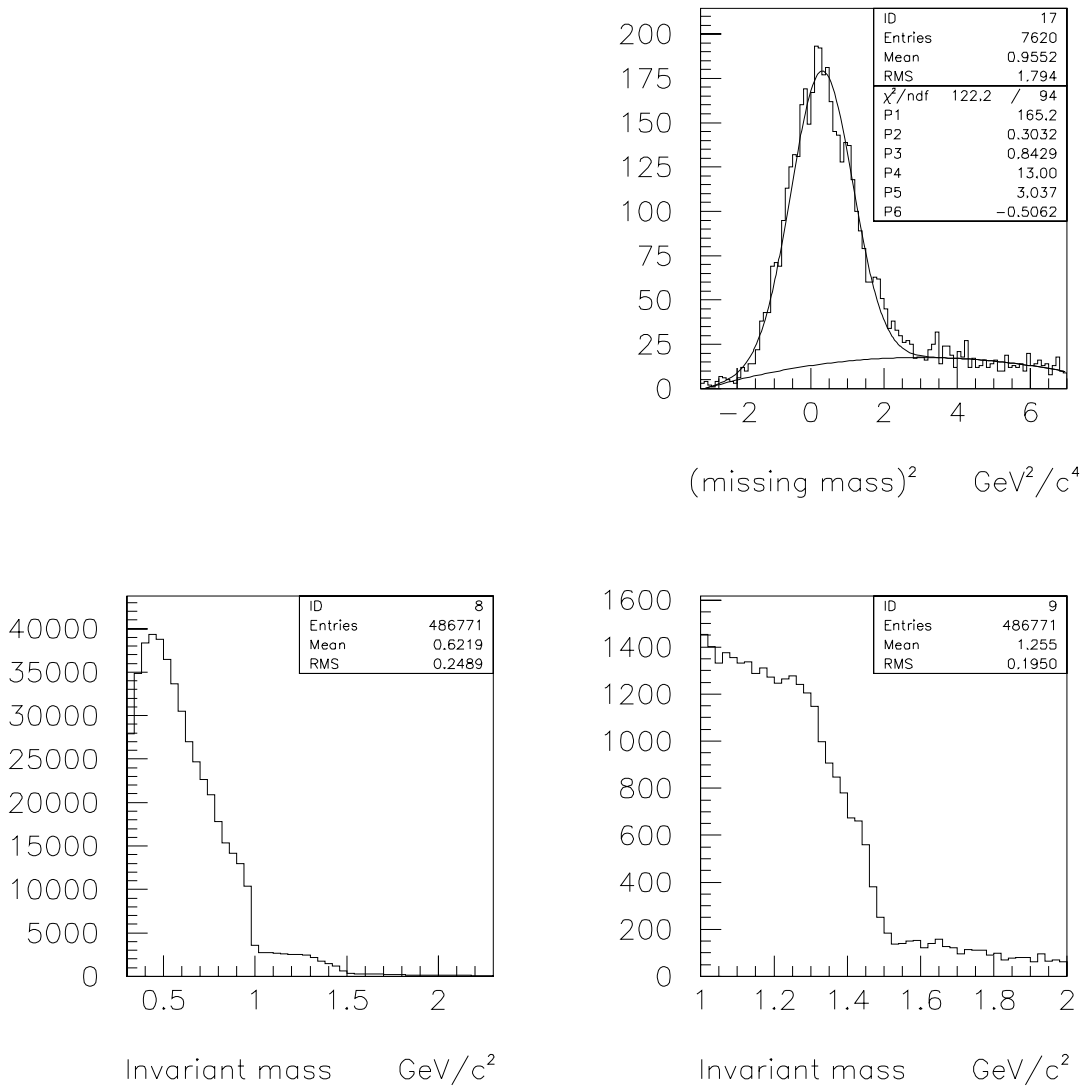


Figure 3: $\pi^+\pi^-$ mass spectrum in experiment E690. The upper plot shows the missing mass squared for these events, and the two lower plots show the mass spectrum for all events, and in the region of the $f_0(1520)$, respectively, using 2% of the total data sample. Notice the drops in the intensity distributions in the $f_0(980)$ and $f_0(1520)$ regions.

# 2 APPARATUS

Experiment E690 at Fermilab is an experiment designed to study diffraction dissociation processes with high accuracy. The E690 spectrometer (figs.4,5,6) was designed to measure high multiplicity charged final states from proton–proton interactions at high rates, and to isolate a large sample of fully reconstructed reactions, being able to operate at a rate of over $10^6$ interactions per second. It is the continuation of experiment E766 at Brookhaven National Laboratory[36, 37, 38, 39, 40, 41]. The apparatus had two main components: (a) the open geometry Main spectrometer (the Jolly Green Giant Spectrometer, JGGS, fig.5), and (b) the Beam spectrometer (see fig.4). The Main spectrometer was designed to measure particles produced in the target system. For events containing light mesons, the Main spectrometer measures particles produced in the backward hemisphere in the interaction's center–of–mass frame. The Beam spectrometer was used to make a high precision measurement of the difference between the incoming 800 $GeV/c$ beam proton and the scattered beam proton, measuring the latter in the $x_F$ range from $\sim$0.8 to 1.0.

The principal characteristics of the Main spectrometer are: 1) a 2% interaction length hydrogen target, 2) horizontal and vertical geometric acceptances of $\pm$580 and $\pm$410 mrad, respectively, 3) very good momentum resolution from 0.2 $GeV/c$ up to about 15 $GeV/c$, 4) a Freon 114 Čerenkov counter counter with a pion threshold of 2.6 $GeV/c$, and 5) a time–of–flight system with a $\pi - p$ separation up to 1.6 $GeV/c$.

The principal characteristics of the Beam spectrometer are: 1) a transverse momentum acceptance up to 0.8 $GeV/c$, 2) a longitudinal momentum acceptance from 800 $GeV/c$ down to 600 $GeV/c$, 3) a transverse momentum resolution of $\sigma \sim 7$ $MeV/c$, and 4) a longitudinal momentum resolution of $\sigma \leq 400$ $MeV/c$.

During the 1991 Fermilab fixed target run, experiment E690 wrote five billion events to tape. In the following Sections, we shall describe the various components of the apparatus. A more detailed description can be found in Ref.[42, 34].

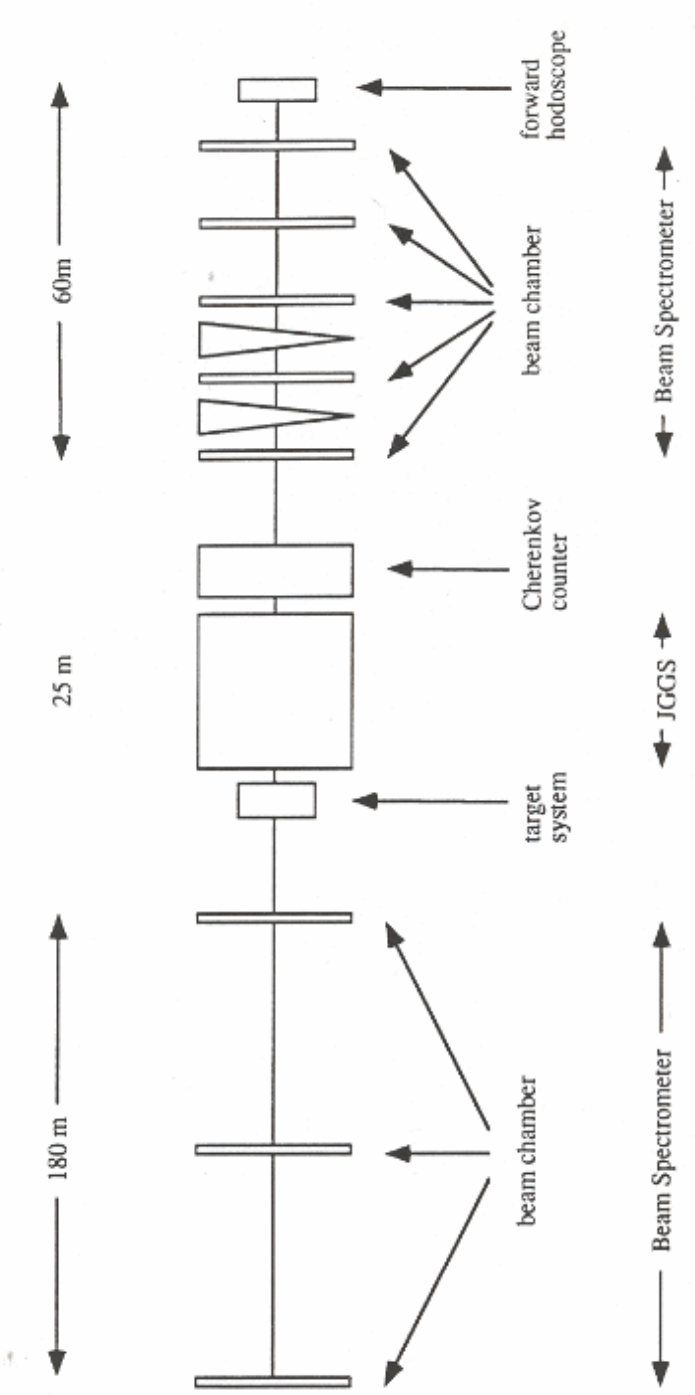


Figure 4: The E690 spectrometer (not to scale)

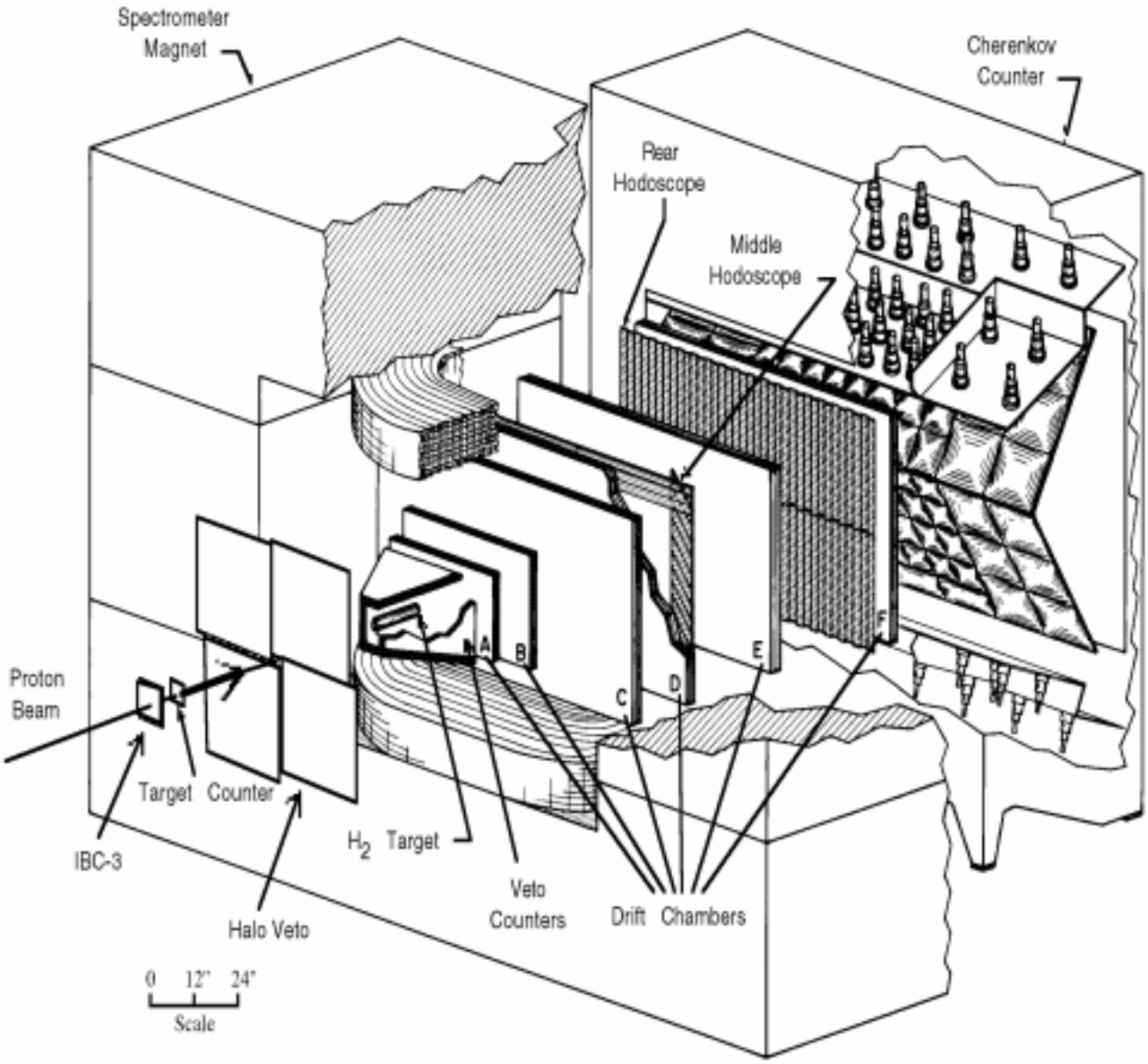


Figure 5: The JGG spectrometer.

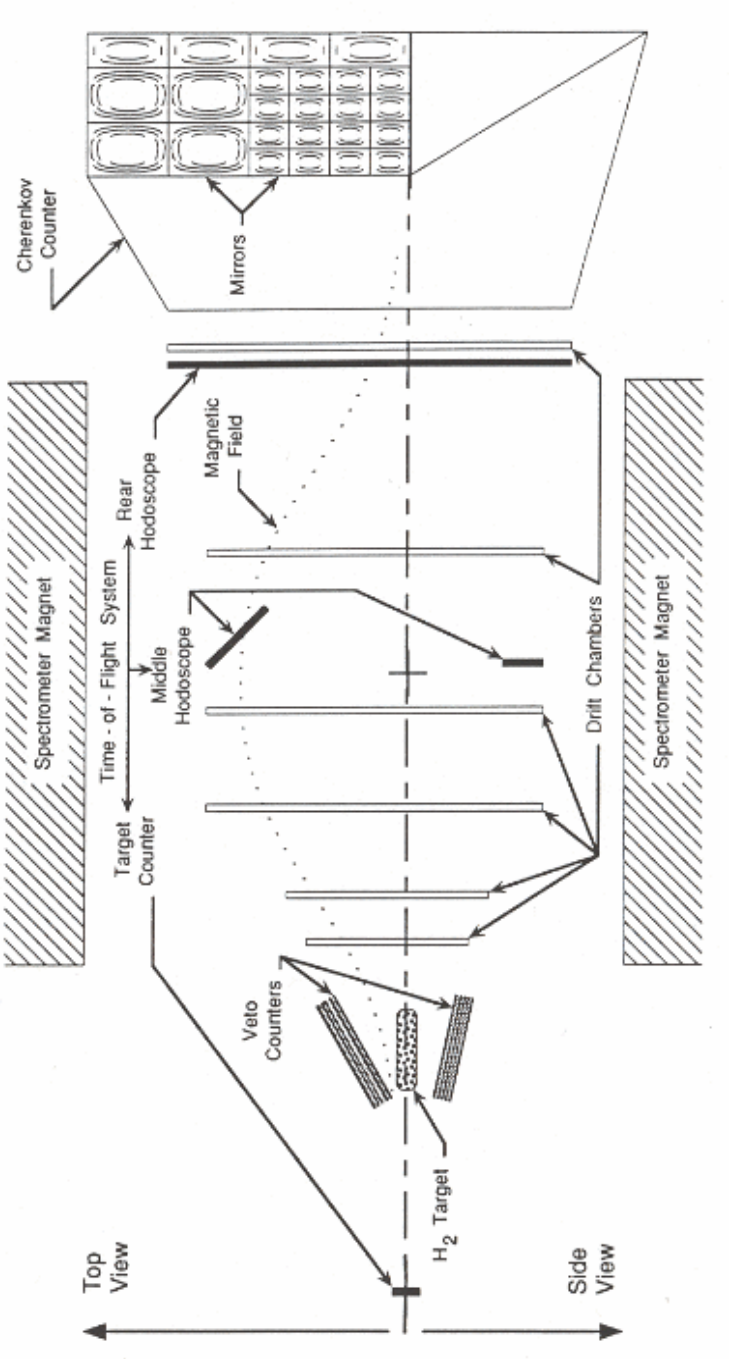


Figure 6: Schematic view of the main spectrometer. The top view ($xz$ plane) is represented above the center line; the side view ($yz$ plane) is represented below the center line. The dotted line is a profile of the main (vertical) component of the magnetic field along the beam axis of the spectrometer.

## 2.1 Beam Spectrometer.

The E690 apparatus was located in the Neutrino East (NE) beam line of Fermilab. Protons were accelerated by the Tevatron and delivered to the liquid hydrogen target with a momentum of 800 $GeV/c$ and dispersion $\delta$p/p$< 1.5 \times 10^{-4}$, for approximately twenty seconds every sixty seconds. The beam line was configured to provide a 20 mm by 2 mm horizontal ribbon beam profile at the target, with a beam intensity of $10^8$ protons per spill, on the average, corresponding to an average rate of 5 MHz. Figure 7 depicts the locations of the key elements forming the beam line.

The beam spectrometer was designed to have high position and momentum resolution, and very high rate capability. This required the use of very long lever arms, large bends, and a system of small cell and pressurized drift chambers. The beam spectrometer consisted of six 15×10cm and two 38×20 cm pressurized drift chambers spaced over 265 meters (see fig.5). Three chambers were used to measure the incoming proton trajectory into the target, with error of $\pm 10^{-6}$ rad. Five chambers, together with five beam line magnets, were used to measure the scattered proton trajectory. The magnets provided a momentum kick of 12 $GeV/c$, with a momentum resolution better than 400 $MeV/c$. The acceptance of the outgoing spectrometer was from 600 to 800 $GeV/c$ in longitudinal momentum, and of $\pm 1$ $GeV/c$ for transverse momentum.

The beam chambers consisted of a stack of four anode planes, five shared cathode planes, and two ground planes, with no field shaping wires in them. The anode planes were wound with Tungsten–Rhenium alloy wire (3% Rh), gold plated to 3-5% by weight. Fine (12 $\mu$m or 15 $\mu$m) anode wires were used with a spacing of 1 mm. or 1.5 mm. During the data taking, the chambers were operated with a gas mixture consisting of 82% argon, 15% isobutane, and 3% methylal, with a gain of approximately $10^5$.

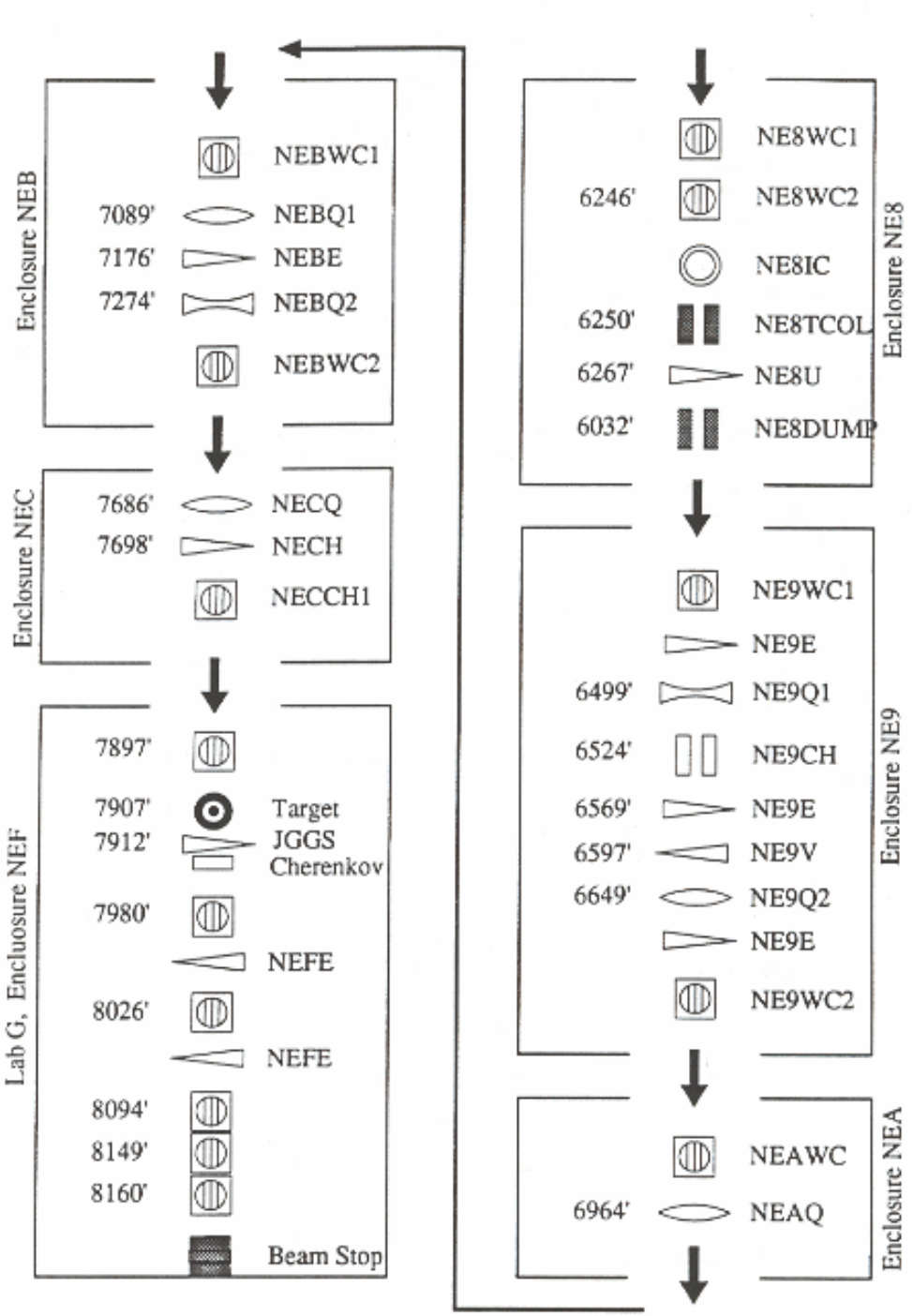


Figure 7: Fermilab Neutrino East beam line. The numbers on the left are distances from the Tevatron.

The four anode planes in a chamber were oriented at angles -21.6°, -7.93°, +7.93° and +21.6° with respect to the vertical. The cathode and ground planes were made of aluminum foil. The five cathodes were connected to a common high voltage connector through current limiting resistors.

Preamplifiers mounted on the chambers drove small differential signals to leading edge discriminators, and these drove differential signals to TDC's for drift time measurements. The TDC's encoded drift time using 2.5 nsec bins, which, for an average electron drift velocity of 40 $\mu$m/nsec in the gas mixture, corresponded to 100 $\mu$m in a chamber. Detailed specifications for the beam chambers are listed in Table 2. Construction details and performance results on these beam chambers have been presented elsewhere[43].

Downstream from the last beam spectrometer chamber was a scintillator array, called the Forward Hodoscope (FH), used to detect beam protons deflected from the 800 $GeV/c$ proton beam trajectory due to scattering in the target. Figure 8 shows FH configuration and the two types of counters of which it was made. The 3.2 cm by 1.3 cm rectangular aperture along the beam line allowed beam protons through, without triggering any of the counters. To avoid accidental triggers, two layers of counters and their coincidence signal were used for the fast trigger logic (see Sect.2.6)

## 2.2 The Target System.

The target counter, located in front of the target, was a 51 mm $\times$ 51 mm $\times$ 2 mm piece of scintillator attached to a photomultiplier. It detected and signaled the arrival of an incoming beam proton, starting various processes that read out the information coming from other parts of the detector, and determining the starting time T0 for time–of–flight measurements (see Section 2.6). T0 was the nominal time relative to which all other times in the detector were measured. Incident particles from the beam halo were rejected using an array of four scintillator counters (The Veto Thing, TVT), forming a square with a 3.2 cm by 1.3 cm rectangular aperture to allow the beam protons through.

| Beam Chamber Number | 1,2,3,4,5,6 | 7,8 |
|---|---|---|
| Horizontal Aperture (m) | 0.152 | 0.381 |
| Vertical Aperture (m) | 0.102 | 0.203 |
| Average Z Coordinate (m) | -188,-62,-5,21,35,56 | 71,78 |
| Anode Wire Diameter ($\mu$m) | 12 | 15 |
| Cathode Plane | 13 $\mu$m hard temper aluminum foil | 13 $\mu$m hard temper aluminum foil |
| Ground Plane | 13 $\mu$m hard temper aluminum foil | 25 $\mu$m hard temper aluminum foil |
| Anode to Anode Wire Spacing (mm) | 1.0 | 1.5 |
| Plane–Plane Spacing (mm) | 1.4 | 1.4 |
| Anode Wire Tension (gram) | 20 | 35 |
| Anode Wires per Plane | 160 | 256 |
| Instrumented Wires per Plane | 64,64,64,160,160,160 | 192,256 |
| Cathode Voltage (kV) | -2.1,-1.8,-2.2,-2.1,-2.1,-2.1 | -1.4,-1.4 |
| Average Efficiency (%) | >99 | >99 |
| Material in Radiation Lengths | 0.24% | 0.39% |
| Material in Interaction Lengths | 0.06% | 0.12% |
| Gas mixture | Argon 82%, Isobutane 15%, Methylal 3% | |

Table 2: Beam chamber parameters and operating characteristics.

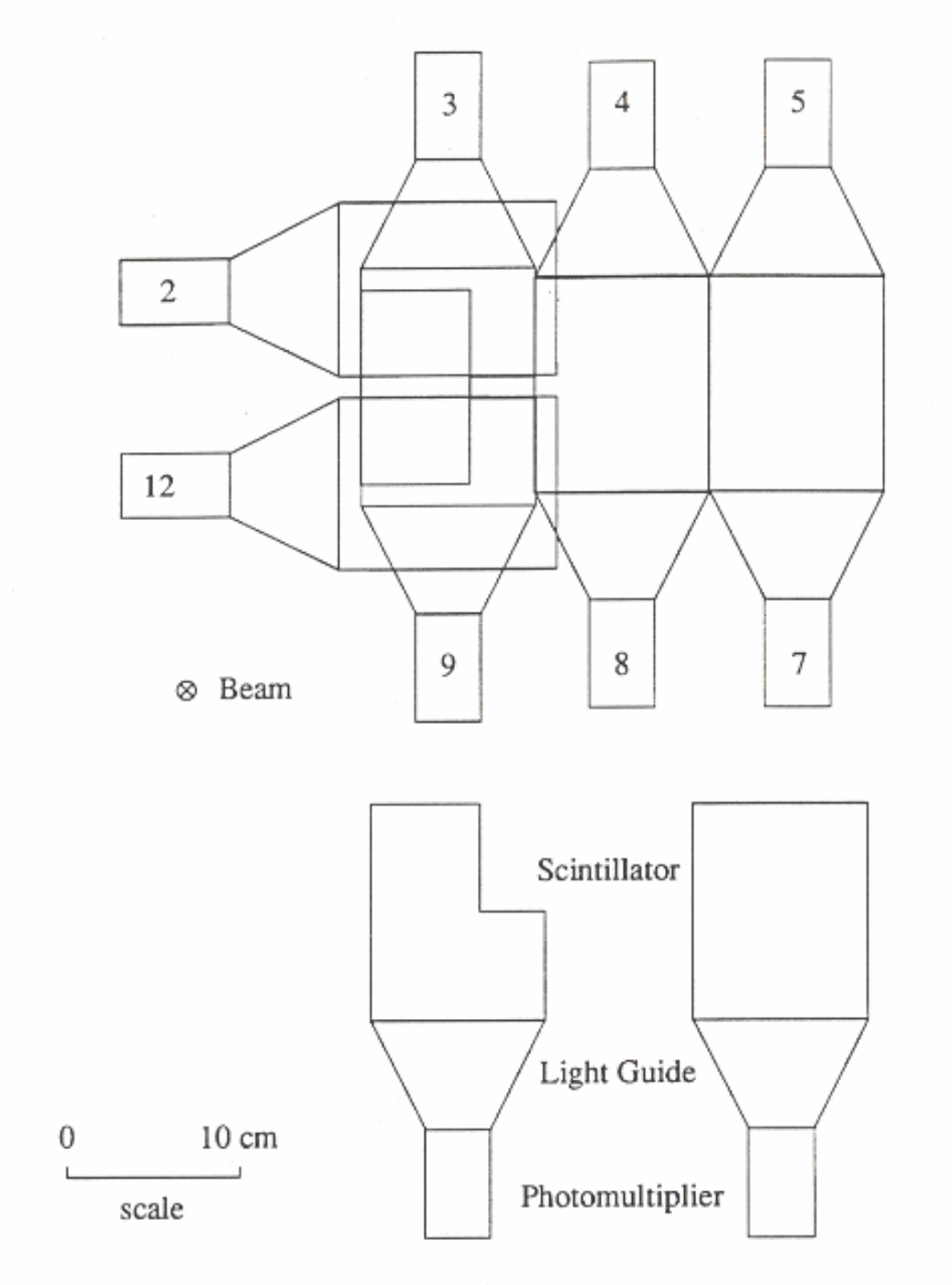


Figure 8: The forward hodoscope (top), and the two types of counters used in it (bottom).

The liquid hydrogen target was contained inside a mylar flask of cylindrical shape with semi–spherical end caps (fig.9). The target was 3.8 cm in diameter and 14.3 cm long, which corresponded to a 2% interaction length for the beam proton. The target, a cover of Rohacell and fiber glass, and the veto counters, were enclosed by an aluminum box kept under helium to minimize multiple scattering and ionization losses of the particles passing through. There were two Kapton windows at the downstream end of the veto box and the upstream end of the helium volume. All of the surrounding material in the direct path of the beam was equivalent to 0.6 cm of liquid hydrogen.

Twelve scintillator–lead sandwiches of trapezoidal shape, forming a truncated pyramid, were used to detect both charged and neutral particles that were produced at very wide angles with respect to the beam direction and that would miss the detector aperture. Each one of these Veto Counters consisted of four pieces of 3 mm thick lead and five pieces of 3 mm thick scintillators interleaved with each other. Another set of four veto counters with similar structure, between the target box and the first chamber of the JGGS, forming a picture frame outside of the chamber aperture, served the same purpose. In some stages of the run, the fast trigger system used the signals from the veto counters to reject events[44, 41].

## 2.3 The JGG Spectrometer.

The JGG spectrometer consisted of six large drift chambers imbedded in the non-uniform field of a large dipole magnet. A schematic view of the system is shown in figs.5-6. The dual constraints of large geometric acceptance and high position segmentation required that the detector be as close to the interaction target as possible, allowing the total area of the detector systems to be relatively small. The volume of the system was further reduced by placing the drift chambers inside the spectrometer magnet aperture, and the small number of chambers also lowered the amount of material in the spectrometer, reducing the probability of multiple Coulomb scattering and particle reinteraction.

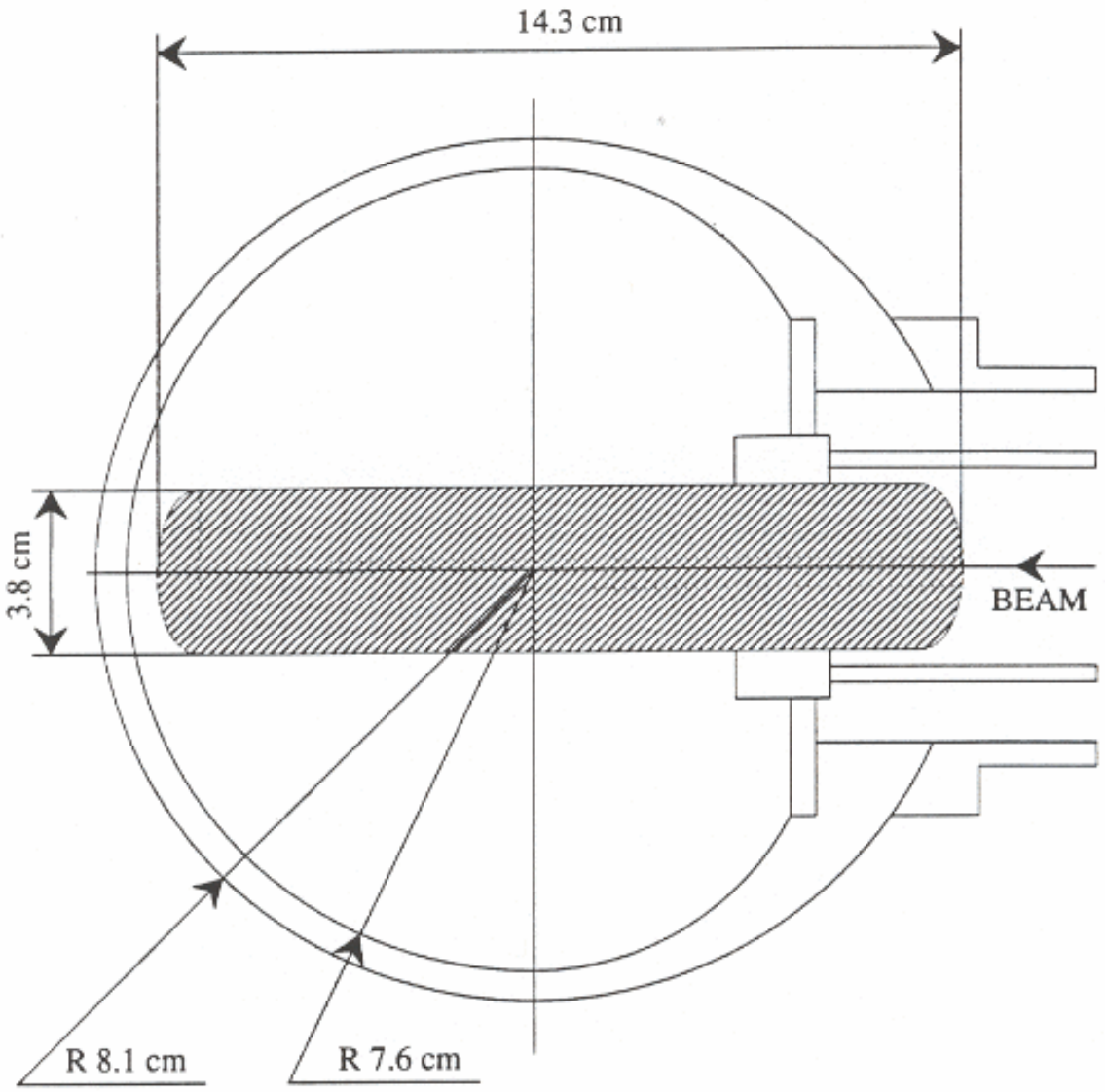


Figure 9: The liquid hydrogen target (not to scale).

The spectrometer magnet was 1.2 m high, 2.5 m wide and 2.2 m deep, with the main component of the field pointing in the vertical direction, and providing an average transverse momentum kick of 350 $MeV/c$. The three components of the magnetic field were measured using the Fermilab ZIPTRACK system[45]. The center of the spectrometer magnet served as the origin (0,0,0) for the coordinate system, with respect to which all the components of the detector were referred to.

Each drift chamber consisted of eleven wire planes: four anode planes (at -21.6°, -7.93°, 7.93°, and 21.6°), five cathode planes and two ground planes. The wires in the cathode and ground planes were positioned vertically, and there were no field shaping wires in the system. The anode-to-anode wire spacing ranged from 2 mm for the chamber closest to the target, to 3.5 mm for the chamber at the rear of the spectrometer magnet. The small anode-to-cathode spacing (3 mm) minimized the chamber memory time, and permitted the chambers to operate efficiently at megacycle rates in conjunction with fast electronics. There was a total of 11,264 instrumented wires. Each channel of the drift chamber electronics consisted of a preamplifier, a discriminator, and a time-to-digital converter (TDC). The inner-chamber volumes were filled with helium gas to reduce the amount of material. Each chamber constituted only 0.15% of radiation length of material. The drift chamber parameters and operating characteristics are listed in Table 3.

The narrow wire spacing provided high detection efficiency, allowing the reconstruction of trajectories without use of the measured drift times. The drift times were used later to improve the measurement of the previously found and fitted tracks. These trajectory measurements, and a precise knowledge of the magnetic field, made it possible to obtain with high accuracy the charge and momenta of each particle.

The JGG spectrometer achieved single plane efficiencies of greater than 99%. The spatial resolution of each plane, when fully optimized, was in the range of 150-200 $\mu$m. The horizontal and vertical geometric acceptances in the lab were $\pm$580 mrad and $\pm$410 mrad, respectively.

| Drift Chamber Number | 1 | 2 | 3 | 4 | 5 | 6 |
|---|---|---|---|---|---|---|
| Horizontal Aperture (m) | 0.762 | 0.914 | 1.524 | 1.524 | 1.524 | 1.829 |
| Vertical Aperture (m) | 0.457 | 0.610 | 1.016 | 1.016 | 1.016 | 1.219 |
| Average Z Coordinate (m) | -1.017 | -0.839 | -0.513 | -0.138 | 0.456 | 1.229 |
| Anode Wire Diameter ($\mu$m) | 20 | 20 | 25 | 25 | 25 | 25 |
| Cathode Wire Diameter ($\mu$m) | 102 | 102 | 102 | 102 | 102 | 102 |
| Gound Wire Diameter ($\mu$m) | 102 | 102 | 102 | 102 | 102 | 102 |
| Anode to Anode Wire Spacing (mm) | 2.0 | 2.0 | 3.2 | 3.2 | 3.2 | 3.5 |
| Cathode to Cathode Wire Spacing (mm) | 1.1 | 1.1 | 1.1 | 1.1 | 1.1 | 1.1 |
| Ground to Ground Wire Spacing (mm) | 2.0 | 2.0 | 3.2 | 3.2 | 3.2 | 3.5 |
| Anode to Cathode Plane Spacing (mm) | 3.2 | 3.2 | 3.2 | 3.2 | 3.2 | 3.2 |
| Anode to Wire Tension (gram) | 65 | 65 | 90 | 90 | 90 | 90 |
| Number of Instrumented Wires | 1536 | 1920 | 1920 | 1920 | 1920 | 2048 |
| Cathode Voltage (kV) | -2.60 | -2.60 | -2.15 | -2.10 | -2.10 | -2.05 |
| Average Efficiency (%) | >99 | >99 | >99 | >99 | >99 | >99 |
| Gas mixture | Argon 71%, Isobutane 25%, Methylal 4% | | | | | |

Table 3: JGG drift chamber parameters and operating characteristics.

The system was capable of measuring charged particles with momenta in the range of 150 $MeV/c$ to 20 $GeV/c$, with momentum resolution $\Delta$P/P=0.002 P (FWHM). The mass resolution of the reconstructed $\Lambda^\circ$ and $K_s^0$ are 1.75 and 4.5 $MeV/c^2$ (FWHM), respectively. Further details of the drift chamber construction, performance, and electronics have been presented elsewhere[36, 37].

## 2.4 Time-of-Flight System.

The Time–of–Flight (TOF) system provided direct particle identification for non-relativistic charged particles having momentum less than 1 $GeV/c$ for $\pi$-$K$ separation, and less than 1.6 $GeV/c$ for $\pi$-$p$ separation. The identification is bassed on the fact that lighter particles travel faster than heavier particles of the same momentum. Thus, it is possible to distinguish between pions, kaons, and protons by comparing the time the particle used to travel a given distance to the predicted time for a pion, kaon or proton, relative to the nominal "event T0" determined by the target counter.

The TOF system consisted of 102 plastic scintillator counters arranged in two hodoscopes. The middle hodoscope, located between chambers 4 and 5, consisted of 30 counters arranged in a picture frame to cover only the outer region of the detector aperture, and was used to detect particles that passed through the first four chamber, but would most likely not reach the rear hodoscope. The rear hodoscope consisted of 72 counters covering the full downstream aperture of the spectrometer magnet (see fig.10). Twelve of the middle hodoscope counters consisted of 762 mm $\times$ 51 mm $\times$ 13 mm pieces of scintillator, and eighteen (positioned at a 45° angle) consisted of 298 mm $\times$ 79 mm $\times$ 13 mm pieces of scintillator. Each rear hodoscope counter consisted of a 610 mm $\times$ 51 mm $\times$ 3 mm pieces of scintillator, except for the middle four counters, which were 5 cm shorter to leave a 10 cm $\times$ 10 cm rectangular aperture in the middle of the hodoscope, to allow beam protons to pass without triggering any of these counters.

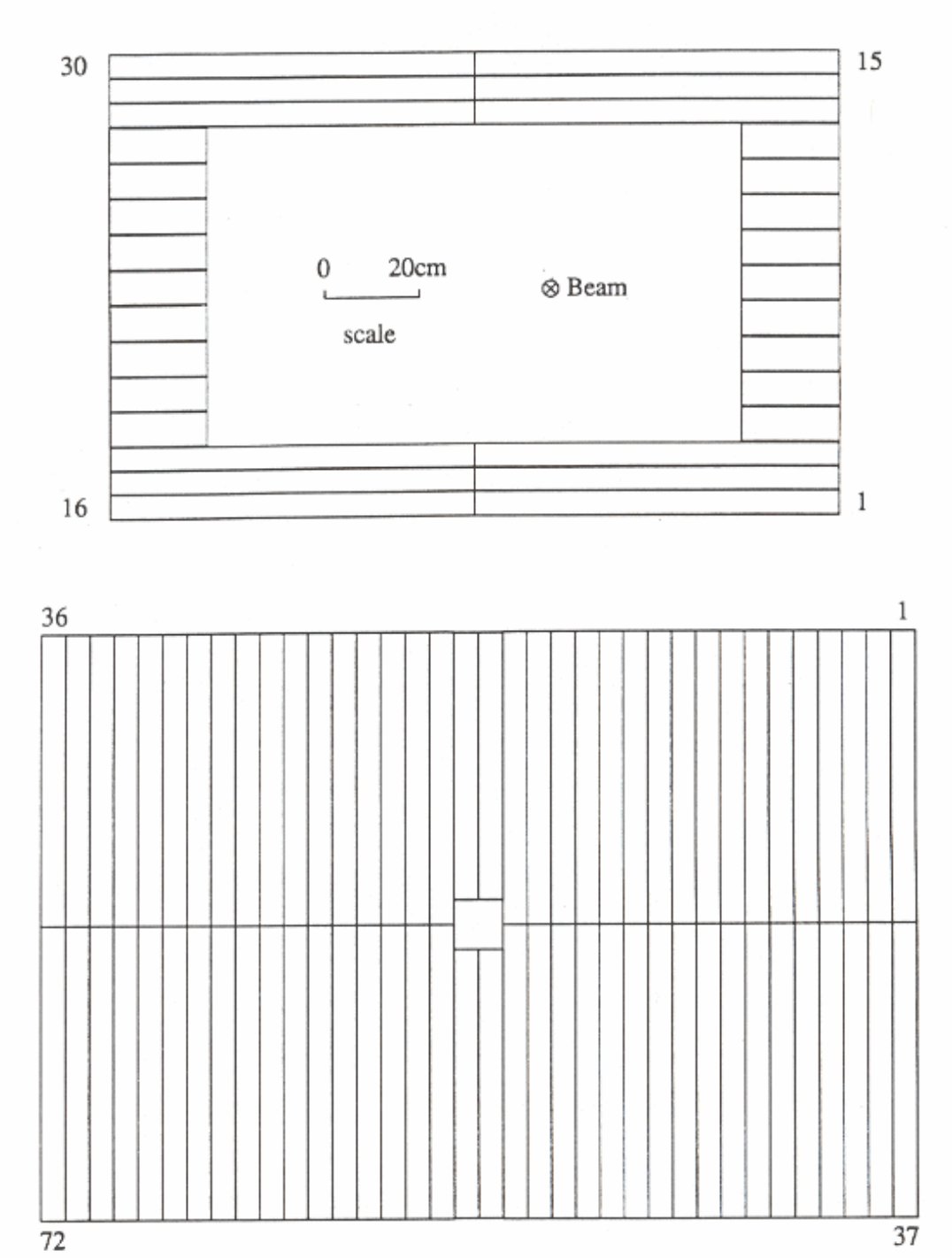


Figure 10: Layouts of scintillators for the Middle (top) and Rear (bottom) Hodoscopes.

The light collected in the counter was guided to a photomultiplier tube by a Lucite light guide glued at one end, and was first amplified by the photomultiplier base. Each photomultiplier base generated one analog and two digital signals: an analog signal for the pulse area measurement, proportional to the ionization produced by the particle, one digital signal for fast event triggering, and the other one for measuring the arrival time. Details of the electronics for amplification, discrimination and digitization of these signals have been described elsewhere[44, 37]. This system achieved greater than 95% detection efficiency and a $\sigma$ =600 psec arrival time measurement, providing a $\pi$-$K$ separation up to 1 $GeV/c$, and a $\pi$-$p$ separation up to 1.6 $GeV/c$ for the rear hodoscope.

## 2.5 The Čerenkov Counter.

The Čerenkov counter provided direct identification of charged particles having momenta above the range where the TOF could be used. This measurement is based on the Čerenkov effect: a charged particle radiates light in a medium if the speed of that particle exceeds the speed of light in that medium.

The Čerenkov counter was located immediately downstream of chamber 6 and had the same aperture as this chamber (see fig.6). It was used to distinguish pions, kaons and protons, and in some cases electrons. The medium was Freon 114 ($C_2Cl_2F4$) at atmospheric pressure, with a refraction index of 1.0015. This means that a charged particle with a speed exceeding 0.9985c radiated light inside the counter. The momentum thresholds for pions, kaons and protons were 2.5, 9.0 and 17.1 $GeV/c$, respectively. The threshold momentum for electrons was 0.0093 $GeV/c$, and thus, any electron that reached the Čerenkov detector would radiate light. The Čerenkov counter consisted of 96 mirrors arranged in two planes forming an angle of 120° between them, and 30° with respect to the vertical (see fig.11). Toroidal mirrors were used to reflect and focus the Čerenkov light from the counter mirrors onto photomultiplier tubes, which measured the arrival time and intensity of the light. Each photomultiplier was surrounded by a reflective cone to increase the amount of light collected.

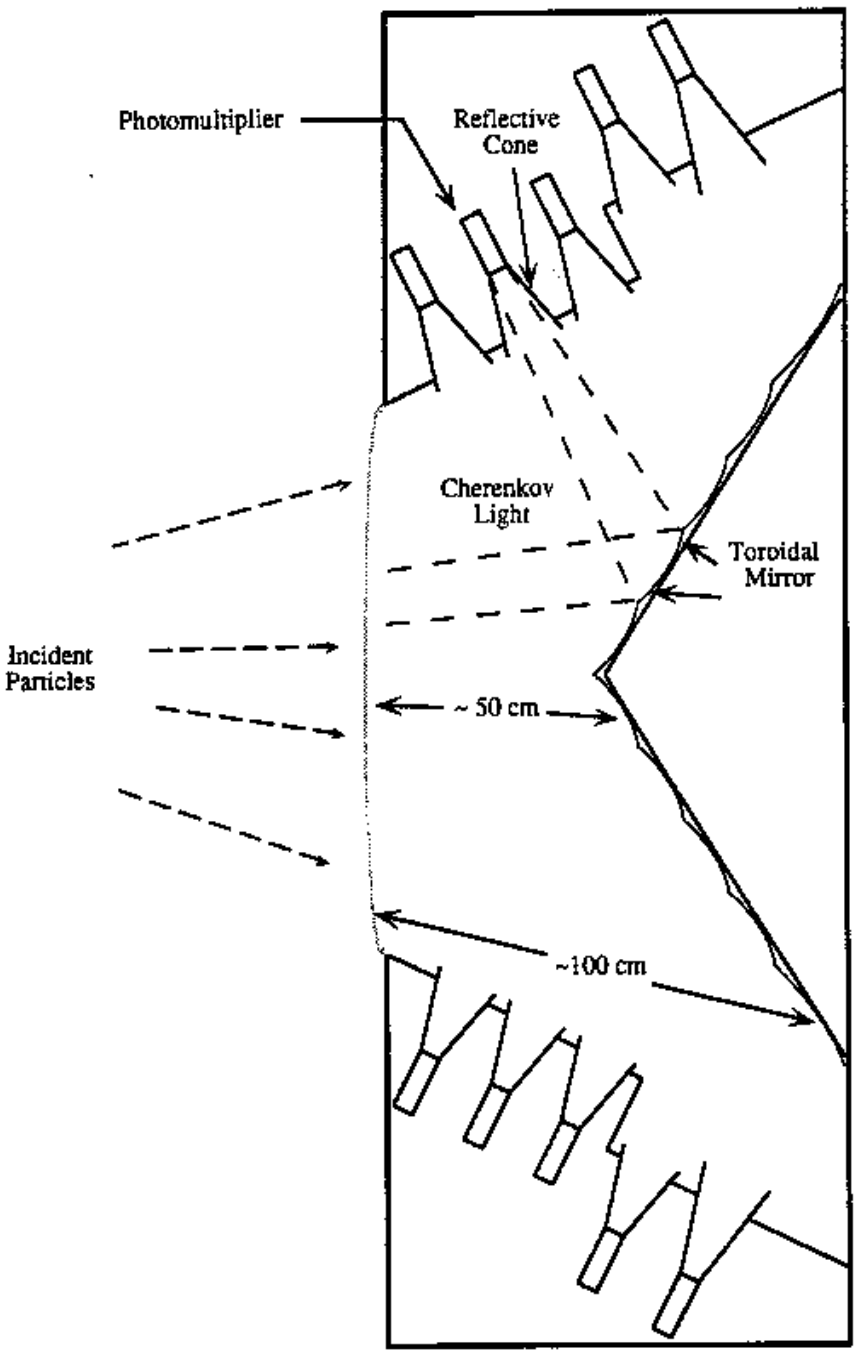


Figure 11: Side view of the Čerenkov counter. The radiator is Freon 114.

Small mirrors covered the central part of the counter, where most of the particles passed through (rapid pions and kaons produced in the $pp$ interaction).

The alignment of mirrors, photomultipliers, and reflecting cones maximized light collection for an infinite momentum particle (a straight line trajectory) that projected upstream to the target. Because the quantum efficiency of the photocathodes is highest at an optical wavelength of $\sim$ 4200 Å, all photomultiplier faces were coated with P-terphenyl that converted ultraviolet light to 4600 Å so that more Čerenkov light could be detected. Each photomultiplier generated three signals: two digital signals which gave the arrival time of the light, and an analog signal which gave the area of the output pulse, proportional to the amount of Čerenkov light radiated. The area measurement of the analog signal was converted to number of photoelectrons, and then compared to the number of photoelectrons predicted for a particular hypothesis: $e$, $\pi$, $K$, or $p$. Details of the design and construction of the Čerenkov counter have been presented elsewhere[36, 46].

## 2.6 Trigger and Data Acquisition System.

E690 trigger and data acquisition system was designed to trigger and read out events at rates higher than 10 MHz of beam, with a rate of about 1 MHz interactions in the liquid hydrogen target. It made use of low cost, easily implemented and maintained electronics. The architecture of this system provided zero suppression (only channels containing measurement information would be read), maximum "wire hit" limits (a drift chamber might have a cluster of wires turned on with actually only one track), and high level digital signal processing. The trigger and data acquisition system is shown in fig.12.

The trigger system was designed to detect an incoming beam proton, determine whether the proton interacted with a target proton (by looking at the signals in the spectrometer counters), determine that the interaction was not due to the beam halo, and determine whether the beam proton had lost enough energy to produce an interesting high missing mass event.

The data acquisition system contained four levels of triggering:

1. trigger gate initial (TGI),

2. trigger gate 2 (TG2),

3. trigger gate 3 (TG3), and

4. the multiplicity logic (MLOG).

A typical TGI required the presence of a signal from the target counter (TC) and from at least one counter from either the middle or the rear hodoscopes (this signal is called "FOR", Fast OR). It also required the absence of a TGI signal in the previous 30 ns, and the presence of the Master Gate signal. The Master Gate signal had a true value when the beam was present, the high voltage in the drift chamber systems was on, the beam line magnets were on, and the manual gate switch was on.

A typical TG2 required the presence of the TGI, the absence of halo counter ($\overline{\text{TVT}}$) and veto counter ($\overline{\text{VETO}}$) signals, a signal from the Majority Logic that at least one counter from either the middle or rear hodoscopes was on (GT0), and that the readout sequence for a previous event was not in progress. A detailed description of the TGI and TG2 electronics can be found in ref.[37]

Many of the events that triggered the TGI could not be processed, because a previous event was being read out. The TG2 electronics recorded the number of TGI triggers that were processed, and these triggers were referred to as live TGI triggers. After a preset number of live TGI triggers (typically 256 or 4096), an event was accepted without any requirements. These events were called prescale events, and were tagged so that they could be identified and used in the data calibration and analysis.

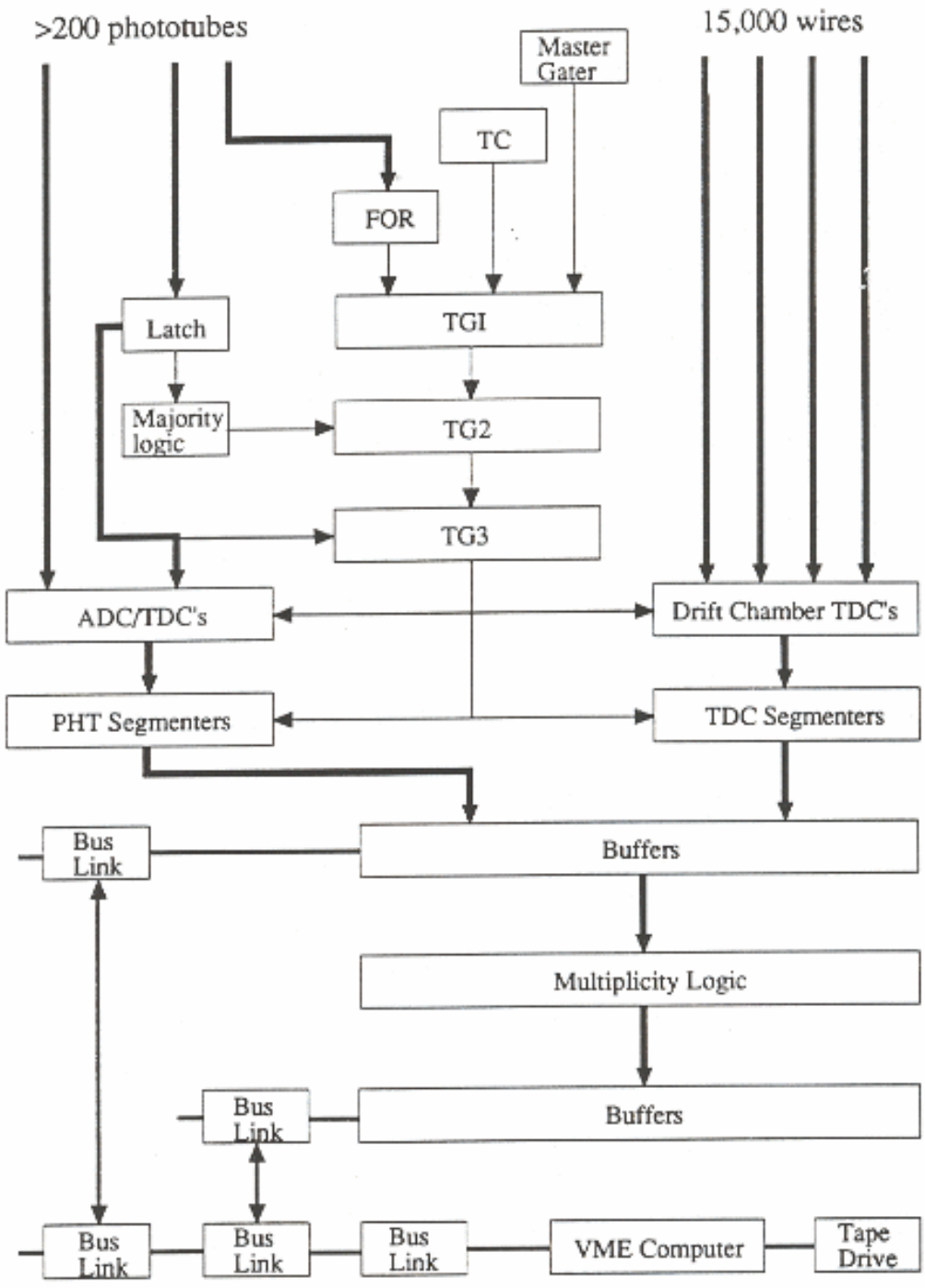


Figure 12: E690 data acquisition system.

The signal from each set of the forward hodoscope counters (FH1 and FH2) was used to select preferentially diffraction dissociation events. In order to reduce random triggers from photomultipliers noise, TG3 was made of the coincidence of FH1 and FH2. A positive decision at TG3 level would initiate the digitization of the detector signal information, which had been 'stored' by cable delay.

The time required to read out the measurement data for an event was greatly reduced by limiting the amount of data that could be read out of the drift chambers to 31 wires per drift chamber plane. The process of triggering, digitizing, and reading out an event took from a few hundred nanoseconds to a few microseconds (average $4\mu$s) depending on the number of tracks in the event. Once read out, the detector information was stored in a set of buffers and then transferred through the Nevis Transport System (NTS [47, 37]) to the MLOG, where the last trigger decision was made, based on the number of clusters of hit wires in the drift chamber system, to estimate the multiplicity of final state charged particles. The MLOG trigger requirement ensured that the beam track of an event had an excellent chance to be reconstructed off-line. Thus, rather stringent conditions were imposed on the beam chamber multiplicity. Only loose conditions were applied to the JGG chamber system.

Table 4 lists both the beam chamber and JGG chamber requirements for the MLOG trigger. The four columns of numbers shown in the table indicate the lower and upper limits (inclusive) imposed on the number of clusters found in the drift chambers. Two basic types of MLOG triggers were used. The first required numbers of wire clusters consistent with a single beam proton. The second also allowed a second beam proton.

Finally, events that passed all triggers were written to tape. They were transferred from the MLOG through a set of buffers to the memory of a VMEbus computer (FORCE CPU-29). The computer then sent the data to a Honeywell VLDS tape drive. The data acquisition system of this spectrometer system was capable of a digitization and readout rate of $12 \times 10^6$ bytes/sec, corresponding to roughly $12 \times 10^3$ events/sec. It took about $6 \times 10^6$ events and 40 minutes, depending on the trigger, to fill a VLDS tape. The various trigger conditions

and number of events written with each trigger are listed in Table 5. The table lists the two TGI trigger conditions, two TG2 trigger conditions, two TG3 trigger conditions, one MLOG trigger condition, and corresponding number of events in each category. Approximately $5.5 \times 10^9$ events were recorded in a 100-day period.

| TRG_12 | | | | |
|---|---|---|---|---|
| TRIGGER | 1 | 2 | 3 | 4 |
| JGG–2–2 | [2,31] | — | [3,31] | — |
| JGG–3–2 | — | [2,31] | — | [3,31] |
| IBC–123–2 | [3,4] | [3,4] | [3,8] | [3,8] |
| IBC–123–3 | [4,5] | [4,5] | [4,9] | [4,9] |
| OBC–12–1 | [1,31] | [1,31] | [2,31] | [2,31] |
| OBC–12–3 | [2,31] | [2,31] | [3,31] | [3,31] |
| OBC–3–3 | [1,8] | [1,8] | [3,10] | [3,10] |
| OBC–45–1 | [1,8] | [1,8] | [3,10] | [3,10] |
| OBC–45–3 | [1,8] | [1,8] | [3,10] | [3,10] |

Table 4: Processor multiplicity trigger (MLOG).

| Group | TGI | TG2 | TG3 | MLOG | Events ($\times 10^9$) |
|---|---|---|---|---|---|
| 4–5 | TC | GT1•$\overline{\text{TVT}}$ | — | TRG_12 | 0.72 |
| 6 | TC | GT0•$\overline{\text{TVT}}$ | FH1•FH2 | TRG_12 | 0.06 |
| 7–12 | TC•FOR | GT0•$\overline{\text{TVT}}$ | FH1•FH2 | TRG_12 | 2.96 |
| 13 | TC•FOR | GT0•$\overline{\text{TVT}}$ | FH1•FH2 | TRG_12 | 0.54 |
| 13 | TC•FOR | GT0•$\overline{\text{TVT}}$ • $\overline{\text{VETO}}$ | FH1•FH2 | TRG_12 | 0.36 |

Table 5: E690 run summary.

## 2.7 The Hardware Processor

The hardware processor [48, 37, 40] consisted of over 700 modules, each assembled on a separate printed circuit board. It was used to perform off-line event reconstruction to process the entire data sample of $5.5 \times 10^9$ events. It can be described as the hardware implementation of a computer program, but with boards functioning independently, simultaneously, and with

no external intervention. Each board performed its specific arithmetic or logical operation whenever a valid data was present at its input.

Figure 13 shows a block diagram of the processor. The hardware was arranged in nine different subroutines. It could deliver 40 Giga operations per second, and had a band width on the order of Gigabytes per second. The processor track reconstruction performed four functions for each track: track finding, matching, fitting, and cleaning-up. The number of tracks, the charge of each particle and the vector momenta of the particles were available to determine if this event should be discarded or saved for further analysis.

Events satisfying the following criteria were selected:

1. at most one of the veto counters on,
2. at least two JGG tracks,
3. at least one beam track,
4. (longitudinal momentum balance) $\leq$ $(3 + \Delta P_z^{beam}) GeV/c$,
5. about 10% of the prescale events,

where $\Delta P_z^{beam}$ is the longitudinal momentum loss by the incoming beam proton. These criteria reduced the number of events written to the output tape by a factor of 20. Studies show that only about 50% of the exclusive candidates were lost in this process, with an increase of signal to background ratio by a factor of 10.

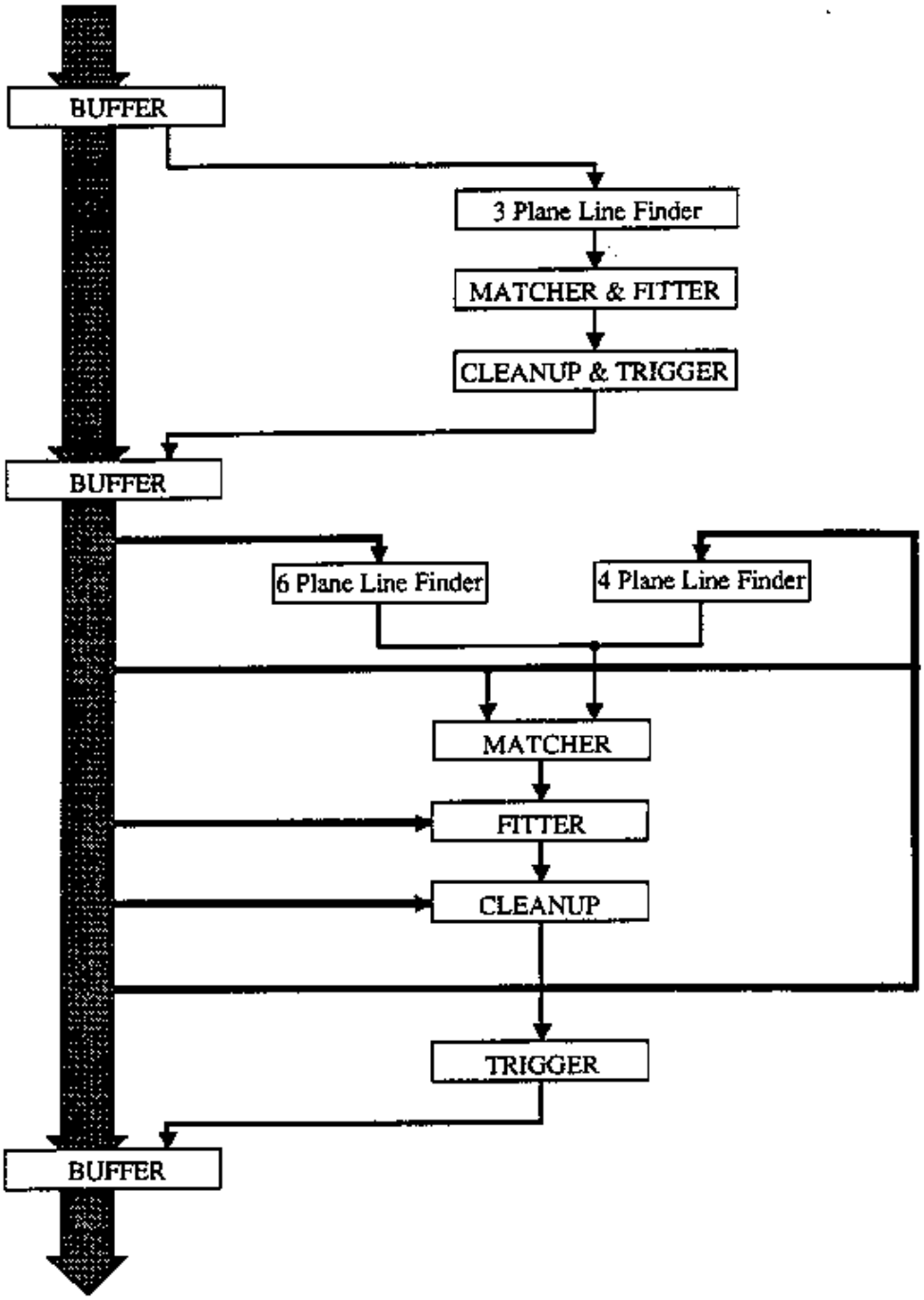


Figure 13: The block diagram of the E690 processor.

# 3 EVENT RECONSTRUCTION AND SELECTION

The data selection is performed in four analysis steps. At the first step, the raw drift chamber data is used to reconstruct charged particle trajectories through the magnetic field. This step was executed by a special purpose computer[48], the "hardware processor", with programmable selection criteria. This step is referred to as PASS1. The second reconstruction step finds any remaining trajectories and the vertices formed by the intersection of the tracks. This step of the analysis is referred to as PASS2. The third step corresponds to the selection of events with a particular topology, in this case, those which correspond to the process

$$p\ p\ \rightarrow\ p_{missing}\ K^0_s K^0_s\ p_{fast}$$

and the fourth step corresponds to the physics analysis.

## 3.1 PASS1: Track Reconstruction.

Drift chambers were used to measure the positions of charged particles produced in proton-proton interactions. A pattern recognition algorithm used these trajectories to find straight tracks in the the beam spectrometer, and curved tracks consistent with the motion of charged particles in the non-uniform magnetic field of the JGG spectrometer.

PASS1 reconstructed four types of tracks: 3-chamber beam tracks, and 6-chamber, front 4-chamber and back 4-chamber JGG tracks. Particles passing through the three incoming beam chambers, or the last three of the five outgoing beam chambers, were reconstructed as 3-chamber straight beam tracks, since there was no magnetic field in these regions. The JGG tracks were fit to trajectories through the non-uniform magnetic field of the JGGS. The fitted track parameters provided the charge and momenta of the trajectories, which were later used to reconstruct the interaction and decay vertices.

The track reconstruction consisted of four stages: track finding, matching, fitting and cleaning-up. PASS1 reconstructed particle trajectories from the list of wire addresses, the corresponding drift times, and a set of constants generated from measurements of the mag-

netic field and chamber geometry. In the beam chambers, PASS1 looked for 3-chamber tracks first, by looking for all combinations of first chamber and last chamber wire hits, and predicting the hits at the middle one. If the hit existed within a 5-wire wide road, the pair was tagged as a track candidate. The track candidates were then paired and the other two views were predicted. An iterative least-square fit was performed using the wire hits from the three chambers (twelve planes in all). At the end, the clean-up routine removed duplicate tracks.

In the JGGS, PASS1 looked for the most constrained tracks first, the 6-chamber tracks, which had 19 constraints (4-chamber tracks had 11 constraints) if all wire hits were present. In each view of the drift chambers, PASS1 obtained three wire numbers and the deviation from a straight line to represent the track, called sagitta (see fig.14). Combinations of hits in the chambers were used to define track candidates. In the ideal case, each particle would generate four track candidates, one for each of the four views. By checking for similar sagittas, the PASS1 matcher subroutine matched the tracks found in one view with the corresponding tracks found in a second view to obtain 3-dimensional particle trajectories. It then used those trajectories to generate wire predictions in the other two views. If predicted wires were found, the pair of trajectories was considered a track candidate. The same procedure was repeated to obtain a second 3-dimensional trajectory using the track candidates in the other two views, to avoid reconstruction inefficiencies. Figure 13 shows the logic flow of the PASS1 algorithm.

The pattern recognition described above used only wire addresses and ignored drift times. The fitter calculated the initial parameterization from the set of wire addresses received from the matcher. It then performed an iterative least-square fit to find the parameters that best fit the particle trajectory. After three iterations the drift times were included for another three iterations to utilize the increased precision of the measurements in the drift chambers.

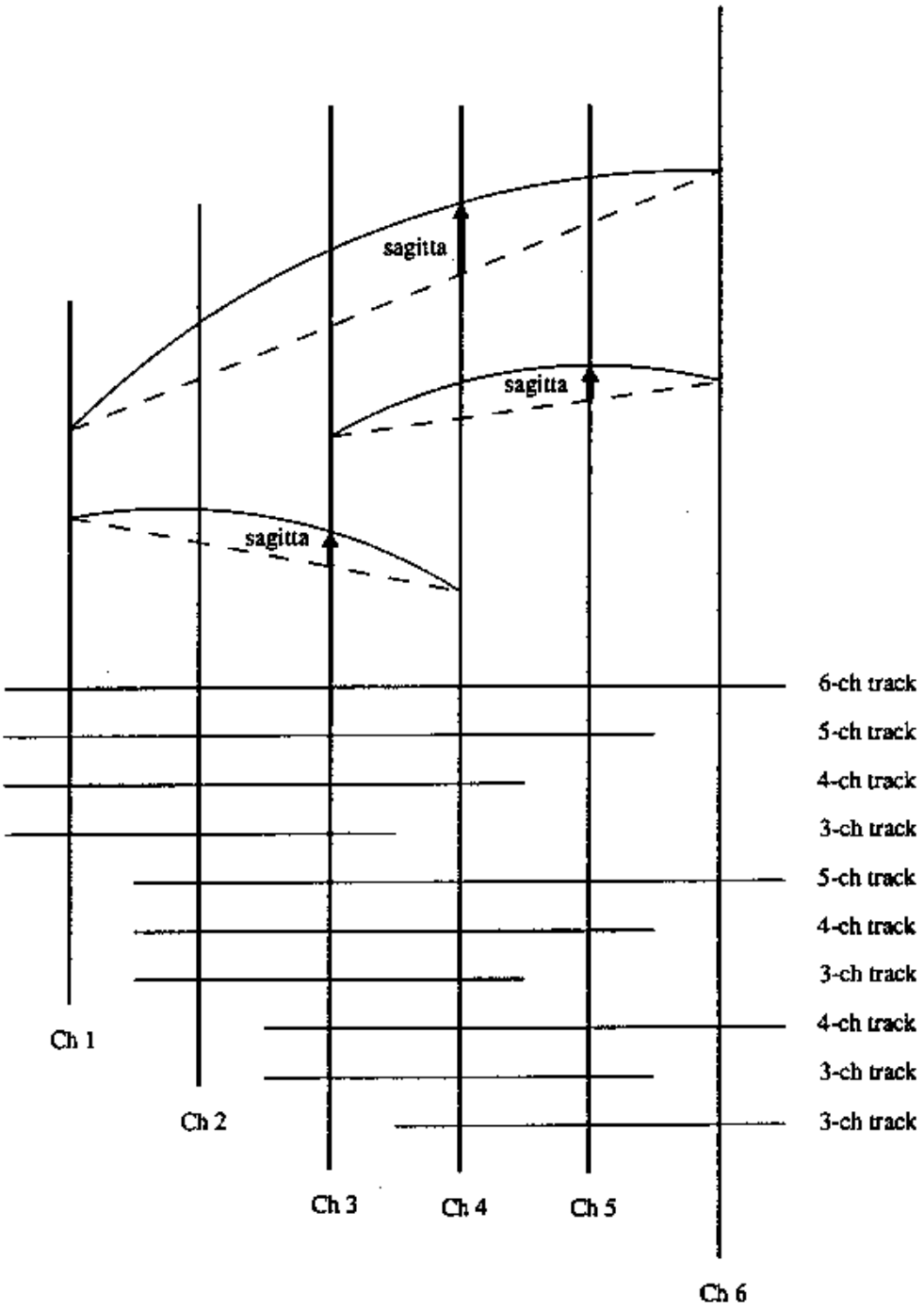


Figure 14: PASS1 and PASS2 track types and parameter definition.

Finally, the clean-up subroutine eliminated duplicate tracks, and tagged the wire addresses utilized for 6-chamber, front 4-chamber, and back 4-chamber tracks. The average event had one beam proton in and out, and four charged tracks from the break-up of the target system, though events with more than twelve tracks were not rare.

## 3.2 PASS2: Vertex Reconstruction.

The next step in the analysis was to locate the vertices where the particles interacted or decayed. PASS2 found the vertices formed by the track trajectories, improved PASS1 track reconstruction, and found any remaining tracks.

This process began by matching the incoming 3-chamber beam tracks, to the outgoing 3-chamber beam tracks, to generate the JGGS beam track(s). Any wire hits on the beam track were tagged, so that they would not be used in the subsequent reconstruction. The excellent reconstruction of the beam trajectory was used to locate the interaction vertex.

PASS2 removed duplicate tracks that survived the clean-up stage of the PASS1 track reconstruction, and refit the PASS1 tracks. Those wire hits that remained unassigned were used to form candidate tracks and trajectories not found by PASS1. This class of trajectories included low momentum trajectories that were difficult to reconstruct in the non-uniform magnetic field of the spectrometer magnet, and trajectories that PASS1 was not designed to find, like 3-chamber tracks and 4-chamber tracks starting in chamber-2 and ending in chamber-5, etc. (see fig.14).

The search for a primary vertex, the initial point of collision between a beam and a target proton, used the well defined beam track as a constraint. This constraint limited the primary vertex's $x$- and $y$-coordinates to those of the beam track, and only allowed the $z$-coordinate to vary. The JGG tracks were assigned to groups of closest approach to the beam track. Assuming there was only a primary vertex, it was defined as the most upstream multiparticle vertex inside the target, or the one with higher number of crossing tracks, in the case of more than one primary vertex candidates.

If a primary vertex was not found, PASS2 would combine two tracks at a time to see if they intersected. If they did, PASS2 generated a composite track and asked if the composite track intercepted the beam track. This algorithm would find events with only two tracks in the JGGS forming a $V^0$ (such as $\Lambda^\circ$ or $K_s^0$) which intersected the beam trajectory in the liquid hydrogen target. Then, all assigned tracks were refit to a primary vertex. Not all tracks would pass close enough to the vertices found in this procedure, to be considered part of a vertex. These tracks were referred to as unassigned tracks.

PASS2 then looked for other vertices using the unassigned tracks first, and the list of assigned tracks. If an assigned track was found to form a secondary vertex, it was removed from the assigned list and the event was refit.

Reconstructed vertices could provide particle identification by using track momenta to measure the invariant mass of long-lived particles. Children particles were constrained kinematically to have an invariant mass equal to the parent mass. The tracks forming a separated vertex were assigned all possible particle identities ($e^\pm$, $\pi^\pm$, $K^\pm$, $p$, $\bar{p}$, compatible with Čerenkov information). If the mass of the decayed particle was within broad limits of the accepted value for a known particle, the separated vertex was labeled as the decay point of that particle, and particle identities were permanently assigned to the child particles. Nine different particles were identified this way: $\gamma$, $K_s^0$, $\Lambda^\circ$, $\bar{\Lambda}^\circ$, $\Xi^-$, $\bar{\Xi}^+$, $\Omega^-$, $\bar{\Omega}^+$, $K^\pm$ (see fig.15).

PASS2 used another kinematic constraint which involved only the measured three-momenta of the child particles. Figure 16 shows a scatter plot of $P_T^*$ versus the asymmetry parameter, defined as $(P_L^+ - P_L^-)/(P_L^+ + P_L^-)$, for pairs of oppositely charged particles that form distinct vertices. $P_T^*$ and $P_L$ are the transverse and longitudinal components of the children momenta with respect to the parent. The largest of the three elliptical distributions is formed by $\pi^+$-$\pi^-$ pairs from $K_s^0$ decay. $p$-$\pi^-$ pairs from $\Lambda^\circ$ decay form the ellipse on the right side of the plot, and $\bar{p}$-$\pi^+$ pairs from $\bar{\Lambda}^\circ$ decay form the mirror image on the left.

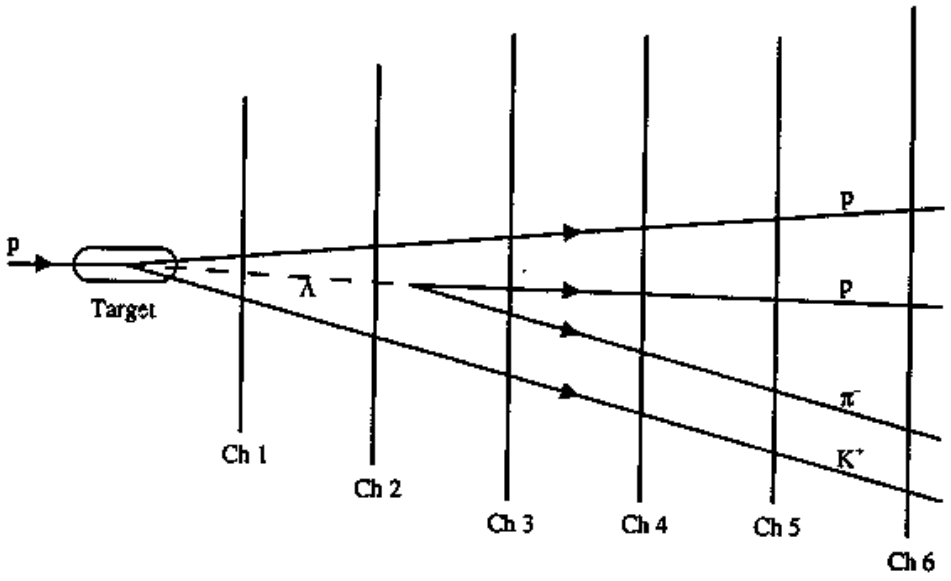


Figure 3.2 Illustration of PASS2 vertex reconstruction.

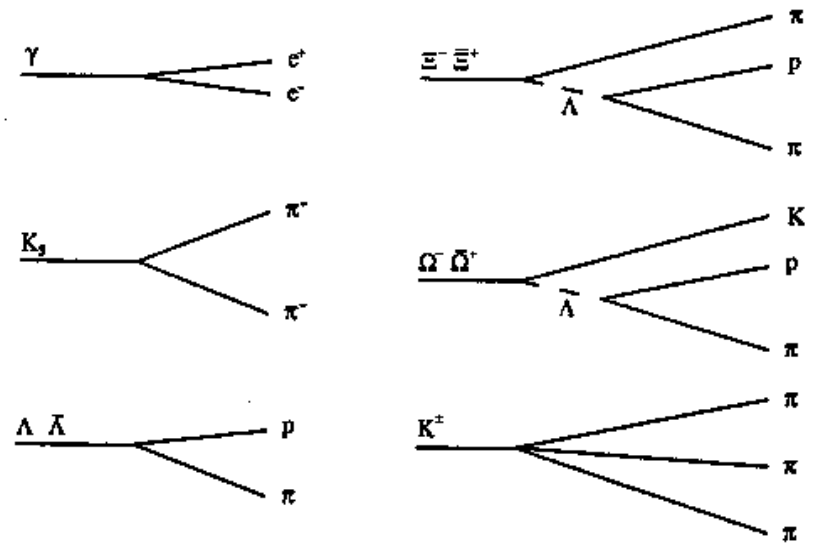


Figure 15: PASS2 vertex reconstruction (upper plot), and PASS2 vertex types and their reconstructed decay modes (six lower plots).

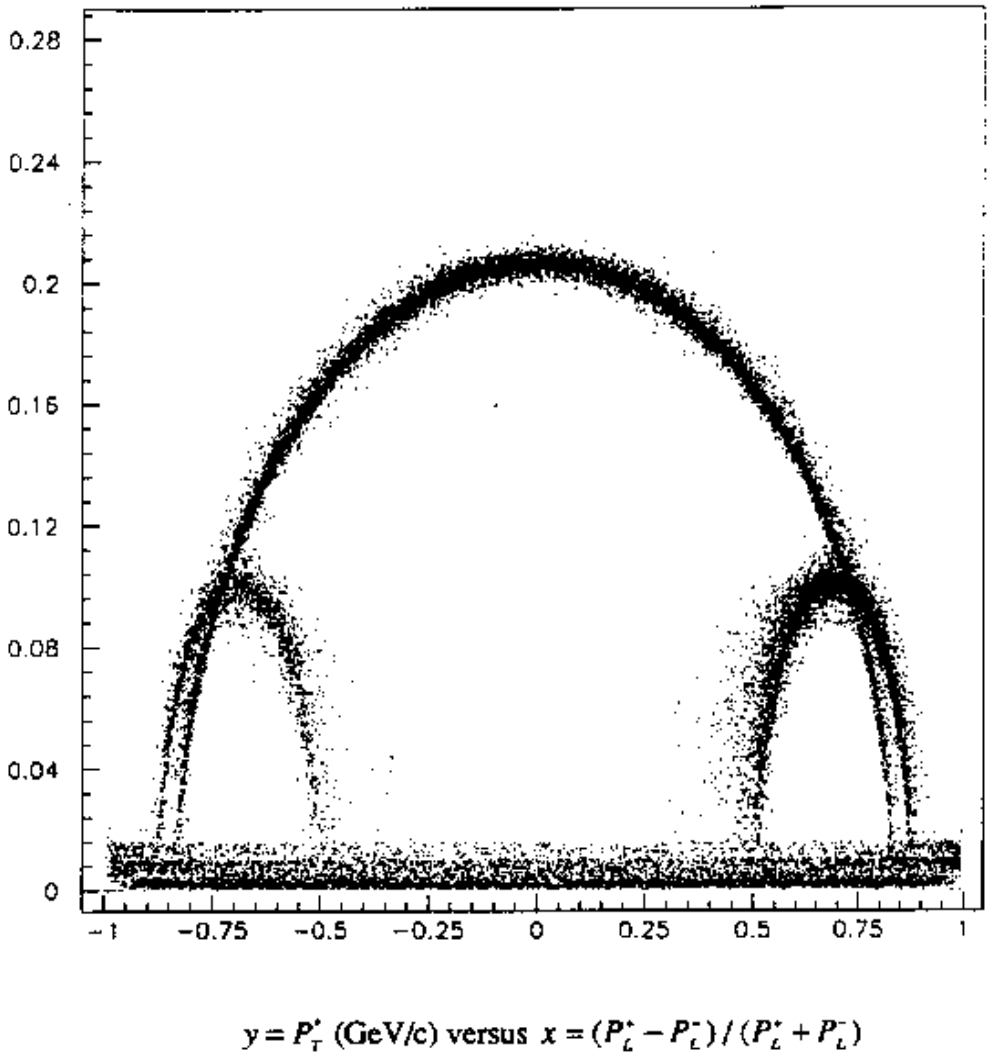


Figure 16: $P_T^*$ versus $(P_L^+ - P_L^-)/(P_L^+ + P_L^-)$ for vertices formed by a pair of oppositely charged particles reconstructed in the JGGS. $P_T^*$ is the transverse momentum, and $P_L^+$, $P_L^-$ are the longitudinal momenta of the positive and negative particles, respectively, defined with respect to the momentum sum of the pair. The large ellipse corresponds to $K_s^0 \to \pi^+ + \pi^-$ decays. The smaller ellipses on the right and left correspond to $\Lambda^0 \to p + \pi^-$ and $\bar{\Lambda}^0 \to \bar{p} + \pi^+$ decays, respectively. Photon conversions to $e^+e^-$ pairs in material contribute the band at small $P_T^*$.

The locations of the maximum in these distributions depend only on the rest masses of the parent and children particles. Their intercepts with the horizontal axis depend on the velocity of the children particles in the parent's rest frame. Non-relativistic parent particles cause horizontal smearing of the distribution outer edges. The band at the bottom contains $e^+$-$e^-$ pairs from $\gamma$ conversion. Note that while the density of the $K_s^0$, $\Lambda^\circ$ and $\bar{\Lambda}^\circ$ distributions decrease with decreasing $P_T^*$ (due mainly to phase space), on the scale shown, the $e^+$-$e^-$ distributions increases slightly with decreasing $P_T^*$. In the rest frame of a decaying particle there is a maximum available momentum for the child particles. Background can be reduced by not considering pairs of tracks as candidates for a determined vertex, if either track has a transverse momentum greater than the maximum allowed value, $P_T^* \leq P_{max}$. Figure 16 also shows regions of kinematic overlap, were we are not able to determine uniquely the identity of the secondary vertex by kinematics only. In these cases, the use of the Čerenkov counter and Time-of-Flight for direct particle identification could be used. The Čerenkov and Time-of-Flight were not use for the $K_s^0 K_s^0$ analysis.

In summary, there were three cuts imposed by PASS2 in searching for secondary vertices: 1) the distance of closest approach; 2) the maximum momentum, $P_T^* \leq P_{max}$, and 3) the invariant mass, $M - \Delta \leq M_X \leq M + \Delta$.

## 3.3 Data Selection for $K_s^0 K_s^0$ Analysis.

The sample we used for this analysis consisted of $\sim 546 \times 10^6$ events, that is, around 10% of the total number of events recorded by this experiment. The Select sample obtained after PASS2[2] consisted of $\sim 89 \times 10^6$ events. From this, we selected 28309 events of the type $pp \to pK_s^0 K_s^0 p$ using the following criteria:

a) one primary vertex (see fig.17), with two secondary vertices (with two charged tracks each) and a fast forward proton assigned to it,

b) zero good unassigned tracks in the event,

c) each secondary vertex should be $K_s^0$ compatible.

[2]For the $K_s^0 K_s^0$ analysis, we used events processed with version 13 of PASS2 (PASS2V13).

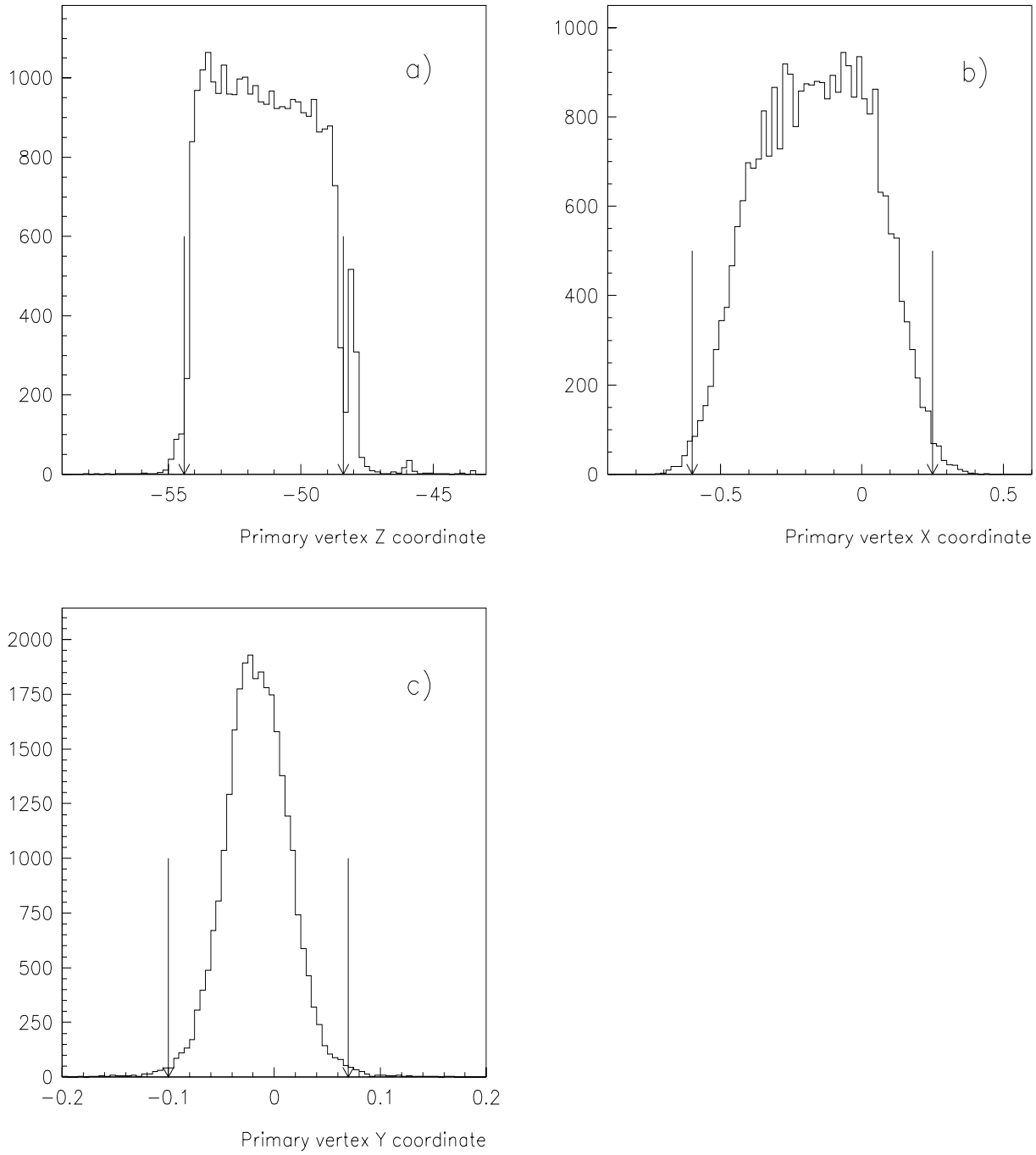


Figure 17: $z$, $x$ and $y$ coordinates (a,b,c, respectively) of the primary vertex (in inches) for the selected events. Arrows denote the cuts imposed on the primary vertex position to ensure that the vertex lies inside the LH2 target. The peak at the right in the $z$–coordinate corresponds to the Rohacell cover of the target.

## 3.4 Background Analysis.

In the analysis we present here, for the reaction $pp \rightarrow p_s(X)p_f$, the slow proton is reconstructed using energy–momentum conservation relations, that is, we do not use fully reconstructed events, and this makes it very likely that $X$ not only consists of two $K^0_s$, but also of neutral particles that would not be detected by the spectrometer, like $\pi^0$'s, or charged particles which do not enter the geometrical acceptance of the spectrometer. What one does is to use the different parts of the spectrometer, and kinematical constraints, to cut the background events. After that, one has to make an estimate of the number of remaining background events, in order to subtract this number from the sample to obtain the number of real events.

In the next two Sections we present the methods we used to take into account background events. First, we describe the way we used the veto counters and the veto collar to cut events in which, beside the missing proton, there is a signature of other unwanted particles. Secondly, we describe the method used to "count" the number of background events under the missing mass squared peak, that could not be removed using the different parts of the spectrometer, nor using kinematical requirements.

### 3.4.1 Using the Vetoes to Cut Background Events.

Figure 18 shows upper and side views of the veto counter and veto collar arrays, together with the first two drift chambers in the magnet aperture, and the LH2 target. One can see in this figure that the spectrometer has a limited acceptance for tracks with high $p_T$. The vertical acceptance ($y$–axis in the laboratory frame) was $\pm 410$ mrad, while the horizontal acceptance was $\pm 580$ mrad. The particles that do not enter the spectrometer are very likely to hit one of the vetoes (or two, in the case of overlapped vetoes). Then, if the missing proton had enough energy to leave the LH2 target, it is feasible to know if it actually hit the veto that is on, or if it was something else that hit it.

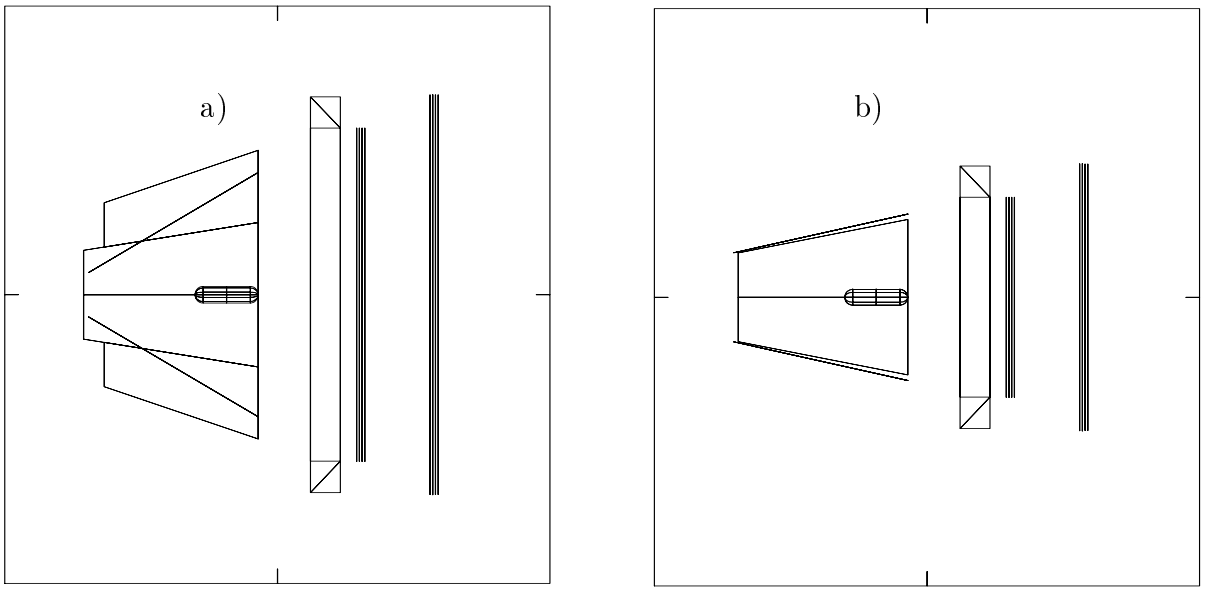


Figure 18: (a) Top and (b) side view of the veto box and veto collar. The first two chambers downstream are also visible.

In order to know if the missing proton hit a veto that is on, we used the missing transverse momentum, $p_T$, which our spectrometer measures with high accuracy, and a very simple idea: look at the angle traced by the missing proton in the $x$–$y$ plane in the laboratory, $\phi = \arctan(p_y/p_x)$, and compare it with the geometrical acceptance of each veto in this angle. If the veto is off, keep the event. Then look at the TDC and ADC signal coming from each veto, if that veto is on. If the veto is on, and the missing proton is pointing to it, keep the event. If the veto is on, but the missing proton is not pointing to it, and the ADC signal is high, meaning that a real particle hit this veto, throw away the event.

A few plots will help to clarify this matter. In fig.19 we plot the mentioned variables for veto counter number 1. In fig.19a we see the distribution of angle $\phi = \arctan(p_y/p_x)$, representing the direction of the missing proton, for events when this veto is on. We can see a clear peak around 250° (shaded area), meaning that these are the events in which the missing proton hit the veto. We keep these events. The other entries in this plot could be due to electrical noise in the veto, knock on electrons (which we do not consider part of the event), or particles coming from the interaction of the beam with the target, that is, particles

that are part of the event, additional to the two $K_s^0$ and the protons. This last possibility is part of the background, and one should cut these events. Therefore, we look for more information coming from the veto. Figure 19b shows the ADC *vs* TDC for all events when the veto is on. We can see a flat band in 0<ADC<20 units, and another distribution around 70 units in TDC. The flat band we assume are knock on electrons, or electrical noise, in the veto. The other structure we consider it as coming from particles belonging to the event. In fig.19c, we have the same plot as in fig.19b, but for the events with the missing proton pointing to the veto (shaded area in fig.19a). We can see a clear distribution for high ADC, and the same band as in (a) but with fewer events. All events in this plot are kept. In fig.19d we see the cases when the missing proton is not pointing to the veto. From this events, we keep those in the flat band (noise in the veto), and cut the events above this band, which are events with extra particles from the $pp$ interaction hitting the veto.

Our original sample consisted of 28309 events. In 20379 events (∼72%) there was at least one veto on, where veto means one of the veto counters or one of the counters in the veto collar. Of these, 6436 (∼23%) had the missing proton pointing to the veto (each veto covering a different $\phi$ region), and 10580 had a ADC–TDC signal in the "noise" region (flat band in fig.19). The remaining 3363 events (∼12%) had at least one veto on, the missing proton not pointing to any of these vetoes, and a high ADC signal. These events were cut, and we ended up having 24946 events. In fig.20a we plot the missing mass squared for all the events that survived the veto–cut (solid line). The shaded area represents the events cut. Figure 20b is the same as fig.20a but in the region of interest for us, $1.4 \leq M(K_s^0 K_s^0) \leq 1.9\ GeV/c^2$. We can see again that most of the background under the missing mass squared peak is in the low mass region. We also plot the $K_s^0 K_s^0$ invariant mass for events that passed the veto–cut, fig.20c, and cut events, fig.20d. One can see that there is no evident structure in the region of interest, the cut events having an exponentially decaying distribution.

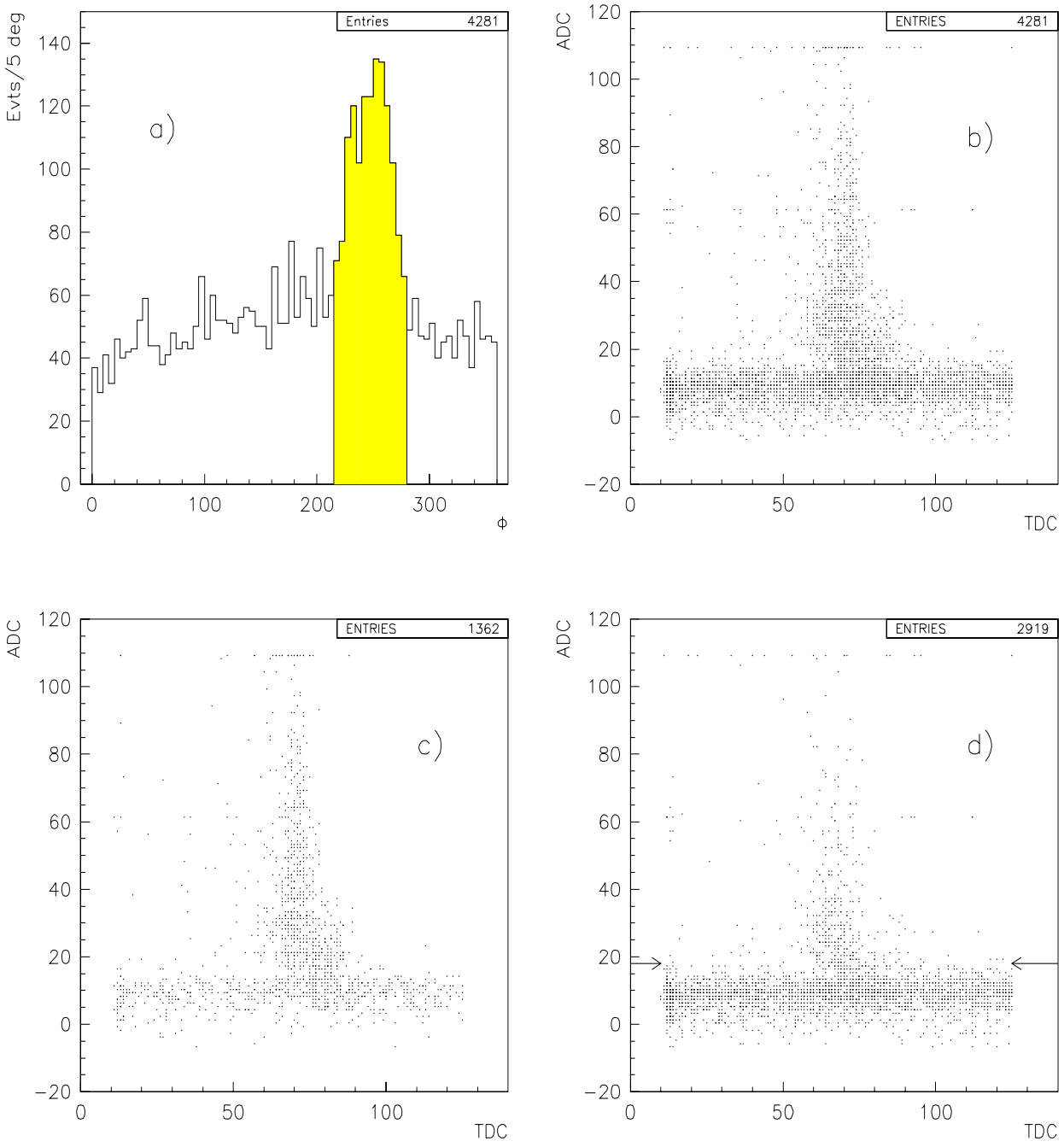


Figure 19: (a) $\phi$ distribution and (b) TDC *vs.* ADC when veto #1 in the veto box is on. (c) $p_s$ pointing to cell, (d) not pointing.

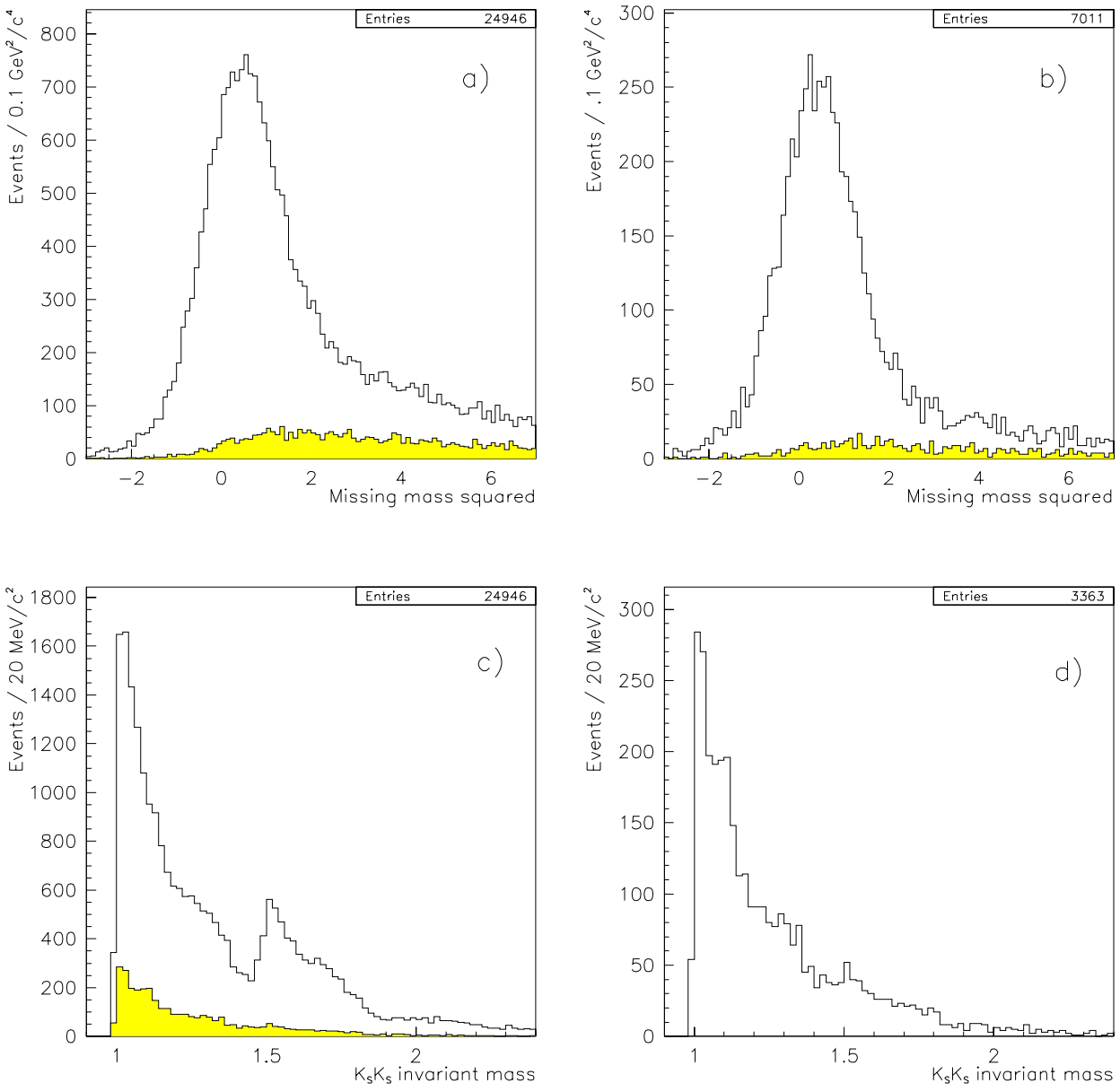


Figure 20: Missing mass squared peak for (a) all events that passed the veto–cut, and (b) those in the region $1.4 \leq M_{K_s^0 K_s^0} \leq 1.9\ GeV/c^2$. $K_s^0 K_s^0$ invariant mass for (c) the events that passed the cut, and (d) for those cut. The shaded areas in all plots represent the distribution of the events cut using the vetoes.

### 3.4.2 Counting the Number of Remaining Background Events.

We only used the veto counters and the veto collar for removing background events, but the remaining ones had to be counted for background subtraction in the amplitudes or moments analysis. In order to do this, we made an estimation of the number of background events in the region $1.0 \leq M(K_s^0 K_s^0) \leq 2.0\ GeV/c^2$ only. However, since we ended up fitting a function to the distribution curve of background events, the results can be extended to higher $K_s^0 K_s^0$ mass regions. For this purpose we selected events with a $K_s^0$ mass between 0.477 and $0.517 GeV/c^2$, and we imposed a cut on $-0.22 \leq x_F \leq -0.02$, which is the region of good acceptance in our spectrometer for central production. 11979 events survived these cuts (see fig.21). The fit in fig.21b was made on the central bins only, because various types of tracks enter this plot. These types are related to the number of chambers that the charged pions hit, and the number of iterations PASS2 does for each one of these types. For example, events with three–chamber–tracks have a different distribution to that of 6–chamber–tracks, giving a non–gaussian form to the combined distribution. We can also see that there is very little background under the $\pi^+\pi^-$ peak.

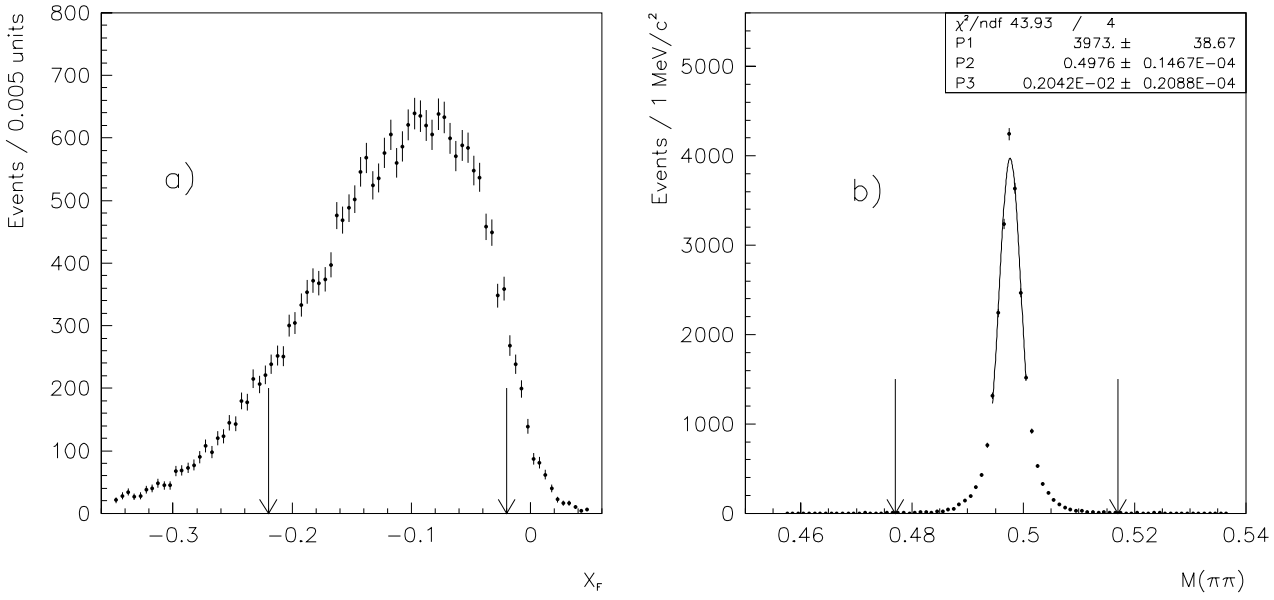


Figure 21: (a) $x_F$ for events that passed the veto–cut, the arrows show the region used for the analysis. (b) $\pi^+\pi^-$ invariant mass; the cut here was used to remove the tails in mass from PASS2 reconstruction.

To count background events under the missing mass squared peak, we assumed that the real signal had a gaussian–like distribution, and the background had a polynomial–like distribution. Thus we divided in bins of 100 $MeV/c^2$ in the $K^0_s K^0_s$ invariant mass, and chose the polynomial such that it vanished, and had zero slope, at $M^2_m - m^2_p = -3\ GeV^2/c^4$, where $M^2_m$ is the squared of the missing mass in the event, and $m_p$ is the mass of the proton. The reasoning to choose a function that vanishes and has zero slope at -3 $GeV^2/c^4$, is based on the topology of the process. We are looking for events of the form $pp \to (X)K^0_s K^0_s p$, where $X$ should be a proton. Therefore, $X$ consists of a mass greater or equal to the mass of the proton. On the other hand, to measure a mass of the order of 1 $GeV/c^2$ with a system that calibrates 800 $GeV/c$ protons is a tough thing to do, and the missing mass peak shows up to be a broad peak, as can be seen in fig.20a. Now, for $X$ consisting only of a proton and a small mass, say a $\pi^0$, the background can at most have the same form that the missing mass squared when $X$ consists only of a proton (left–hand side in fig.20a), and it must have a different shape for $X$ consisting of more particles, as in the right-hand side in fig.20a. Thus, the function used to fit the background must have the same shape as the missing mass squared peak, on the left hand side of the later.

In fig.22 we plot the fits in the ten bins described. The function used for the fit is

$$\begin{aligned} f(M^2_m) &= \left\{ p_1 e^{-p_2 (M^2_m - p_3)^2} \right\} \\ &+ \left\{ (M^2_m - m^2_p + 3)^2 p_4 + (M^2_m - m^2_p + 3)^3 p_5 + (M^2_m - m^2_p + 3)^4 p_6 \right\} \end{aligned} \qquad (1)$$

where the first term in brackets represents the gaussian used for the signal, and the second term represents the polynomial used for the background. From these plots it is obvious that there is a lot of background at threshold, and that it decreases when going to higher masses, such that in the region of more interest for us, there is little background.

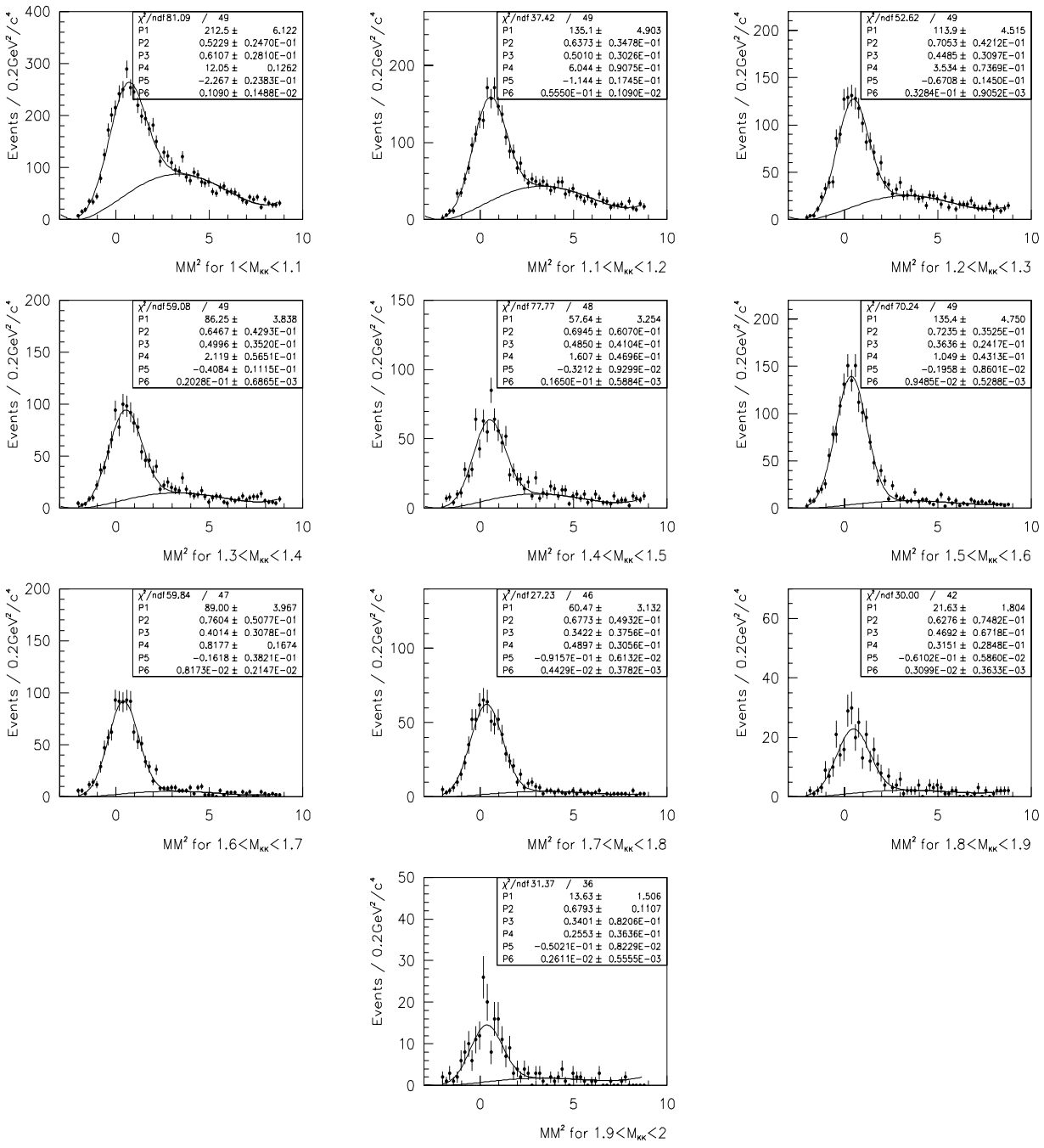


Figure 22: Fit to the missing mass squared peak, in 100 $MeV/c^2$ bins of the $K_s^0 K_s^0$ invariant mass. As we can see, the number of background events decreases for higher masses.

As can be seen in fig.20a, and fig.22, the shape of the curve of events cut using the vetoes, and that of the fit to background events, do not peak at the same position in the missing mass squared. The reason for this is that the background particles from events that were cut using the vetoes, have different momentum distributions than those from events in which the vetoes were not used. The particles that hit the vetoes are, for the most part, low momentum wide angle particles that give a lower missing mass than, for example, higher momentum missing neutrals that go into the spectrometer.

The parameters of the fits are shown in the plots. We used them to integrate the function $f(M_m^2)$ to make an estimation of the number of background and signal events, in a given region of the missing mass squared peak, in 100 $MeV/c^2$ bins of the $K_s^0 K_s^0$ invariant mass. We chose to integrate in the region where we perform the physics analysis, $-2.5 < M_m^2 - m_p^2 < 1.0\ GeV^2/c^4$, since after $1.0\,GeV^2/c^4$ the signal to background ratio is very small (see fig.reffig:bkgfit3a).

The number of background events obtained for each bin were in turn fitted with a function

$$b(m_{KK}) = \frac{e^{\,p_1 + p_2\, m_{KK}}}{m_{KK} - p_3} \tag{2}$$

where a pole in $p_3$ was used since the exponential term was not enough to account for the steep rise of the number of background events at low masses.

In fig.23a we plot the fit to the number of background events as a function of the $K_s^0 K_s^0$ invariant mass, and in fig.23b we plot the mean value of the missing mass squared peak, obtained from the gaussian fit ($p_3$ in fig.22). We can see in that this mean value is around $0.45\ GeV^2/c^4$, for all bins, and therefore, it is not equal to the squared of the proton mass. This shift is completely due to the forward spectrometer calibration, but it is not relevant for the physics analysis. This small miscalibration only affects the calculation of the missing mass, and has no effect in our measurement other than shifting the missing mass peak. For our analysis we only use well measured quantities, like the pion's momentum and the $p_T$ of the beam proton, plus energy and momentum conservation.

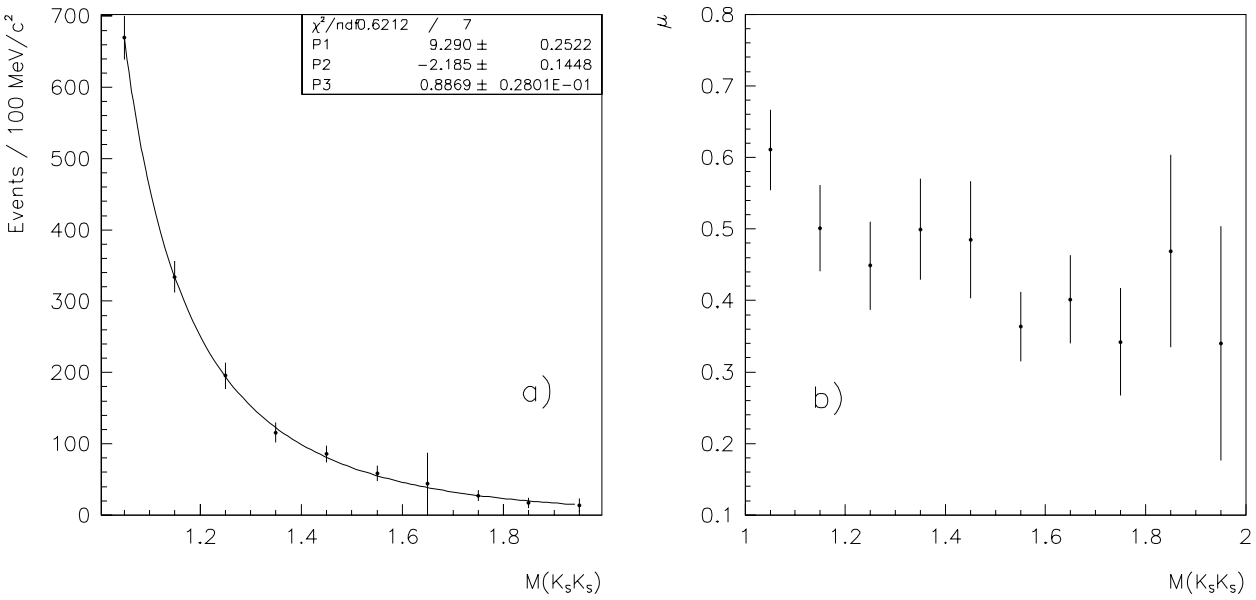


Figure 23: (a) Fit to the number of background events. (b) Mean value of the missing mass squared peak, obtained from the fit in fig.22.

Figure 24a is a plot of the $K_s^0 K_s^0$ invariant mass for events used in this analysis, in 20 $MeV/c^2$ bins, and the lower curve is the function $b(m_{KK})$ in the same bins. In fig.24b we plot the number of events after background subtraction.

Two things are important here. First, we can get the fraction of background from the fits to the missing mass squared, as a function of the $K_s^0 K_s^0$ invariant mass. Second, one would like to know how good these fits to the background are. One way to do this is to compare the form of the background fit in terms of the $K_s^0 K_s^0$ invariant mass, with events that one can be sure that are background. One can not just take the events which have a missing mass squared far from the peak, to compare with the background fit, since this fit was done in terms of those events. What we do, then is to compare the events estimated by fitting the missing mass squared with the events cut by the vetoes. Of the events cut by the vetoes, only those with $m^2_{missing} - m_p^2 > 1.5\ GeV/c^2$ were used. This was done to avoid including any real events that may have been cut out by, for example, veto noise.

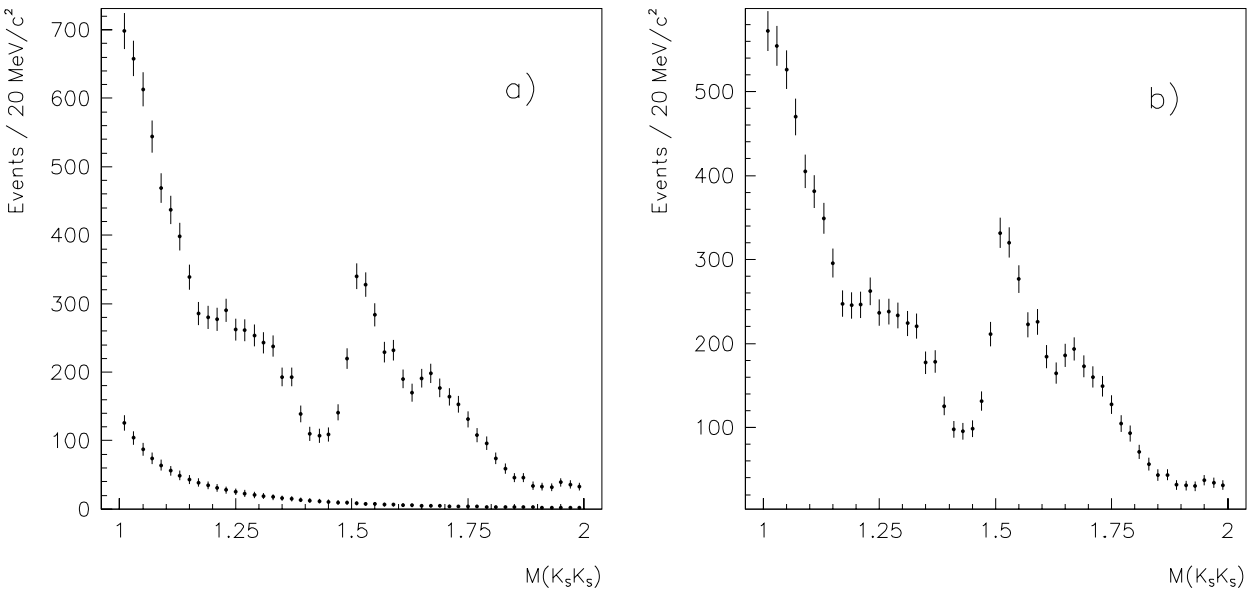


Figure 24: (a) Upper curve: $K_s^0 K_s^0$ invariant mass for all events; lower curve: number of background events. (b) Number of events after background subtraction.

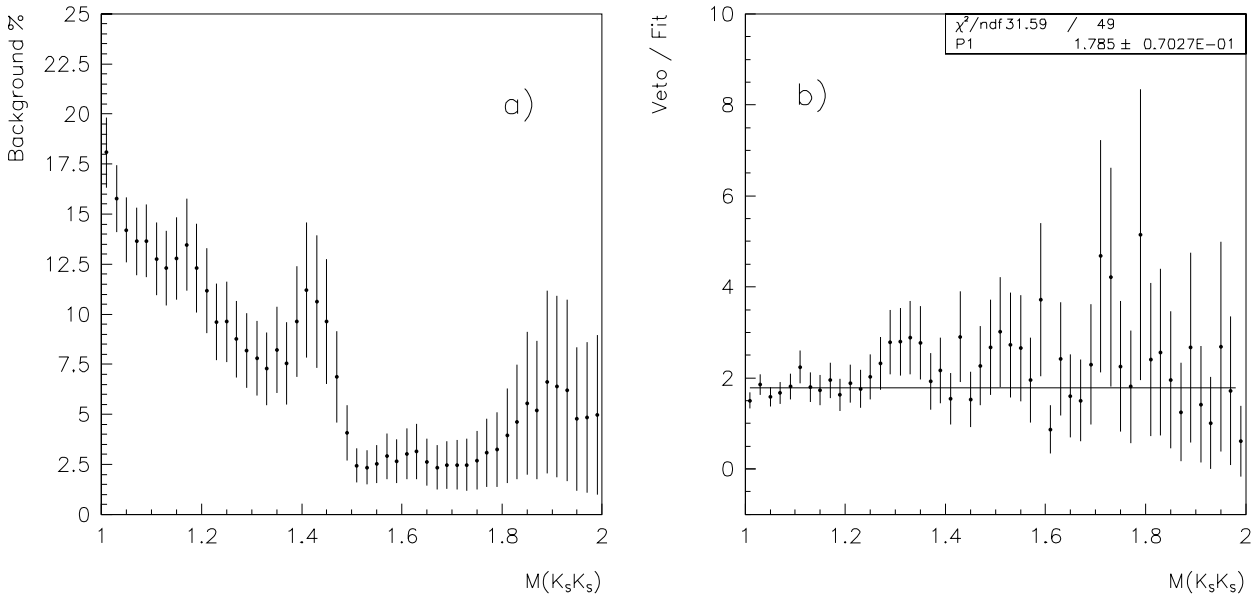


Figure 25: (a) Percentage of background events. (b) Ratio of background events from the veto–cut, to number of events from the background fit.

In fig.25a we plot the background percentage as a function of the $K_s^0 K_s^0$ invariant mass, with respect to the total number of events, that is (background)/(signal+background). We can see that, at threshold there is about 20% of background, and that it decreases for higher masses, being less than 5% in the region $1.5 \leq M_{K_s^0 K_s^0} \leq 1.8$, which is the region of interest in this study. In fig.25b we plot the ratio of the number of events that were cut using the vetoes, for $M_m^2 - m_p^2 > 1.5\ GeV^2/c^4$, to the number of events from the background fit. We can see that a fit to this plot using a constant function gives a $\chi^2$ of less than 0.6, which tells us that the background fit has essentially the same form as real background events.

## 3.5 Features of the Data.

The only cuts we used in the data for the partial wave analysis are

1. a primary vertex in the LH2 target,

2. Feynman $x_F$ in $-0.22 \leq x_F \leq -0.02$, and

3. missing mass squared in $-2.5 \leq m_m^2 - m_p^2 \leq 1 GeV^2/c^4$

In fig.26 we show the $p_t^2$ distribution of the slow (missing) and fast proton, for all events that passed these cuts, and for those in the region $1.4 \leq M(K_s^0 K_s^0) \leq 1.9\ GeV/c^2$. In fig.26a we can see the uncorrected $p_t^2$ distribution for the slow proton for all events. In fig.26b we see the $p_t^2$ distribution for the slow proton, but in the region $1.4 \leq M(K_s^0 K_s^0) \leq 1.9\ GeV/c^2$. In figs.26c–d we plot the $p_t^2$ distributions for the fast proton, for all events and in the region $1.4 \leq M(K_s^0 K_s^0) \leq 1.9\ GeV/c^2$. Note the change in horizontal axis. In these cases, there seems to be only one slope. Note also the drop in the first two bins in the $p_t^2$ of the fast proton. This drop is due to the geometric acceptance of the spectrometer.

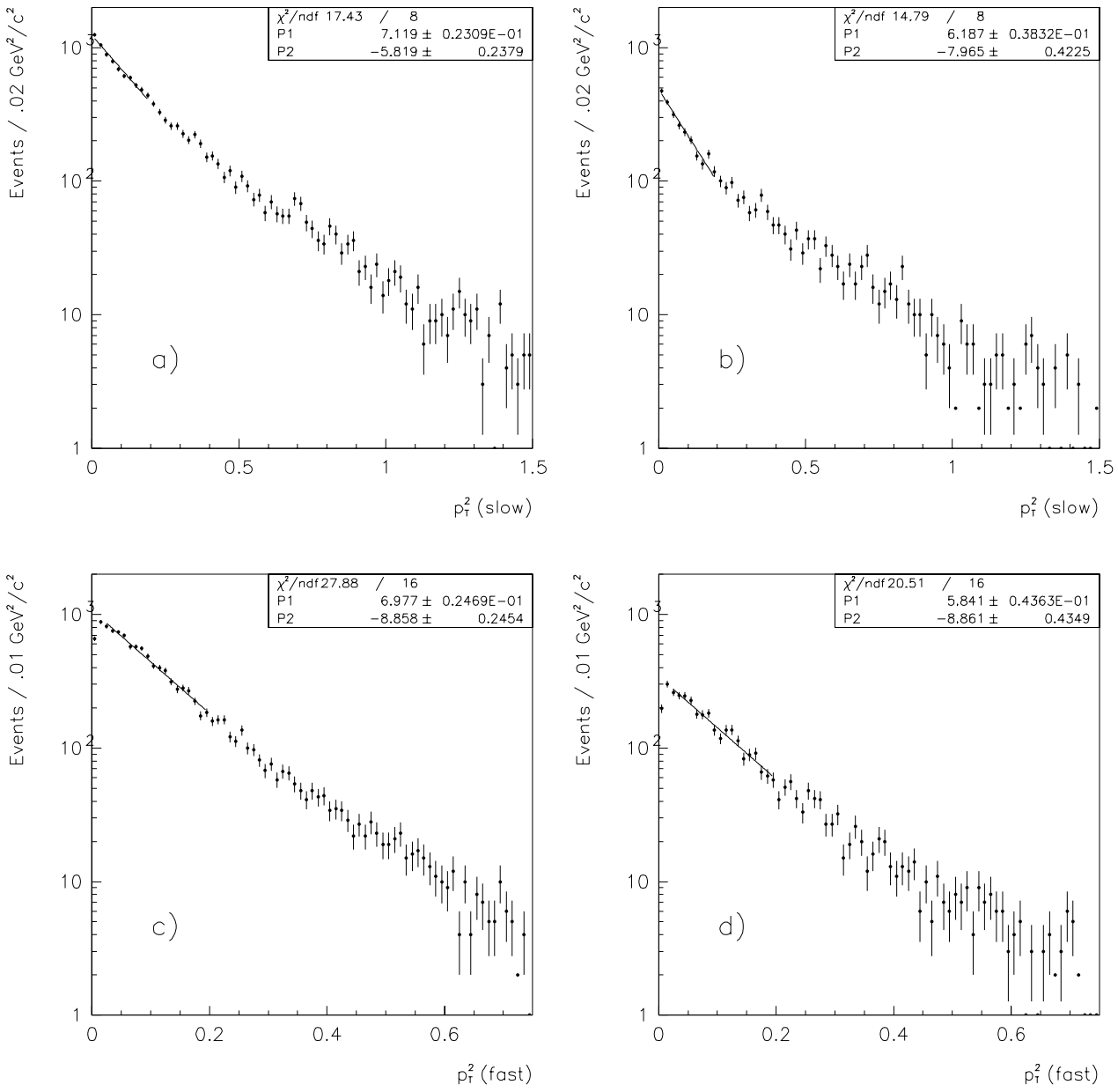


Figure 26: $p_t^2$ distributions for the slow and fast protons, for all events a) and c), and in the region $1.4 \leq M(K_s^0 K_s^0) \leq 1.9\ GeV/c^2$ b) and d), respectively.

The secondary vertices were chosen as $K_s^0$ compatible. This means that the invariant mass of the two charged tracks can also be compatible with other neutral particles. The $K_s^0$ vertices used in this analysis, can be compatible with a photon, a lambda or an antilambda vertex. In table 6 we give the number of events for the different categories of vertex type. When it is compatible with only one kind of vertex we call it unambiguously identified.

| Vtx. #1 type | Vtx. #2 type | # of events |
|---|---|---|
| $K_s^0$ | $K_s^0$ | 11132 |
| $K_s^0$,$\gamma$ | $K_s^0$ | 17 |
| $K_s^0$,$\Lambda$ | $K_s^0$ | 160 |
| $K_s^0$,$\overline{\Lambda}$ | $K_s^0$ | 170 |
| $K_s^0$ | $K_s^0$,$\gamma$ | 23 |
| $K_s^0$,$\gamma$ | $K_s^0$,$\gamma$ | 0 |
| $K_s^0$,$\Lambda$ | $K_s^0$,$\gamma$ | 0 |
| $K_s^0$,$\overline{\Lambda}$ | $K_s^0$,$\gamma$ | 0 |
| $K_s^0$ | $K_s^0$,$\Lambda$ | 277 |
| $K_s^0$,$\gamma$ | $K_s^0$,$\Lambda$ | 0 |
| $K_s^0$,$\Lambda$ | $K_s^0$,$\Lambda$ | 2 |
| $K_s^0$,$\overline{\Lambda}$ | $K_s^0$,$\Lambda$ | 2 |
| $K_s^0$ | $K_s^0$,$\overline{\Lambda}$ | 188 |
| $K_s^0$,$\gamma$ | $K_s^0$,$\overline{\Lambda}$ | 0 |
| $K_s^0$,$\Lambda$ | $K_s^0$,$\overline{\Lambda}$ | 4 |
| $K_s^0$,$\overline{\Lambda}$ | $K_s^0$,$\overline{\Lambda}$ | 4 |

Table 6: $K_s^0$ vertex compatibility.

We see that the number of events when one of the two vertices has been unambiguously identified as a $K_s^0$ is 11967, and only 12 events do not have at least one vertex unambiguously identified as a $K_s^0$. When we ask that both vertices be $K_s^0$, we get 11132 events. In fig.27a we plot the $K_s^0 K_s^0$ invariant mass for the events with at least one vertex unambiguously identified as a $K_s^0$. In fig.27b, one of the vertices is allowed to be compatible with another neutral vertex, and in fig.27c, we plot the events with both vertices compatible with other neutral type vertex. Even in this last plot, the $K_s^0 K_s^0$ invariant mass has the same structure as in the two previous plots.

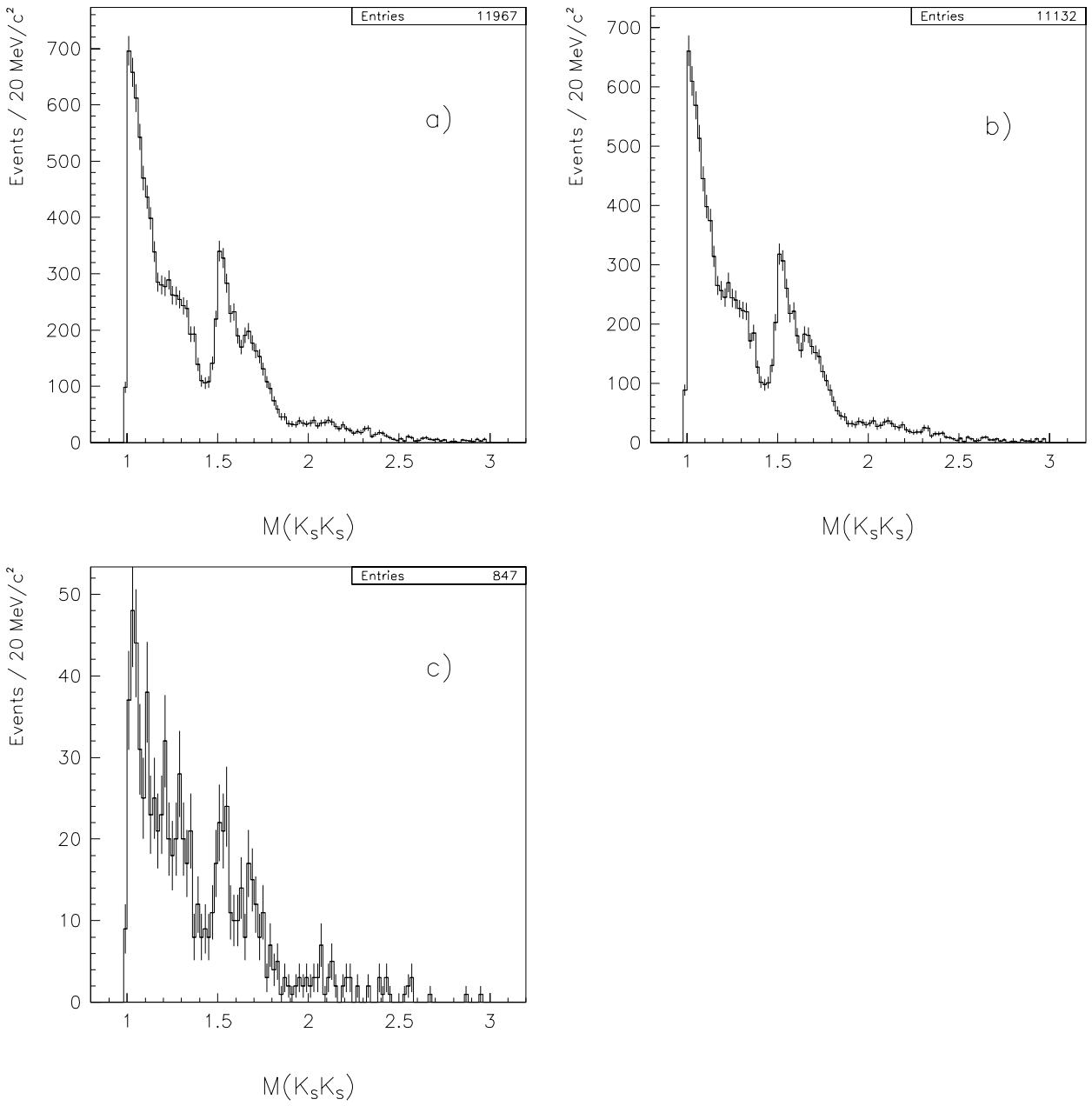


Figure 27: $K_s^0 K_s^0$ invariant mass for (a) events with either secondary vertex unambiguously identified as $K_s^0$, (b) both vertices unambiguously identified as $K_s^0$, (c) neither vertex unambiguously identified as $K_s^0$.

We did not throw away these events because, as can be seen in fig.28 the $\cos\theta_\pi$ distribution for one of the pions from the first $K^0_s$ in these events shows that cutting these events would produce a hole in the angular distribution close to $\cos\theta_\pi = \pm 1$, and, since we are trying to measure angular distributions, we do not want to create holes in these angular distributions with our selection cuts.

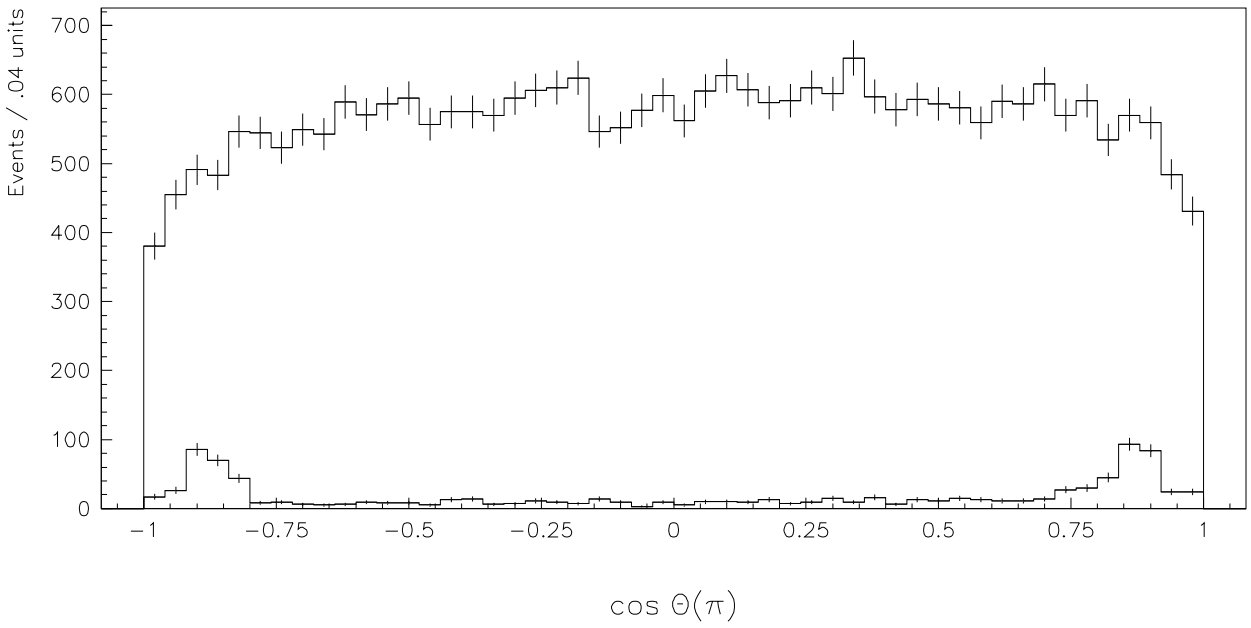


Figure 28: $\cos\theta_\pi$ distribution for the positive pion from the first $K^0_s$. The upper histogram is for all events, and the lower histogram is for the events where the $K^0_s$ is compatible with a $\Lambda$. We can see that cutting these events would produce a hole in the angular distribution close to $\cos\theta = \pm 1$.

We mentioned in Sect.3.2 that the secondary vertices leave a differentiable signature in the plot of the asymmetry versus the $P^*_T$, where this quantities were defined in the laboratory system. A scatter plot of the asymmetry versus $P^*_T$ for the $K^0_s$'s of our selected sample can be seen in fig.29. The upper plots are for both $K^0_s$'s before the cuts on the primary vertex, $x_F$ and missing-mass-squared, and the lower plots are for the events that survive these cuts. We can see that the plots after the cuts are essentially clean, and there is a little $\Lambda$ contamination.

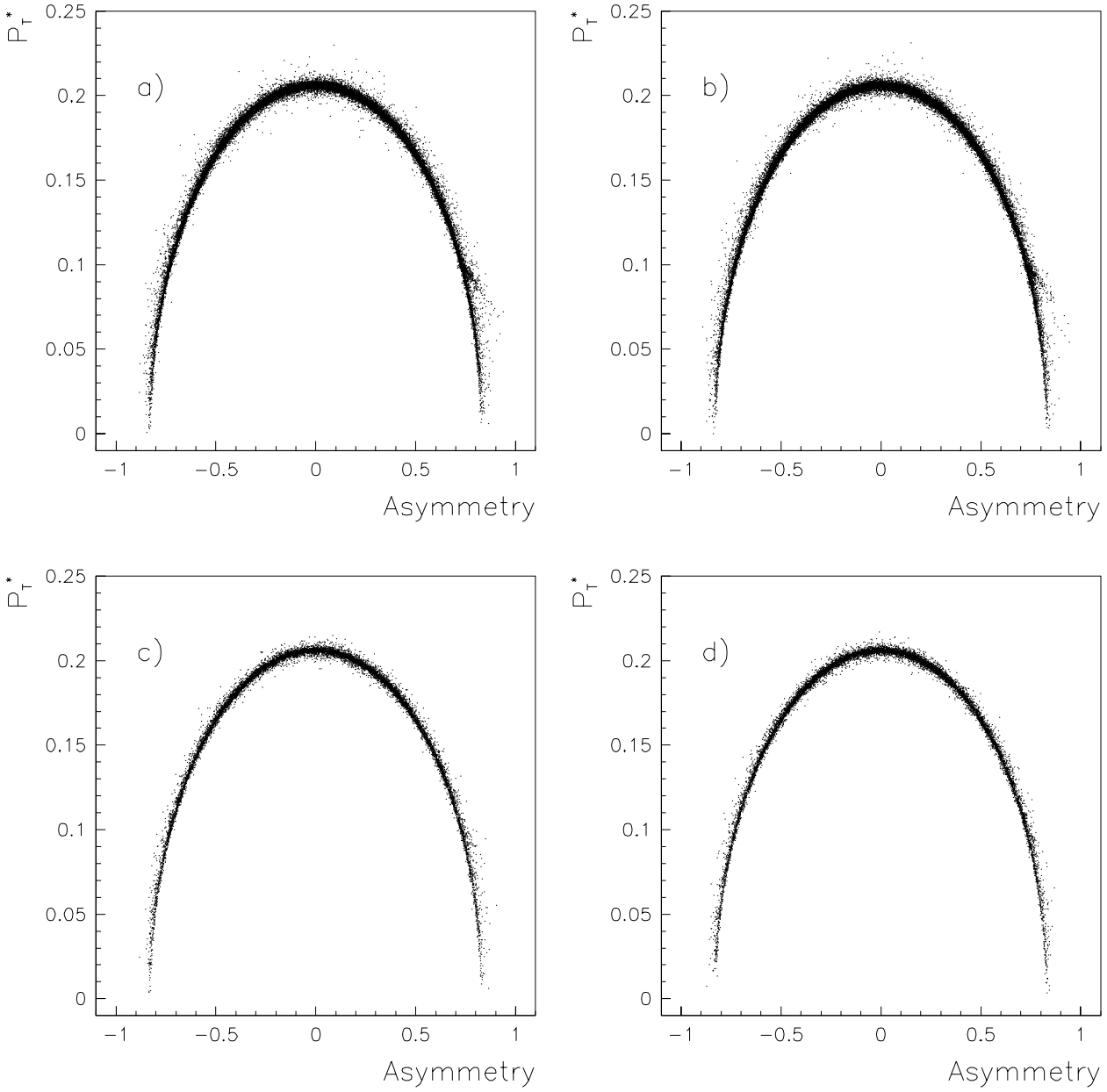


Figure 29: Asymmetry versus $P_T^*$ for the two $K_s^0$'s in the selected events, (a-b) before kinematical cuts, and (c-d) after the kinematical cuts. We can see how much the sample cleans after these cuts.

In fig.30a we plot the rapidities for all events that are going to be used in the analysis. The peak close to zero units is the rapidity of the slow proton, the central distribution corresponds to the $K_s^0 K_s^0$ system, and the sharpest peak, around seven rapidity units, corresponds to the fast proton. The rapidities are measured in the lab frame, and the boost to the CMS system of the two protons shifts the rapidities in -3.721 rapidity units. We can see that the rapidities for the protons and the $K_s^0 K_s^0$ are very well separated, as is the case of central production, an important quality for exotics production, since it favors gluon–rich production. The fast proton is separated by at least three units of rapidity from the $X$ system (see fig.30c), and the slow proton is separated by at least a unit from it (see fig.30b).

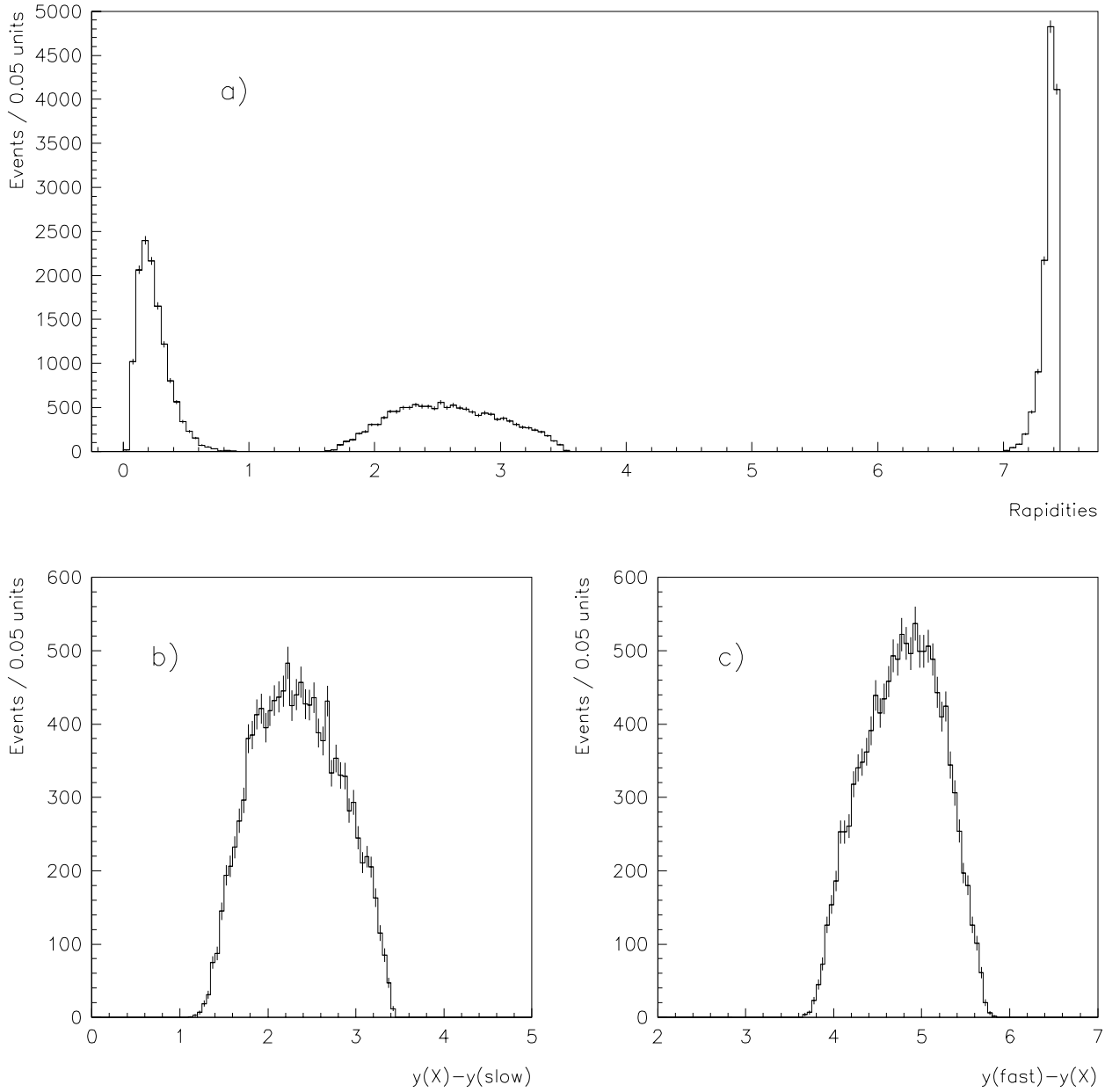


Figure 30: a) Rapidities for the slow proton (left), fast proton (right), and $X$ system. We can see the typical central production distributions, which favors gluon–rich production. b) and c) show the difference in rapidities between the $X$ system and the slow proton, and between the fast proton and the $X$ system, respectively.

# 4 PARTIAL WAVE ANALYSIS

## 4.1 Angular Distributions in the $X$ Decay.

After getting a sample of events, we proceed to perform the physics analysis. The reaction under study is

$$p\ p \rightarrow p_{missing}\ (X)\ p_{fast} \quad (3)$$

$$X \rightarrow K^0_s K^0_s \quad (4)$$

$$K^0_s \rightarrow \pi^+\pi^-$$

This reaction is studied in two steps: the production of the $X$ system (eq.(3)), with mass $M_X$, and, the decay of $M_X$ (eq.(4)). We need six variables to characterize the production process, $3 \times 3 - 4 + 1 = 6$, since we have the momenta of the two protons and of the $X$ system, there are four constraints due to energy–momentum conservation, and we considered that we do not know the mass of $X$. The variables we chose are:

| | |
|---|---|
| 1:2) $p^2_{t_m},\ \phi_m$ | transverse momentum of missing proton |
| 3:4) $p^2_{t_f},\ \phi_f$ | transverse momentum of fast proton |
| 5) $x_F$ | Feynman $x$ of the $X$ system |
| 6) $M_X$ | mass of the $X$ system |

The generic name $x$ will be used for the production variables, $x \equiv \left\{p^2_{t_m}, \phi_m, p^2_{t_f}, \phi_f, x_F, M_X\right\}$. We could also have used the four momentum transfer ($t$) from the beam to fast proton, and from the target to the slow (missing) proton. However, these variables depend directly on the longitudinal momentum of the particles, and our spectrometer was designed to do a much better measurement on transverse momentum, relative to the beam momentum, than on longitudinal momentum. Due to the rotation symmetry around the beam axis, the cross section will only depend on the difference $\phi_m - \phi_f$, but the acceptance can depend on both $\phi_m$ and $\phi_f$.

For the $X$ decay, two more variables are needed: $3 \times 2 - 4 = 2$. They are chosen as the Gottfried–Jackson angles of one of the $K^0_s$'s in the $X$ rest frame, with the generic name $\Omega$

given to them: $\Omega \equiv \{\theta, \phi\}$. The $K^0_s$ used to define the angles was randomly chosen. We selected the decay axis in the following way:

i) The $z$–axis was chosen in the direction of the momentum transfer from the beam to the fast proton in the CMS of the $K^0_s K^0_s$ system, that is, in the direction of the beam pomeron, $\hat{z} \propto \vec{\mathcal{P}}_{beam}$.

ii) The $y$–axis was chosen as the cross product of the vectors defined by the momentum transfer of the beam to fast proton, and the target to slow proton. This cross product is calculated in the CMS of the protons, and boosted to the $X$ rest frame, $\hat{y} \propto \vec{\mathcal{P}}_{beam} \times \vec{\mathcal{P}}_{tgt}$.

iii) The $x$–axis is the cross product of $\hat{y} \times \hat{z}$.

The $p_t^2$ distributions for the slow and fast protons, as well as the $M(X)$, and $x_F$ distributions, have already been shown in Section 3.5. The uncorrected angular distributions can be seen in figs.31–33. In fig.31 we plot the $\cos\theta$ distributions, and in fig.32 we plot the $\phi$ distributions. In fig.33 we made scatter plots of $\cos\theta$ *vs* $\phi$.

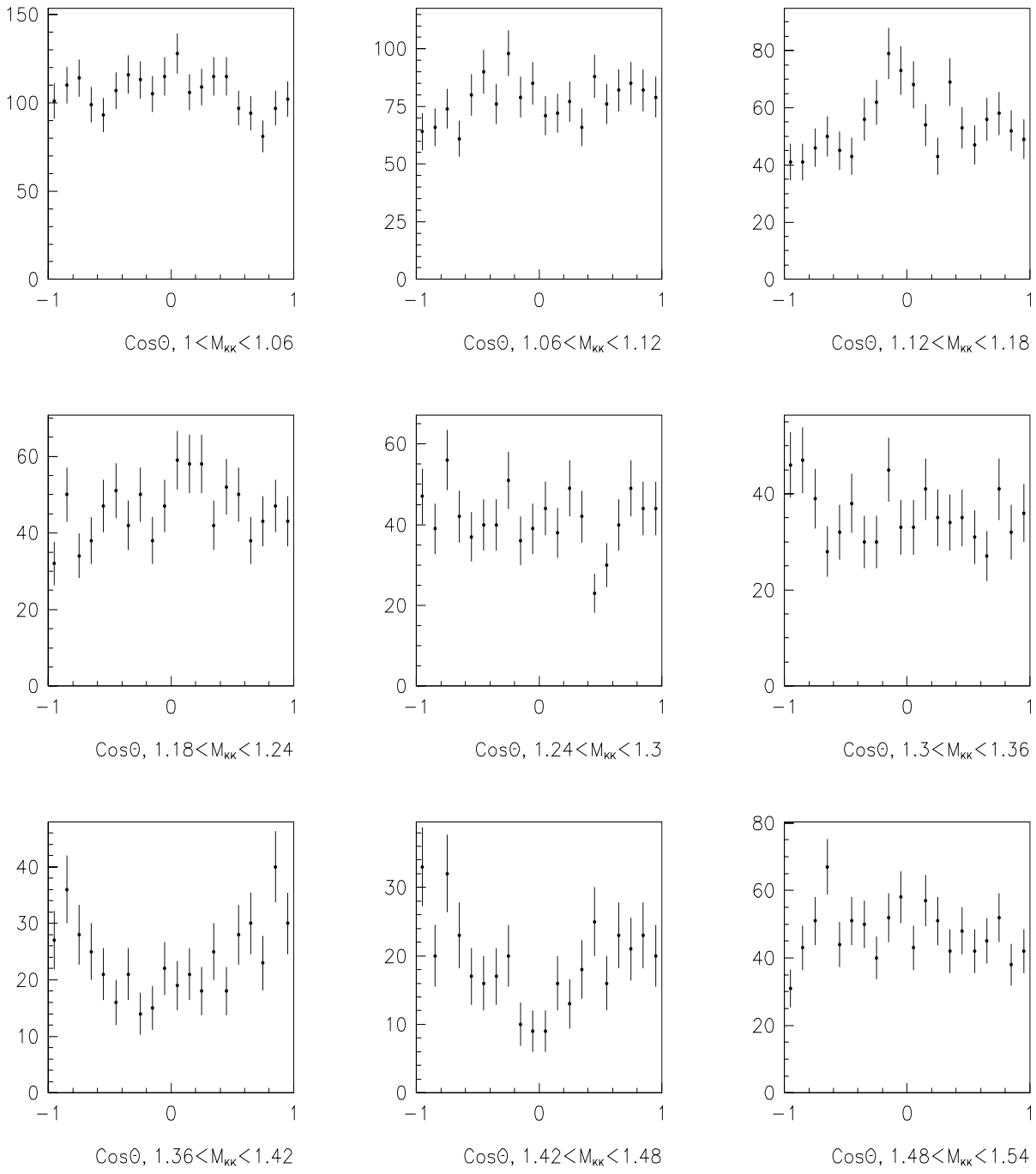


Figure 31: Uncorrected cos$\theta$ distributions in bins of 60 $MeV/c^2$ of the $K_s^0 K_s^0$ invariant mass, for $1.00 \leq M(K_s^0 K_s^0) \leq 2.02\ GeV/c^2$.

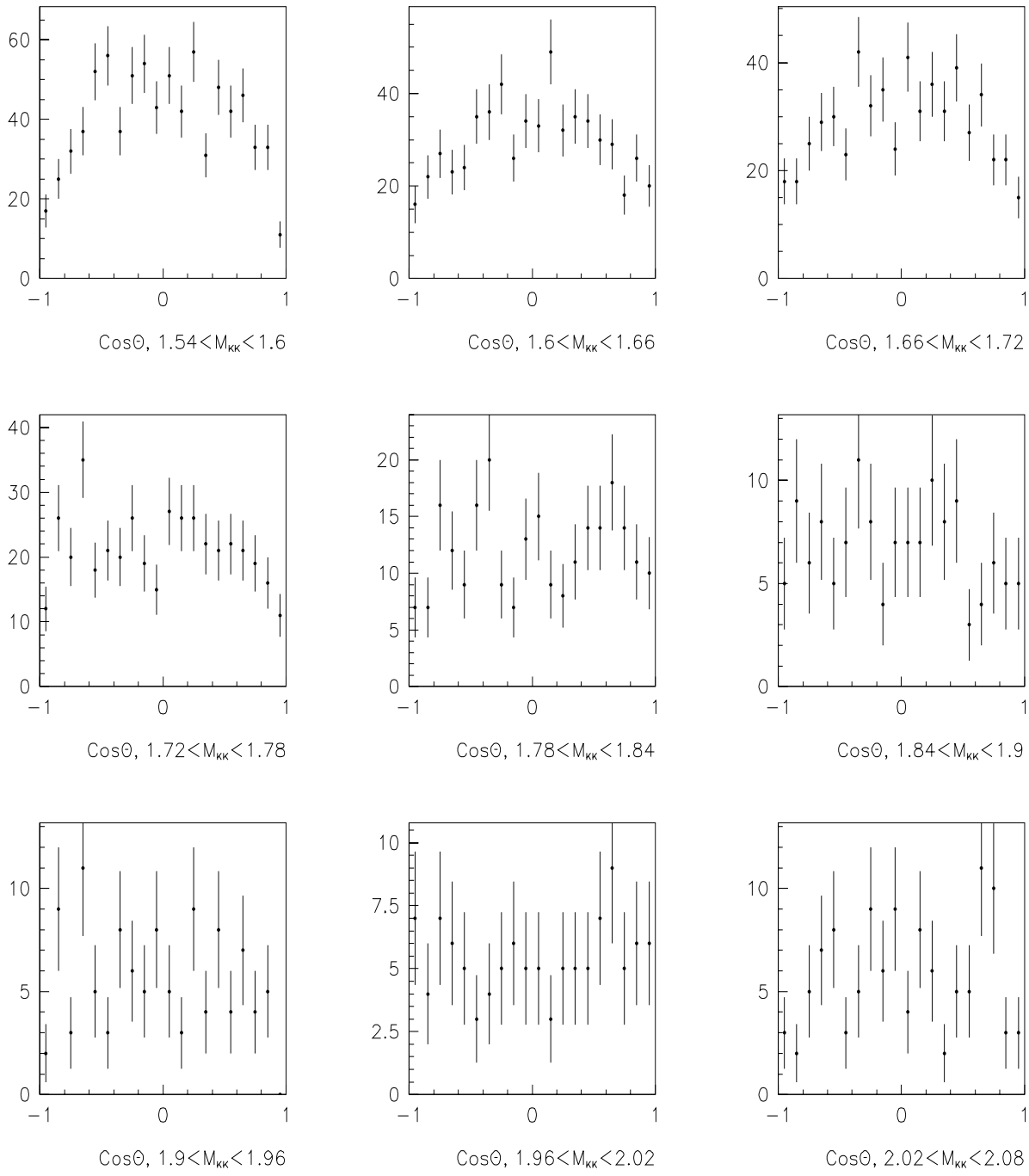


Figure 31 Continued.

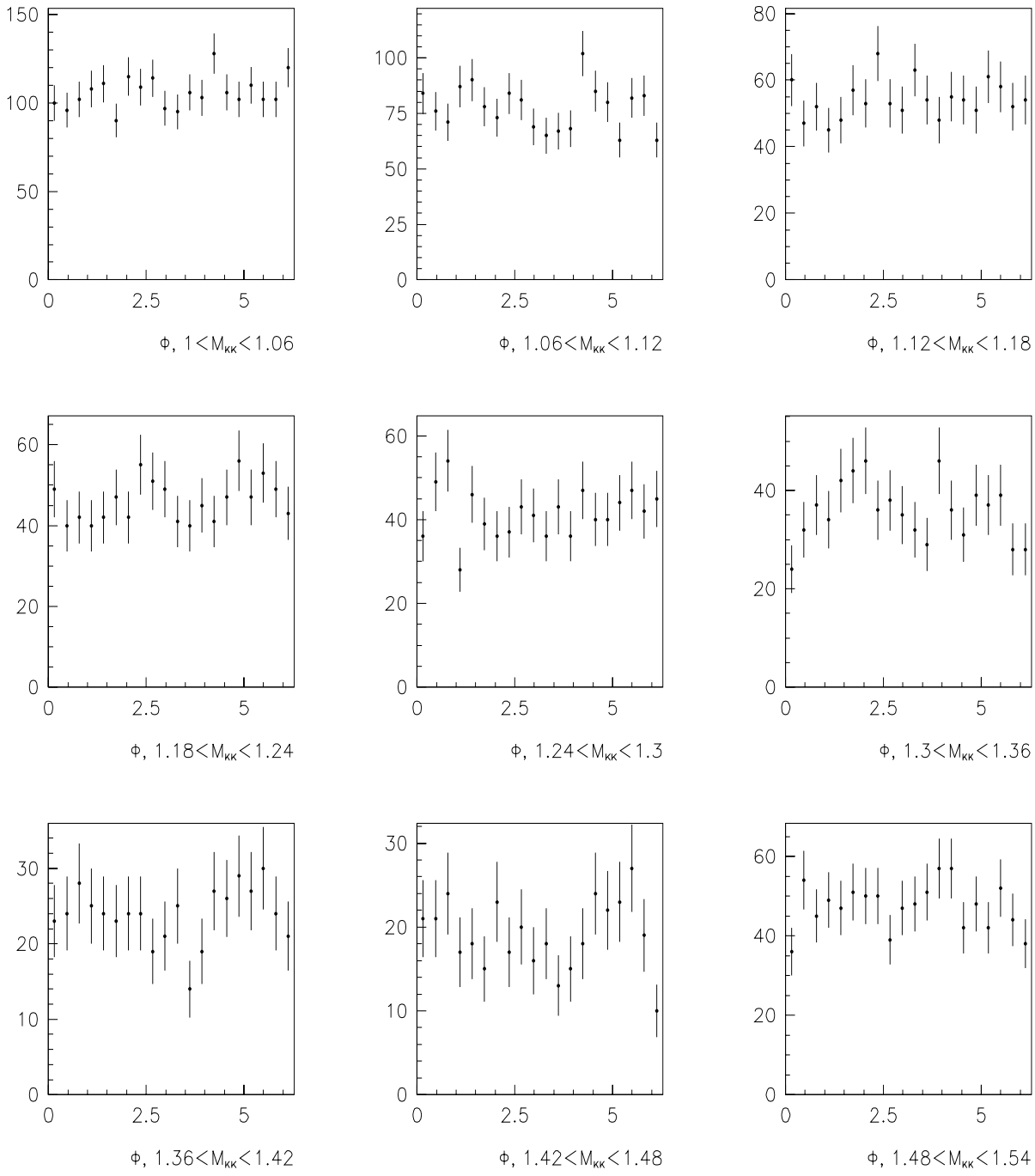


Figure 32: Uncorrected $\phi$ distributions in bins of 60 $MeV/c^2$ of the $K^0_s K^0_s$ invariant mass, for $1.00 \leq M(K^0_s K^0_s) \leq 2.02\ GeV/c^2$.

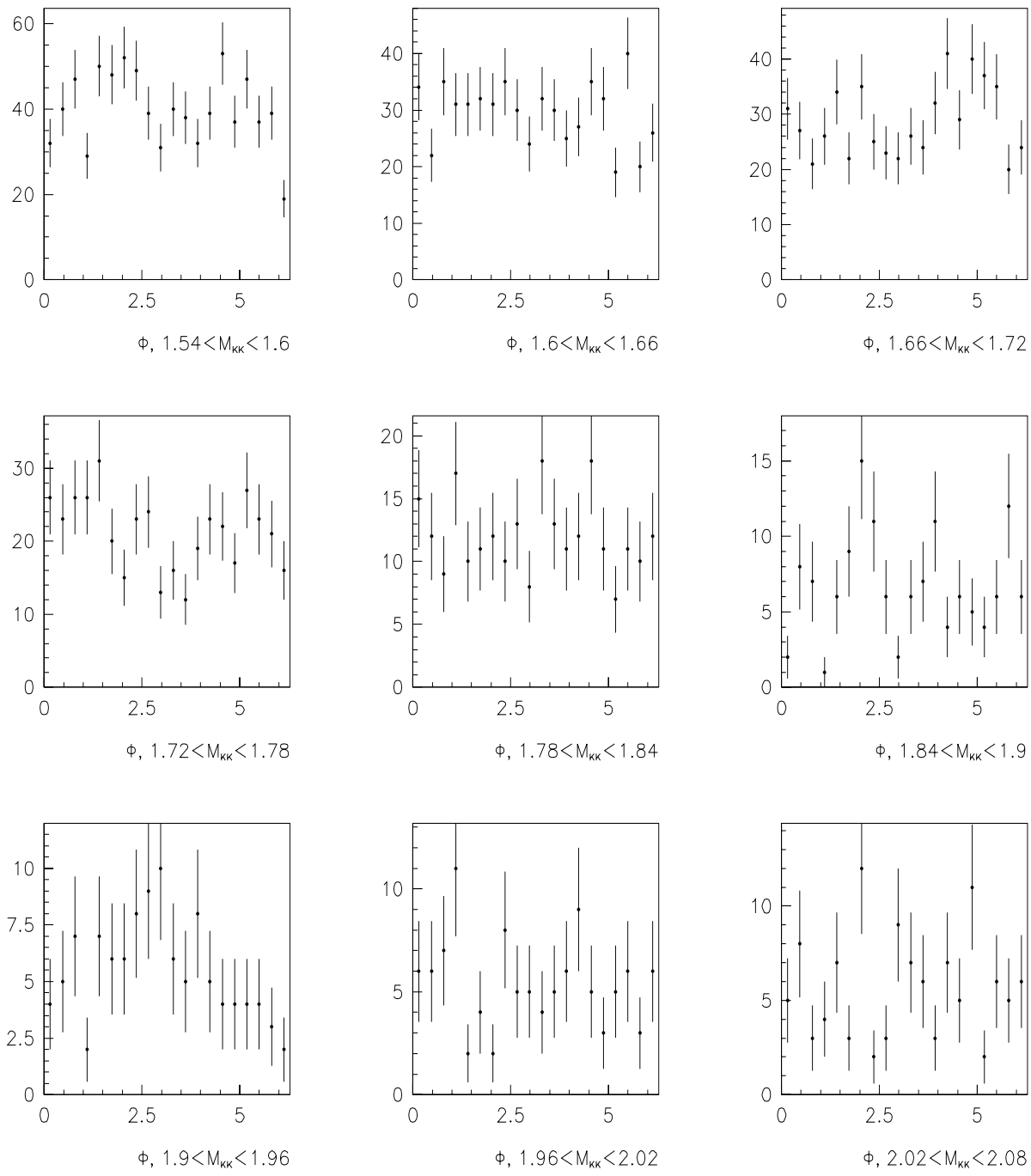


Figure 32 Continued.

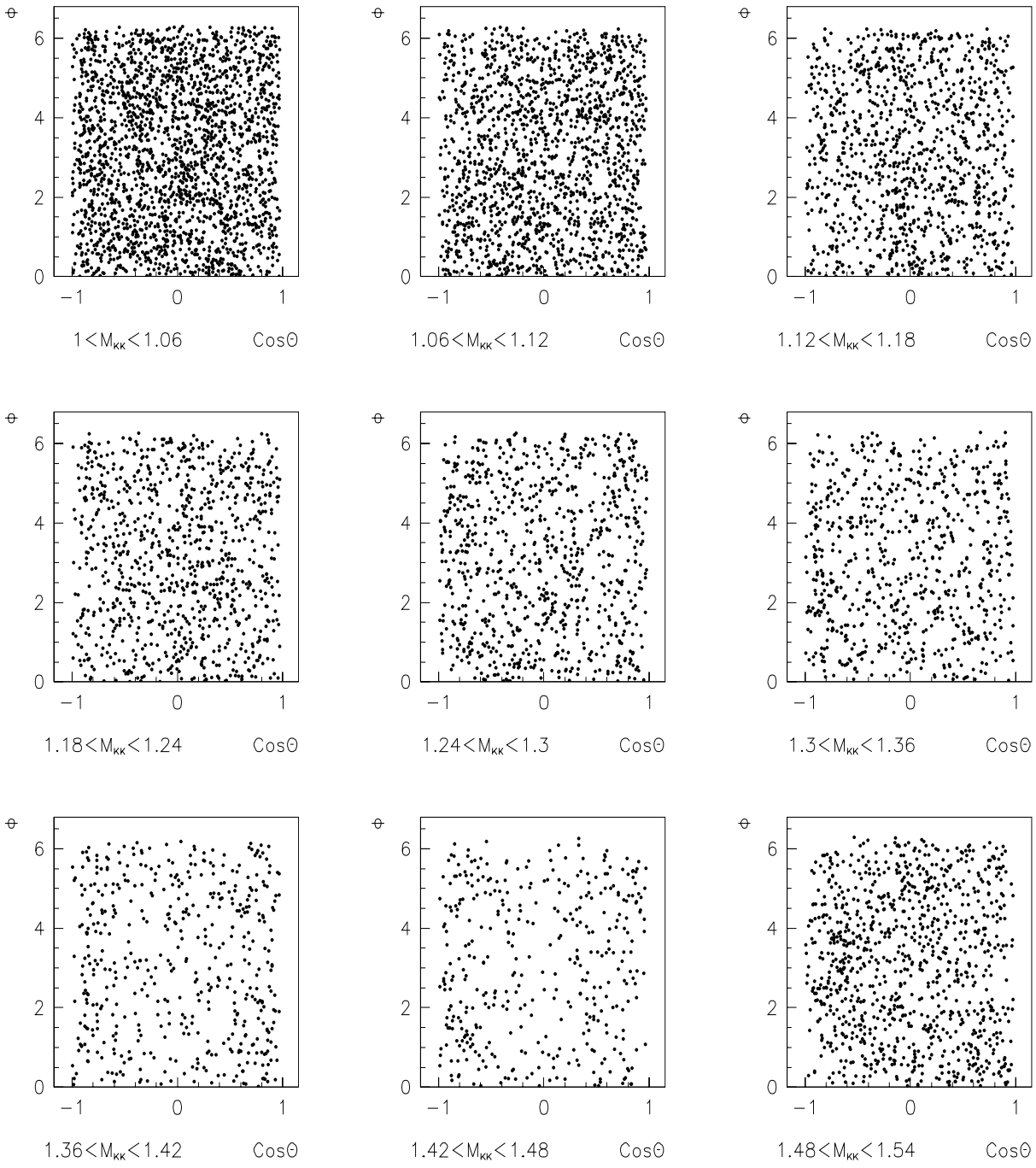


Figure 33: Uncorrected ($\cos\theta$, $\phi$) scatter plot for $1.00 \leq M(K_s^0 K_s^0) \leq 2.02\ GeV/c^2$.

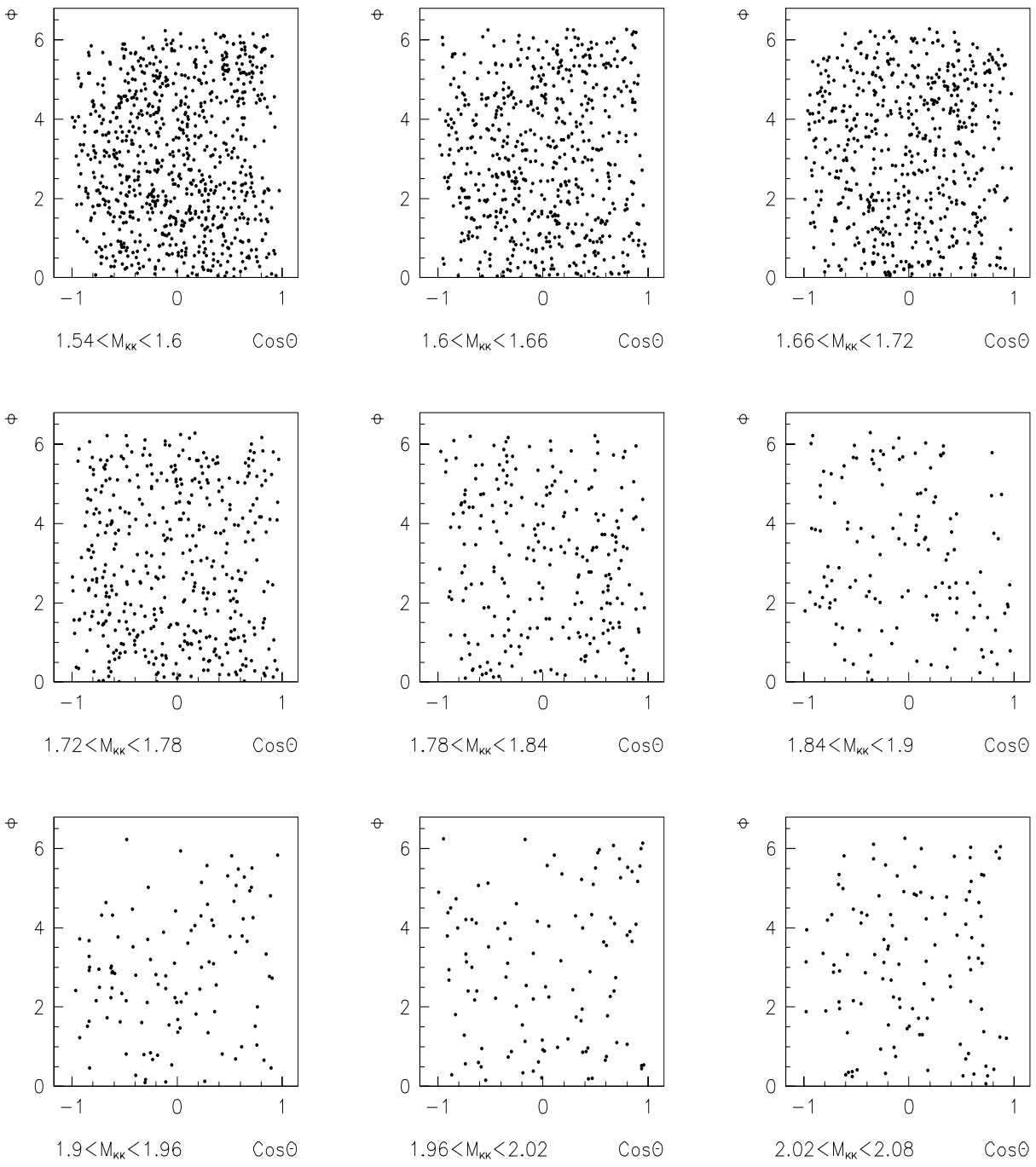


Figure 33 Continued.

## 4.2 Acceptance Corrections for the Angular Distributions.

The kinematics of the process can be described completely by the set of independent kinematical variables $\{x, \Omega\}$ (see Sect.4.1). The differential cross section may be defined as an intensity distribution in these variables: $I_{prod}(x, \Omega)$. Only part of the distribution $I_{prod}(x, \Omega)$ is accepted by the geometry of the detector, and the relation between the accepted and produced intensities is given by

$$I_{\rm acc}(x, \Omega) = A(x, \Omega)\, I_{\rm prod}(x, \Omega) \tag{5}$$

where the acceptance probability $A(x, \Omega)$ takes the values 0 or 1 depending on whether the event $(x, \Omega)$ lies inside the geometry of the apparatus or not.

The raw angular distributions shown in the previous Section most surely do not show the real angular distributions produced in the physical process of eqs.(3,4), but these distributions modified by the geometrical acceptance of the spectrometer, or the inefficiencies in the reconstruction process. The whole set of factors that modify the real distributions of the process, and are due to the apparatus or hardware performance, is called the "spectrometer acceptance". One has to calculate the acceptance corrections that need to be done to perform the physics analysis, and the straight forward way to do this is to generate Monte Carlo events, process them through the whole chain of reconstruction programs, and calculate the corrections by comparing the distributions of the generated and accepted events.

To calculate the acceptance corrections for the angular distributions we generated Monte Carlo events with the following characteristics:

1) $M_X$ flat in the region 1.00 to 2.02 $GeV/c^2$,

2) $\cos\theta$ flat in [-1,1],

3) $\phi$ flat in [0,2$\pi$],

4) $p_t^2$ of the fast and slow protons distributed according to $e^{-8\,p_t^2}$, and

5) Feynman $x_F$ of the $X$ system flat in [-0.22,-0.02].

As a check of the reliability of the reconstruction of the angles, we generated Monte Carlo

events with definite values for some variables of interest, to see how good this reconstruction was. We plot in fig.34 the results for these events after processing them through the whole reconstruction chain. The standard deviations for the angular variables are $\sigma(\cos\theta)/2 \leq 1\%$, and $\sigma(\phi)/2\pi \leq 1\%$. The reconstruction of the masses gives a sigma of 2 $MeV/c^2$ for the $K_s^0$ mass, which is what we found in the data distribution, as can be seen in fig.21b, and of 5 $MeV/c^2$ for a $K_s^0 K_s^0$ mass of 1.6 $GeV/c^2$. Fig.35 is a scatter plot of $\cos\theta$ versus $\phi$ for another set of fixed values for these variables. So, our resolution is about a factor of 5 smaller than our bin size, since there are only twenty bins for $\cos\theta$ and $\phi$, which gives 5% of the angular range, compared to a sigma of 1%.

To see how does the acceptance affect the angular distributions, we selected two regions of the $K_s^0 K_s^0$ mass. In fig.36 we plot the angular distributions in the $f_2'(1525)$ region, $1.45 \leq M(K_s^0 K_s^0) \leq 1.59\, GeV/c^2$, and the $f_J(1710)$ region, $1.59 \leq M(K_s^0 K_s^0) \leq 1.83\, GeV/c^2$, before and after acceptance corrections. We selected these two regions in order to compare with the results of experiment WA76 [31], which is a very similar experiment to ours. They used 300 $GeV/c$ protons inciding on liquid hydrogen, to study the reaction

$$p\, p \;\rightarrow\; p\, (K^+ K^-)\, p$$

From the angular distributions shown in fig.1, they favored spin $J = 2$ for the $f_J(1710)$. We can see that the angular distributions we found in this region are essentially flat (see fig.36), in disagreement with WA76 results. However, it is important to consider that this experiment studied $K^+K^-$ events, where it is possible to have odd waves, in addition to even waves, which is not the case in $K_s^0 K_s^0$ events, where only even waves can be found.

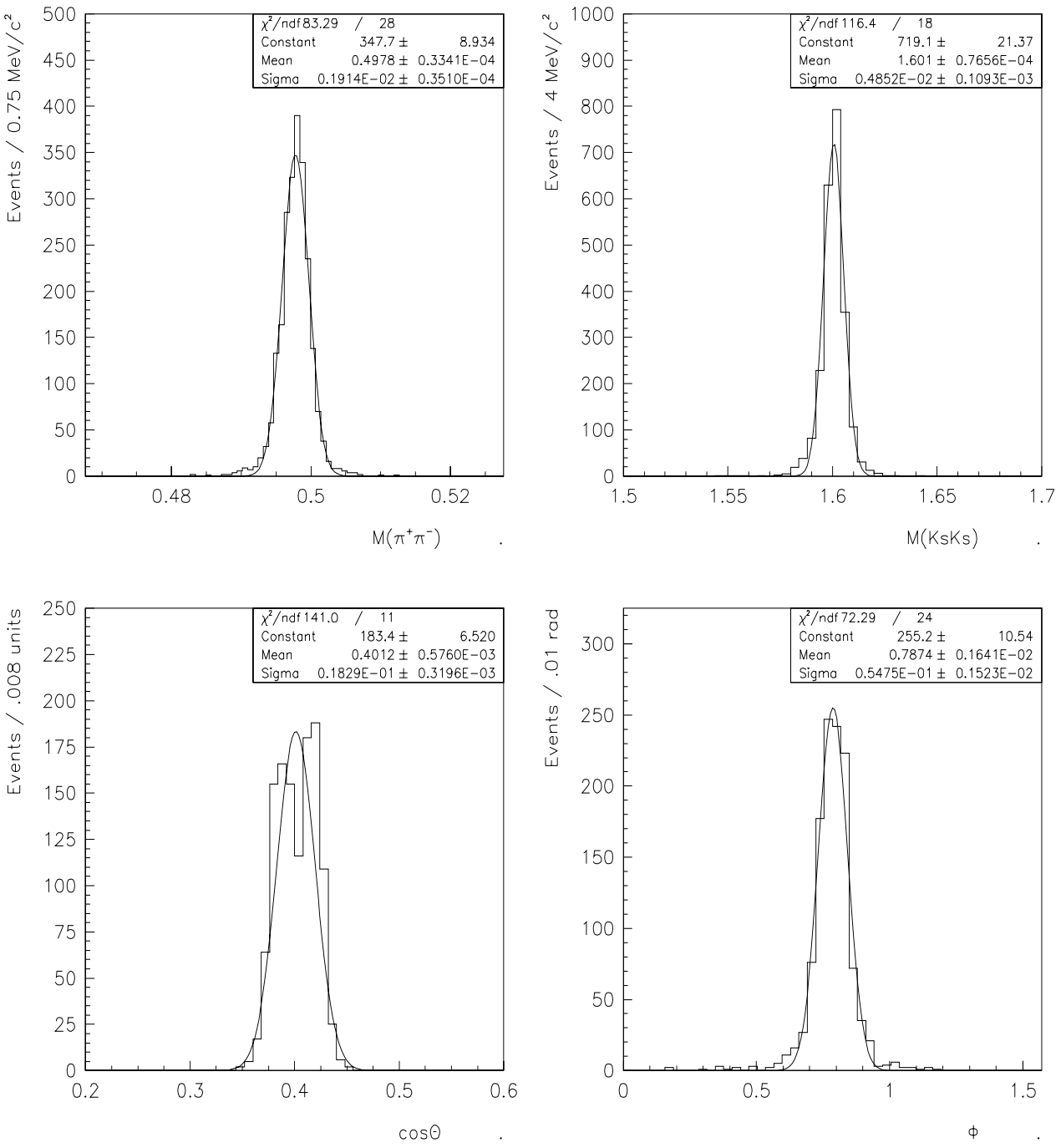


Figure 34: MC events generated with definite values for $m(\pi\pi) = m(K_s^0)$ (upper left), $m(K_s^0 K_s^0) = 1.6\ GeV/c^2$ (upper right), $\cos\theta = 0.4$ (lower left), and $\phi = 0.7854$ (lower right).

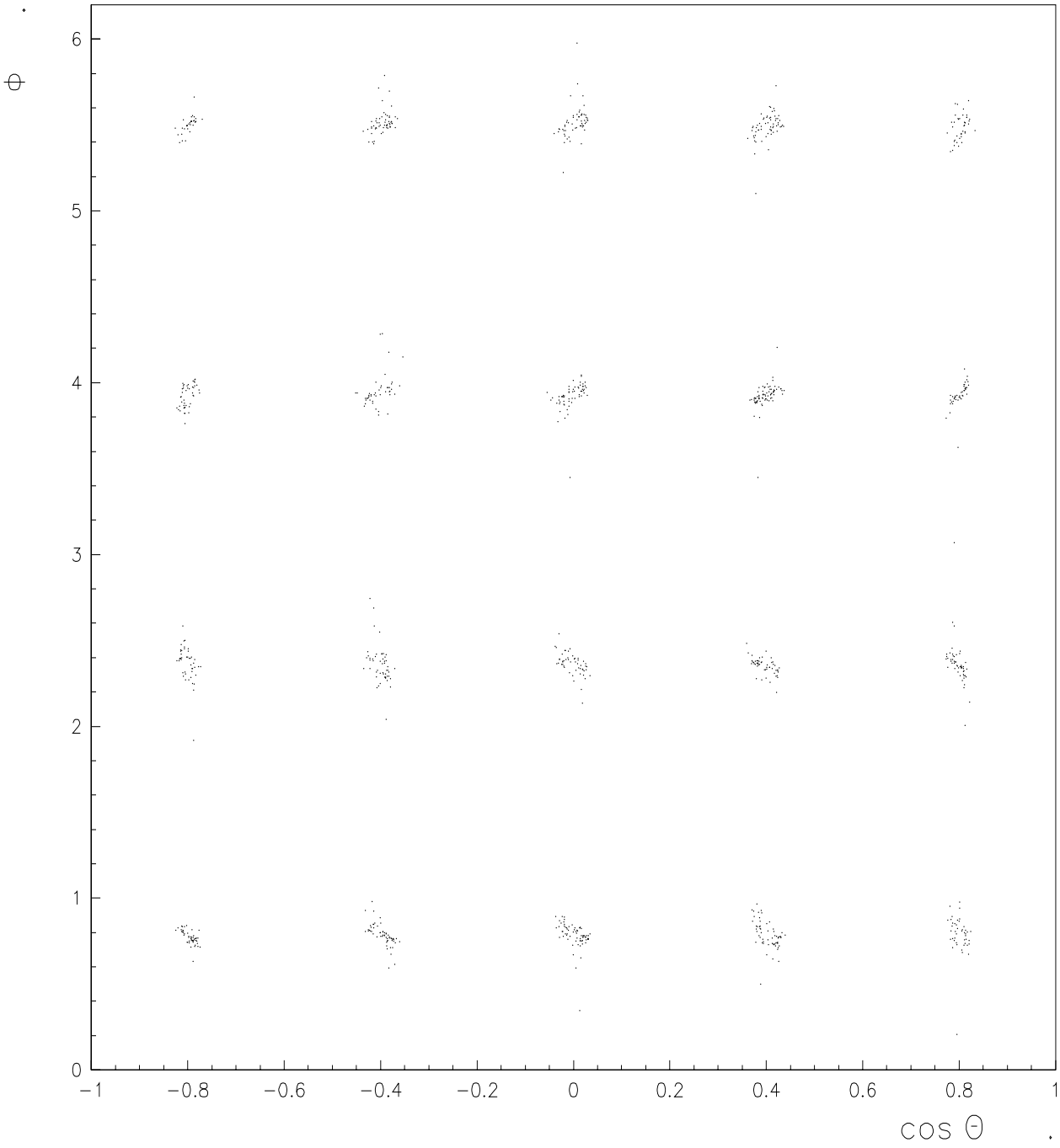


Figure 35: Scatter plot of MC events generated with definite values for $\cos\theta$ and $\phi$.

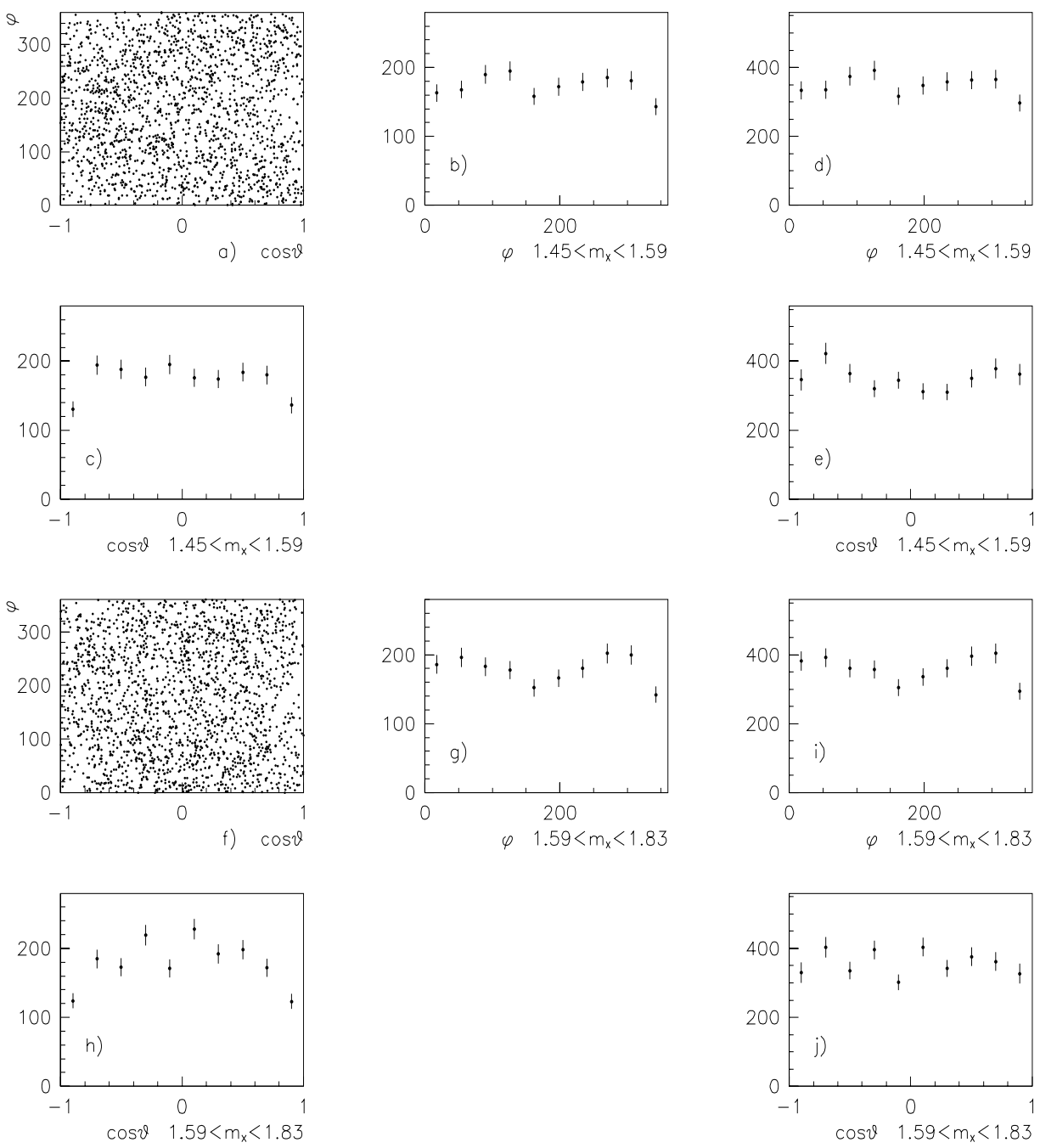


Figure 36: (a-c) $(\cos\theta, \phi)$ scatter plot with $\cos\theta$ and $\phi$ projections in the Gottfried–Jackson frame for the $f_2'(1525)$ region; (d-e) show the acceptance corrected distributions in the same region. (f-h) $(\cos\theta, \phi)$ scatter plot with $\cos\theta$ and $\phi$ projections in the Gottfried–Jackson frame for the $f_J(1710)$ region; (i-j) show the acceptance corrected distributions in the same region. The regions are defined as $1.45 \leq M(K_s^0 K_s^0) \leq 1.57\, GeV/c^2$, and $1.57 \leq M(K_s^0 K_s^0) \leq 1.85\ GeV/c^2$, respectively.

## 4.3 Amplitudes in the $K_s^0 K_s^0$ System.

The process (3–4) can be viewed as the protons interchanging two particles, which we shall call Pomerons[3], $\mathcal{P}$. These particles interact to produce the $X$ system, which subsequently decays into two $K_s^0$'s. Since the decay of the $X$ system is into two particles, and only two (angular) variables are needed to describe this process, we will use the spherical harmonics $Y_m^J(\theta, \phi)$ as the basis for the expansion of the probability distribution. In this thesis we study two different expansions for the probability distribution, one linear and a second one quadratic in terms of the spherical harmonics. We shall describe the linear expansion in a later Section. Here we shall introduce the quadratic expansion, which is directly related to the amplitudes of the waves that are present in the process, this being the main objective of the thesis.

The intensity distribution can be written as

$$\begin{aligned} I_{\rm acc}(x,\Omega) &= \sum_{\lambda} (const)\,(phase\ space)\,A(x,\Omega)\ |\mathcal{M}_\lambda|^2 \\ &= (const)\,(phase\ space)\,A(x,\Omega)\ |\mathcal{M}|^2 \end{aligned} \tag{6}$$

where $\mathcal{M}$ is the Lorentz invariant matrix element, or Lorentz invariant amplitude (see Sect.B.2 for the values of the constant and phase–space factors), and the sum in the first part of eq.(6) is over the possible helicities $\lambda$ of the protons, while in the second part of this equation we dropped the sum over helicities assuming that the matrix element does not depend on the helicities of the protons. The matrix element $\mathcal{M}$ can be expressed as a series in terms of the spherical harmonics $Y_m^J$. However, since the Pomerons and the $K_s^0$'s are all in the same plane, it is better to use a combination of the spherical harmonics that makes use of the symmetry of the system. Such a basis is called the *naturality basis* (or reflectivity basis), and the functions in that basis are related to the spherical harmonics in the following

[3] We are not studying the production process, so we do not attempt to know what particles are really being interchanged, and the name Pomeron is only used as a reminder of the statement that central production processes are supposed to have a big contribution from Double Pomeron Exchange processes

way

$$Y_m^{J\,\epsilon} = c_m \left( Y_m^J - \epsilon(-1)^{J-m} Y_m^J \right) \tag{7}$$

where $\epsilon$=+1 for positive naturality states and $\epsilon$=−1 for negative naturality states, and

$$c_m = \begin{cases} \frac{1}{2} & \text{if } m = 0 \\ \frac{1}{\sqrt{2}} & \text{if } m \neq 0 \end{cases}$$

The principal characteristics of this basis are: 1) the reflection operator $\Pi_{\hat{n}}$, defined as a product of the parity operator followed by a rotation around the normal $\hat{n}$ to the pane of the particles, leaves all relevant momenta invariant; 2) it was shown by Chung and Trueman[49] that the the spin-density matrix in the reflectivity basis breaks up into block-diagonal form, owing to parity conservation in the production process, and 3) as a consequence of this last statement, the angular distributions in the decay of the $X$ system do not contain interference terms of opposite reflectivity.

For example, the spin–0 and spin–2 states in the reflectivity basis are, for naturality $\epsilon = -1$

$$\begin{aligned} \mathcal{S}_0^- &= Y_0^0 \\ \mathcal{D}_0^- &= Y_0^2 \\ \mathcal{D}_1^- &= \frac{1}{\sqrt{2}} \left( Y_1^2 - Y_{-1}^2 \right) \\ \mathcal{D}_2^- &= \frac{1}{\sqrt{2}} \left( Y_2^2 + Y_{-2}^2 \right) \end{aligned} \tag{8}$$

and for naturality $\epsilon = +1$

$$\begin{aligned} \mathcal{D}_1^+ &= \frac{1}{\sqrt{2}} \left( Y_1^2 + Y_{-1}^2 \right) \\ \mathcal{D}_2^+ &= \frac{1}{\sqrt{2}} \left( Y_2^2 - Y_{-2}^2 \right) \end{aligned} \tag{9}$$

In this case, the waves $\mathcal{D}_1^+$ and $\mathcal{D}_2^+$ do not interfere with the waves $\mathcal{S}_0^-$, $\mathcal{D}_0^-$, $\mathcal{D}_1^-$ and $\mathcal{D}_2^-$. As one can see, a flat angular distribution can be described using only a $\mathcal{S}_0^-$ wave ($Y_0^0 = 1$), but it is also possible to produce a flat distribution by adding equal amounts of waves with

the same spin, with all possible projections, but *without interference*, for example:

$$\left|\mathcal{D}_0^-\right|^2 + \left|\mathcal{D}_1^-\right|^2 + \left|\mathcal{D}_2^-\right|^2 + \left|\mathcal{D}_1^+\right|^2 + \left|\mathcal{D}_2^+\right|^2 = \frac{5}{4\pi}$$

Considering spin $J = 0$ and $J = 2$, if the angular distributions do not show dependence on the azimuthal angle $\phi$ then only the projection $m = 0$ would be present, and there would only be two interfering waves, $\mathcal{S}_0^-$ and $\mathcal{D}_0^-$. We considered this simple case as a first approach to the partial wave analysis. With only these two waves, and normalizing the cross section to the number of events, one can write

$$\begin{aligned} \frac{\mathrm{d}\sigma}{\mathrm{d}\Omega} &= \left| S_0^- \mathcal{S}_0^- + D_0^- \mathcal{D}_0^- \right|^2 \\ &= \frac{1}{2}\left\{ P_1 + \frac{5}{4}\left(3\cos^2\theta - 1\right)^2 P_2 + \sqrt{5P_1P_2}\cos P_3 \left(3\cos^2\theta - 1\right) \right\} \end{aligned} \tag{10}$$

where $S_0^-$ and $D_0^-$ are the (complex) amplitudes of the waves, $P_1 = \left|S_0^-\right|^2$, $P_2 = \left|D_0^-\right|^2$ and $P_3$ is the relative phase between the amplitudes. The results of fitting the angular distributions with eq.(10) can be seen in figs.37–38. The fits were done in 60 $MeV/c^2$ bins of the $K_s^0 K_s^0$ invariant mass. In fig.37 we plot the fits to the angular distributions, and in fig.38 we plot the amplitude squared of the waves and their relative phase. One can see that the fit gives little $\mathcal{D}$ wave, but looking at the angular distributions in fig.37 one would expect more $\mathcal{D}$ wave. This is due to the fact that it is only necessary to have little $\mathcal{D}$ wave to modify drastically a flat distribution[4], and one has to remember that it is assumed that the $\phi$ distribution is also flat, which does not allow for other projections $m$ for $\mathcal{D}$ waves.

These fits were done on the raw angular distributions, but one can also correct these distributions for the acceptance of the spectrometer, as was mentioned above, and perform the same fits. In order to do this, we generated Monte Carlo events with the characteristics described in Sect.4.2, and corrected bin by bin the angular distributions, by multiplying the bin size by the ratio of the generated to accepted Monte Carlo events for that bin (see the Appendix). The results can be seen in figs.39-40. The acceptance corrections do not change the relative amount of $\mathcal{S}$ and $\mathcal{D}$ waves, and only put a little more $\mathcal{D}$ wave at high mass.

[4]the reader can perform this simple exercise to convince himself of this statement

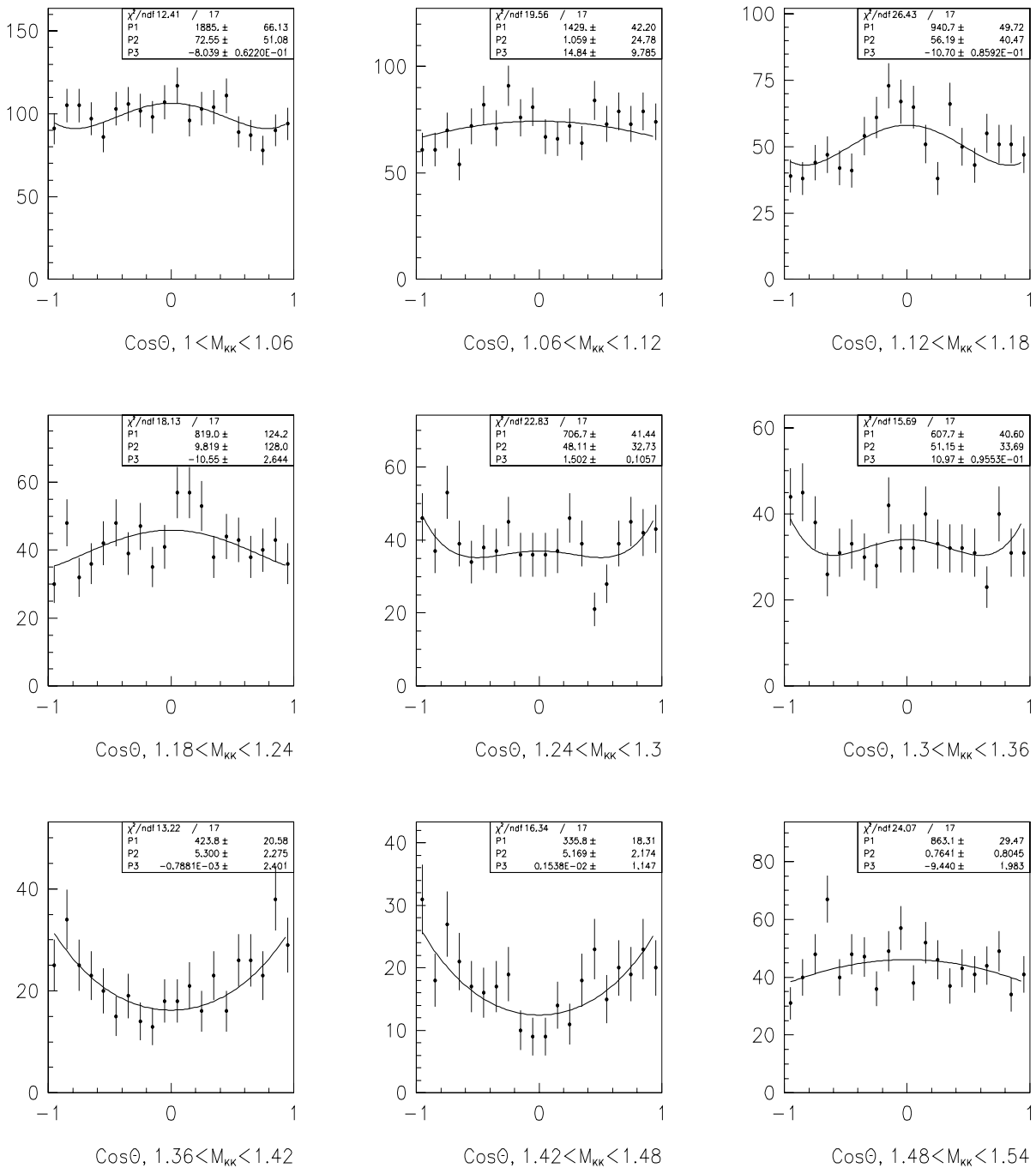


Figure 37: Fits to the $\cos\theta$ distributions using only two waves.

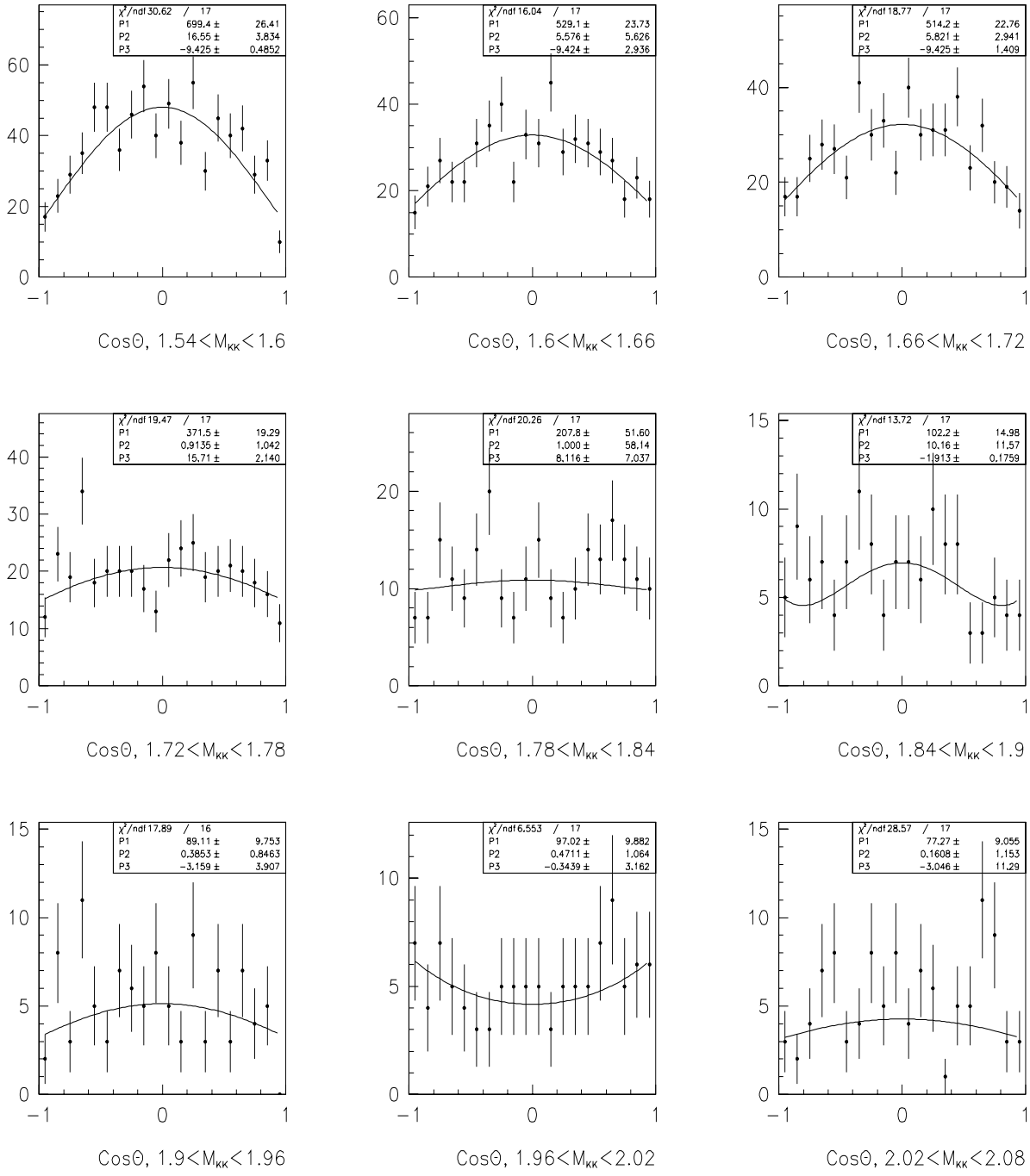


Figure 37 Continued.

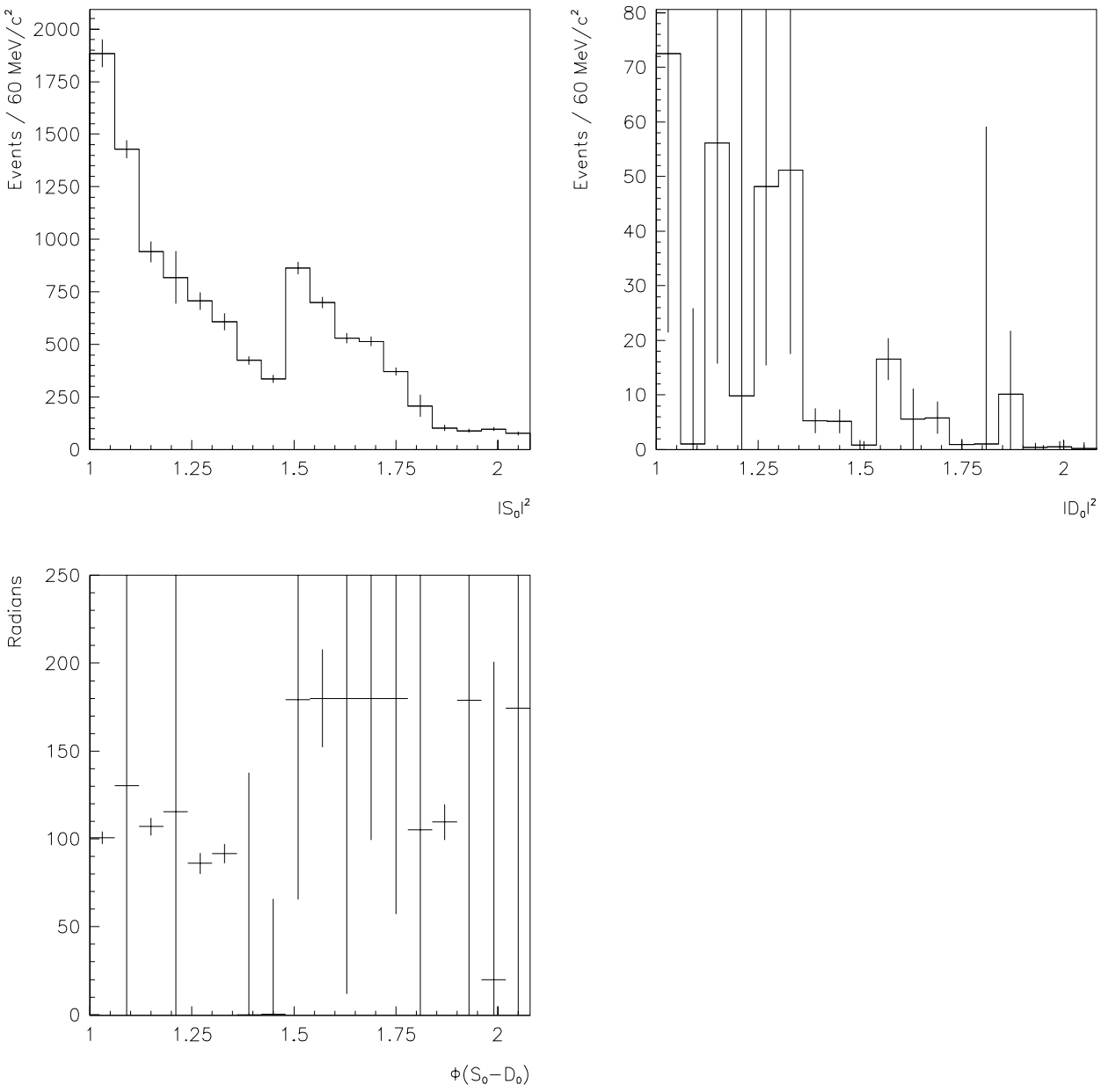


Figure 38: Number of events in the $\mathcal{S}_0^-$ and $\mathcal{D}_0^-$ waves, from fits to the $\cos\theta$ distributions, as a function of the $K_s^0 K_s^0$ invariant mass ($x$-axis). The upper left plot is the squared of the $S_0$ amplitude, and the upper right is the squared of the $D_0$ amplitude. The lower plot is the relative phase between the amplitudes. We see that the fits give very little $\mathcal{D}_0^-$ wave.

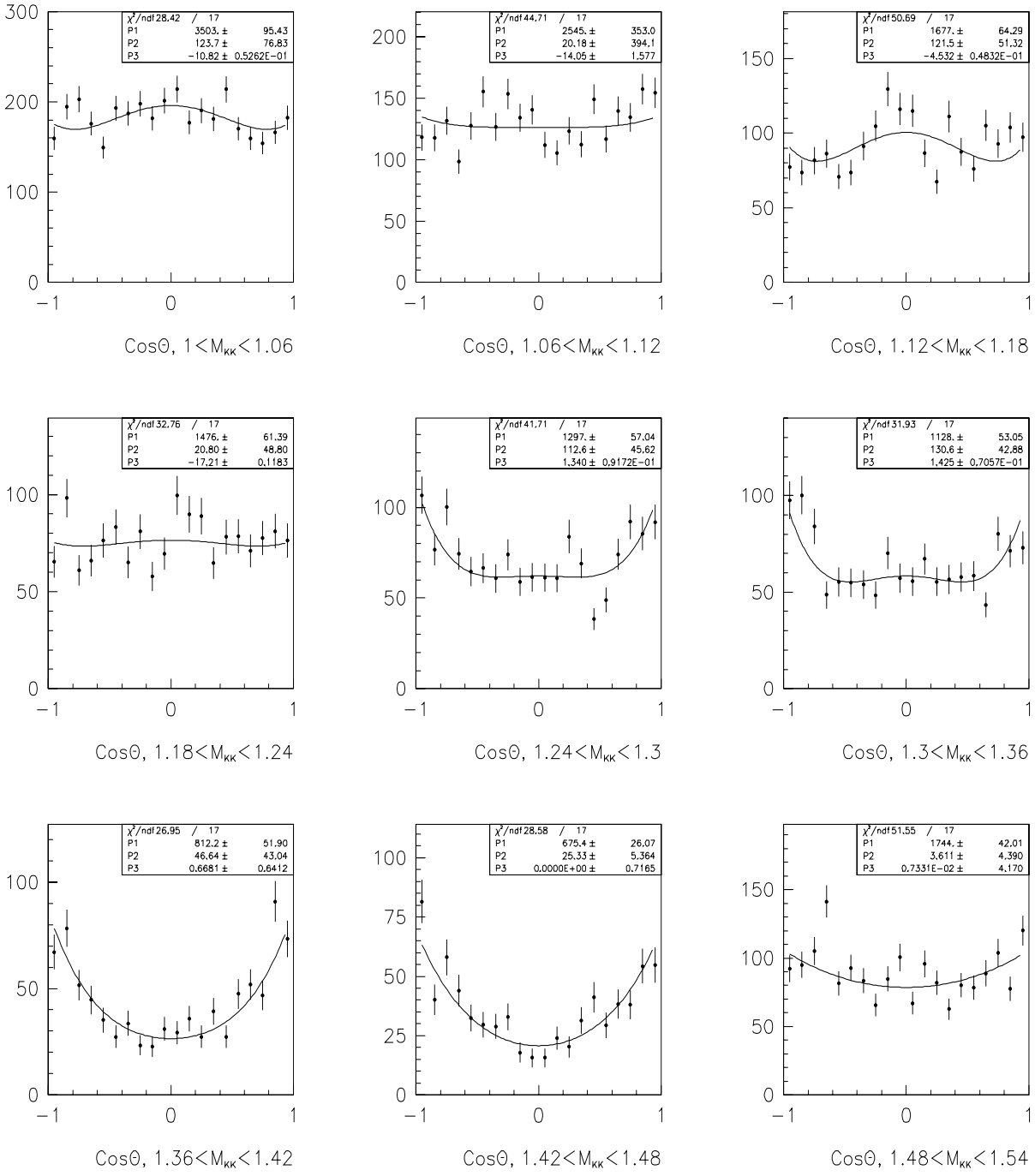


Figure 39: Fits to the $\cos\theta$ distributions using only two waves, after acceptance corrections.

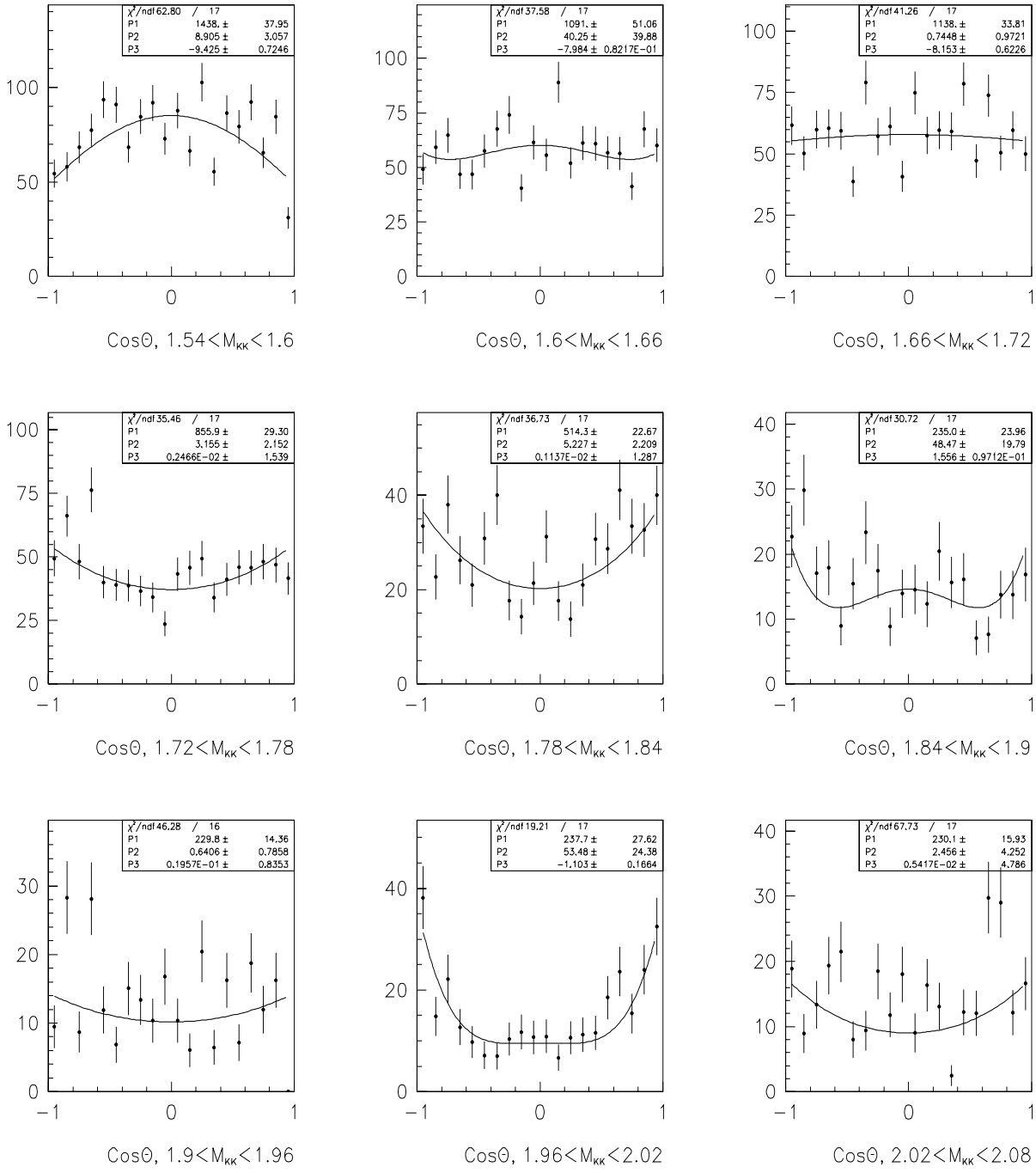


Figure 39 Continued.

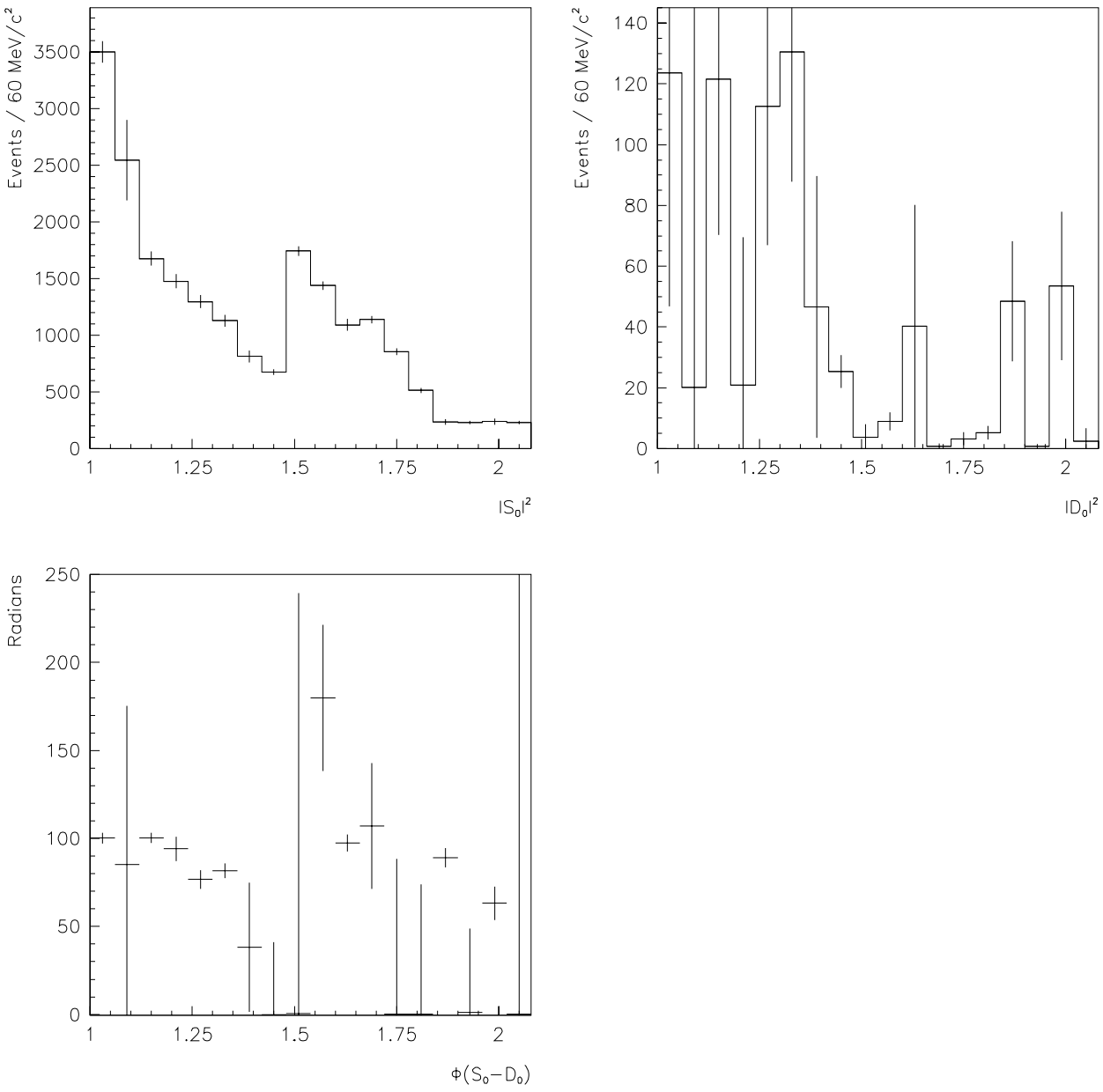


Figure 40: Number of events in the $\mathcal{S}_0^-$ and $\mathcal{D}_0^-$ waves, from fits to the $\cos\theta$ distributions, after acceptance corrections, as a function of the $K_s^0 K_s^0$ invariant mass ($x$-axis). Comparing to fig.38, we see that there is still little $\mathcal{D}_0^-$ wave, and the acceptance corrections just put few more events into this wave.

## 4.4 Maximum Likelihood Method.

Doing a fit on the angular distributions has some disadvantages. For example, the histograms must contain very many events for the fit to converge, since a fit to a plot with few events gives a large $\chi^2$; the fits can only use a few parameters, since putting several parameters makes it difficult for the fit to converge, and it is also very difficult to add more parameters. Therefore, one should look for other ways to estimate the amplitudes of the partial waves that reproduce the observed angular distributions.

From a theoretical point of view, the most important general method of estimation so far known is the *method of maximum likelihood*. In particular cases, this method was already used by Gauss[50]; as a general method of estimation it was first introduced by R. A. Fisher in a short paper of 1912[51].

If the probability density function of variable (or set of variables) $X$ is $P(X)$, then the joint density of the sample $X_1,\ X_2,\ X_3, \ldots,\ X_n$ is given by

$$g(X_1, X_2, X_3, \ldots, X_n) = P(X_1)P(X_2)P(X_3)\cdots P(X_n) = \prod_{i=1}^{n} P(X_i) \tag{11}$$

If the density function $P(X)$ contains the parameters $\alpha_1,\ \alpha_2,\ \alpha_3, \ldots,\ \alpha_k$, then this joint probability depends upon these parameters. Considered as a function of the parameters of the probability distribution, the joint probability is called the *likelihood* of the parameters, given the sample, and is denoted by

$$L(\alpha_1, \alpha_2, \alpha_3, \ldots, \alpha_k) = g(X_1, X_2, X_3, \ldots, X_n) = P(X_1)P(X_2)P(X_3)\cdots P(X_n) \tag{12}$$

Consider the probability distribution $I(\Omega)$ of the angular variables $\Omega = \{\cos\theta, \phi\}$ consisting of $N$ events. Assume that it can be described by a Poisson distribution and that we are using sufficiently small intervals $\Delta\Omega$ so that at most one can find one event in each interval. The Poison distribution says that the probability of finding $n$ events in a sample with $\bar{n}$ mean number of events, is given by

$$P_{\bar{n}}(n) = e^{-\bar{n}}\frac{\bar{n}^n}{n} \tag{13}$$

so that

$$P_{\bar{n}}(0) = e^{-\bar{n}} \qquad \text{and} \qquad P_{\bar{n}}(1) = \bar{n}e^{-\bar{n}}$$

Suppose that there are no events in the first interval, one event in the second, zero in the third, one in the fourth,... Since the average number of events in the $i$–th interval is given by

$$\bar{n}_i = \int_{\Delta\Omega_i} I(\Omega)\mathrm{d}\Omega$$

the probability is given by

$$\begin{aligned} \mathrm{P} &= e^{-\int_{\Delta\Omega_1} I(\Omega)\mathrm{d}\Omega} I(\Omega_2)\mathrm{d}\Omega_2 e^{-\int_{\Delta\Omega_2} I(\Omega)\mathrm{d}\Omega} e^{-\int_{\Delta\Omega_3} I(\Omega)\mathrm{d}\Omega} I(\Omega_4)\mathrm{d}\Omega_4 e^{-\int_{\Delta\Omega_4} I(\Omega)\mathrm{d}\Omega} \times \cdots \\ &= \underbrace{e^{-\int_{4\pi} I(\Omega)\mathrm{d}\Omega} I(\Omega_2)I(\Omega_4)\cdots I(\Omega_n)}\, \mathrm{d}\Omega_2\mathrm{d}\Omega_4\cdots\mathrm{d}\Omega_n \end{aligned} \tag{14}$$

In the case of the data analysis, the probability distribution $I$ is a function of the angular variables $\Omega$, but any expansion of this distribution in terms of functions of the angular variables introduces parameters particular to that expansion. This is the case when we expand the probability in terms of spherical harmonics, where the parameters are the so called moments, and when we expand it in terms of wave functions in the naturality basis, where the parameters are the wave amplitudes. When considered as a function of these parameters, the term underbraced in eq.(14) is called the likelihood of the distribution,

$$\mathcal{L} = e^{-\int_{4\pi} I(\Omega)\mathrm{d}\Omega} I(\Omega_2)I(\Omega_4)\cdots I(\Omega_n) \tag{15}$$

and the sample of events is used to estimate the most likely value of the parameters that is necessary to specify the angular distribution. Since the maximum of the logarithm of $\mathcal{L}$ gives the maximum of $\mathcal{L}$, what one does is to minimize the function

$$-\ln\mathcal{L} = -\sum_{i=1}^{N} \ln I(\Omega_i) + \int_{4\pi} I(\Omega)\mathrm{d}\Omega \tag{16}$$

For the data analysis we used the CERN program MINUIT to find the minimum of eq.(16).

Maximum likelihood is a particularly important method because if the distribution assumed for the population is correct, then parameters estimated this way are consistent, efficient and sufficient, in the analytical sense.

We used the maximum likelihood method to calculate the amplitudes (and moments, see next Section) in the $K^0_s K^0_s$ system. The results for more than two waves will be shown in Section 4.7, here we present the results when using only two waves, to compare with what was obtained with the fits to the $\cos\theta$ distributions. In figs.41-42 we show the results from maximum likelihood, before and after acceptance corrections, respectively.

For the acceptance corrections we used the Monte Carlo events generated as described in Sect.4.2, to calculate the acceptance integrals for the partial waves. For a given bin of the $K^0_s K^0_s$ invariant mass, the acceptance integrals for the generated (accepted) events, are defined as the sum over all the events generated (accepted) in that bin, of the probability for each event. The probability of each event is given by the differential cross section as a function of the generated (reconstructed) kinematical variables for that event, weighted by the matrix element, which consists of the products of the amplitudes of the interfering waves. That is, the differential cross section for $N_g$ events generated in the $k$-th bin is given by

$$\begin{aligned}
\frac{\mathrm{d}\sigma}{\mathrm{d}x\mathrm{d}\Omega} &= \frac{1}{N_g}\sum_{i=1}^{N_g}(const)\,(phase\ space)\,A(x,\Omega)\ |\mathcal{M}|^2 \\
&= \frac{1}{N_g}\sum_{i=1}^{N_g}(const)\,(phase\ space)\,A(x,\Omega)\ \left|\sum_J \mathcal{D}_J\right|^2 \\
&= (const)\sum_{i=1}^{N_g}\sum_{J_1,J_2}(phase\ space)\,A(x,\Omega)\,\mathcal{D}_{J_1}\mathcal{D}^*_{J_2} \\
&= (const)\sum_{J_1,J_2} A_{J_1,J_2}(x,\Omega) \qquad (17)
\end{aligned}$$

where

$$A_{J_1,J_2}(x,\Omega) = \sum_{i=1}^{N_g}(phase\ space)\,A(x,\Omega)\,\mathcal{D}_{J_1}\mathcal{D}^*_{J_2} \qquad (18)$$

is the acceptance integral for the amplitudes $\mathcal{D}_{J_1},\ \mathcal{D}_{J_2}$. The constant term is irrelevant, since

it will be absorbed in the normalization process. More on the acceptance corrections can be found in the Appendix.

Comparing to figs.37-40, we see that the results are identical, within error bars, but one has to remember that using maximum likelihood gives a better estimation of the parameters of the fit. The fact that the error bars in the phase are so big, may be due to the use of very few events in the mass bin (which is not the case, since each mass bin consists of hundreds of events), or to the fact that one is trying to parametrize a mass region so big, that the angular distribution changes a lot, and the parametrization is not good enough. In the latter case, one should use smaller mass bins. This is what we found to be truth, and therefore we shall use smaller mass bins in the following Sections, when doing the analysis.

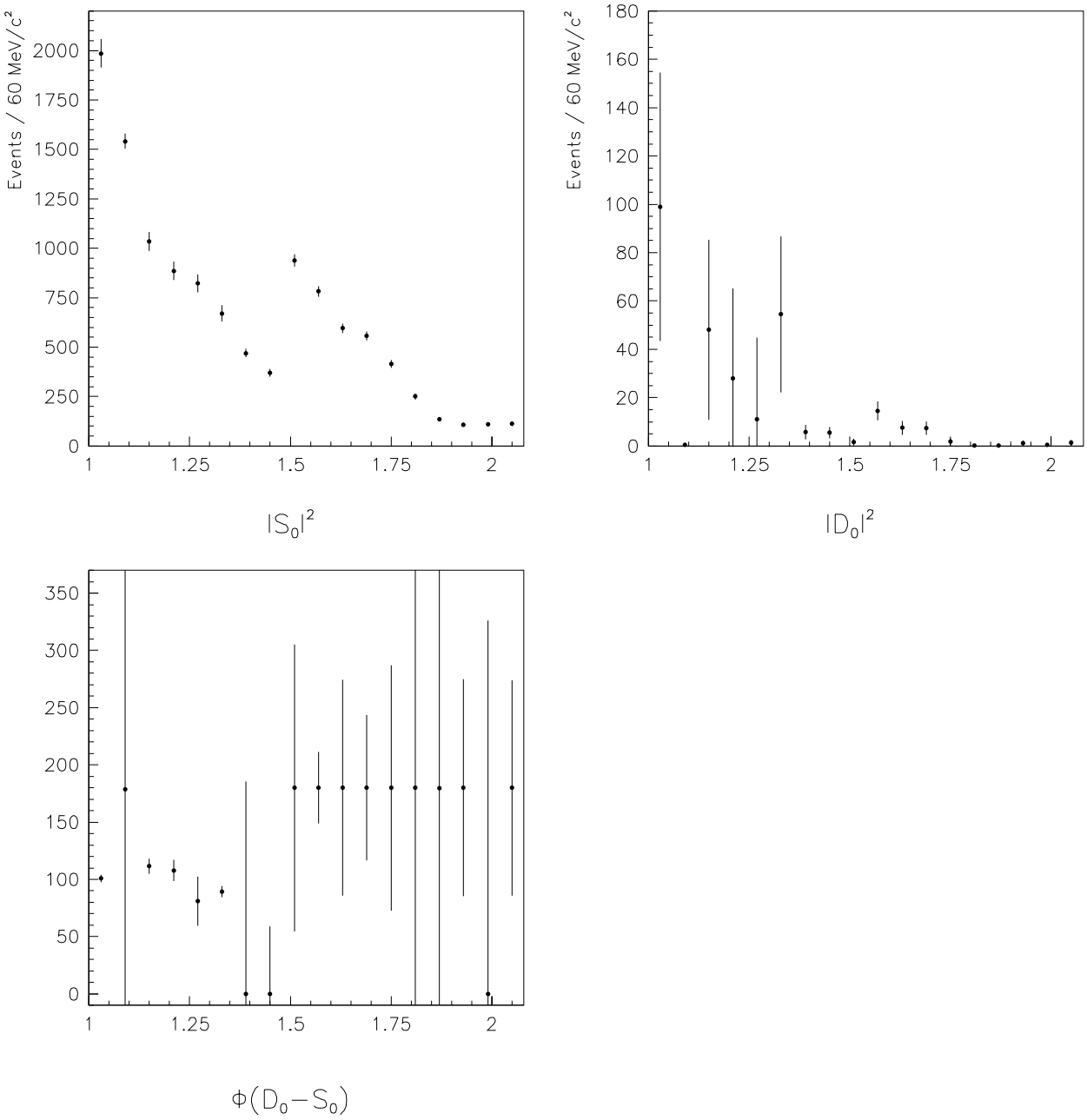


Figure 41: Number of events in the $\mathcal{S}_0^-$ and $\mathcal{D}_0^-$ waves, from maximum likelihood, as a function of the $K_s^0 K_s^0$ invariant mass ($x$-axis). Comparing to fig.38, we see that within error bars both methods give the same amounts for each wave, although maximum likelihood is a better estimation of the parameters used to describe the intensity distribution.

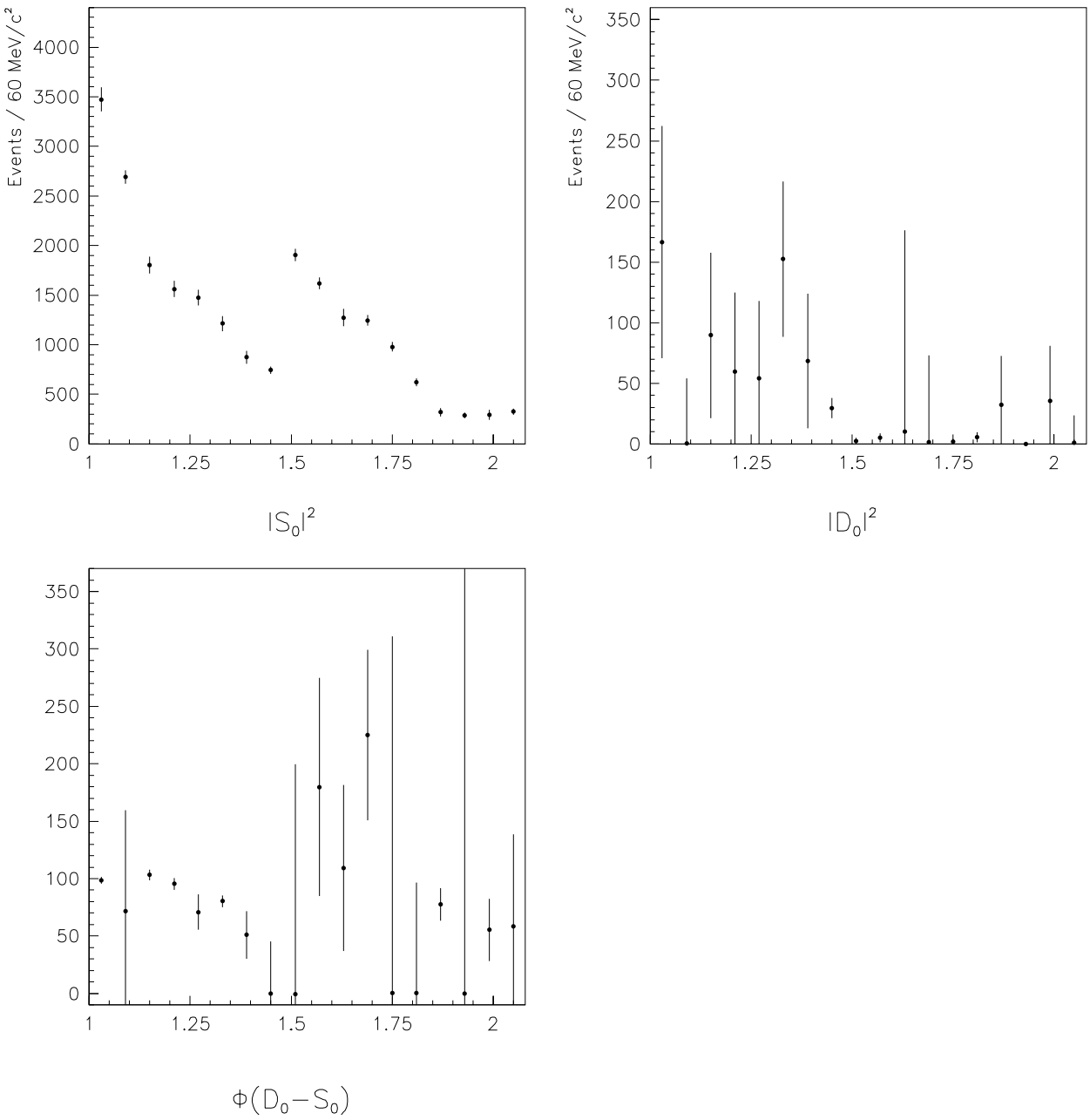


Figure 42: Number of events in the $\mathcal{S}_0^-$ and $\mathcal{D}_0^-$ waves, from maximum likelihood, after acceptance corrections, as a function of the $K_s^0 K_s^0$ invariant mass ($x$-axis). Compare to fig.40.

## 4.5 Moments in the $K_s^0 K_s^0$ System.

In the previous Sections we described the way to analyze the data using an expansion of the invariant matrix amplitude, $\mathcal{M}$ in terms of the reflectivity eigenstates. This in turn gives a quadratic expansion for the cross section in terms of the spherical harmonics. Another way to perform the analysis is to write the intensity distribution as a linear expansion in terms of the spherical harmonics

$$\begin{aligned} I(\Omega) &= \frac{1}{\sqrt{4\pi}} \sum_{\ell,m} t_{\ell m}\, Y_m^\ell(\Omega) \\ &= \frac{1}{\sqrt{4\pi}} \sum_{\ell,m\geq 0} c_m\, t_{\ell m}\, \mathrm{Re} Y_m^\ell(\Omega) \\ &= \frac{1}{\sqrt{4\pi}} \left\{ \sum_{\ell=0,2,4,\ldots} t_{\ell 0}\, Y_0^\ell(\Omega) + \sum_{\ell=2,4,\ldots} t_{\ell m}\, 2\mathrm{Re} Y_m^\ell(\Omega) \right\} \end{aligned} \tag{19}$$

where, for a system consisting of two $K_s^0$ only $\ell = 0, 2, 4, \ldots$ are allowed, and

$$c_m = \begin{cases} 1 & m = 0 \\ 2 & m > 0 \\ 0 & m < 0 \end{cases}$$

which give the normalization

$$\int^{4\pi} I(\Omega)\, \mathrm{d}\Omega = t_{00} \tag{20}$$

The coefficients $t_{\ell m}$ are called *moments*, and the method used to find the wave amplitudes, based on this expansion, is called the *method of moments*.

In practice, the detector has a limited acceptance. The observed event distribution can be written as

$$I_{acc}(\Omega) = A(\Omega)\, I(\Omega) \tag{21}$$

Multiplying both sides of this equation with $Y_m^{\ell\,*}(\Omega)$ and integrating over the solid angle, one gets

$$\begin{aligned} \int \mathrm{d}\Omega\, Y_m^{\ell\,*}(\Omega)\, I_{acc}(\Omega) &= \int \mathrm{d}\Omega\, Y_m^{\ell\,*}(\Omega)\, A(\Omega) \frac{1}{\sqrt{4\pi}} \sum_{\ell',m'} t_{\ell' m'}\, Y_{m'}^{\ell'}(\Omega) \\ &= \frac{1}{\sqrt{4\pi}} \sum_{\ell',m'} \left\{ \int \mathrm{d}\Omega\, Y_m^{\ell\,*}(\Omega)\, A(\Omega)\, Y_{m'}^{\ell'}(\Omega) \right\} t_{\ell' m'} \end{aligned} \tag{22}$$

The uncorrected moments $t'_{\ell m}$ are defined by

$$t'_{\ell m} = \sum_{\ell m} A_{\ell m, \ell' m'} t_{\ell' m'} \tag{23}$$

They can be directly calculated from the onserved angular distributions, in bins of the $K^0_s K^0_s$ invariant mas, using the following identity

$$t'_{\ell m} = \int \mathrm{d}\Omega \, I(\Omega) \, Y_m^{\ell\,*}(\Omega) \; \simeq \sum_{i=1}^{N_{obs}} Y_m^{\ell\,*}(\Omega_i) \tag{24}$$

where the sum (integral) is over the $N_{obs}$ observed events in the mass bin. The *acceptance integrals* $A_{\ell m, \ell' m'}$ are defined as

$$A_{\ell m, \ell' m'} = \int \mathrm{d}\Omega \, Y_m^{\ell\,*}(\Omega) \, A(\Omega) \, Y_{m'}^{\ell'}(\Omega)$$

They were calculated using Monte Carlo techniques: we generated six million MC events in the region $1.0 \leq M(K^0_s K^0_s) \leq 2.4 \, GeV/c^2$, processed them through the whole reconstruction chain, and fit the results for each moment with a cubic equation

$$t'_{\ell m} = P_1 + P_2 M_{KK} + P_3 M^2_{KK} + P_4 M^3_{KK}$$

the results can be found in Section B.4.

For the calculation of uncertainties in the (uncorrected) moments, $t'_{\ell m}$, one uses the same technique as described in Section B.3, where the calculation of uncertainties for the acceptance integrals is explained. The result for the moments error matrix $E_{\mu\nu}$ (where $\mu = \{\ell, m\}$ and $\nu = \{\ell', m'\}$) is

$$E_{\mu\nu} = \sum_{i=1}^{N_{obs}} Y_\mu(\Omega_i) Y_\nu(\Omega_i) - \frac{1}{N_{obs}} t'_\mu t'_\nu \tag{25}$$

and the uncertainty for the uncorrected moment $t'_\mu$ is

$$\sigma^2(t'_\mu) = E_{\mu\mu}$$

The uncorrected moments obtained from the data using the previous description are shown in figs.43-44. The moment $t'_{00}$ does not have error bars, since it represents only

the number of events in the mass bin ($\sigma^2(t_{00}) = 0$). The most prominent distributions in the uncorrected moments can be seen in the moments $t'_{20}$ and $t'_{21}$. In particular, the odd moments, $t'_{\ell m},\ \ell = 1, 3, \ldots$, should be zero, from parity conservation.

The moments in eq.(19) can be written in terms of the real part of the spherical harmonics. One can verify that the imaginary part is consistent with zero for a system of two identical bosons. A plot of the uncorrected moments "$t'_{\ell m}$" calculated using the imaginary part of $Y_{\ell m}$ in eq.(19), instead of the real part, for the first six moments which are not identically zero, is shown in fig.45. $t_{21}$ and $t_{22}$ show some structure in the low mass region, the region with more background, and the rest of the plots are consistent with zero.

The relevant uncorrected moments, with $\ell = 0, 2, 4$, are plotted in fig.46. One can also use maximum likelihood to calculate the moments. The results of this are shown in fig.47. Comparing fig.46 and fig.47 we see that the results are identical. We have also seen that the results of using maximum likelihood for the amplitudes analysis gives identical results to the results when doing a fit. In the next Sections we shall only use maximum likelihood to calculate amplitudes and moments, since this is the best method of estimation of parameters when the statistics are not very high.

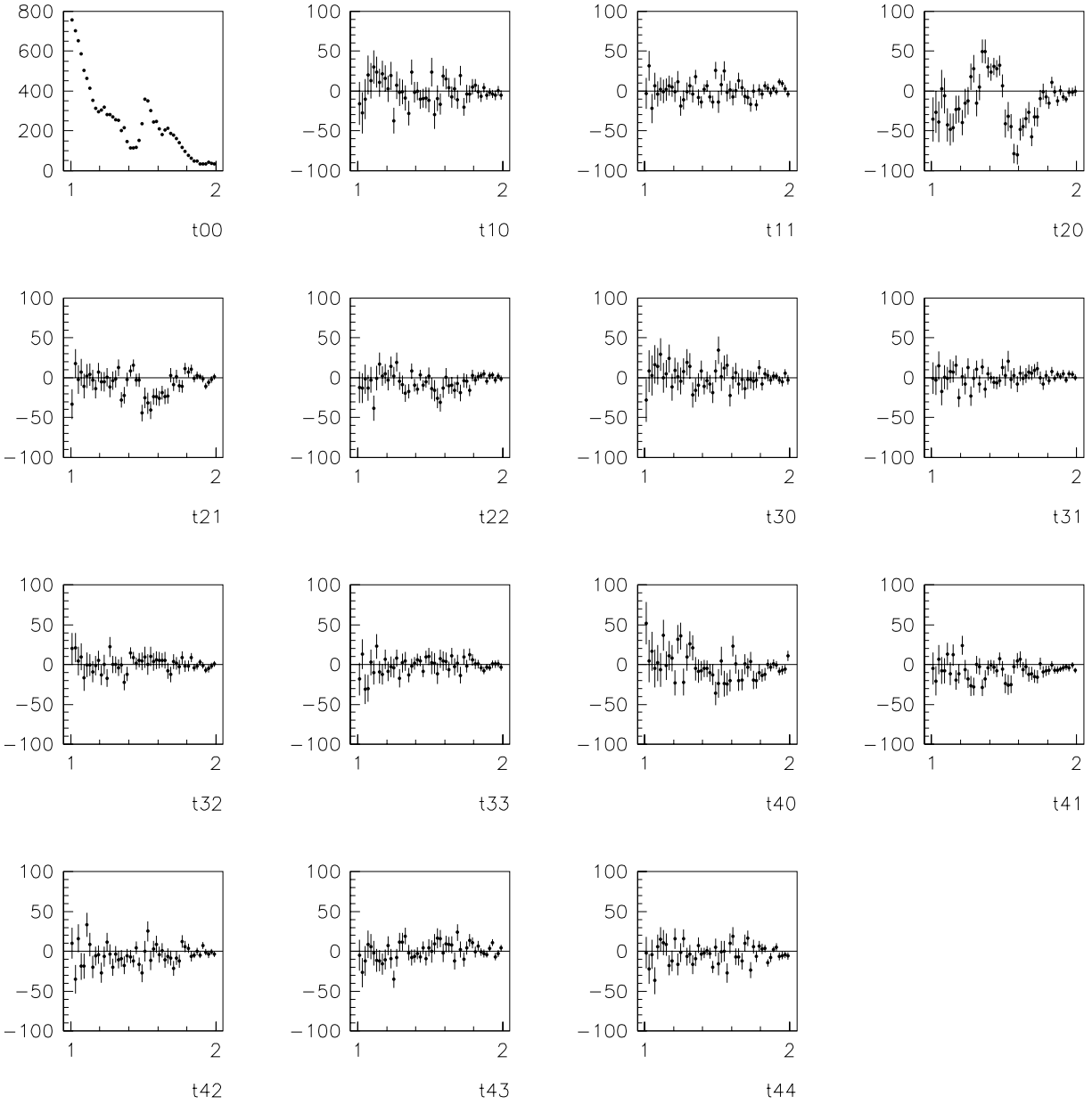


Figure 43: Uncorrected moments $t'_{\ell m}$ for $\ell = 0, \ldots, 4$, $m = 0, \ldots, \ell$, as a function of the $K^0_s K^0_s$ invariant mass ($x$-axis).

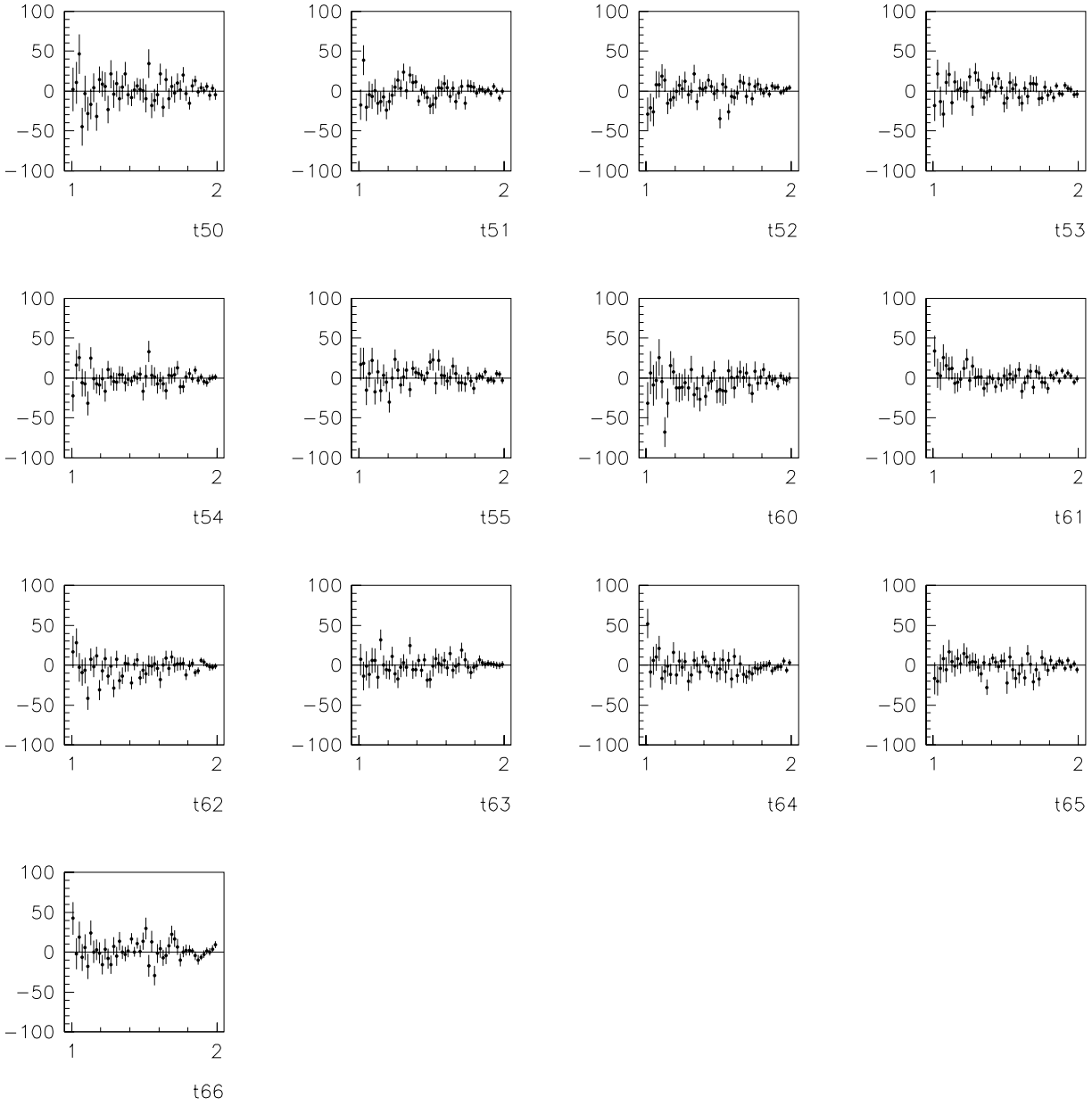


Figure 44: Uncorrected moments $t'_{\ell m}$ for $\ell = 5, 6$, $m = 0, \ldots, \ell$, as a function of the $K^0_s K^0_s$ invariant mass ($x$-axis).

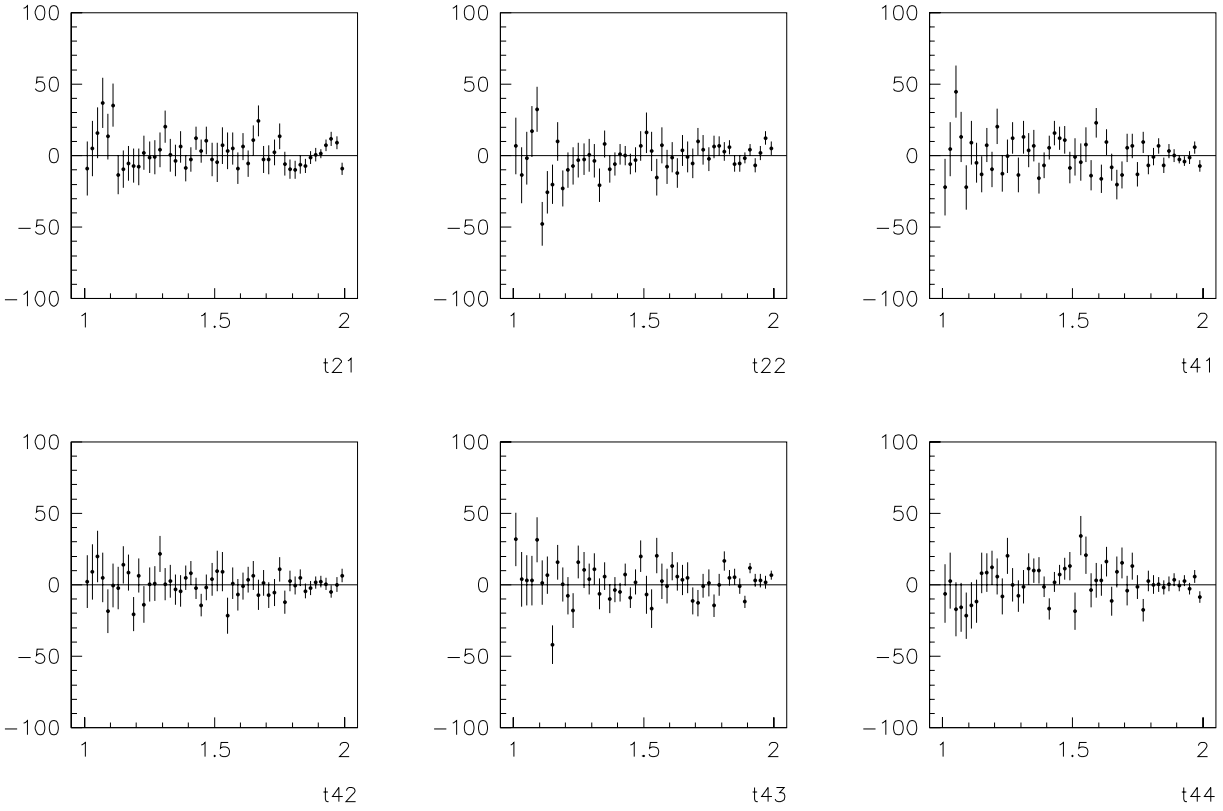


Figure 45: Uncorrected moments calculated using the imaginary part of the spherical harmonics, for $\{\ell, m\} = \{2,1\},\ \{2,2\},\ \{4,1\},\ \{4,2\},\ \{4,3\}, \{4,4\}$, as a function of the $K^0_s K^0_s$ invariant mass ($x$-axis).

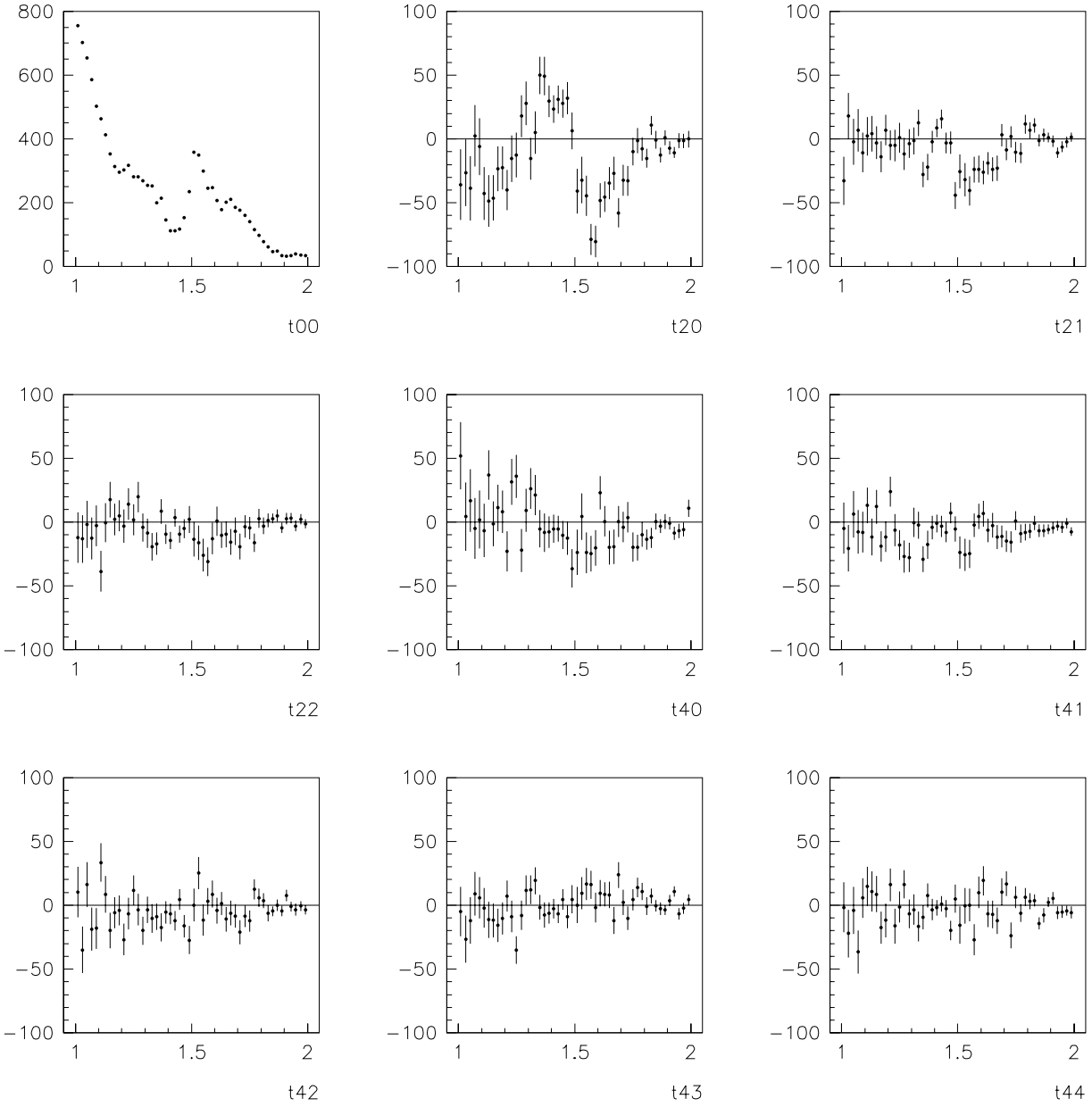


Figure 46: Relevant uncorrected moments, with $\ell = 0, 2, 4$, as a function of the $K^0_s K^0_s$ invariant mass.

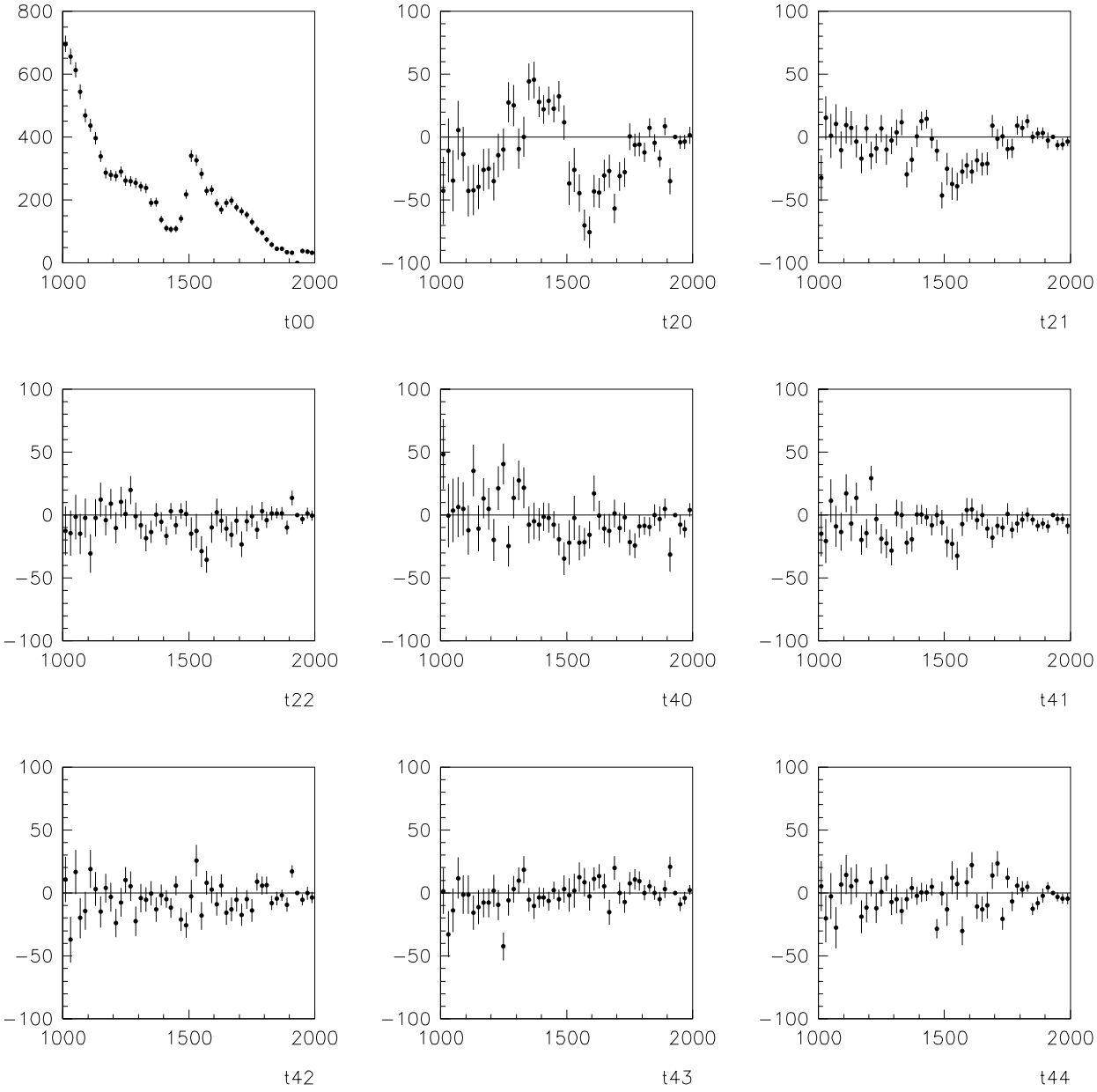


Figure 47: Relevant uncorrected moments, with $\ell = 0, 2, 4$, using maximum likelihood, as a function of the $K^0_s K^0_s$ invariant mass.

### 4.5.1 Relation to Amplitudes.

The parametrizations of the intensity distribution in terms of amplitudes or in terms of moments are identical, and should give the same results

$$\frac{\mathrm{d}\sigma}{\mathrm{d}x\mathrm{d}y} = (const)\,(P.S.)\left|\sum_J \mathcal{D}_J\right|^2 = (const)\,(P.S.)\,\frac{1}{\sqrt{4\pi}}\sum_{\ell,m\geq 0} c_m\, t_{\ell m}\,\mathrm{Re}Y^\ell_m(\Omega) \qquad (26)$$

where $(P.S.)$ is the phase space factor. The way to relate moments and amplitudes is by using the well known properties of the rotation matrices $D^\ell_{mn}$

$$\int \mathrm{d}\Omega D^{j_1}_{\mu_1 m_1}(\phi,\theta,0)D^{j_2}_{\mu_2 m_2}(\phi,\theta,0)D^{j_3 *}_{\mu_3 m_3}(\phi,\theta,0) = \frac{4\pi}{2j_3+1}(j_1\mu_1 j_2\mu_2\|j_3\mu_3)(j_1 m_1 j_2 m_2\|j_3 m_3) \qquad (27)$$

$$D^{\ell *}_{m0}(\phi,\theta,0) = \sqrt{\frac{4\pi}{2\ell+1}}Y^\ell_m(\theta,\phi) \qquad (28)$$

These relations together give the following form for the moments, in terms of the spherical harmonics, or in terms of Clebsch-Gordan coefficients

$$t_{\ell m} = \int \mathrm{d}\Omega Y^{\ell_1 *}_{\mu_1} Y^{\ell_2}_{\mu_2} Y^{\ell *}_m = \sqrt{4\pi}\sqrt{\frac{(2\ell_1+1)(2\ell+1)}{2\ell_2+1}}(\ell_1\mu_1\ell m\|\ell_2\mu_2)(\ell_1 0\ell 0\|\ell_2 0) \qquad (29)$$

The relations of the moments, up to $\ell = 4$, to the amplitudes, up to $\ell = 2$, are given by

$$\begin{aligned}
t_{00} &= \left|S^-_0\right|^2 + \left|D^-_0\right|^2 + \left|D^-_1\right|^2 + \left|D^-_2\right|^2 + \left|D^+_1\right|^2 + \left|D^+_2\right|^2 \\
t_{20} &= 2\mathrm{Re}\left(S^-_0 D^{-*}_0\right) + \sqrt{\tfrac{5}{49}}\left(\left|D^-_1\right|^2 + \left|D^+_1\right|^2\right) - \sqrt{\tfrac{20}{49}}\left(\left|D^-_2\right|^2 + \left|D^+_2\right|^2\right) \\
t_{21} &= \sqrt{2}\mathrm{Re}\left(S^-_0 D^{-*}_1\right) + \sqrt{\tfrac{10}{49}}\mathrm{Re}\left(D^-_0 D^{-*}_1\right) + \sqrt{\tfrac{30}{49}}\left(\mathrm{Re}\left(D^-_1 D^{-*}_2\right) + \mathrm{Re}\left(D^+_1 D^{+*}_2\right)\right) \\
t_{22} &= \sqrt{2}\mathrm{Re}\left(S^-_0 D^{-*}_2\right) + \sqrt{\tfrac{15}{98}}\left(\left|D^-_1\right|^2 - \left|D^+_1\right|^2\right) - \sqrt{\tfrac{40}{49}}\mathrm{Re}\left(D^-_0 D^{-*}_2\right) \\
t_{40} &= \tfrac{6}{7}\left|D^-_0\right|^2 - \tfrac{4}{7}\left(\left|D^-_1\right|^2 + \left|D^+_1\right|^2\right) + \tfrac{1}{7}\left(\left|D^-_2\right|^2 + \left|D^+_2\right|^2\right) \\
t_{41} &= \sqrt{\tfrac{60}{49}}\mathrm{Re}\left(D^-_0 D^{-*}_1\right) - \sqrt{\tfrac{5}{49}}\left(\mathrm{Re}\left(D^-_1 D^{-*}_2\right) + \mathrm{Re}\left(D^+_1 D^{+*}_2\right)\right) \\
t_{42} &= \sqrt{\tfrac{30}{49}}\mathrm{Re}\left(D^-_0 D^{-*}_2\right) + \sqrt{\tfrac{10}{49}}\left(\left|D^-_1\right|^2 - \left|D^+_1\right|^2\right) \\
t_{43} &= \sqrt{\tfrac{5}{7}}\left(\mathrm{Re}\left(D^-_1 D^{-*}_2\right) - \mathrm{Re}\left(D^+_1 D^{+*}_2\right)\right) \\
t_{44} &= \sqrt{\tfrac{5}{14}}\left(\left|D^-_2\right|^2 - \left|D^+_2\right|^2\right)
\end{aligned} \qquad (30)$$

## 4.6 Background Subtraction Revisited.

In Sect.3.4.2 we presented a method to count the number of background events. The idea there was to know how many events should be introduced in the analysis as background. We are performing the analysis in two different ways: 1) using the partial wave amplitudes, and 2) using the moments. The question now is: Where do we subtract the background?

We shall proceed as we did in Sect.3.4.2, where we compared the shape of the estimated number of background events, in terms of the $K_s^0K_s^0$ invariant mass, to the shape of the $K_s^0K_s^0$ invariant mass for the events dropped using the vetoes in the region of high missing mass squared. The idea here is to do the amplitudes and moments analysis in a set of the data that we know is composed of background only, and from the results infere where we should subtract the number of background events. For this purpose we selected data in the high missing mass squared region, $m^2_{missing} - m_p^2 \geq 1.5\ GeV/c^2$, with no other cuts, to have enough statistics.

For the analysis of the background region, in terms of the amplitudes, we used four waves, $\mathcal{S}_0^-$, $\mathcal{D}_0^-$, $\mathcal{D}_1^-$, $\mathcal{D}_1^+$,. Therefore, we used only six parameters, the four squared amplitudes, and two phases, $\phi(D_0 - S_0)$ and $\phi(D_1^- - S_0)$, which are the phases of the $D_0^-$ and $D_1^-$ amplitudes with respect to amplitude $S_0^-$. The results are shown in fig.48[5]. The two top plots are the squared amplitude $\left|S_0^-\right|^2$ and the sum of the squared amplitudes of the $\mathcal{D}$ waves. The three plots in the middle are the squared amplitudes for each of the $\mathcal{D}$ waves, and the plots in the bottom are the phases of the negative reflectivity $\mathcal{D}$ waves with respect to the $\mathcal{S}$ wave. The $K_s^0K_s^0$ invariant mass was divided in 20 $MeV/c^2$ bins. What these plots tell us, is that the estimated number of background events should be considered as a non-interfering $S_0$ wave background, and therefore subtracted only in the amplitude $\left|S_0^-\right|^2$.

Remember that for the data analysis we are trying to minimize the logarithm of the

[5]When using these four waves there are always two solutions, as will be explained in Sect.4.7. The second solution in this case gives the same contribution for each $\mathcal{D}$ wave, and little $\mathcal{S}$ wave, which reminds us that a flat distribution can be described by a $\mathcal{S}$ wave alone, or by summing all contributions from non-interfering $\mathcal{D}$ waves, with the same weights.

likelihood

$$-\ln\mathcal{L} = -\sum_{i=1}^{N}\ln I(\Omega) + \int I(\Omega)\mathrm{d}\Omega \tag{31}$$

but now, the $N$ events in the mass bin consists of $N_{ev}$ physically meaningful events, and $N_{bk}$ background events, in a non-interfering $\mathcal{S}$ wave, and hence the probability $I(\Omega)$ can be separated as

$$I(\Omega) = I_{ev}(\Omega) + I_{bk}(\Omega)$$

In terms of amplitudes, we can write

$$I(\Omega) = \left|A^{-}\right|^{2} + \left|A^{+}\right|^{2} + N_{bk} \tag{32}$$

where $A^{-}$, $A^{+}$ represent the invariant amplitudes for negative and positive reflectivity, respectively, which do not interfere among themselves. Considering the background as a non-interfering $\mathcal{S}$ wave, we can write

$$\begin{aligned} I(\Omega) &= \sum_{\alpha\beta} D_{\alpha}{D_{\beta}}^{*}\mathcal{D}_{\alpha}\mathcal{D}_{\beta}^{*} + \left|A^{+}\right|^{2} + N_{bk}\left|\mathcal{S}_{0}^{-}\right|^{2} \\ &= \left(\left|S_{0}^{-}\right|^{2} + N_{bk}\right)\left|\mathcal{S}_{0}^{-}\right|^{2} + {\sum_{\alpha\beta}}' D_{\alpha}{D_{\beta}}^{*}\mathcal{D}_{\alpha}\mathcal{D}_{\beta}^{*} + \left|A^{+}\right|^{2} \end{aligned} \tag{33}$$

where the prime in the sum is to indicate that the term with $\left|\mathcal{S}_{0}^{-}\right|^{2}$ has been extracted from it. This form of $I(\Omega)$ must be introduced in eq.(31), to perform the analysis.

If one uses only these four waves for the amplitudes, it is obvious from eq.(30) that there are seven nonzero moments, but one of them is proportional to another: $t_{42} = \sqrt{\frac{4}{3}}t_{22}$. Thus, there are again six independent parameters, $t_{00}$, $t_{20}$, $t_{21}$, $t_{22}$, $t_{40}$, and $t_{41}$. Since we are going to subtract the number of background events only in the moment $t_{00}$, we can write the intensity in the following way, using $\alpha = \{\ell, m\}$

$$\begin{aligned} I(\Omega) &= \sum_{\alpha} t_{\alpha}Y_{\alpha}(\Omega) + N_{bk} \\ &= \sum_{\alpha} t_{\alpha}^{ev}Y_{\alpha}(\Omega) + t_{00}^{bk}Y_{00}(\Omega) \end{aligned} \tag{34}$$

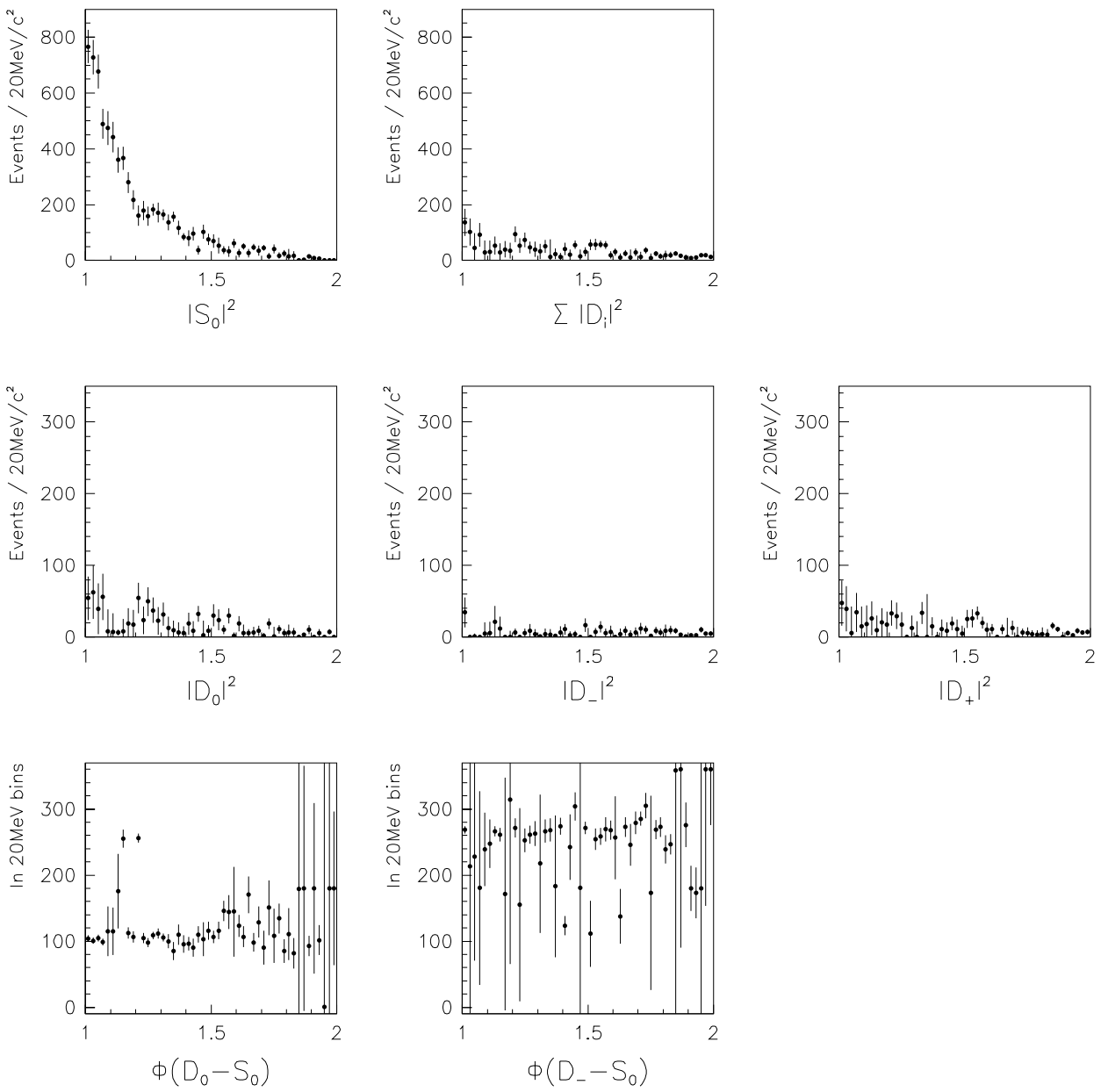


Figure 48: Amplitudes for events in the region $m^2_{missing} - m^2_p \geq 1.5\ GeV/c^2$, as a function of the $K^0_s K^0_s$ invariant mass ($x$-axis). These plots tell us that the estimated number of background events should be considered as a non-interfering $\mathcal{S}_0$ wave background, and therefore subtracted only in the amplitude $\left|S^-_0\right|^2$.

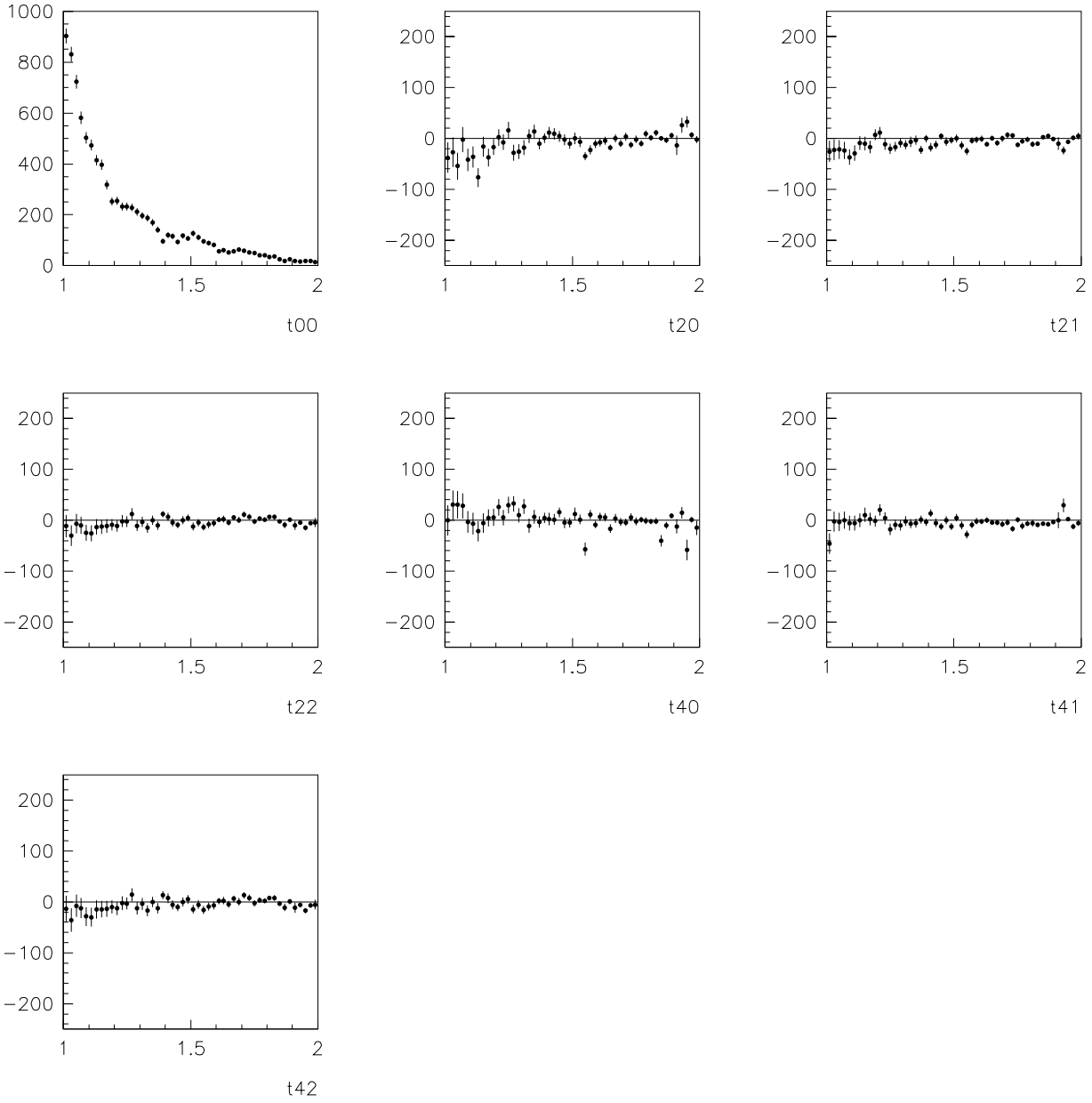


Figure 49: Moments for events in the region $m^2_{missing} - m^2_p \geq 1.5\ GeV^2/c^4$, as a function of the $K^0_s K^0_s$ invariant mass. As we can see, these plots tell us that the estimated number of background events should be subtracted only in the moment $t_{00}$.

The relevant moments, up to $\ell = 4$, after acceptance corrections and background subtraction, are shown in fig.50. We can see that moments $t_{43}$ and $t_{44}$ are compatible with zero, and since they are proportional to the helicity $m = 2$ waves, we assume that only waves with helicity $m = 0, 1$ are present in the data.

The acceptance integrals for moments depend only on the particular moment calculated, that is, there is no interference between different moments. Therefore, it is straight forward to add the acceptance integrals and background subtraction in the moments analysis. This is not true for the amplitudes analysis, where waves of the same reflectivity do interfere, and one has to subtract the background in a proper way, so that it does not interfere with negative reflectivity waves.

From here on we shall use background subtraction as well as acceptance corrections when plotting amplitudes or moments.

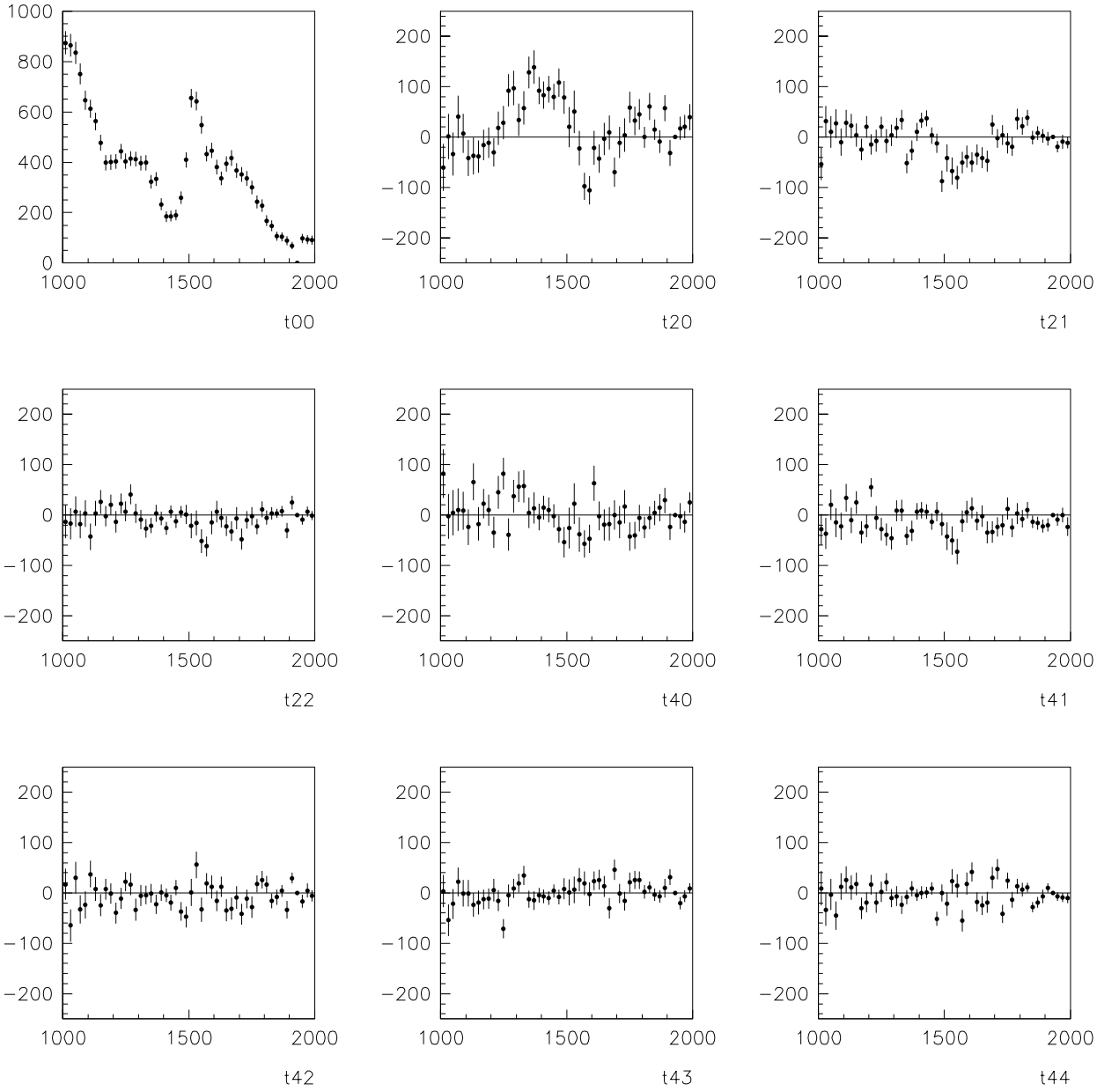


Figure 50: Acceptance corrected moments after background subtraction, as a function of the $K_s^0 K_s^0$ invariant mass ($x$-axis).

## 4.7 Amplitude Analysis of a System of two Identical Spinless Particles.

This Section describes the formalism necessary for exploring partial–wave amplitudes in a system involving two spinless particles. Here we work in some detail the cases of interest for our analysis, and refer the reader to the works by S.U.Chung [52, 53], and Sadovsky [54], where a complete description of the general method can be found. These works were based on a prervious paper by Barrelet[55].

If a system consists of two identical spinless particles, then only even waves are allowed due to Bose symmetry. Let $\ell_m$ be the maximum even wave present at a given mass bin, and let $\theta$ be the Jackson angle for the two–particle system. Consider, for example, the following reaction

$$\pi^- p \to \pi^0 \pi^0 n \tag{35}$$

for production of a dipion system in the forward direction, i.e. approximately along the beam line. Assume that the cross section for this process is independent of the helicities of the nucleons. In the Jackson frame, the amplitudes may be written

$$^{\epsilon}U(\Omega) = \sum_{\ell m} {}^{\epsilon}V_{\ell m}\, {}^{\epsilon}A_{\ell m}(\Omega) \tag{36}$$

where

$$^{\epsilon}A_{\ell m}(\Omega) = \sqrt{\frac{2\ell+1}{4\pi}}\, {}^{\epsilon}D^{\ell *}_{m0}(\phi,\theta,0) \tag{37}$$

are the decay amplitudes. The modified $D$–functions in the reflectivity basis are given by

$$^{\epsilon}D^{\ell *}_{m0}(\phi,\theta,0) = C(m)\left[D^{\ell *}_{m0}(\phi,\theta,0) - \epsilon(-)^m D^{\ell *}_{-m0}(\phi,\theta,0)\right] \tag{38}$$

with

$$C(m) = \begin{cases} 1/\sqrt{2} & m > 0 \\ 1/2 & m = 0 \\ 0 & m < 0 \end{cases} \tag{39}$$

It is seen that the modified $D$–functions in the reflectivity basis are given by

$$\begin{aligned} {}^{-}D^{\ell *}_{m0}(\phi,\theta,0) &= 2C(m) d^{\ell}_{m0}(\theta)\cos m\phi \\ {}^{+}D^{\ell *}_{m0}(\phi,\theta,0) &= 2iC(m) d^{\ell}_{m0}(\theta)\sin m\phi \end{aligned} \tag{40}$$

The resulting angular distribution is

$$I(\Omega) = \left|{}^{+}U(\Omega)\right|^2 + \left|{}^{-}U(\Omega)\right|^2 \tag{41}$$

The partial waves ${}^{\epsilon}V_{\ell m}$ stand for the production amplitudes for the ket states $|\epsilon \ell m\rangle$ , and $\epsilon$ is the reflectivity, set equal to the naturality of the exchanged Reggeon in reaction (35).

The angular distribution may be expanded in terms of the moments $t_{LM}$ via

$$I(\Omega) = \sum_{LM} t_{LM} \sqrt{\frac{2L+1}{4\pi}}\, D^{L*}_{M0}(\phi, \theta, 0) \tag{42}$$

The moments $t_{LM}$ are measurable quantities, since

$$t_{LM} = \sqrt{\frac{2L+1}{4\pi}} \int d\Omega\, I(\Omega)\, D^{L}_{M0}(\phi, \theta, 0) \tag{43}$$

which, by means of the orthogonality properties of the $D$ functions, gives

$$t_{LM} = \sum_{\substack{\ell m \\ \ell' m'}} \left(\frac{(2\ell'+1)(2L+1)}{4\pi(2\ell+1)}\right)^{1/2} V_{\ell m} V^{*}_{\ell' m'}\, (\ell' m' L M | \ell m)(\ell' 0 L 0 | \ell 0) \tag{44}$$

The normalization integral is

$$t_{00} = \int d\Omega\, I(\Omega) \tag{45}$$

The symmetry relations for the moments are well known. From the hermiticity of $\rho = V_{\ell m} V^{*}_{\ell' m'}$ in (44), one gets

$$t^{*}_{LM} = (-)^M\, t_{L-M} \tag{46}$$

and, from the parity conservation in the process, one finds

$$t_{LM} = (-)^M\, t_{L-M} \tag{47}$$

These equations show that the $t$'s are real. The angular distribution can be recast into

$$I(\Omega) = \sum_{LM} \sqrt{\frac{2L+1}{4\pi}} \tau(M)\, t_{LM}\, d^{L}_{M0}(\theta)\, \cos M\phi \tag{48}$$

where

$$\tau(M) = \begin{cases} 2 & M > 0 \\ 1 & M = 0 \\ 0 & m < 0 \end{cases} \tag{49}$$

Because of the identity of the two–final–state particles, the odd $\ell$'s are absent [56], and $t_{LM} = 0$ if $L =$odd.

Suppose that $\ell_m$ is the maximum spin present in a given $\pi\pi$ mass bin. It can be shown [53] that the number of independent non–zero $t$'s is

$$N = 3\ell_m + 1$$

Now, assume that the z–component $m$ of spin $\ell$ can take on the values 0 and 1 only, that is, the production amplitudes ${}^{\epsilon}V$ should be zero if $m > 1$. It is convenient to separate out the $\theta$ dependence from that of $\phi$, as follows:

$$\begin{aligned} {}^{-}U(\Omega) &= \frac{1}{\sqrt{4\pi}}\left[h_0(\theta) + \sqrt{2}h_-(\theta)\cos\phi\right] \\ {}^{+}U(\Omega) &= \frac{1}{\sqrt{4\pi}}\left[\sqrt{2}h_+(\theta)\sin\phi\right] \end{aligned} \tag{50}$$

where

$$\begin{aligned} h_0(\theta) &= \sum_{\ell=0}^{\ell_m}\sqrt{2\ell+1}\ {}^{-}V_{\ell 0}\ d^{\ell}_{00}(\theta) \\ h_-(\theta) &= \sum_{\ell=1}^{\ell_m}\sqrt{2\ell+1}\ {}^{-}V_{\ell 1}\ d^{\ell}_{10}(\theta) \\ h_+(\theta) &= \sum_{\ell=1}^{\ell_m}\sqrt{2\ell+1}\ {}^{+}V_{\ell 1}\ d^{\ell}_{10}(\theta) \end{aligned} \tag{51}$$

which satisfy

$$h_0(-\theta) = +h_0(\theta), \quad \textit{and} \quad h_\pm(-\theta) = \pm h_\pm(\theta) \tag{52}$$

Eq.(50) says that

$$I(\Omega) = \frac{1}{4\pi}\left|h_0(\theta) + \sqrt{2}h_-(\theta)\cos\phi\right|^2 + \frac{1}{4\pi}\left|\sqrt{2}h_+(\theta)\sin\phi\right|^2 \tag{53}$$

or, equivalently, rewrite the angular distribution as

$$I(\Omega) = \frac{1}{4\pi}\left[f_0(\theta) + 2f_1(\theta)\cos\phi + 2f_2(\theta)\cos 2\phi\right] \tag{54}$$

The $f$ functions are experimentally measurable, as they are completely determined given a set of moments $t_{LM}$. Indeed, one finds that

$$f_M(\theta) = \sum_{L=0}^{2\ell_m} \sqrt{4\pi(2L+1)}\, t_{LM}\, d^L_{M0}(\theta) \tag{55}$$

Comparing (53) to (54), one finds

$$\begin{aligned} f_0(\theta) &= |h_0(\theta)|^2 + |h_-(\theta)|^2 + |h_+(\theta)|^2 \\ f_1(\theta) &= \sqrt{2}\mathrm{Re}\left\{h_0(\theta)h^*_-(\theta)\right\} \\ f_2(\theta) &= \frac{1}{2}\left\{|h_0(\theta)|^2 - |h_+(\theta)|^2\right\} \end{aligned} \tag{56}$$

These equations summarize the problem at hand: on the left hand side are the functions involving the measured moments $t_{LM}$, and on the right hand side are the the functions containing the partial waves $V_{\ell m}$ to be determined.

One may eliminate $h_+$ by combining $f_0(\theta)$ and $f_2(\theta)$, and modify $f_1(\theta)$ to obtain

$$\begin{aligned} f_a(\theta) &\equiv f_0(\theta) + 2f_2(\theta) = |h_0(\theta)|^2 + \left|\sqrt{2}h_-(\theta)\right|^2 \\ f_b(\theta) &\equiv 2f_1(\theta) = 2\mathrm{Re}\left\{h_0(\theta)\sqrt{2}h^*_-(\theta)\right\} \end{aligned} \tag{57}$$

The form of $f_a$ and $f_b$ suggest that one can define, from (52),

$$\begin{aligned} G_-(\theta) &= \frac{1}{\sqrt{2}}\left[h_0(\theta) + \sqrt{2}h_-(\theta)\right] \\ G_-(-\theta) &= \frac{1}{\sqrt{2}}\left[h_0(\theta) - \sqrt{2}h_-(\theta)\right] \end{aligned} \tag{58}$$

such that

$$\begin{aligned} f_a(\theta) &= |G_-(\theta)|^2 + |G_-(-\theta)|^2 \\ f_b(\theta) &= |G_-(\theta)|^2 - |G_-(-\theta)|^2 \end{aligned} \tag{59}$$

It can be shown [52] that the function

$$(1+u^2)^{\ell_m} G_-(u) \tag{60}$$

where

$$u(\theta) = \tan(\theta/2) \tag{61}$$

is a polynomial in $u$ of order $2\ell_m$. Moreover, the function

$$\begin{aligned} \mathcal{G}_-(v) &= \frac{1}{u^{\ell_m}} G_-(u) = \frac{1}{u^{\ell_m}} (1+u^2)^{\ell_m} \left[ h_0(u) + \sqrt{2} h_-(u) \right] \\ &= a_{\ell_m} \prod_{k=1}^{\ell_m} (v - v_k) \end{aligned} \tag{62}$$

is a polynomial in $v$ of order $\ell_m$, with $a_{\ell_m}$ the coefficient of $v^{\ell_m}$, and there are $\ell_m$ complex roots $v_k$, the Barrelet zeroes of $\mathcal{G}_-$. The new variable $v$ is related to $u$ via

$$v = \frac{1}{u} - u = 2\cot\theta \tag{63}$$

Since $\mathcal{G}_-(v)$ and $\mathcal{G}_-(-v)$, through (62) and (63), enter as absolute squares in the expression for the $f$–functions [see eq.(60)], the complex conjugate of a root $v_k$ does not perturb $t_{LM}$, leaving the angular distribution invariant, although it could alter the partial waves. Since taking the complex conjugate of all the roots does not lead to a new solution, there are in general $2^{\ell_m - 1}$ solutions. For each new $\mathcal{G}_-(v)$, one may calculate

$$\begin{aligned} h_0(\theta) &= \frac{1}{\sqrt{2}} \left[ g(\theta) + g(-\theta) \right] \\ h_-(\theta) &= \frac{1}{2} \left[ g(\theta) - g(-\theta) \right] \end{aligned} \tag{64}$$

to search for a new set of partial waves ${}^-V_{\ell 0}$, ${}^-V_{\ell 1}$. Next, the third equation of (57) is used to calculate

$$|h_+(\theta)|^2 = |h_-(\theta)|^2 - 2 f_2(\theta) \tag{65}$$

Note that the allowed partial waves, ${}^-V_{\ell 0}$ and ${}^-V_{\ell 1}$, must satisfy the condition that the right hand side of this equation remain non–negative.

The ambiguity among the partial waves ${}^+V_{\ell 1}$ can be treated by examining the function

$$\begin{aligned} \mathcal{G}_+(v) &= \frac{1}{u^{\ell_m}} G_+(u) = \frac{1}{u^{\ell_m}} (1+u^2)^{\ell_m} \, h_+(u) \\ &= c_+ v \prod_{k=1}^{\ell_m/2-1} (v^2 - r_k) \end{aligned} \tag{66}$$

where $c_+$ is the coefficient of $v^{\ell_m-1}$ and comes with $\ell_m/2-1$ complex roots $r_k$. This means that there exists a total of $2^{\ell_m/2-2}$ ambiguous solutions involving ${}^+V_{\ell 1}$, if $\ell_m \geq 4$. Combining the two ambiguities, one concludes that a system containing partial waves for $\ell_m \geq 4$ has a total of $N_a^e = 2^{\ell_m-1} \times 2^{\ell_m/2-2}$ ambiguous solutions.

## 4.8 An Example with $S$– and $D$–Waves.

Consider the case of two identical spinless particles for which $\ell_m = 2$. There are 5 parameters involving the partial waves with unnatural–parity exchange, i.e. $S_0$ (real), $D_0$ (complex) and $D_-$ (complex). There exists only one parameter, $D_+$ (real), for the partial wave produced by natural–parity exchange. So, one sees that a total of 6 parameters are required in this case.

The unnormalized moments are expressed in terms of the partial waves, as follows:

$$\begin{aligned}
t_{00} &= S_0^2 + D_0^2 + D_-^2 + D_+^2 \\
t_{20} &= S_0 D_0 - \sqrt{\frac{20}{49}} D_0^2 + \sqrt{\frac{5}{49}} \left( D_-^2 + D_+^2 \right) \\
t_{21} &= \frac{1}{\sqrt{2}} S_0 D_- + \sqrt{\frac{5}{98}} D_0 D_- \\
t_{22} &= \sqrt{\frac{15}{98}} \left( D_-^2 - D_+^2 \right) \qquad (67) \\
t_{40} &= \frac{6}{7} D_0^2 - \frac{4}{7} \left( D_-^2 + D_+^2 \right) \\
t_{41} &= \sqrt{\frac{15}{49}} D_0 D_- \\
t_{42} &= \sqrt{\frac{10}{49}} \left( D_-^2 - D_+^2 \right) \qquad (68)
\end{aligned}$$

where $A^2$ stands for $|A|^2$ and $AB$ for $2\mathrm{Re}\{AB^*\}$. Note that the moments with $M = 1$ have contributions from the partial waves with unnatural–parity exchange only. Not all 7 moments are independent; one finds, in fact,

$$t_{42} = \sqrt{\frac{4}{3}}\, t_{22} \qquad (69)$$

Therefore, there are 6 independent moments, corresponding to 6 partial–wave parameters to be determined in the problem.

The ambiguities among the partial waves with unnatural parity exchange are determined by the complex roots of the Barrelet function

$$\begin{aligned} \mathcal{G}_-(v) &= S_0\left(\frac{1}{u}+u\right)^2 + \sqrt{5}D_0(v^2-2) - \sqrt{60}D_- v \\ &= a_2 v^2 - a_1 + a_0 \end{aligned} \tag{70}$$

where

$$\begin{aligned} a_2 &= S_0 + \sqrt{5}D_0 \\ a_1 &= 2\sqrt{15}D_- \\ a_0 &= 4S_0 - 2\sqrt{5}D_0 \end{aligned} \tag{71}$$

Solving for $S_0$ and $D_0$ one finds

$$\begin{aligned} 6S_0 &= a_0 + 2a_2 \\ 6\sqrt{5}D_0 &= -a_0 + 4a_2 \end{aligned} \tag{72}$$

The Barrelet zeroes are

$$\{v_1, v_2\} = \frac{a_1 \pm \sqrt{a_1^2 - 4a_0 a_2}}{2a_2} \tag{73}$$

for

$$\mathcal{G}_-(v) = a_2(v - v_1)(v - v_2) \tag{74}$$

such that

$$\begin{aligned} a_1 &= a_2(v_1 + v_2) \\ a_0 &= a_2(v_1 v_2) \end{aligned} \tag{75}$$

Finally, the partial waves can be expressed in terms of the Barrelet zeroes

$$\begin{aligned} 6S_0 &= a_2(2 + v_1 v_2) \\ 6\sqrt{5}D_0 &= a_2(4 - v_1 v_2) \\ 2\sqrt{15}D_- &= a_2(v_1 + v_2) \end{aligned} \tag{76}$$

There exist two ambiguous solutions, corresponding to the sets $v_1, v_2$ and $v_1, v_2^*$.

The one wave with natural–parity exchange, $D_+$, can be set real, and can be determined from any one of the moments $t_{20}$, $t_{22}$, $t_{40}$, or $t_{42}$. There are no ambiguities involving $D_+$. For instance,

$$|D_+|^2 = |D_-|^2 - \frac{14}{\sqrt{30}} t_{22} \tag{77}$$

The two solutions found can be seen in figs.51-52. The first solution has one Barrelet zero with the imaginary part positive, and the other Barrelet zero with the imaginary part negative, for all mass bins. The second solution has both Barrelet zeroes with imaginary parts positive. In the figures, the upper left plot is the squared of the $S_0$ amplitude, and the upper center is the sum of the squares of the $D$ amplitudes, which are plotted separately in the three central plots. The two lower plots represent the phases of the negative–reflectivity $D$ amplitudes with respect to the $S_0$ amplitude. The difference, obviously, is that one solution gives most of the intensity in an $S_0$-wave, and a little contribution of $D$-wave. This is reversed in the second solution.

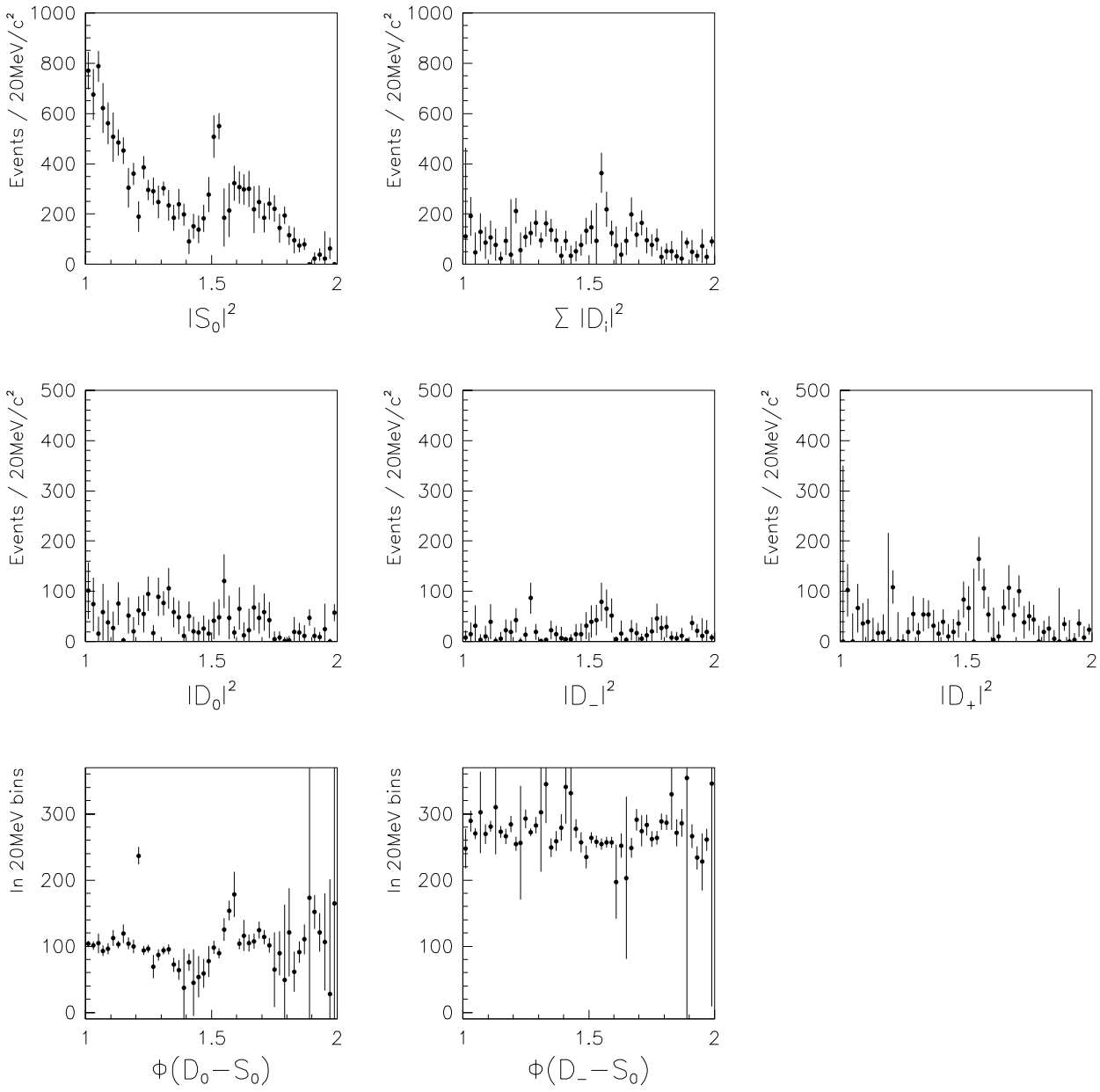


Figure 51: Amplitudes first solution, using four waves, as a function of the $K_s^0 K_s^0$ invariant mass ($x$-axis). Most of the events are in the $\mathcal{S}$ wave, where there is a clear peak around 1530 $MeV/c^2$, and the region of the $f_J(1710)$ is also in this wave. In the $\mathcal{D}$ wave one can see a peak at about 1560 $MeV/c^2$.

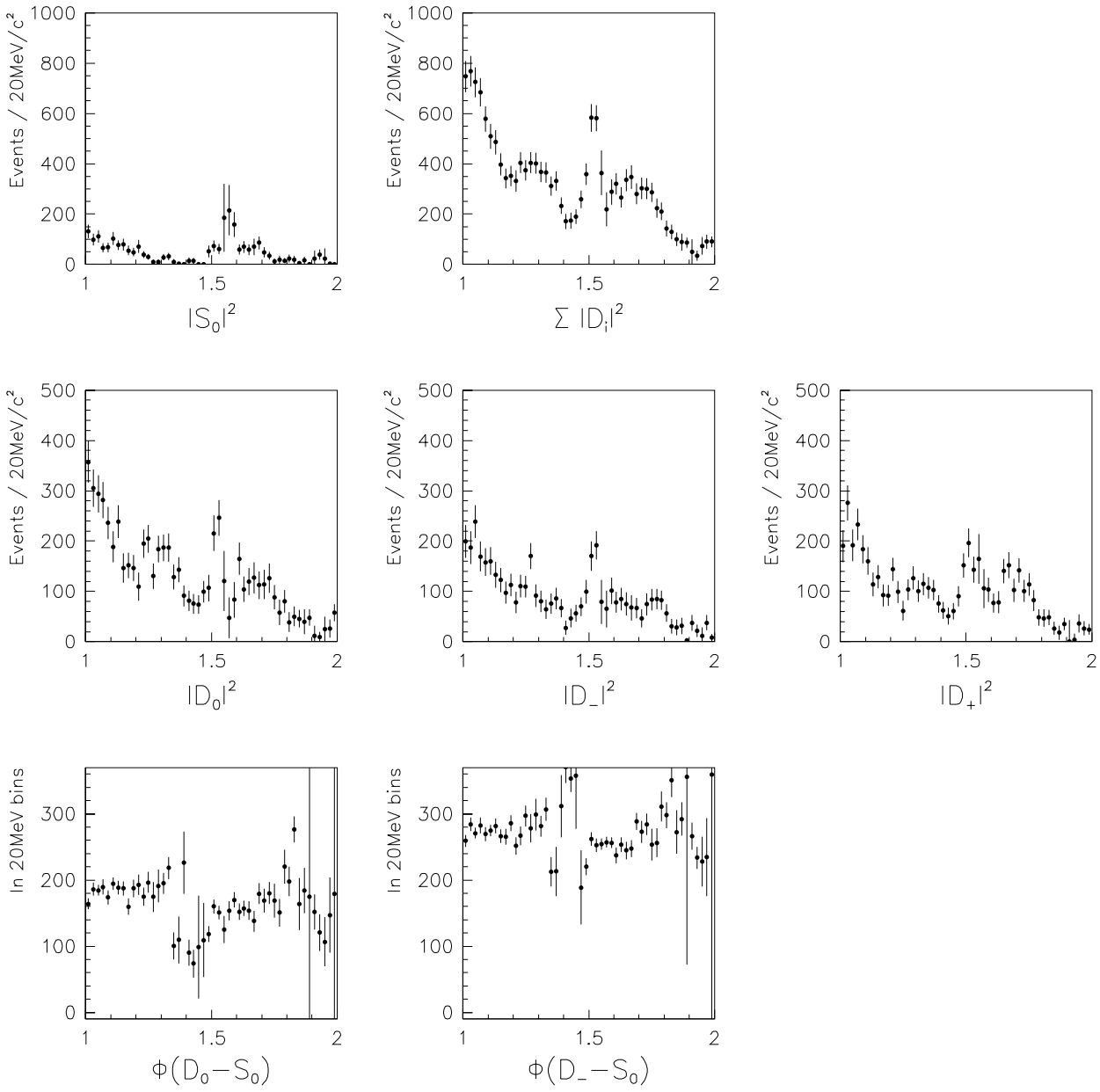


Figure 52: Amplitudes second solution using four waves, as a function of the $K_s^0 K_s^0$ invariant mass. Most of the events are in $\mathcal{D}$ wave, and there is little $\mathcal{S}$ wave, each $\mathcal{D}$ wave component having about the same distribution.

# 5 Discussion and Conclusions.

## 5.1 Ambiguities in the Solutions.

As can be seen in figs.51–52, if the two solutions found were well separated from bin to bin, and one could give a physical reason to discard one of them, then the solution would be clearly established. But looking carefully at the solutions found, one can see that they give the same results in the mass bin from 1560 to 1580 $MeV/c^2$, where one of the Barrelet zeroes becomes real. Therefore, there is a bifurcation point at this bin, and from the two initial solutions we end up with a set of four solutions. For example, the solution which at threshold was mainly $S$ wave, after 1580 $MeV/c^2$ could follow two different paths, one which gives mostly $S$-wave, and another which gives mostly $D$-wave. The two combinations of the solutions in figs.51–52 taking one of them from 1000 to 1560 $MeV/c^2$, and the other one from 1580 to 2000 $MeV/c^2$, can be seen in figs.53–54.

From this set of four solutions we can get rid of two of them. The clue to this is remembering what has been seen in $\pi^+\pi^-$ events (see fig.3). There, a rapid fall of events at around 1 $GeV/c^2$, and a rapid raise in the $K_s^0K_s^0$ spectrum, are both related to the existence of the $f_0(980)$. Therefore, what one expects in the $K_s^0K_s^0$ system, is to see a rapid raise at threshold, with predominancy of $S$-wave. Then, solutions two and four, which give very little $S$ wave at threshold can be discarded, owing to the existence of the $f_0(980)$.

We get again two solutions, but this time both having $S$ wave predominancy at threshold. Both solutions have a clear peak around 1530 $MeV/c^2$ in the $S$-wave, and some structure around 1300 $MeV/c^2$ in $D$-wave. Solution number one, in fig.51, has a clear peak around 1560 $MeV/c^2$ in $D$-wave, and $S$ wave dominance in the $f_J(1710)$ region. Solution number three, in fig.53, has almost no $S$-wave after 1600 $MeV/c^2$, where the three $D$-waves considered seem to have about the same intensity distribution. This solution favors $D$-wave for $f_J(1710)$.

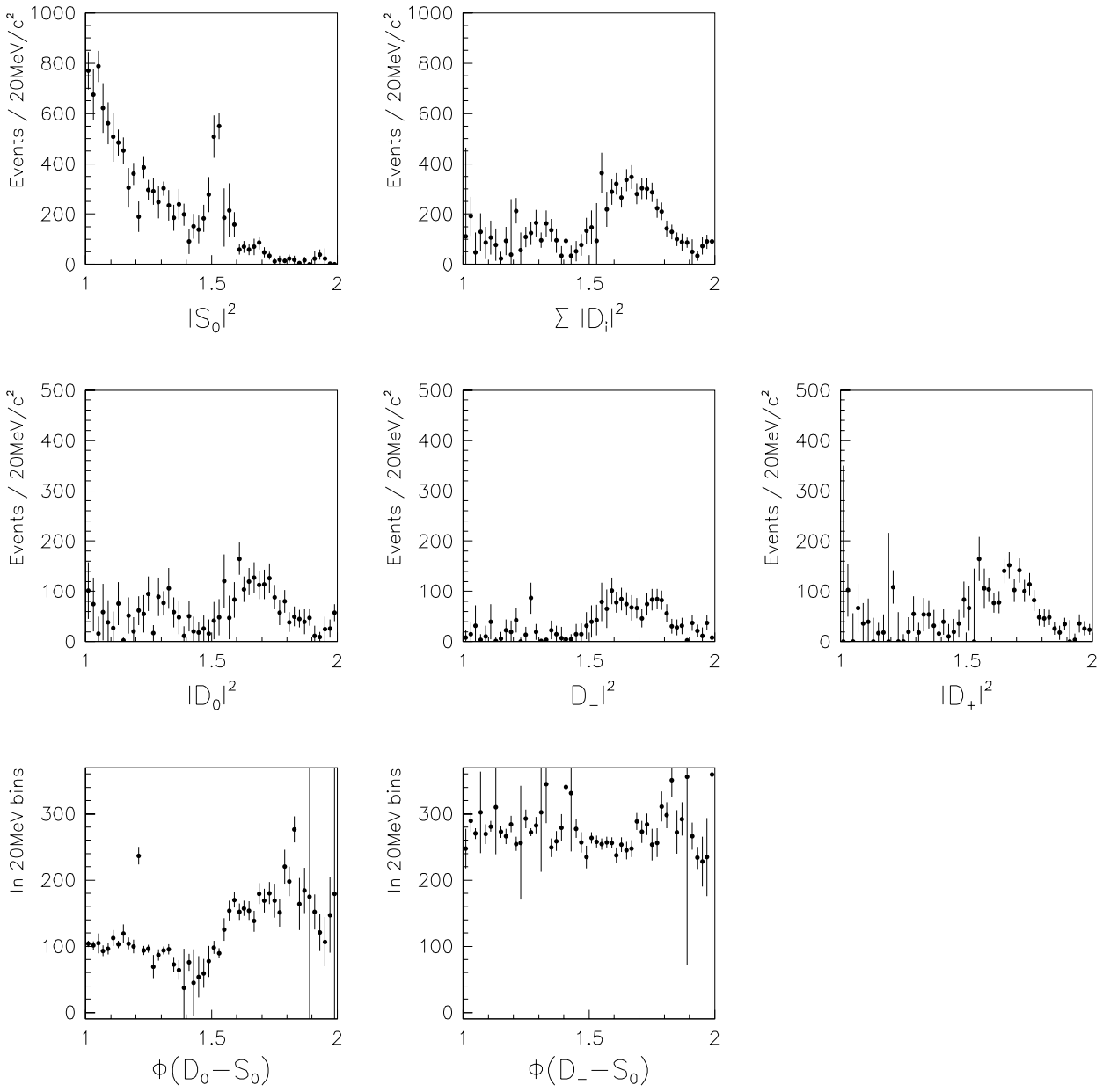


Figure 53: The bifurcation point at the bin 1560-1580 $MeV/c^2$ makes it possible to have two more solutions. This plot corresponds to the third solution. The $x$-axis is the $K_s^0 K_s^0$ invariant mass.

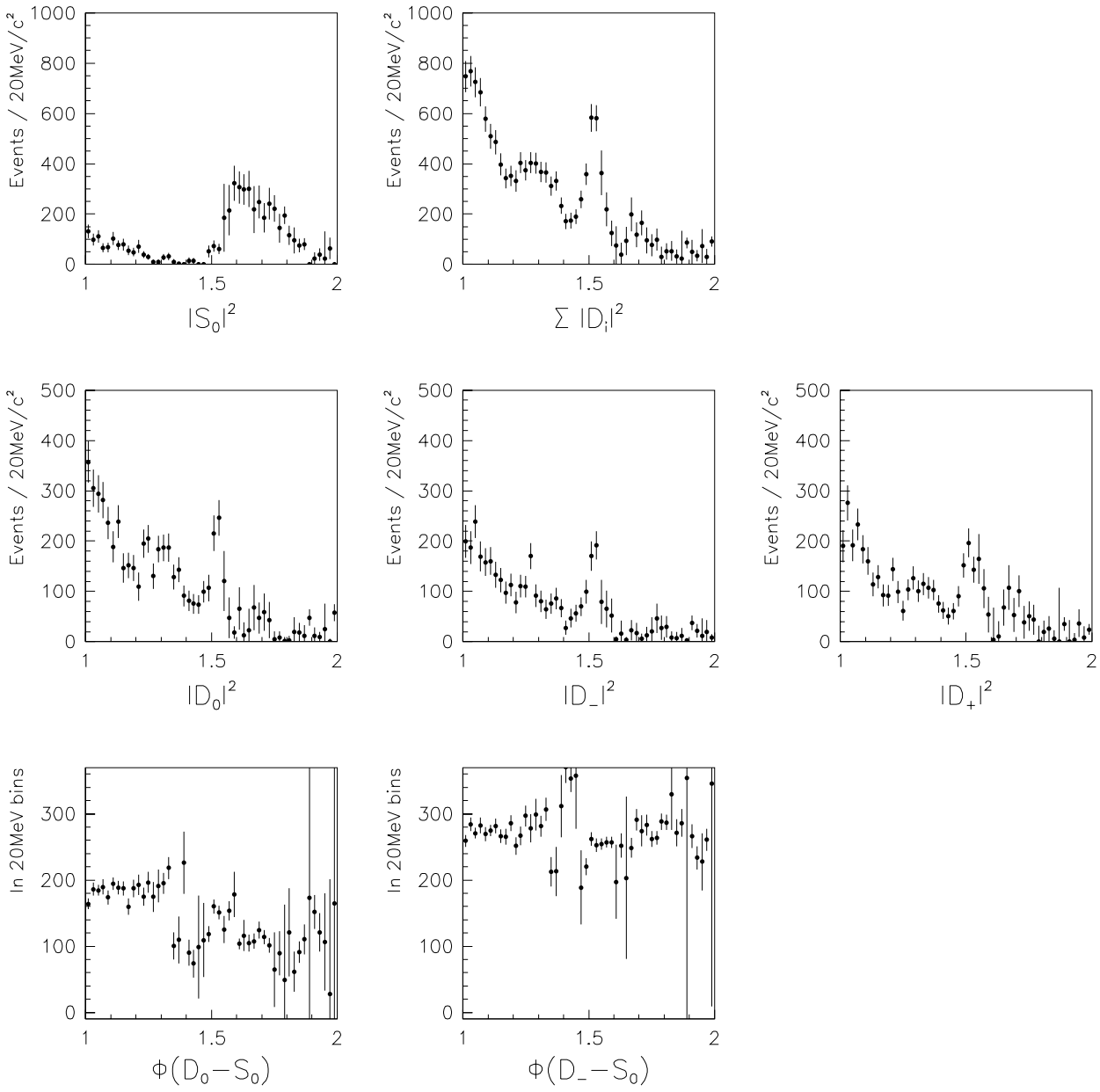


Figure 54: The fourth combination, resulting from the bifurcation point at 1560-1580 $MeV/c^2$.

There is still one extra point which we have not taken into account yet. When we used only two waves, $S$ and $D_0$, to describe the data, we found $S$-wave dominance for all the mass region considered, from 1 to 2 $GeV/c^2$ (see figs.40-42). This fact is enough to support the statement that solution number one, in fig.51, is the correct solution in the amplitudes analysis, when using four waves.

## 5.2 Comparison of the Results from Moments and Amplitudes Analysis.

We claimed in Sect.4.5.1 that moments and amplitudes give the same results, but we have not shown this yet. From the results for the moments in a given bin of mass (six parameters when using four waves), we can construct the corresponding set of amplitudes and waves in that bin (six parameters again), and vice versa. However, the error bars from one set of parameters can not be directly used to determine the error bars in the other set of parameters. This is due to the non-linear relation between moments and amplitudes, where the existence of trigonometric functions makes it impossible to propagate the errors from one set to the other.

Let us consider the case in which the amplitudes and phases of the four waves are the parameters that MINUIT has found when using the maximum likelihood method (the same considerations can be applied to the moments). What one does in this case is to generate Monte Carlo events with the amplitudes distributed according to the correlations found by MINUIT. If there were only two parameters, $p_1$ and $p_2$, with correlated gaussian–like distributions, the likelihood would have the form

$$\mathcal{L} = (const) \times e^{-\frac{1}{2}\left(ap_1^2+2bp_1p_2+cp_2^2\right)} \tag{78}$$

and the logarithm of the likelihood would be

$$\ln \mathcal{L} = \ln(const) - \frac{1}{2}\left(ap_1^2 + 2bp_1p_2 + cp_2^2\right) \tag{79}$$

The matrix of second derivatives of $\ln \mathcal{L}$, in this case, is given by

$$-\left(\frac{\partial^2 \ln \mathcal{L}}{\partial p_1 \partial p_2}\right) = \begin{pmatrix} a & b \\ b & c \end{pmatrix} \equiv \mathcal{M} \tag{80}$$

In general, the covariance matrix is defined as the inverse of the matrix of second derivatives of the logarithm of the likelihood $\mathcal{C} \equiv \mathcal{M}^{-1}$. Then, eq.(79) can be written as

$$\ln \mathcal{L} = \ln(const) - \frac{1}{2} P_c^T \mathcal{C}^{-1} P_c \tag{81}$$

where $P_c$ is the matrix of the correlated parameters. What one knows how to do is to generate uncorrelated parameters. Therefore, instead of using the matrix of correlated parameters, we change to a new basis of uncorrelated parameters, $P_c = U P_u$, where $P_u$ is the matrix of uncorrelated parameters, and $U$ is a $n \times n$ unitary matrix ($U^T = U^{-1}$), which diagonalizes the covariance matrix

$$U^{-1}\mathcal{C}^{-1}U = \begin{pmatrix} \sigma_1^{-2} & 0 & \cdots \\ 0 & \sigma_2^{-2} & \\ \vdots & & \ddots \end{pmatrix} \tag{82}$$

or, equivalently

$$U^{-1}\mathcal{C}U = \begin{pmatrix} \sigma_1^{2} & 0 & \cdots \\ 0 & \sigma_2^{2} & \\ \vdots & & \ddots \end{pmatrix} \tag{83}$$

Thus, diagonalizing $\mathcal{C}$ gives both the errors $\sigma_n^2$, and the uncorrelated parameters, $P_u$.

The values for the amplitudes calculated by MINUIT are used to obtain the central values for the moments, and the Monte Carlo events generated according to the distributions given by the covariance matrix are used to calculate the error bars above and below those central values.

The six independent moments obtained from the maximum likelihood analysis are plotted in fig.55, together with $t_{42} = \sqrt{\frac{4}{3}} t_{22}$. The moments obtained from the amplitudes, with the error bars calculated as explained above, are shown in fig.56. We can see that both plots are identical. The same method was applied to obtain the amplitudes from the moments. The results are shown in figs.57-58. Again, we can see that these plots are identical to those of figs.51-52.

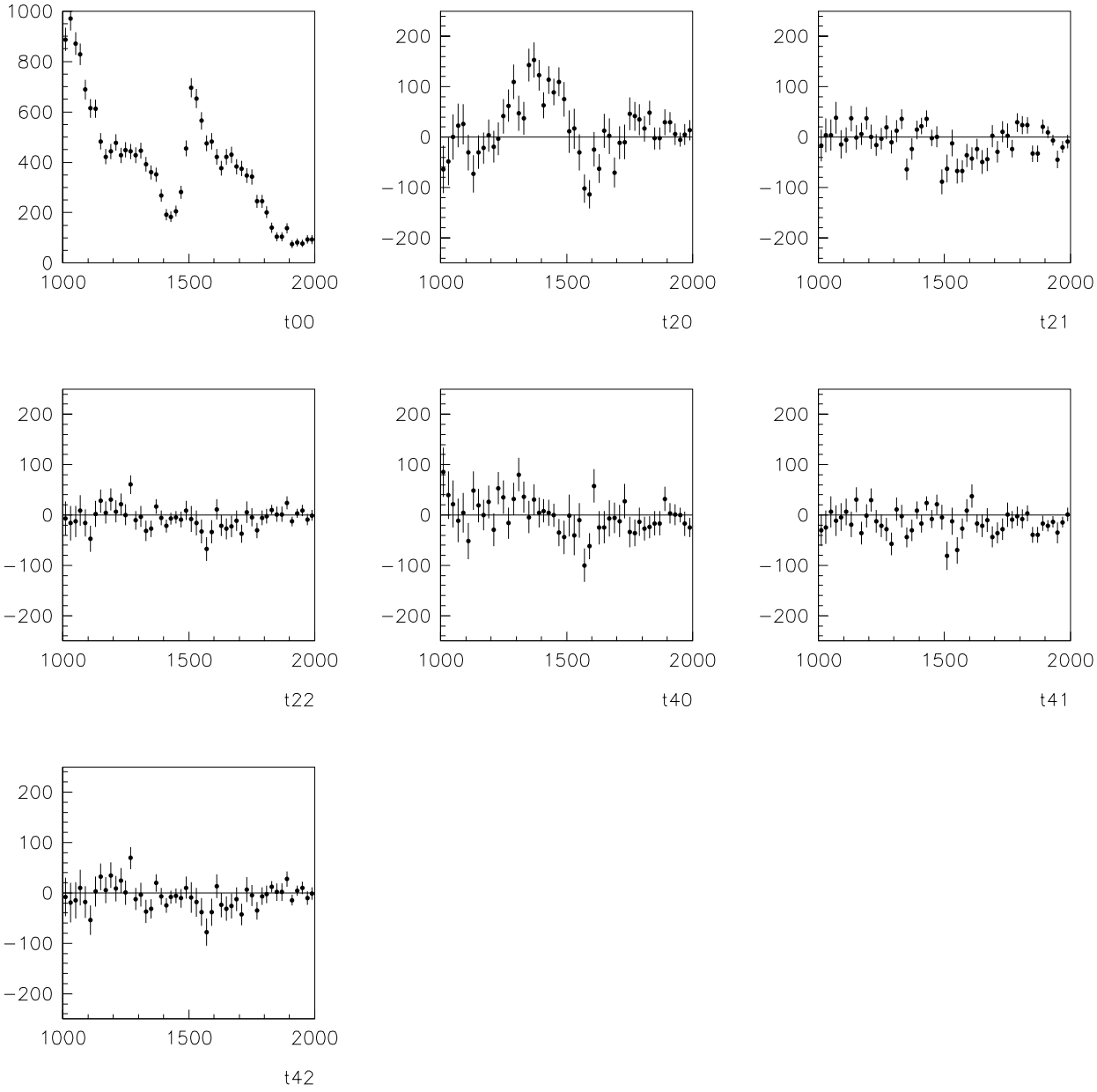


Figure 55: Non-zero moments when using four waves, as a function of the $K^0_s K^0_s$ invariant mass. These were obtained using the expansion of the intensity distribution directly in terms of moments.

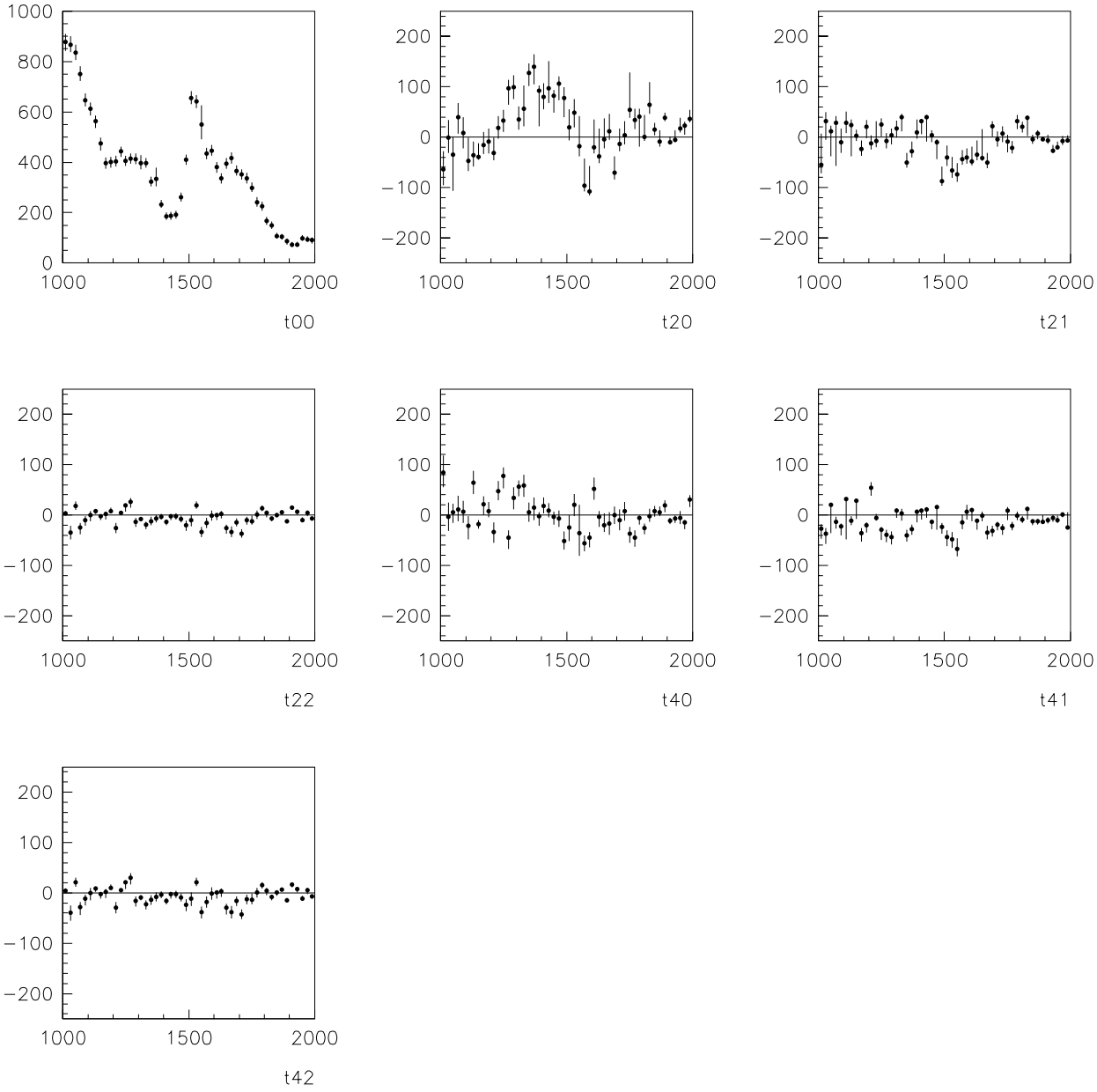


Figure 56: Moments from the amplitudes, using four waves, as a function of the $K_s^0 K_s^0$ invariant mass. In this case, we used the MC events obtained using the correlations between amplitudes, as given by MINUIT, to calculate the moments.

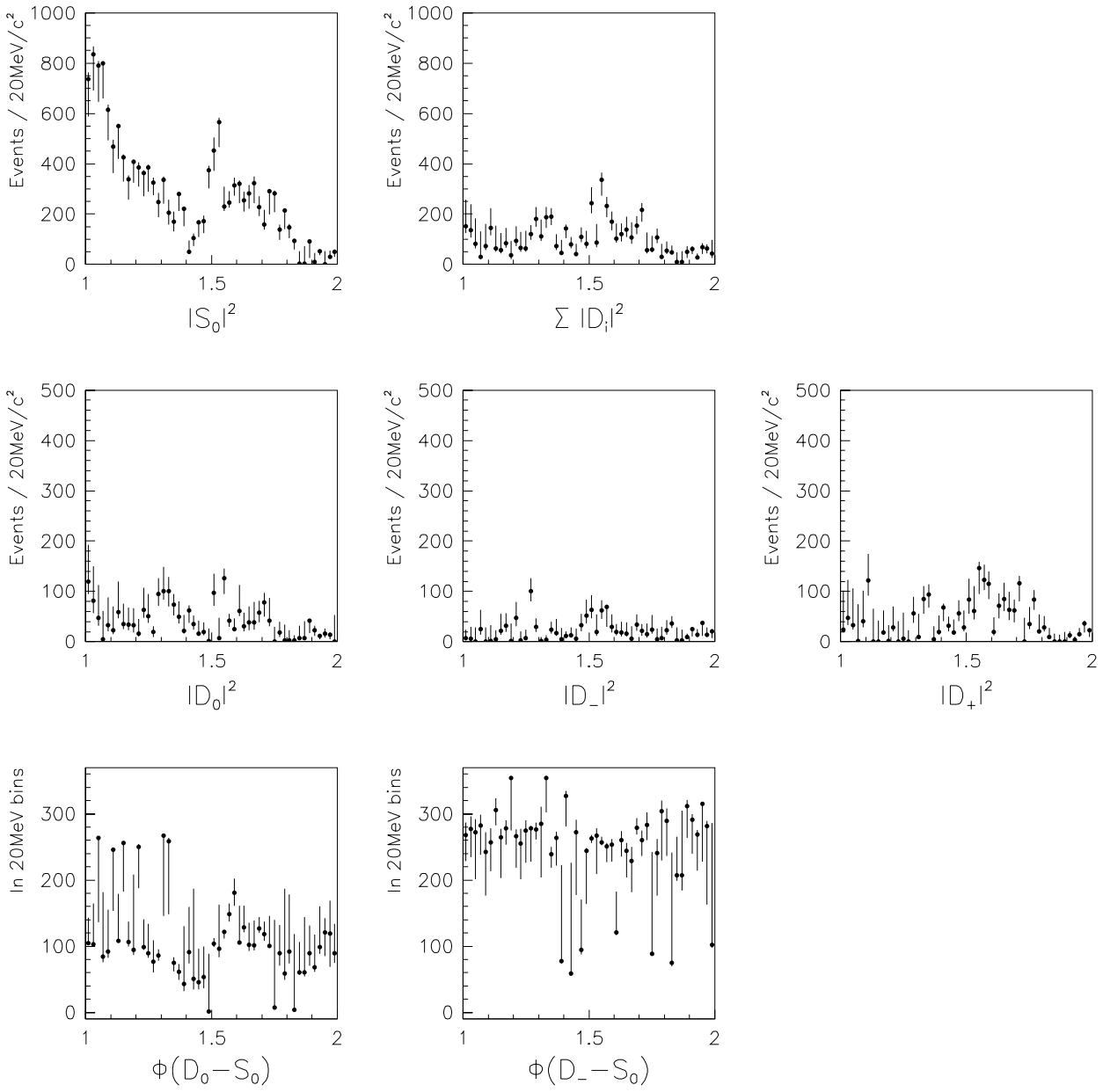


Figure 57: Amplitudes first solution, as a function of the $K_s^0K_s^0$ invariant mass, from the MC events obtained using the moments correlations, as given by MINUIT. Compare to fig.51.

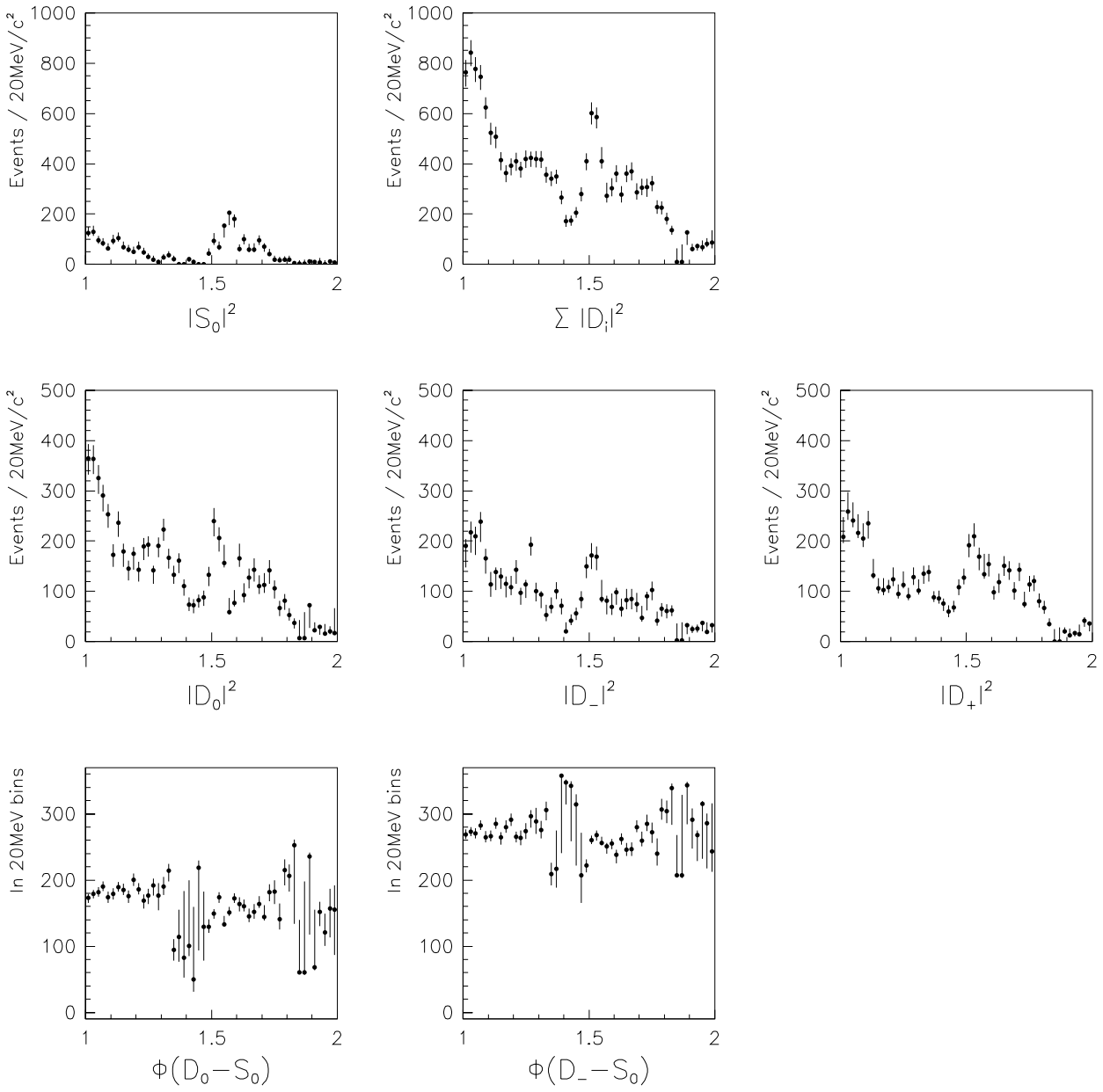


Figure 58: Amplitudes second solution, from moments, as a function of the $K_s^0 K_s^0$ invariant mass. Compare to fig.52.

## 5.3 Conclusions

We have performed a partial wave analysis on the centrally produced $K_s^0 K_s^0$ system at 800 $GeV/c$, using two methods: 1) directly calculating the amplitudes, and 2) calculating the amplitudes using the method of moments. In both cases we used the CERN program MINUIT, and maximum likelihood techniques, to perform the analysis. Both methods gave the same results.

We used four waves, $\mathcal{S}_I$, $\mathcal{D}_I$, $\mathcal{D}_-$ and $\mathcal{D}_+$, in the analysis, where $\mathcal{D}_\pm \equiv \mathcal{D}_1^\pm$, based on the assumption that the moments $t_{43}, t_{44}$ were consistent with zero. as can be seen in fig.46, and on the relations between amplitudes and moments, depicted in eq.(30). This equation states that if $t_{43} = t_{44} = 0$, then one can assume that $D_2^- = D_2^+ = 0$, leaving $m = 0, 1$ only. With these four waves, we found two different solutions for the amplitudes.

At 1560-1580 $MeV/c^2$, the two solutions are identical. At this bin, thus, the solutions bifurcate, leading to a total of four possible combinations of solutions. Of these four solutions, two of them have a large $\mathcal{D}$ wave component at threshold, which contradicts the well known fact that, at threshold, the intensity distribution is dominated by the $f_0(980)$, which is $\mathcal{S}$ wave. From the other two solutions, we favor the solution depicted in fig.51, owing to the fact that when using only two waves, there is $S$-wave predominancy, as can be seen in fig.40. This solution has the following characteristics:

1. The intensity distribution from 1 to 2 $GeV/c^2$ in the $K_s^0 K_s^0$ invariant mass is predominantly $\mathcal{S}$–wave.

2. There is some $\mathcal{D}$-wave structure at 1300 $GeV/c^2$.

3. There is a clear peak in $\mathcal{S}$-wave at about 1530 $MeV/c^2$, which can be related to the glueball candidate $f_0(1520)$.

4. A peak in $\mathcal{D}$-wave is also seen at about 1560 $MeV/c^2$.

5. The $f_J(1710)$ region, the other candidate for the lightest scalar glueball, is essentially composed of $\mathcal{S}$-wave, contrary to what was observed by experiment WA76.

It is important to notice that this is the first experiment to report the observation of the $f_0(1520)$ in central production.

Still, we can not definitively rule out the possibility that the solution depicted in fig.53 is the correct one. This solution gives also an $\mathcal{S}$-wave peak at around 1530 $MeV/c^2$, but favors unpolarized $\mathcal{D}$ wave in the region of the $f_J(1710)$.

# 6 Appendix

# A Use of the Veto Box and Veto Collar for Background Analysis

In Section 3.4 we made a description of the use of one of the vetoes in the veto box, to cut background events, and the relevant features of the procedure can be seen in fig.19. In this Section we show the plots for each one of the vetoes in the veto box and the veto collar.

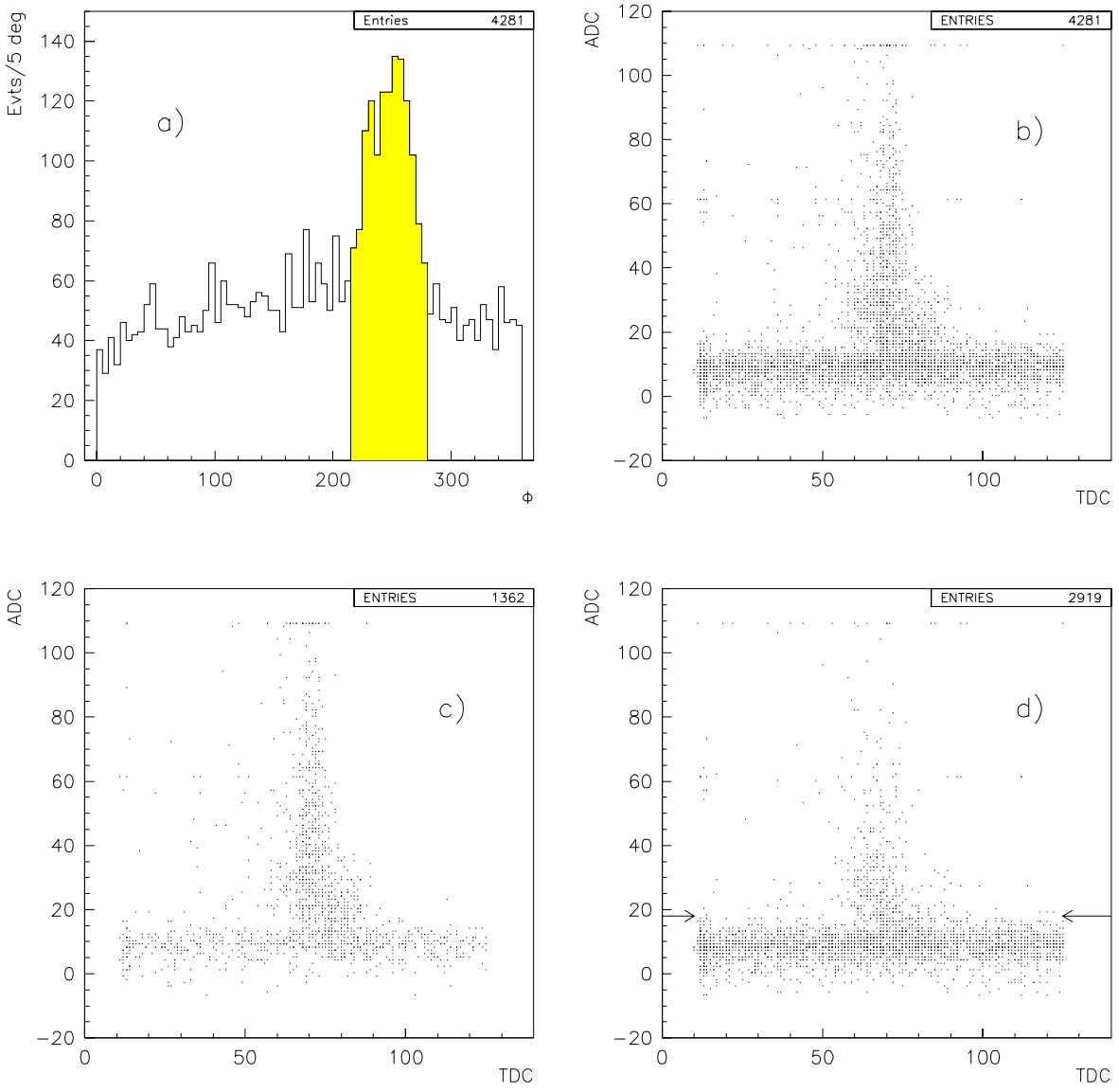


Figure 59: (a) $\phi$ distribution and (b) TDC *vs.* ADC when veto #1 in the veto box is on. (c) $p_m$ pointing to cell, (d) not pointing. The events with hits above the arrows were cut.

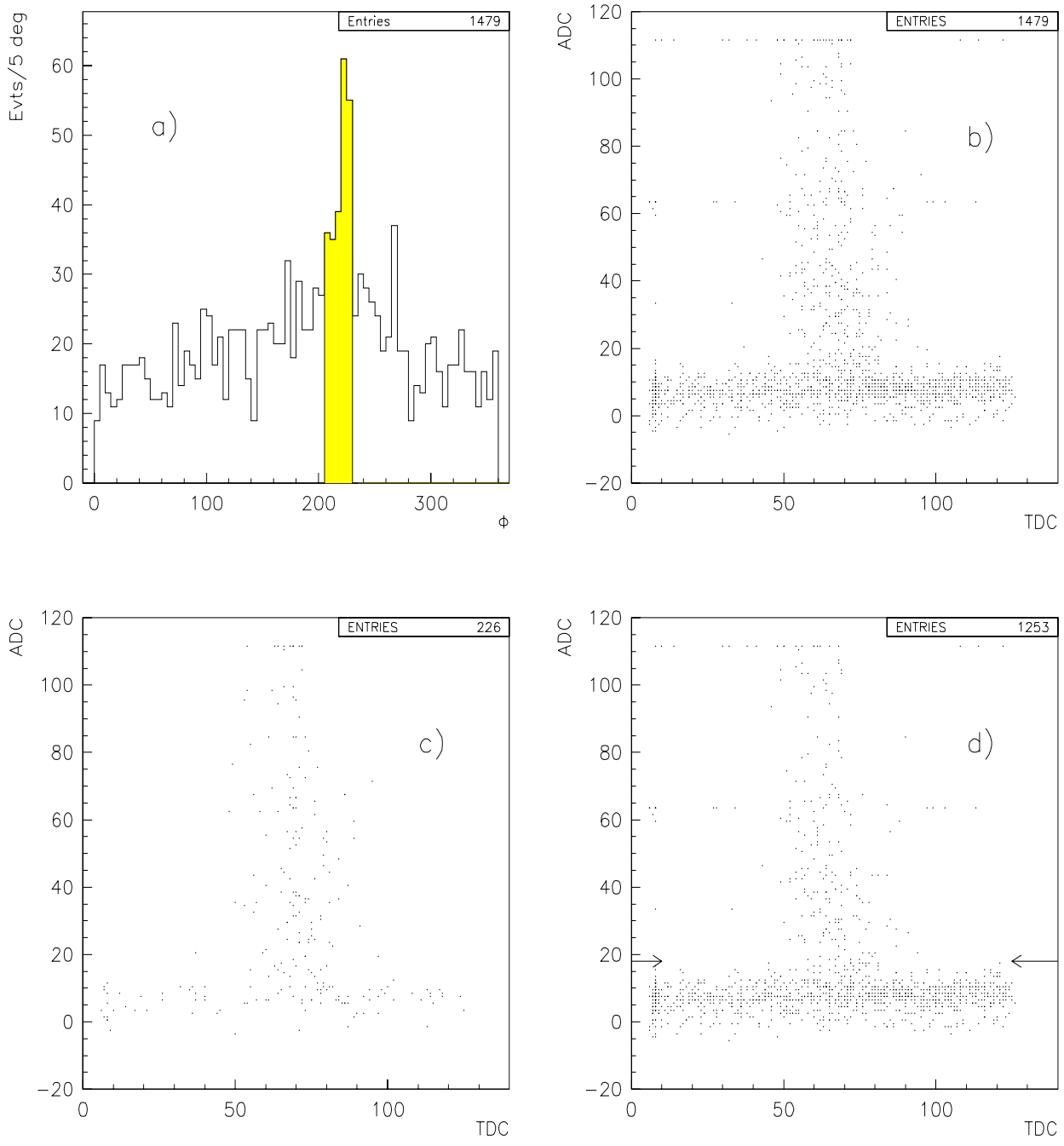


Figure 60: (a) $\phi$ distribution and (b) TDC *vs.* ADC when veto #2 in the veto box is on. (c) $p_m$ pointing to cell, (d) not pointing. The events with hits above the arrows were cut.

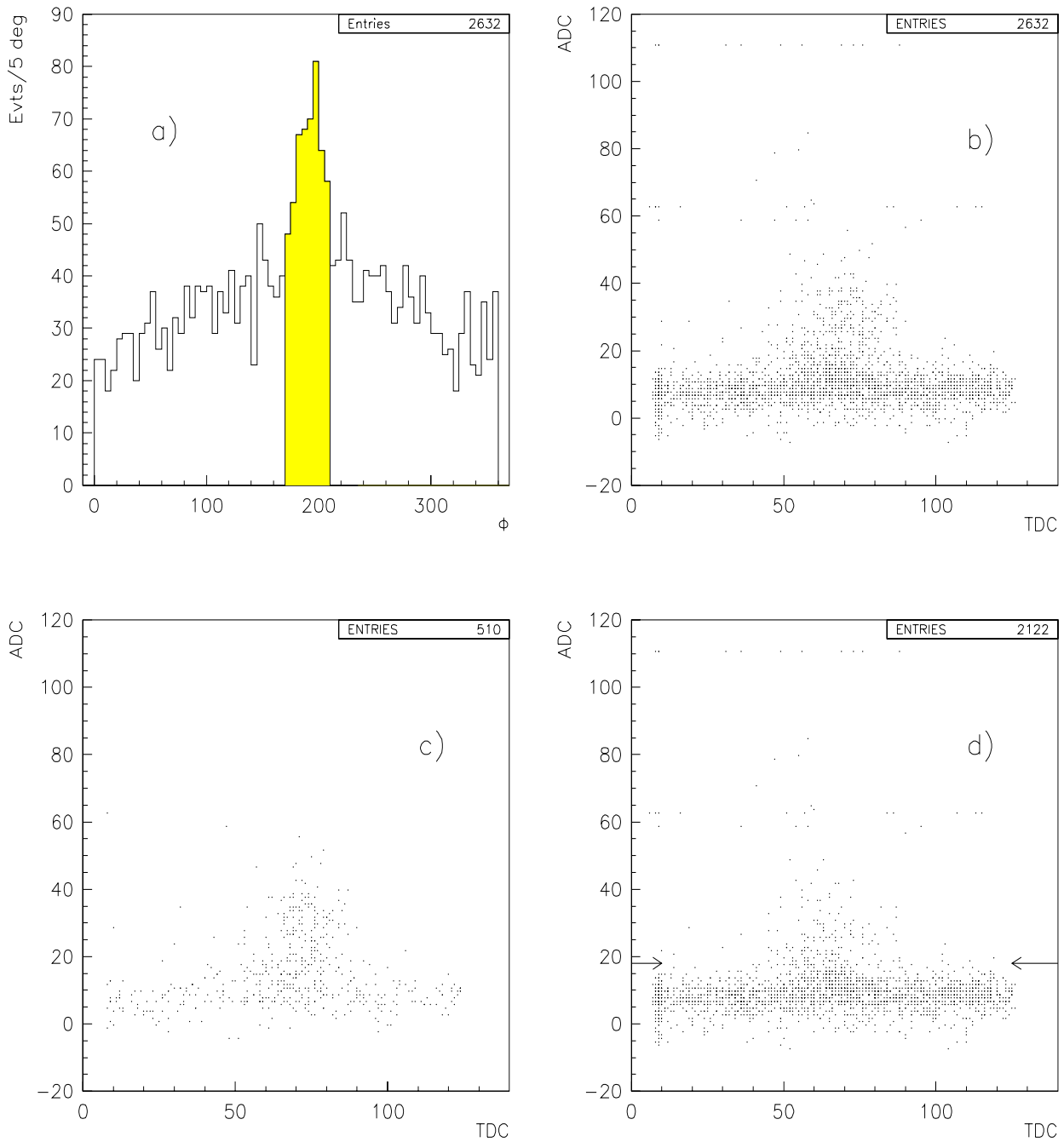


Figure 61: (a) $\phi$ distribution and (b) TDC *vs.* ADC when veto #3 in the veto box is on. (c) $p_m$ pointing to cell, (d) not pointing. The events with hits above the arrows were cut.

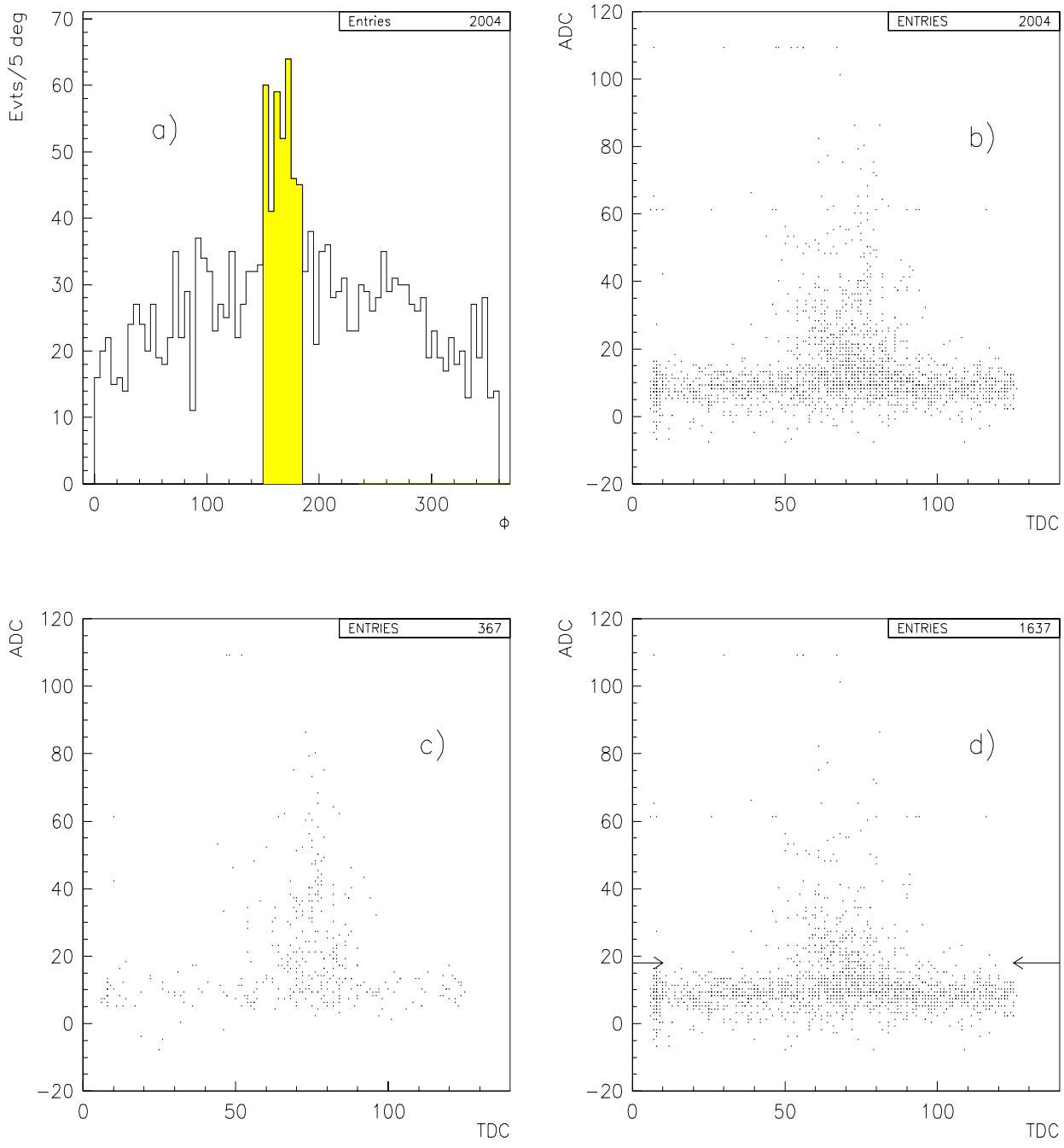


Figure 62: (a) $\phi$ distribution and (b) TDC *vs.* ADC when veto #4 in the veto box is on. (c) $p_m$ pointing to cell, (d) not pointing. The events with hits above the arrows were cut.

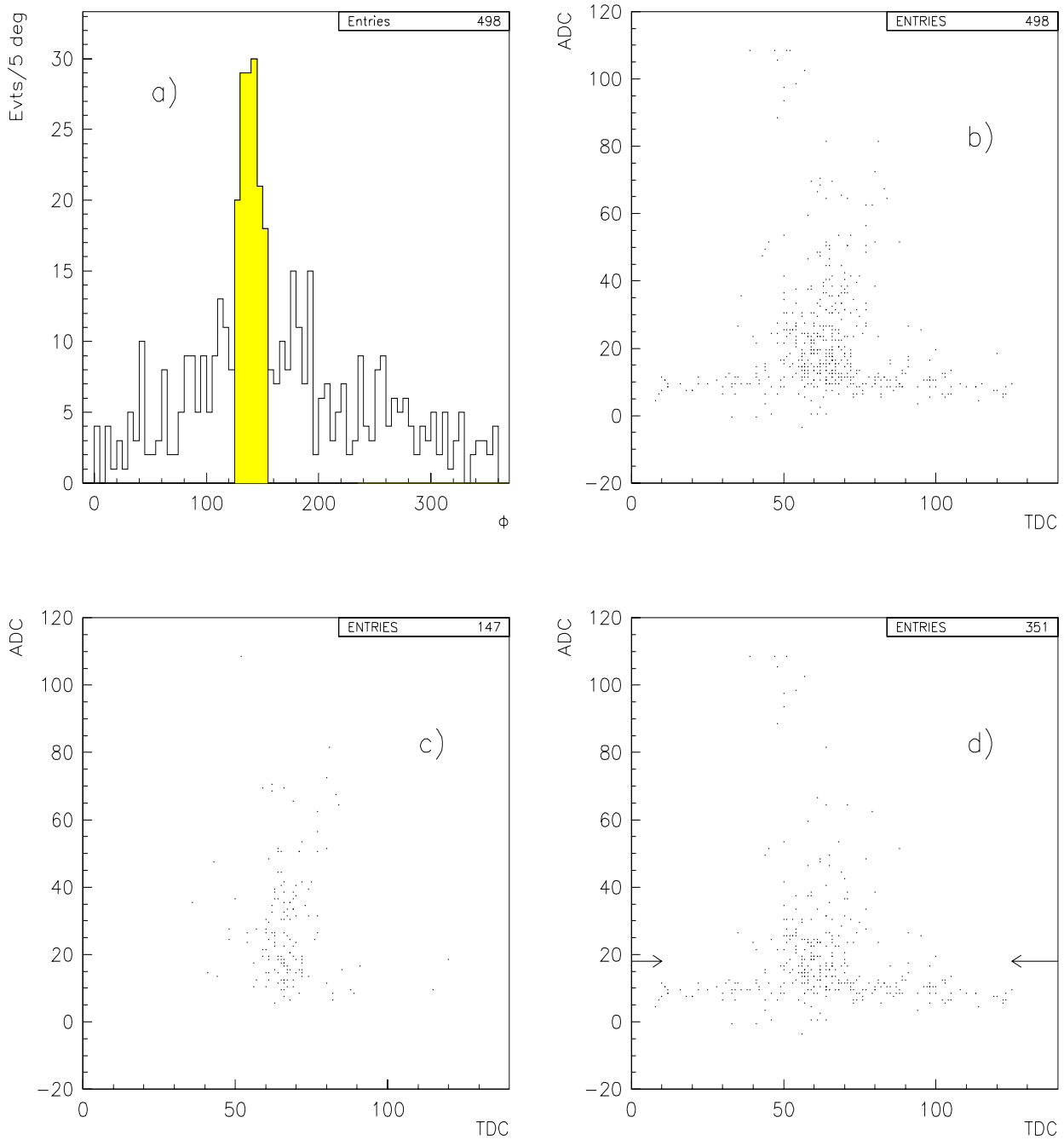


Figure 63: (a) $\phi$ distribution and (b) TDC *vs.* ADC when veto #5 in the veto box is on. (c) $p_m$ pointing to cell, (d) not pointing. The events with hits above the arrows were cut.

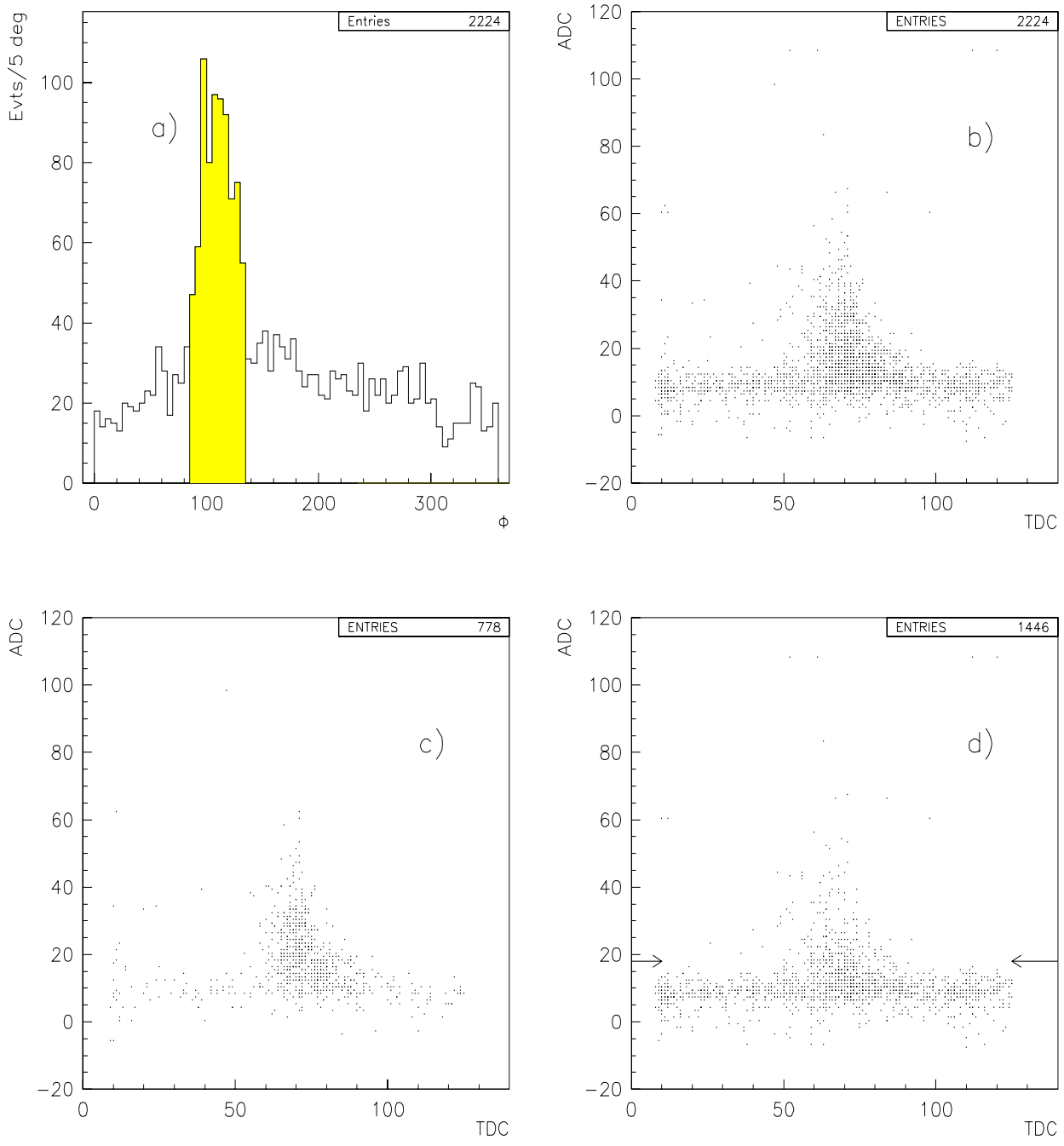


Figure 64: (a) $\phi$ distribution and (b) TDC *vs.* ADC when veto #6 in the veto box is on. (c) $p_m$ pointing to cell, (d) not pointing. The events with hits above the arrows were cut.

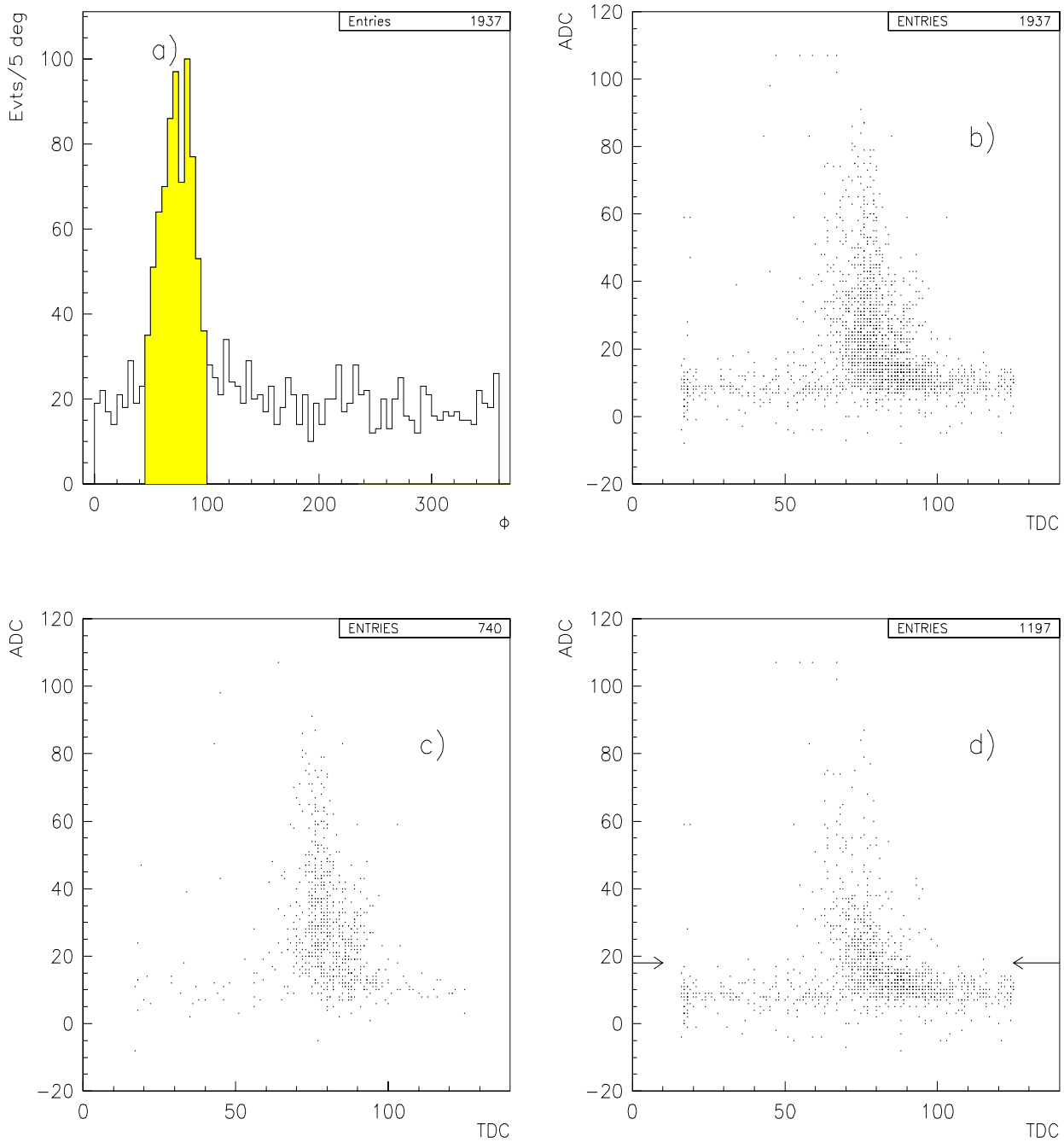


Figure 65: (a) $\phi$ distribution and (b) TDC *vs.* ADC when veto #7 in the veto box is on. (c) $p_m$ pointing to cell, (d) not pointing. The events with hits above the arrows were cut.

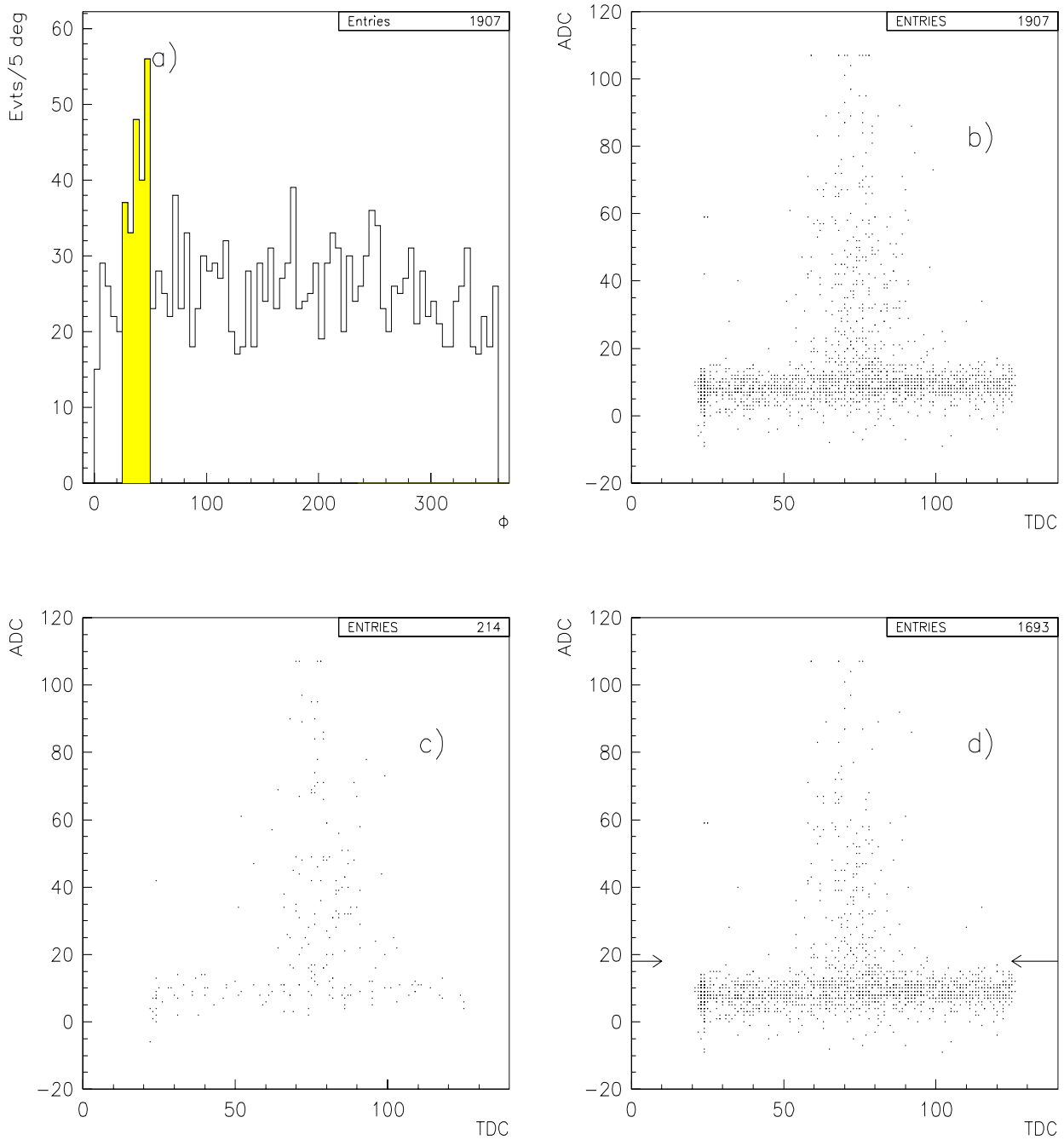


Figure 66: (a) $\phi$ distribution and (b) TDC *vs.* ADC when veto #8 in the veto box is on. (c) $p_m$ pointing to cell, (d) not pointing. The events with hits above the arrows were cut.

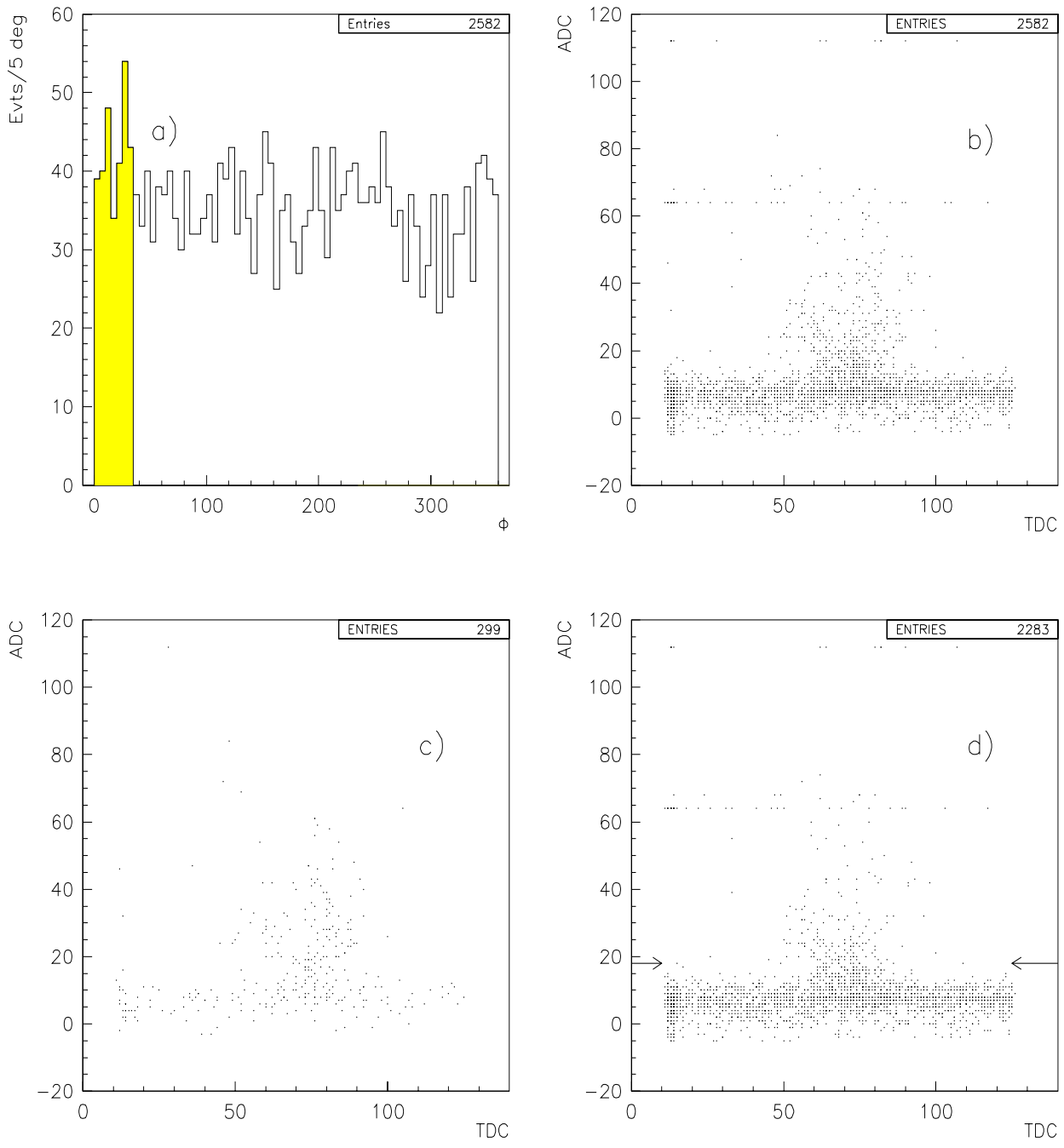


Figure 67: (a) $\phi$ distribution and (b) TDC *vs.* ADC when veto #9 in the veto box is on. (c) $p_m$ pointing to cell, (d) not pointing. The events with hits above the arrows were cut.

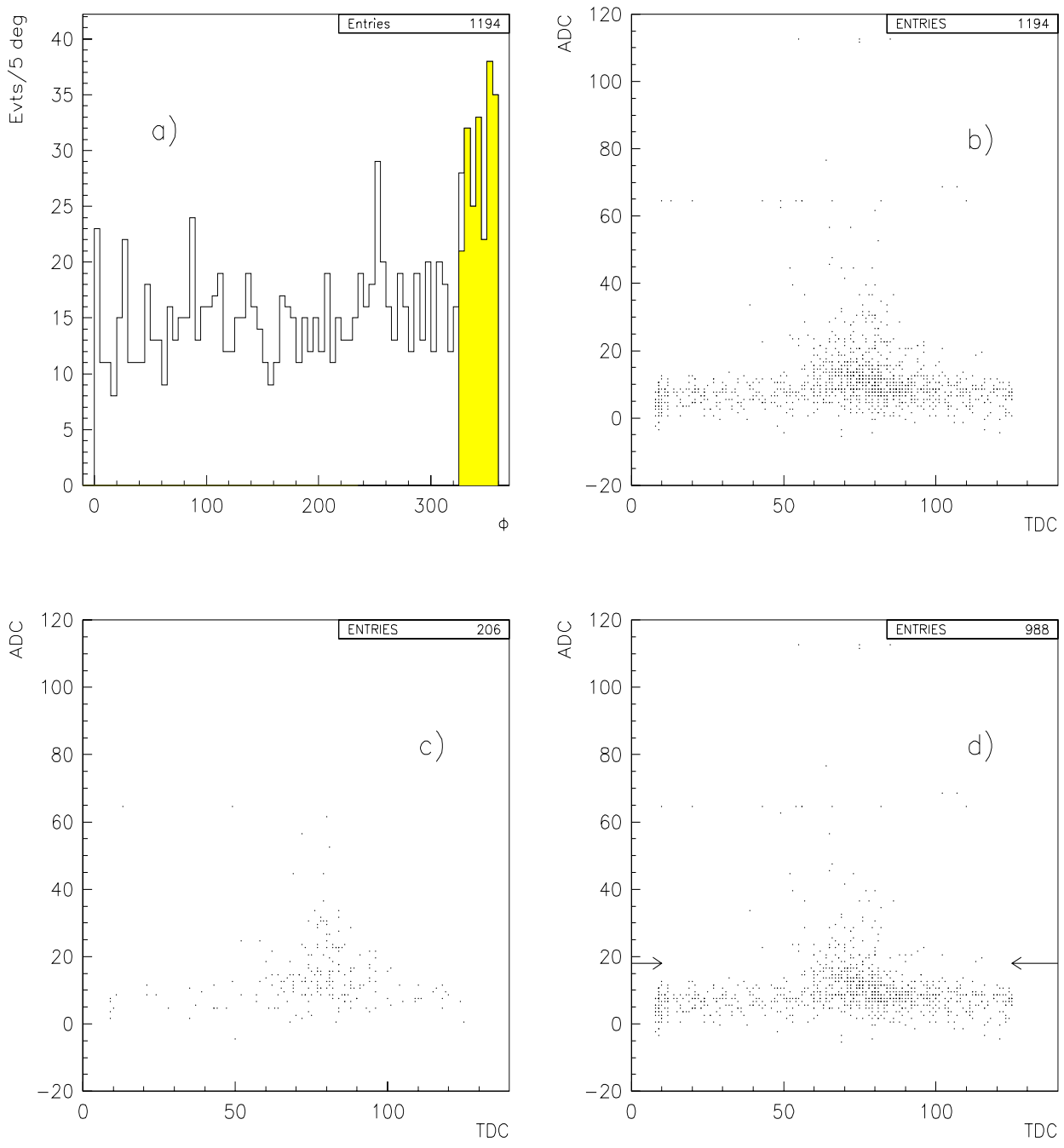


Figure 68: (a) $\phi$ distribution and (b) TDC *vs.* ADC when veto #10 in the veto box is on. (c) $p_m$ pointing to cell, (d) not pointing. The events with hits above the arrows were cut.

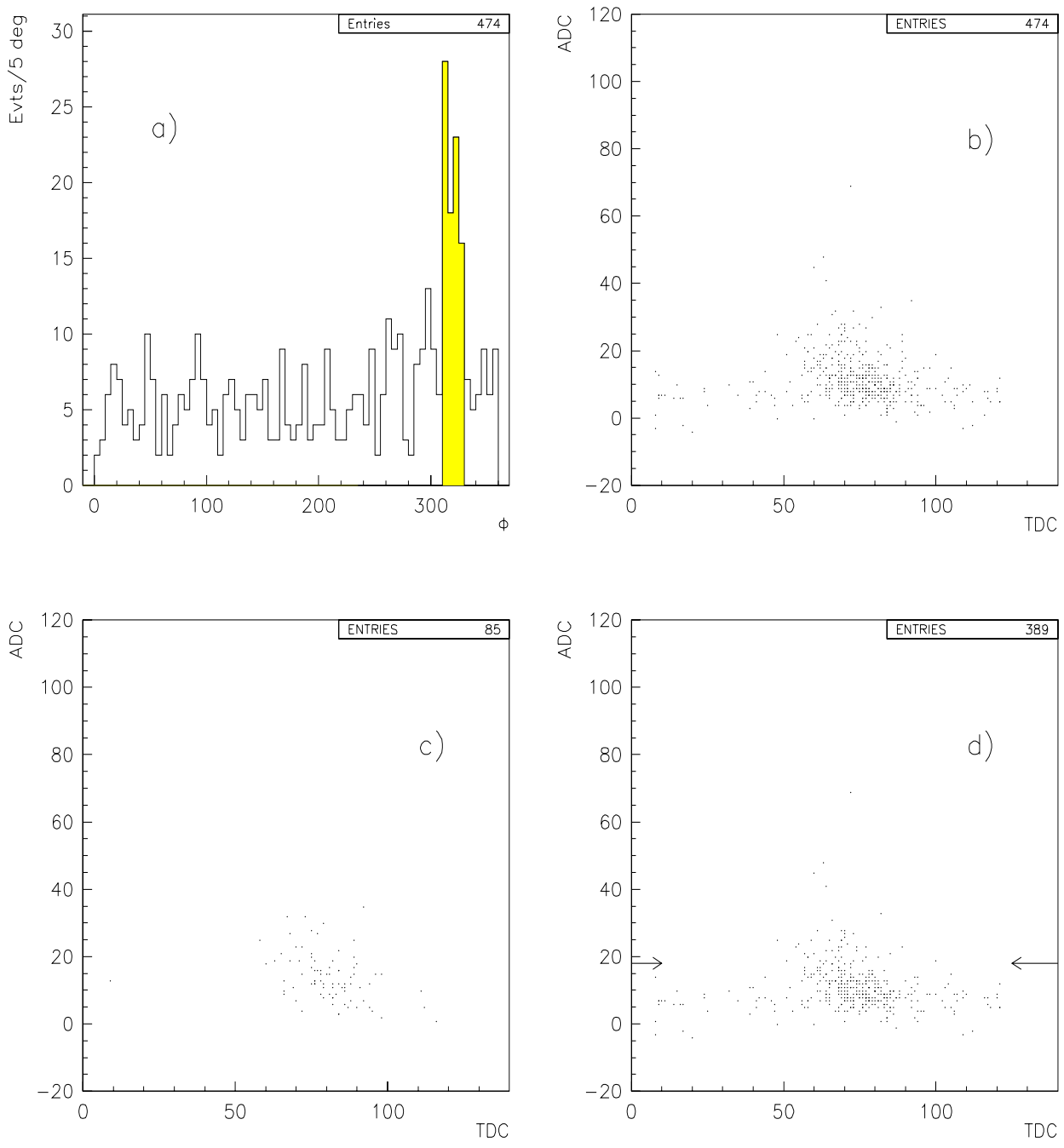


Figure 69: (a) $\phi$ distribution and (b) TDC *vs.* ADC when veto #11 in the veto box is on. (c) $p_m$ pointing to cell, (d) not pointing. The events with hits above the arrows were cut.

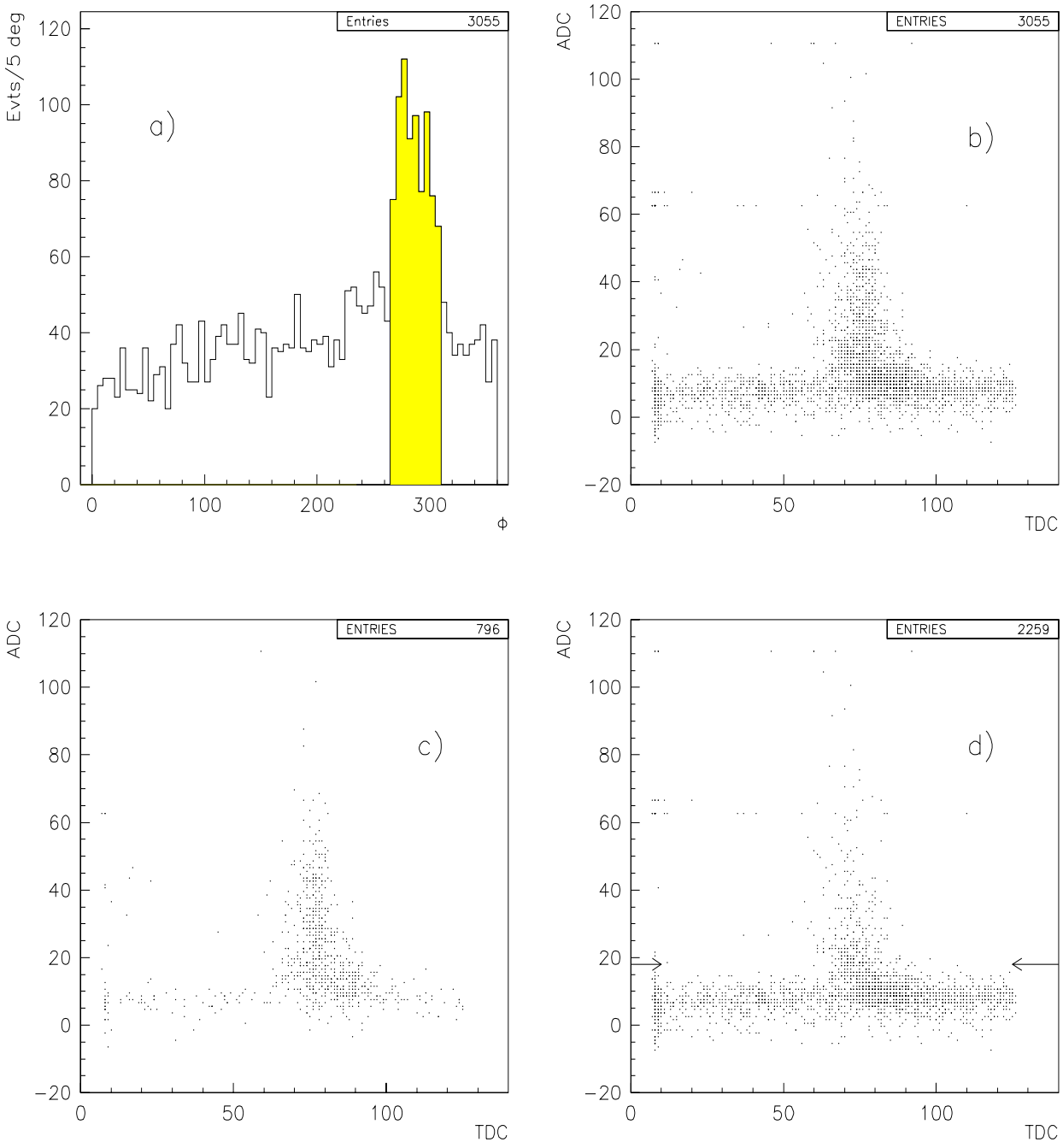


Figure 70: (a) $\phi$ distribution and (b) TDC *vs.* ADC when veto #12 in the veto box is on. (c) $p_m$ pointing to cell, (d) not pointing. The events with hits above the arrows were cut.

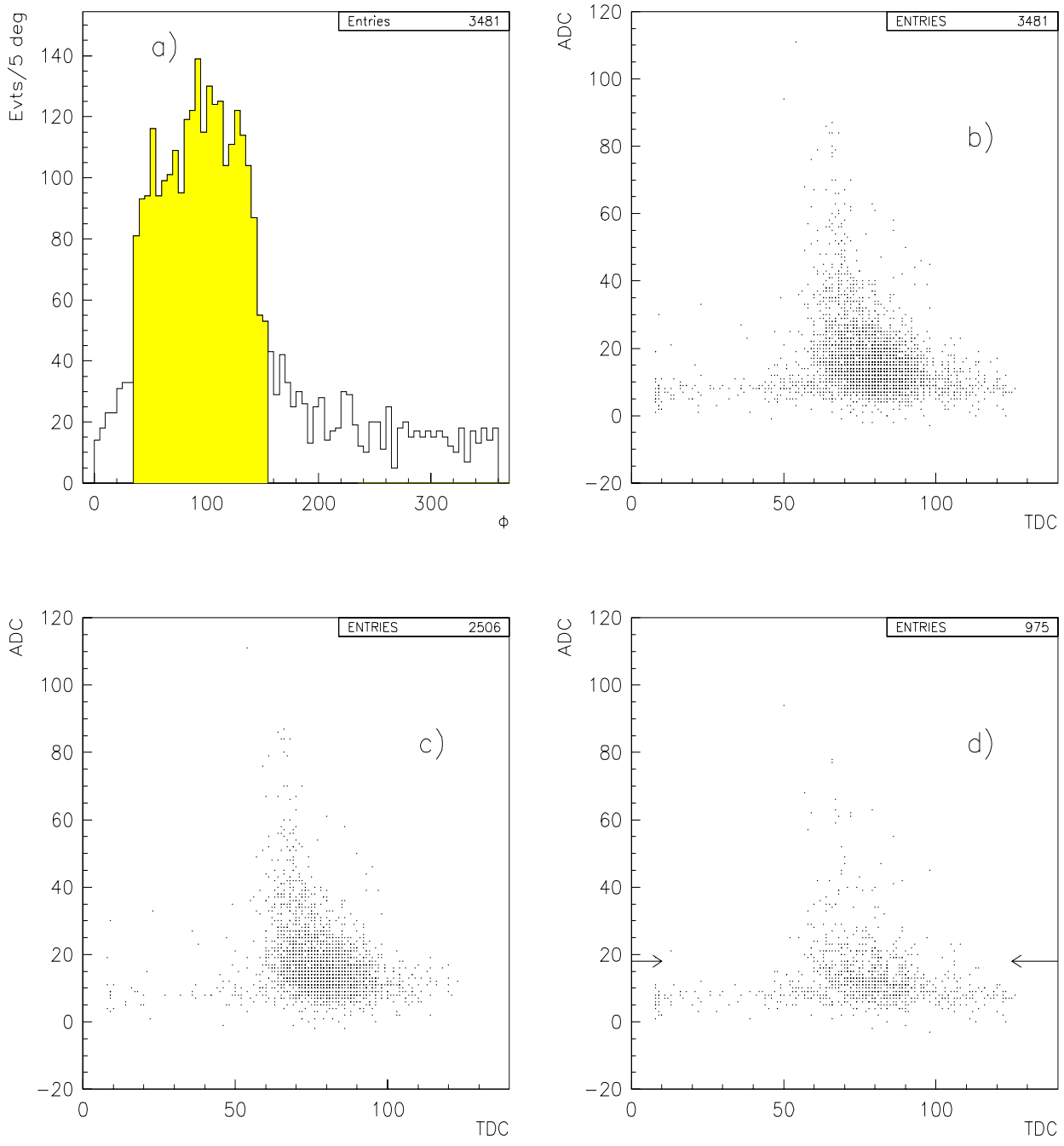


Figure 71: (a) $\phi$ distribution and (b) TDC *vs.* ADC when veto #1 in the veto collar is on. (c) $p_m$ pointing to cell, (d) not pointing. The events with hits above the arrows were cut.

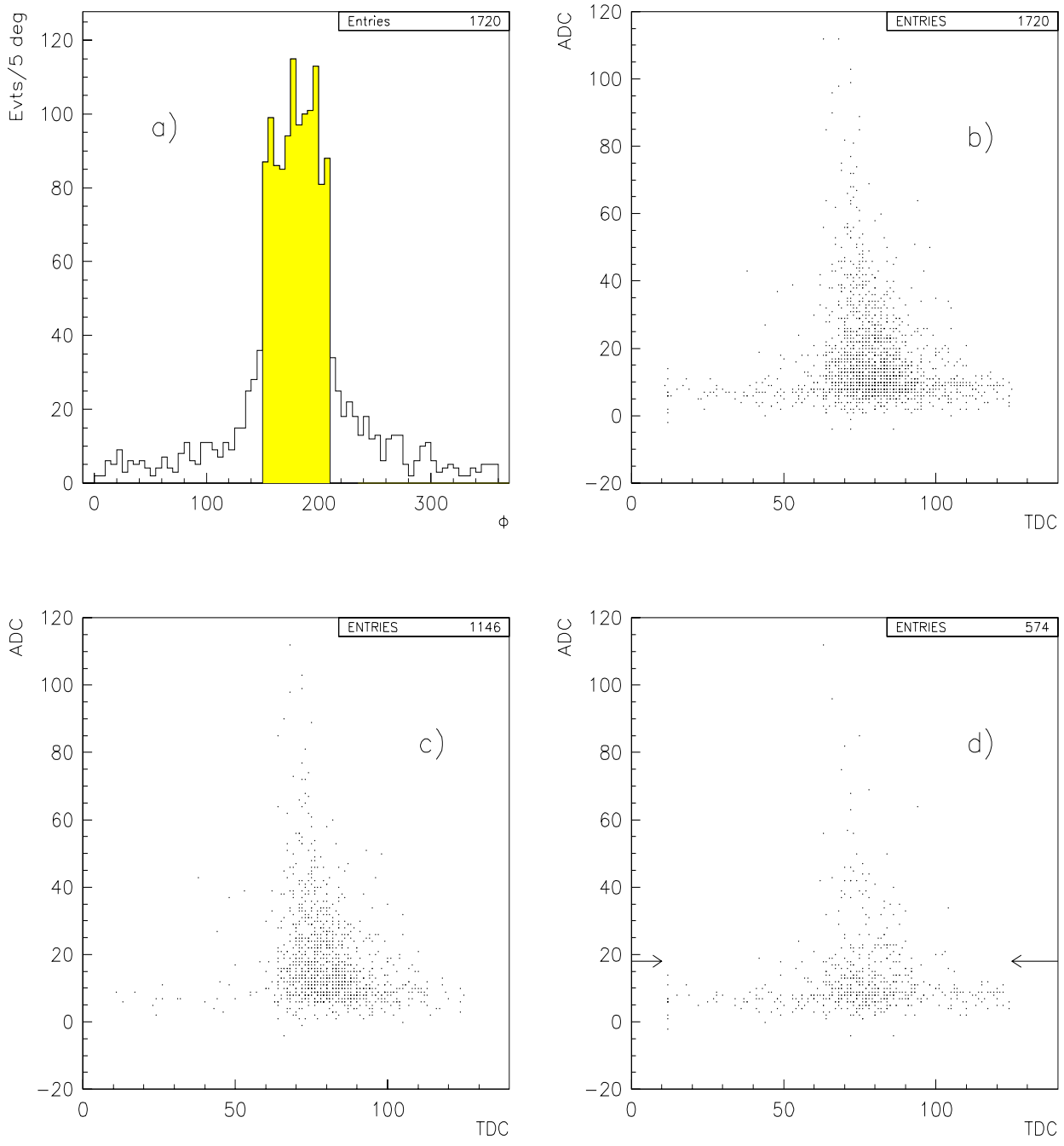


Figure 72: (a) $\phi$ distribution and (b) TDC *vs.* ADC when veto #2 in the veto collar is on. (c) $p_m$ pointing to cell, (d) not pointing. The events with hits above the arrows were cut.

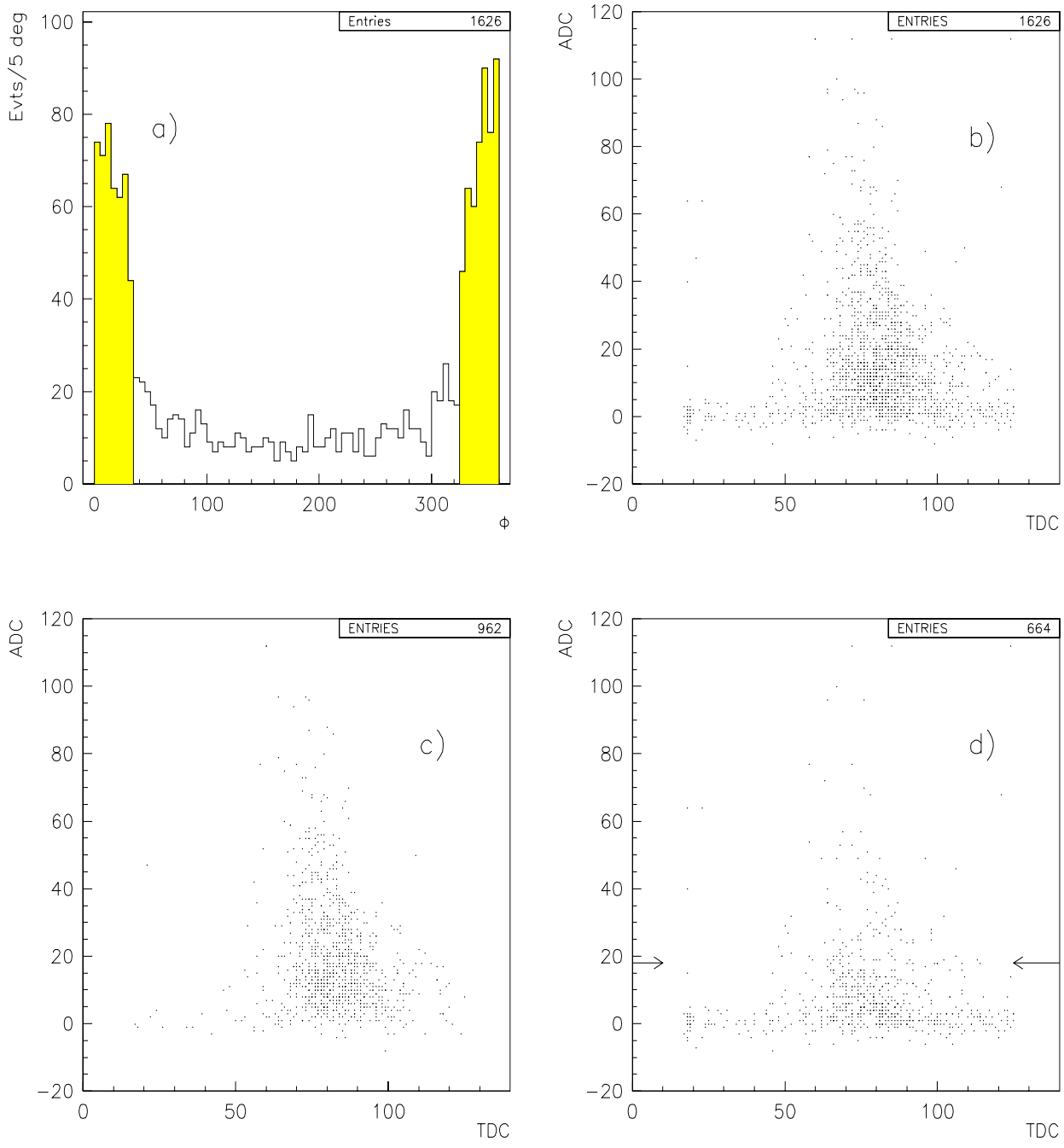


Figure 73: (a) $\phi$ distribution and (b) TDC *vs.* ADC when veto #3 in the veto collar is on. (c) $p_m$ pointing to cell, (d) not pointing. The events with hits above the arrows were cut.

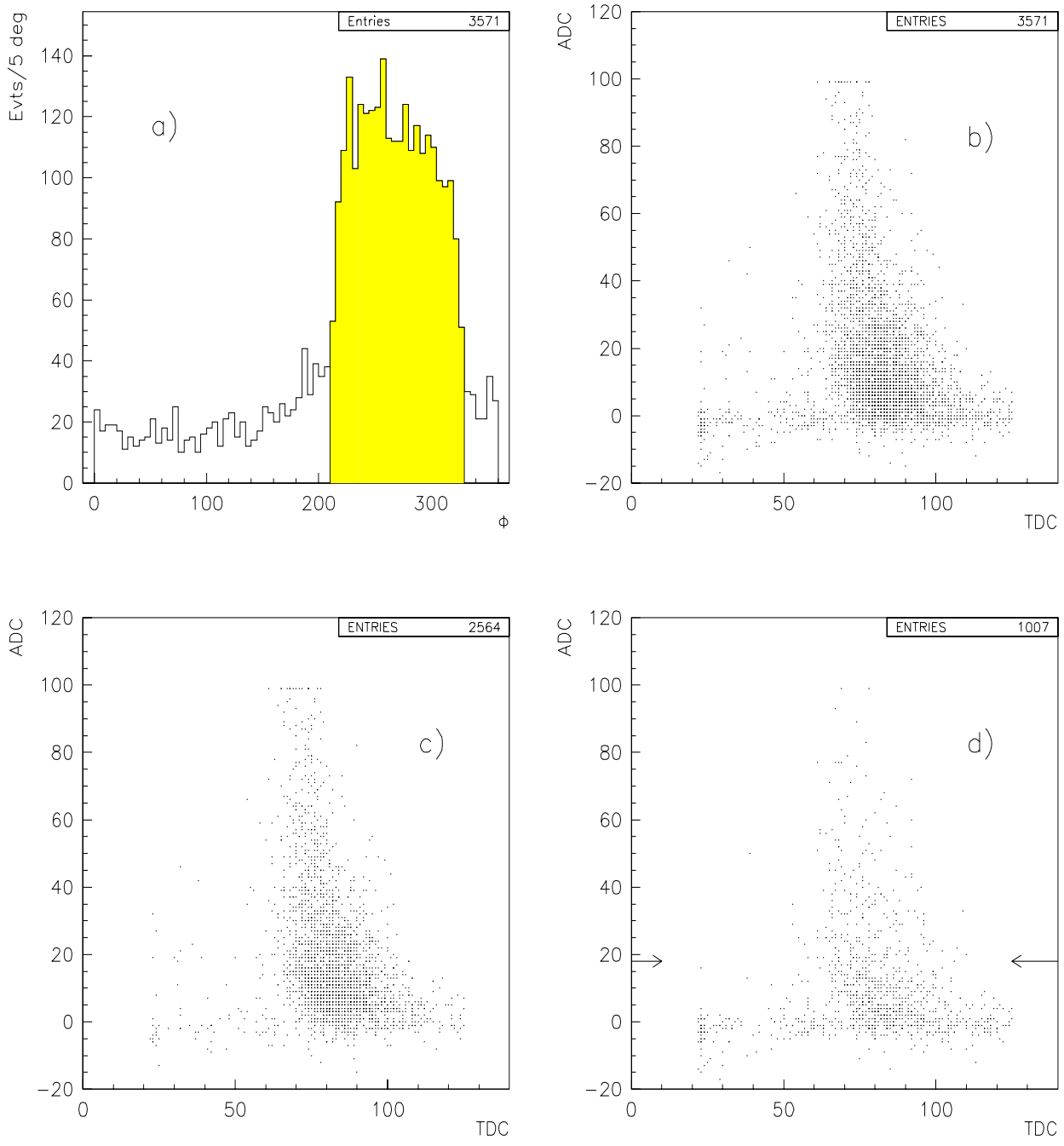


Figure 74: (a) $\phi$ distribution and (b) TDC *vs.* ADC when veto #4 in the veto collar is on. (c) $p_m$ pointing to cell, (d) not pointing. The events with hits above the arrows were cut.

# B Acceptance Corrections Using Monte Carlo Events

## B.1 Angular Distributions Acceptance.

In Section 4 we presented the acceptance corrected angular distributions in bins of 60 $MeV/c^2$. In order to do these acceptance corrections[6], we generated 30000 Monte Carlo events per bin, run these events through the whole reconstruction chain, and calculated the acceptance of the $K_s^0K_s^0$ invariant mass, $K_s^0$ polar angle $\theta$ in the $X$ rest frame, $K_s^0$ azimuthal angle $\phi$, and the $\pi^+$ polar angle in the $K_s^0$ rest frame $\beta$. These are few events for doing acceptance corrections, but the intention is to get an idea of how much the acceptance corrections change the amplitudes resolution. As we can see in Section 4, the changes in the amplitudes solution is minor, due to the high acceptance of our spectrometer. This acceptance in terms of the $K_s^0K_s^0$ invariant mass is shown in fig.75, for the Monte Carlo events used to calculate the acceptance corrections for the angular distributions.

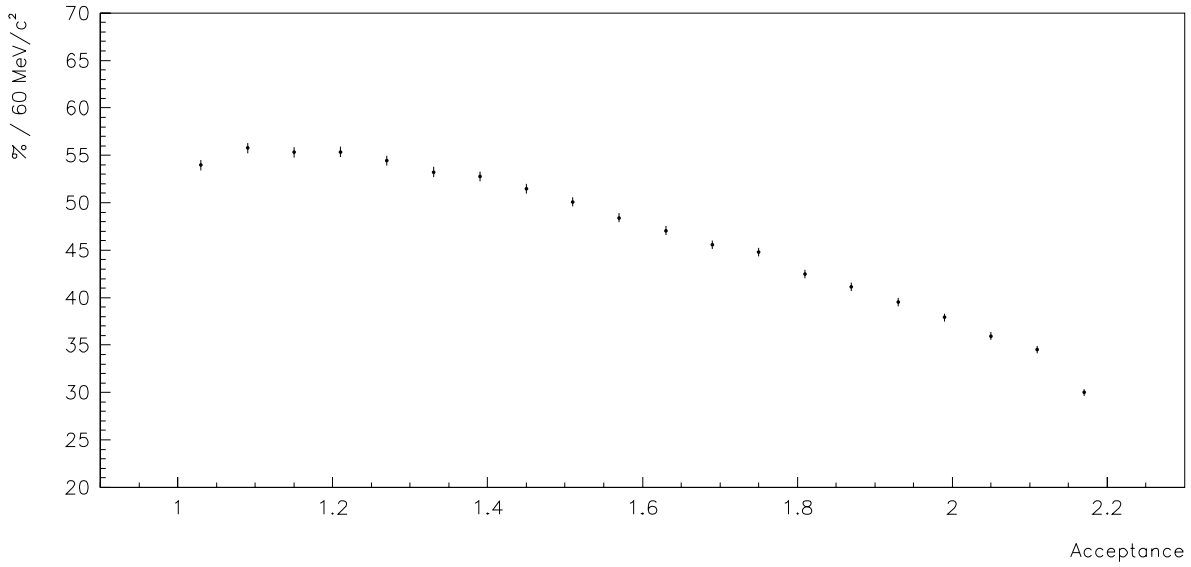


Figure 75: Acceptance as a function of the $K_s^0K_s^0$ invariant mass.

[6]For the acceptance integrals, 6 million Monte Carlo events were used for $1.0 \leq M(K_s^0K_s^0) \leq 2.4GeV/c^2$.

We used the $K_s^0$ angular distributions in the $X$ rest frame, of the Monte Carlo events, to calculate the acceptance in bins of the $K_s^0 K_s^0$ invariant mass, and in bins of $\cos\theta$ and $\phi$. We can see in fig.76 that the acceptance for $\cos\theta$ depends very much on the $K_s^0 K_s^0$ invariant mass, being flat for low mass, and becoming less flat for higher masses, bending towards the edges $\cos\theta = \pm 1$. This means that the acceptance corrections do not affect the $\cos\theta$ distributions for low masses, but make them bend upwards for $\cos\theta = \pm 1$ for high masses. For the azimuthal angle $\phi$, we can see in fig.77 that the distributions are flat for all bins of the $K_s^0 K_s^0$ invariant mass. Therefore, the acceptance corrections in this angle are small. The same is truth for the $\pi^+$ polar angle $\beta$ in the $K_s^0$ rest frame.

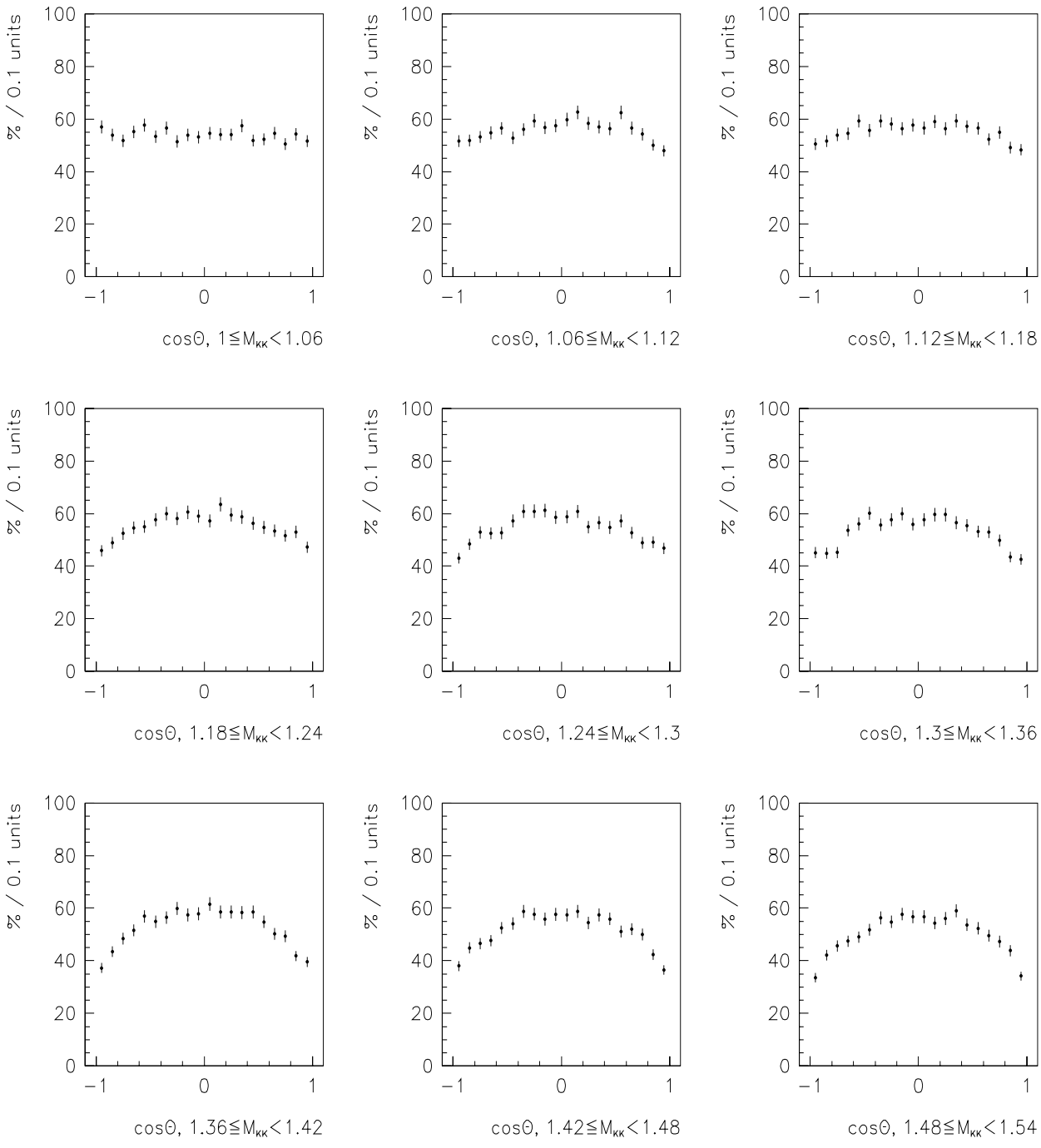


Figure 76: $\cos\theta$ acceptance as a function of the $K_s^0 K_s^0$ invariant mass

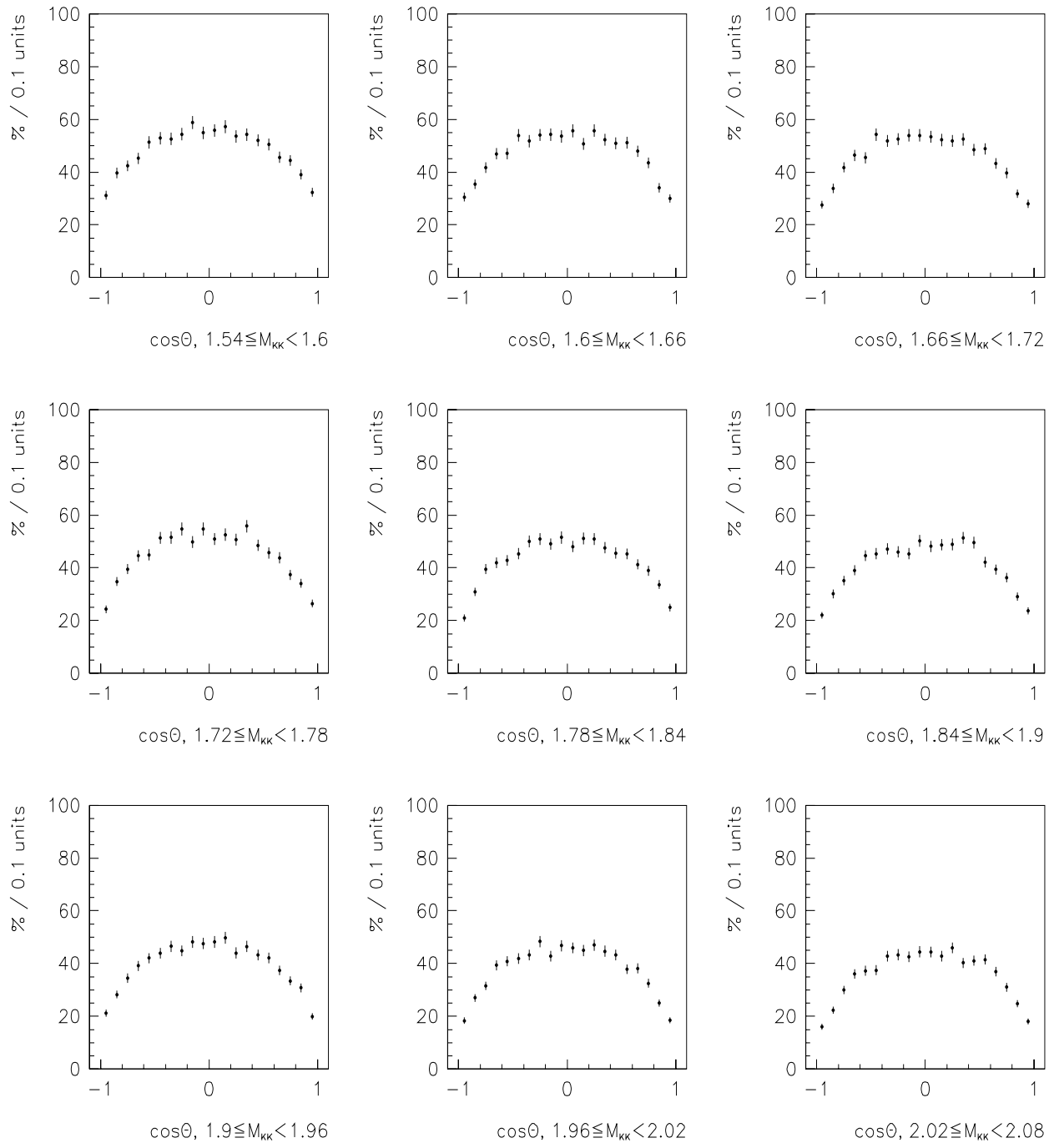


Figure 76 continued.

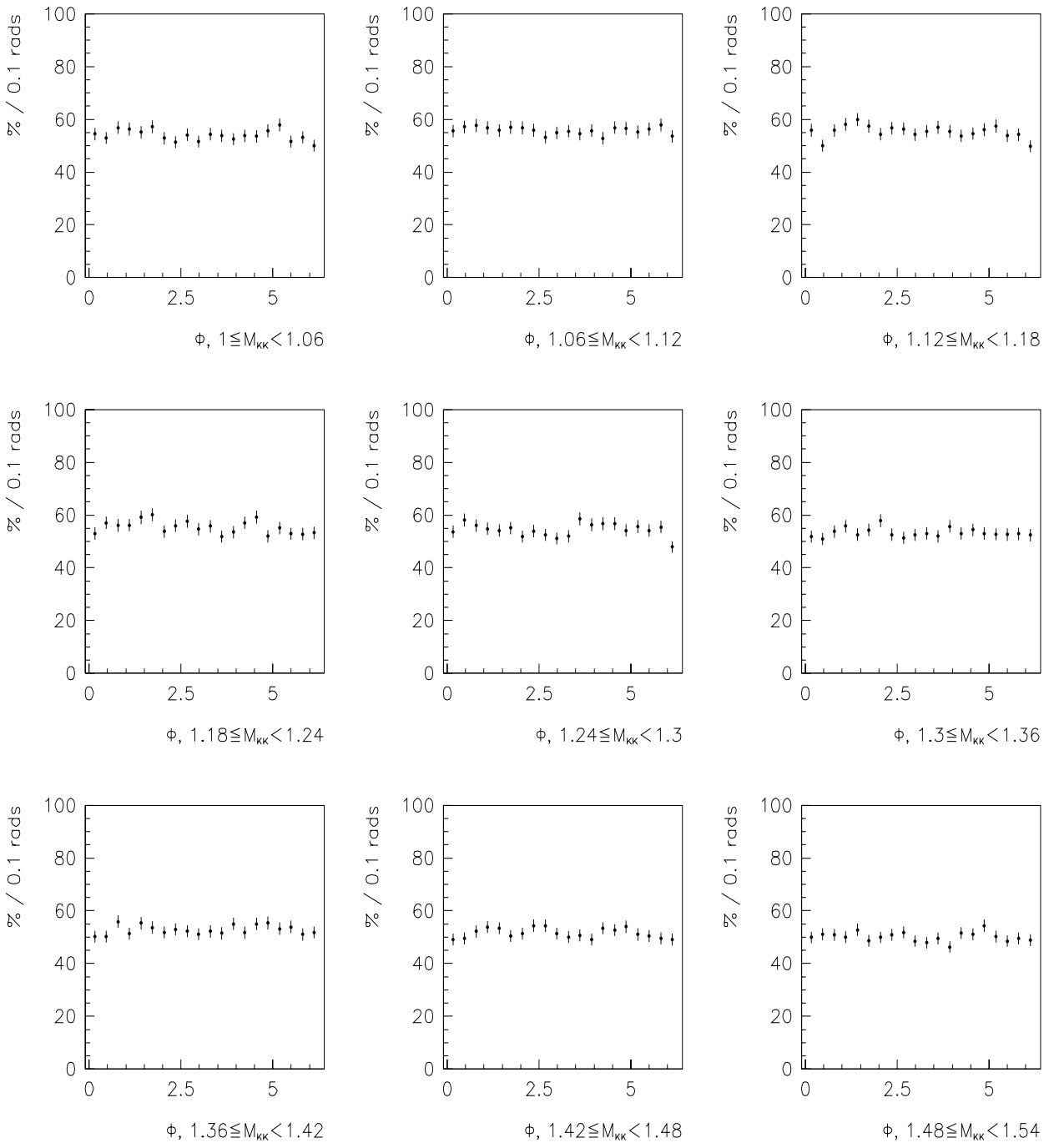


Figure 77: $\phi$ acceptance as a function of the $K_s^0 K_s^0$ invariant mass

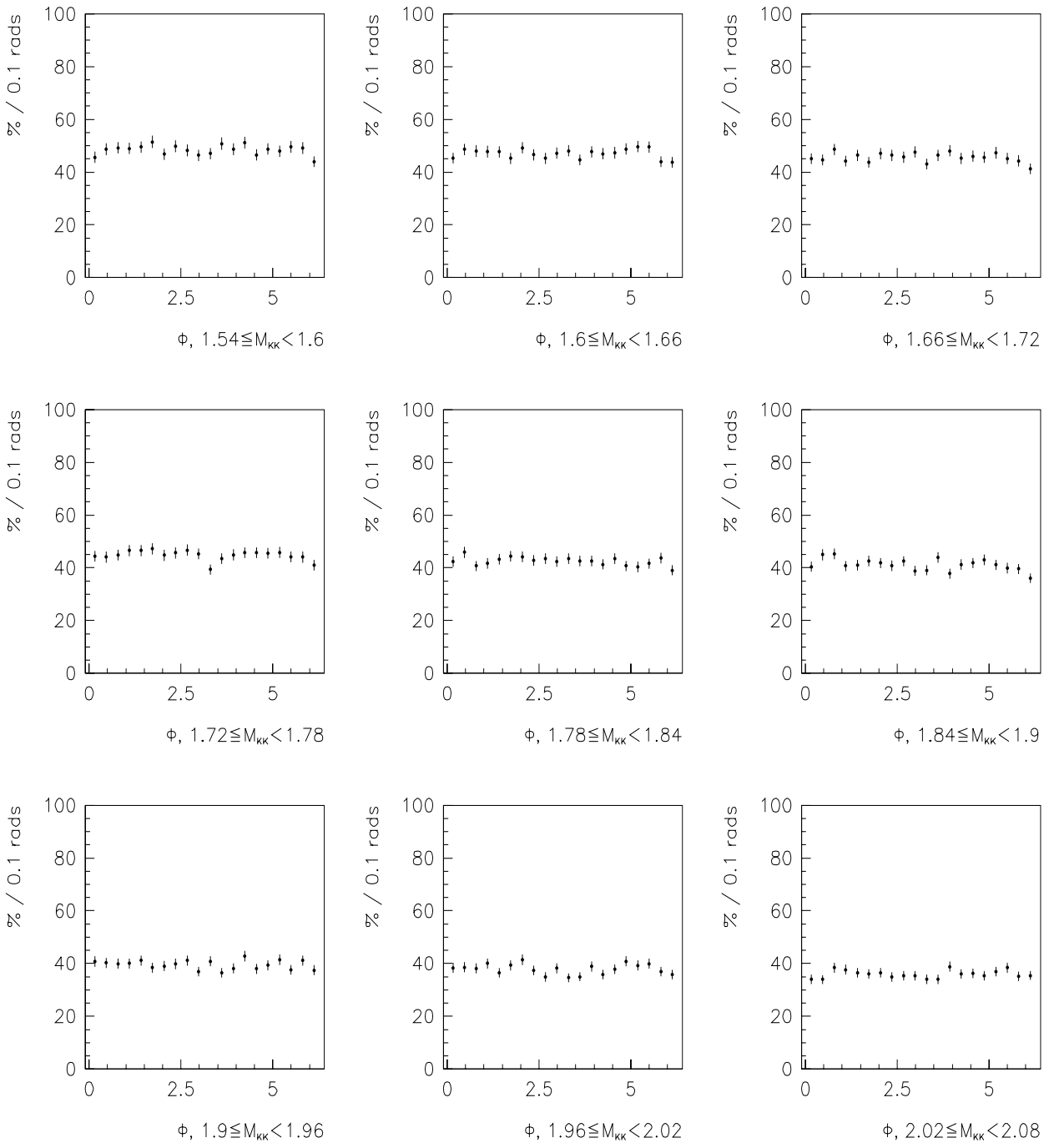


Figure 77 continued.

## B.2 Differential Cross Section.

The production process is a function of the variables $x$, and the decay process is a function of the variables $\Omega$. Independently of the choice of the variables $x$ and $\Omega$, the differential cross section is given by

$$\mathrm{d}^8\sigma_\lambda \;=\; \frac{(2\pi)^4}{4p_0\sqrt{s}}\;|\mathcal{M}_\lambda|^2\;(2\pi)^3\;\mathrm{d}^8\Phi_4(P;p_m,p_2,p_3,p_f) \tag{84}$$

where the index $\lambda$ labels the helicities of the *missing* and *fast* protons, $\mathcal{M}$ is the Lorentz invariant scattering matrix, $p_0$ is the momentum of the protons in the $pp$ center of momentum system (CMS), and $\sqrt{s}$ is the total CMS energy.

Following the Review of Particle Properties [3], we write the four–particle Lorentz invariant phase space as

$$\begin{aligned}
\mathrm{d}\Phi_4(P;p_mp_2p_3p_f) &= \delta^4(P-\sum_{i=1}^{4}p_i)\;\prod_{i=1}^{4}\frac{\mathrm{d}^4p_i}{(2\pi)^3}\;\delta(p_i^2-m_i^2) = \\
&= \delta^4(P-(p_m+q+p_f))\;\prod_{m,f}\frac{\mathrm{d}^4p_i}{(2\pi)^3}\;\delta(p_i^2-m_i^2)\;\delta(q^2-M_X^2)\;\mathrm{d}M_X^2 \\
&\quad\times\;\mathrm{d}^4q\;\delta(q-p_2-p_3)\;\prod_{2,3}\frac{\mathrm{d}^4p_i}{(2\pi)^3}\;\delta(p_i^2-m_i^2) = \\
&= \mathrm{d}\Phi_3(P;p_mqp_f)\;\mathrm{d}\Phi_2(q;p_2p_3)\;(2\pi)^3\;\mathrm{d}M_X^2
\end{aligned} \tag{85}$$

where we have introduced the equalities

$$q = p_2 + p_3 \quad , \qquad q^2 = M_X^2$$

using the deltas

$$\delta^4(q-p_2-p_3)\;\mathrm{d}^4q \quad , \qquad \delta(q^2-M_X^2)\;\mathrm{d}M_X^2$$

$q$ is the four momentum of the $X$ system, and $p_2, p_3$ are the four momenta of the two $K_s^0$. Since both phase space terms are Lorentz invariant, we can choose the reference frame in which we are going to calculate them. The appropriate frames are the CMS, for $\mathrm{d}\Phi_3(P;p_mqp_f)$, and the $X$ rest frame for $\mathrm{d}\Phi_2(q;p_2p_3)$.

### B.2.1 Calculation of the Production Phase Space.

We begin by writing the production phase space as

$$\mathrm{d}\Phi_3 \;=\; \delta^4(P-(p_m+q+p_f))\;\prod_{m,X,f}\frac{\mathrm{d}^3\vec{p_i}}{(2\pi)^3 2E_i}$$

then, perform the integrals over the variables that are not needed. So, we first integrate over the transverse momentum of the $X$ system, $q_x,\ q_y$, and over the longitudinal momentum of the missing proton. That leaves us with only one delta

$$\mathrm{d}\Phi_3 \;=\; \delta(E-(E_m+E_q+E_f))\;\frac{\mathrm{d}p_{x,m}\;\mathrm{d}p_{y,m}\;\mathrm{d}q_z\;\mathrm{d}p_{x,f}\;\mathrm{d}p_{y,f}\;\mathrm{d}p_{z,f}}{8(2\pi)^9 E_m E_X E_f}$$

Here we use the fact that, in the CMS,

$$\begin{aligned}\delta\left(E-\sqrt{m_p^2+p_{t,m}^2+(-p_{z,X}-p_{z,f})^2}\;-\;E_X-\sqrt{m_p^2+p_{t,f}^2+p_{z,f}^2}\right)\;\mathrm{d}p_{z,f}\;&=\\ =\;\frac{E_m E_f}{|-p_{z,m}E_f+p_{z,f}E_m|}&\end{aligned}$$

The result of integrating the deltas is, then,

$$\mathrm{d}\Phi_3 \;=\; \frac{\mathrm{d}p_{x,m}\;\mathrm{d}p_{y,m}\;\mathrm{d}q_z\;\mathrm{d}p_{x,f}\;\mathrm{d}p_{y,f}}{8(2\pi)^9 E_X\,|p_{z,f}E_m-p_{z,m}E_f|}$$

and, using the change of variables $\mathrm{d}x\,\mathrm{d}y \;=\; \rho\,\mathrm{d}\rho\,\mathrm{d}\phi \;=\; \frac{1}{2}\mathrm{d}\rho^2\,\mathrm{d}\phi$, and that, in the CMS, $\mathrm{d}q_z = 2\sqrt{s}\,\mathrm{d}x_F$, we get

$$\mathrm{d}\Phi_3(q;p_2p_3) \;=\; \frac{\sqrt{s}}{2^4(2\pi)^9}\frac{\mathrm{d}p_{t,m}^2\;\mathrm{d}\phi_m\;\mathrm{d}p_{t,f}^2\;\mathrm{d}\phi_f\;\mathrm{d}x_F}{E_X\,|E_m p_{z,f}-E_f p_{z,m}|} \tag{86}$$

### B.2.2 Calculation of the Decay Phase Space.

The Lorentz invariant phase space for the decay is

$$\mathrm{d}\Phi_2(q;p_2p_3) \;=\; \delta^4(q-p_2-p_3)\;\frac{\mathrm{d}^3p_2\,\mathrm{d}^3p_3}{4(2\pi)^6 E_2 E_3}$$

To perform the calculation, integrate over $\vec{p_3}$, that leaves us with

$$\mathrm{d}^3\vec{p_2} \;=\; p_2^2\,\mathrm{d}p_2\,\mathrm{d}(\cos\theta)\,\mathrm{d}\phi$$

thus

$$\mathrm{d}\Phi_2(q;p_2p_3) \;=\; \frac{\delta(E_X-E_2-E_3)\;p_2^2\,\mathrm{d}p_2\,\mathrm{d}(\cos\theta)\,\mathrm{d}\phi}{4(2\pi)^6E_2E_3}$$

Now, $m_2=m_3=m_{K_s^0}$, and in the $X$ rest frame, $\vec{p_2}=-\vec{p_3}$, so

$$\begin{aligned}\delta(E_X-E_2-E_3)\;\mathrm{d}p_2 \;&=\; \delta(E_X-2\sqrt{m_{K_s^0}^2+p_2^2})\;\mathrm{d}p_2 \;= \\ &=\; \left|\frac{E_2}{2p_2}\right| \;=\; \frac{M_X}{4\sqrt{(M_X/2)^2-m_{K_s^0}^2}}\end{aligned}$$

since in the $X$ rest frame $M_X=2E_2,\;p_2^2=(M_X/2)^2-m_{K_s^0}^2$. Thus, the decay phase space is

$$\mathrm{d}\Phi_2(q;p_2p_3) \;=\; \frac{\sqrt{(M_X/2)^2-m_{K_s^0}^2}}{4(2\pi)^6\;M_X}\;\mathrm{d}(\cos\theta)\;\mathrm{d}\phi \tag{87}$$

Finally, the complete phase space for both production and decay is given by

$$\mathrm{d}\Phi_4(P;p_mp_2p_3p_f) \;=\; \frac{\sqrt{s}\sqrt{(M_X/2)^2-m_{K_s^0}^2}}{2^5(2\pi)^{12}\;E_X\;|E_mp_{z,f}-E_fp_{z,m}|}\;\mathrm{d}^6x\,\mathrm{d}^2\Omega$$

and the differential cross section for process (3–4) is given by

$$\mathrm{d}^8\sigma_\lambda \;=\; \frac{1}{2^7(2\pi)^8p_0}\,|\mathcal{M}_\lambda|^2\,\frac{\sqrt{(M_X/2)^2-m_{K_s^0}^2}}{E_X\;|E_mp_{z,f}-E_fp_{z,m}|}\;\mathrm{d}^6x\,\mathrm{d}^2\Omega \tag{88}$$

The first term in this equation is an irrelevant constant, since it will be absorbed in the normalization process.

## B.3 Calculation of Uncertaintiess for Acceptance Integrals.

When calculating the acceptance integrals for the waves or moments analysis, one gets values for these integrals that depend on the number of Monte Carlo events and the binning used to calculate them. The impossibility of having an infinite number of events in each bin causes that one gets a distribution of values that do not have a smooth variation in the range of interest of the parameter on which one is doing the analysis. In the present work, the parameter is $\Omega_i$, the angular distribution for events in the $i$–th bin of the invariant mass of the $K_s^0K_s^0$ system. One way to overcome this lack of smoothness is to fit a function

$f(x)$ to the acceptance integral for each wave or moment, and consider this function as "the acceptance integral" for that wave or moment. This procedure also helps to avoid calculating the acceptance integrals each time one has to change the width or position of the bins. In order to perform this fit, one needs to calculate not only the waves or moments, but also the errors in this calculations. This Section contains the calculations of these errors for a general function $f(\Omega)$ of the angular distribution $\Omega$ of the accepted events.

Suppose we generated $N_g$ Monte Carlo events, with a flat distribution in variables $\Omega_i$. After passing each event through the whole reconstruction chain of programs that simulate the detector, one ends up with $N_a$ accepted events, and would like to find the mean $Q$ of the function $f(\Omega)$ of the angular distribution $\Omega$ of the accepted events

$$Q = \frac{1}{N_g} \sum_{i=1}^{N_a} f'(\Omega_i) = \frac{1}{N_g} \sum_{i=1}^{N_g} f(\Omega_i) \tag{89}$$

where we used the fact that, for the Monte Carlo events, the acceptance factor has values 0 and 1 only, and that the phase–space factor is constant for the bin being considered (thus, it is assumed that this bin is very small, but contains an infinite number of events), to define

$$f(\Omega_i) \equiv f'(\Omega_i) \cdot (\text{Acceptance}) \cdot (\text{Phase Space}) \tag{90}$$

which includes the acceptance and phase space factors. Note that the distribution function $f$ is evaluated on the generated variables $\Omega_i$.

To calculate the error made when calculating $Q$, one has to repeat the "experiment" (Monte Carlo generation of events) a very big (infinite!) $N_r$ number of times, calculate $Q_r$ for each experiment, and from them calculate the mean $\tilde{Q}_{N_r}$, and standard deviation $\sigma^2_{N_r}$

$$\left\{ \begin{array}{ccccc} \Omega_1^1 & \Omega_2^1 & \Omega_3^1 & \cdots & \Omega_{N_g}^1 \\ \Omega_1^2 & \Omega_2^2 & \Omega_3^2 & \cdots & \Omega_{N_g}^2 \\ & & & \vdots & \\ \Omega_1^{N_r} & \Omega_2^{N_r} & \Omega_3^{N_r} & \cdots & \Omega_{N_g}^{N_r} \end{array} \right\} \quad \underset{\substack{N_r \to \infty \\ \text{experiments}}}{\rightarrow} \quad \left\{ \begin{array}{c} \frac{1}{N_g} \sum_{i=1}^{N_g} f(\Omega_i^1) \\ \frac{1}{N_g} \sum_{i=1}^{N_g} f(\Omega_i^2) \\ \vdots \\ \frac{1}{N_g} \sum_{i=1}^{N_g} f(\Omega_i^{N_r}) \end{array} \right\} \tag{91}$$

Hence, $\tilde{Q}_{N_r}$ and $\sigma^2_{N_r}$ are

$$\tilde{Q}_{N_r} = \frac{1}{N_r} \sum_{r=1}^{N_r} Q_r \quad , \qquad \sigma^2_{N_r} = \frac{1}{N_r} \sum_{r=1}^{N_r} \left( Q_r - \tilde{Q}_{N_r} \right)^2 \tag{92}$$

The next step is to look for a simpler form for $\sigma^2_{N_r}$. We have that

$$\begin{aligned}\sigma^2_{N_r} &= \frac{1}{N_r}\sum_{r=1}^{N_r}\left\{\left(\frac{1}{N_g}\sum_{i=1}^{N_g} f(\Omega_i^r) - \tilde{Q}_{N_r}\right)\left(\frac{1}{N_g}\sum_{j=1}^{N_g} f(\Omega_j^r) - \tilde{Q}_{N_r}\right)\right\} \\ &= \frac{1}{N_r}\sum_{r=1}^{N_r}\left\{\frac{1}{N_g^2}\sum_{i,j}^{N_g} f(\Omega_i^r)f(\Omega_j^r) - 2\tilde{Q}_{N_r}\frac{1}{N_g}\sum_{\ell=1}^{N_g} f(\Omega_\ell^r) + \tilde{Q}^2_{N_r}\right\} \qquad (93)\end{aligned}$$

In the limit $N_g \to \infty$, we can write this as

$$\sigma^2_{N_r} = \frac{1}{N_r}\sum_{r=1}^{N_r}\left\{\frac{1}{N_g^2}\sum_{i,j}^{N_g} f(\Omega_i^r)f(\Omega_j^r)\right\} - \tilde{Q}^2_{N_r} \qquad (94)$$

Since the variables $\Omega_i$ were randomly generated, there is no correlation among them. Now, the term in brackets in the last expression of eq.(94), contains the product $f(\Omega_i^r)f(\Omega_j^r)$, which is composed of two terms: one, $f(\Omega_i^r)f(\Omega_i^r)$, in which the terms are totally correlated, and another one, $f(\Omega_i^r)f(\Omega_j^r),\ i \neq j$, in which the terms are totally uncorrelated. Thus, each term should be analyzed separately.

The first term in (94), totally correlated, is

$$\sigma^2_{tc} = \frac{1}{N_r}\sum_{r=1}^{N_r}\left\{\frac{1}{N_g^2}\sum_{i=1}^{N_g} f^2(\Omega_i^r)\right\} = \frac{1}{N_g^2}\sum_{i=1}^{N_g}\left\{\frac{1}{N_r}\sum_{r=1}^{N_r} f^2(\Omega_i^r)\right\} \qquad (95)$$

Moreover, for each $i$, the sum over variable $r$ is on an infinite set $N_r$, which, therefore,consists of all possible values of $\Omega$. Then, all terms in the sum over $i$ are equivalent, so that

$$\sigma^2_{tc} = \frac{1}{N_g}\left\{\frac{1}{N_r}\sum_{r=1}^{N_r} f^2(\Omega^r)\right\} \qquad (96)$$

The totally uncorrelated term is

$$\sigma^2_{tu} = \frac{1}{N_r}\sum_{r=1}^{N_r}\left\{\frac{1}{N_g^2}\sum_{i\neq j}^{N_g} f(\Omega_i^r)f(\Omega_j^r)\right\} = \frac{1}{N_g^2}\sum_{i\neq j}^{N_g}\left\{\frac{1}{N_r}\sum_{r=1}^{N_r} f(\Omega_i^r)f(\Omega_j^r)\right\} \qquad (97)$$

The expression in brackets in (97), for each $r$, consists of a very large number of terms

$$n \text{ subsets} \left\{ \begin{array}{cc} & \Omega_{j_1} \\ & \Omega_{j_2} \\ [\Omega_{i_1}] & \vdots \\ & \Omega_{m_1} \end{array} \right\} m \text{ terms} \quad \left\{ \begin{array}{cc} & \Omega_{j_1} \\ & \Omega_{j_2} \\ [\Omega_{i_2}] & \vdots \\ & \Omega_{m_2} \end{array} \right\} m \text{ terms} \quad , \quad n \times m = N_r \tag{98}$$

$$\vdots \qquad \vdots$$

$$\left\{ \begin{array}{cc} & \Omega_{j_1} \\ & \Omega_{j_2} \\ [\Omega_{n}] & \vdots \\ & \Omega_{m_n} \end{array} \right\} m \text{ terms}$$

One can divide this set of terms in $n$ subsets ($n$ very large), each one having a definite value for $\Omega_i^r$ for fixed $i$, and hence labeled $[\Omega_i]$. Each one of this subsets contains $m$ terms ($n \times m = N_r$), and, $m$ being very large, there are all possible values of $\Omega_j$ in each subset. Using this considerations, it is possible to evaluate $\sigma_{tu}^2$ in the following way

$$\begin{aligned} \sigma_{tu}^2 &= \frac{1}{N_g^2} \sum_{i \neq j}^{N_g} \left\{ \frac{1}{N_r} \sum_{r'=1}^{n} \left( \sum_{r''=1}^{m} f(\Omega_i^{r'}) f(\Omega_j^{r''}) \right) \right\} \\ &= \frac{1}{N_g^2} \sum_{i \neq j}^{N_g} \left\{ \frac{n \cdot m}{N_r} \left( \frac{1}{n} \sum_{r'=1}^{n} f(\Omega_i^{r'}) \right) \left( \frac{1}{m} \sum_{r''=1}^{m} f(\Omega_j^{r''}) \right) \right\} \\ &= \frac{1}{N_g^2} \sum_{i \neq j}^{N_g} \left\{ \left( \frac{1}{n} \sum_{r'=1}^{n} f(\Omega_i^{r'}) \right) \left( \frac{1}{m} \sum_{r''=1}^{m} f(\Omega_j^{r''}) \right) \right\} \end{aligned} \tag{99}$$

Using (96) and (99), $\sigma_{N_r}^2$ can be written as

$$\sigma_{N_r}^2 = \frac{1}{N_g} \left\{ \frac{1}{N_r} \sum_{r=1}^{N_r} f^2(\Omega^r) \right\} + \frac{1}{N_g^2} \sum_{i \neq j}^{N_g} \left\{ \left( \frac{1}{n} \sum_{r'=1}^{n} f(\Omega_i^{r'}) \right) \left( \frac{1}{m} \sum_{r''=1}^{m} f(\Omega_j^{r''}) \right) \right\} - \tilde{Q}_{N_r}^2 \tag{100}$$

This expression is easier to interpret than (92), owing to the following considerations. First, the since we are doing the "experiment" an infinite number of times, $N_r \to \infty$, we can take $n \to \infty$ and $m \to \infty$. In these limits, we have that

$$\frac{1}{n} \sum_{r'=1}^{n} f(\Omega_i^{r'}) \quad \to \quad \tilde{Q}_{N_r}$$

$$\frac{1}{m}\sum_{r"=1}^{m} f(\Omega_j^{r"}) \;\; \rightarrow \;\; \tilde{Q}_{N_r}$$

Second, since it is impossible to repeat the experiment an infinite number of times, what one does is to assume that the mean $\tilde{Q}_{N_g}$ is what one got when doing the experiment

$$\tilde{Q}_{N_g} = \frac{1}{N_g}\sum_{i=1}^{N_g} f(\Omega_i) \tag{101}$$

Then, one can approximate the value of $\sigma^2_{N_g}$ by

$$\begin{aligned}
\sigma^2_{N_g} &= \frac{1}{N_g}\left\{\frac{1}{N_g}\sum_{i=1}^{N_g} f^2(\Omega_i)\right\} + \frac{1}{N_g^2}\sum_{i\neq j}^{N_g}\left\{\left(\frac{1}{N_g}\sum_{r=1}^{N_g} f(\Omega_r)\right)\left(\frac{1}{N_g}\sum_{s=1}^{N_g} f(\Omega_s)\right)\right\} - \tilde{Q}^2_{N_g} \\
&= \frac{1}{N_g^2}\sum_{i=1}^{N_g} f^2(\Omega_i) + \frac{1}{N_g^2}\sum_{i\neq j}^{N_g}\left\{\tilde{Q}^2_{N_g}\right\} - \tilde{Q}^2_{N_g} \\
&= \frac{1}{N_g^2}\sum_{i=1}^{N_g} f^2(\Omega_i) + \frac{1}{N_g^2}\left(N_g^2 - N_g\right)\tilde{Q}^2_{N_g} - \tilde{Q}^2_{N_g} \\
&= \frac{1}{N_g^2}\sum_{i=1}^{N_g} f^2(\Omega_i) - \frac{1}{N_g}\tilde{Q}^2_{N_g}
\end{aligned}$$

Finally

$$\sigma^2_{N_g} = \frac{1}{N_g^2}\sum_{i=1}^{N_g} f^2(\Omega_i) - \frac{1}{N_g^3}\left(\sum_{i=1}^{N_g} f(\Omega_i)\right)^2 \tag{102}$$

(101) and (102) are the quantities one needs to perform fits on any function $f(\Omega)$ of the (angular) variables $\Omega$.

## B.4 Acceptance Integrals for Moments and Amplitudes.

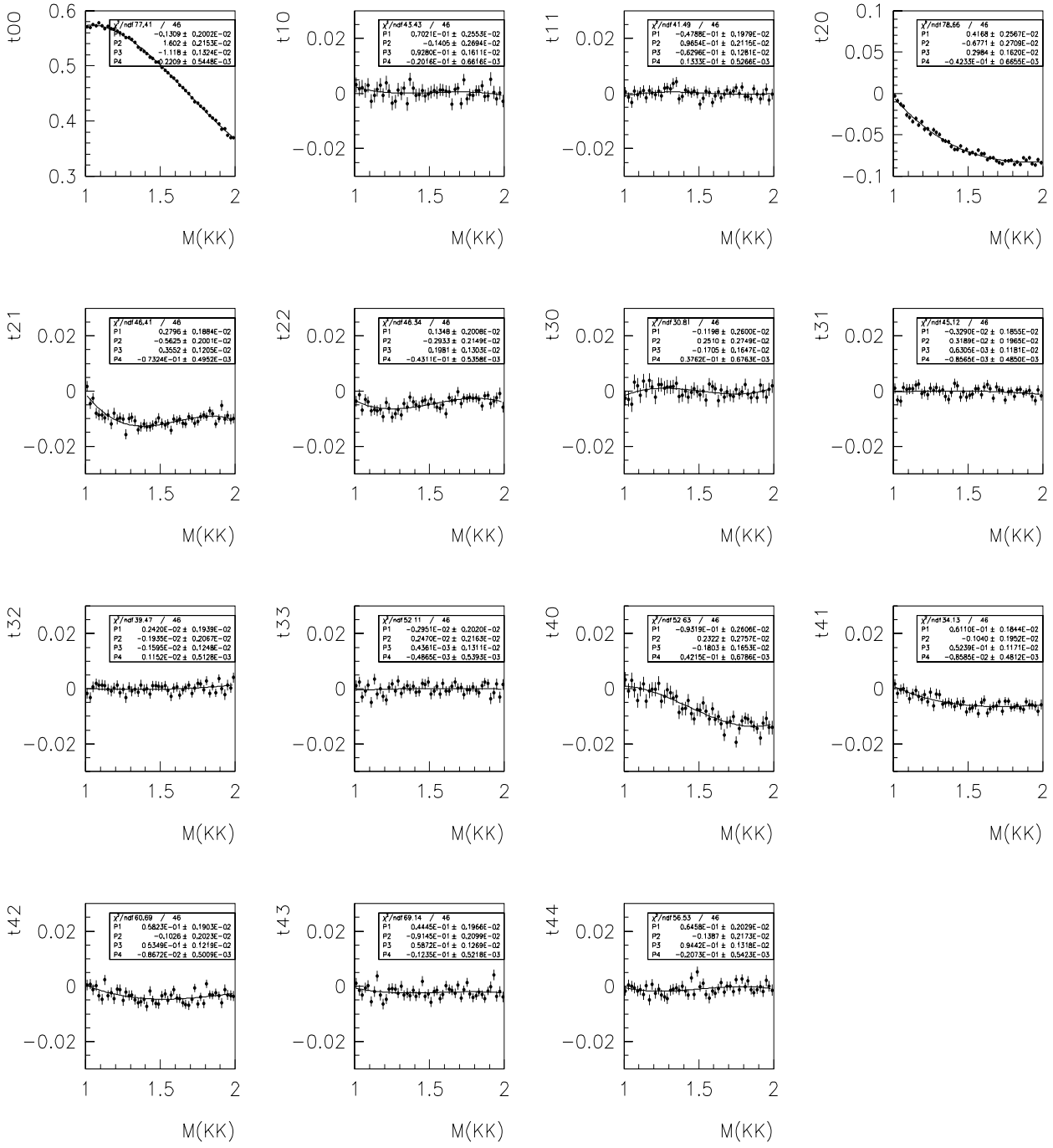


Figure 78: Moments acceptance integrals.

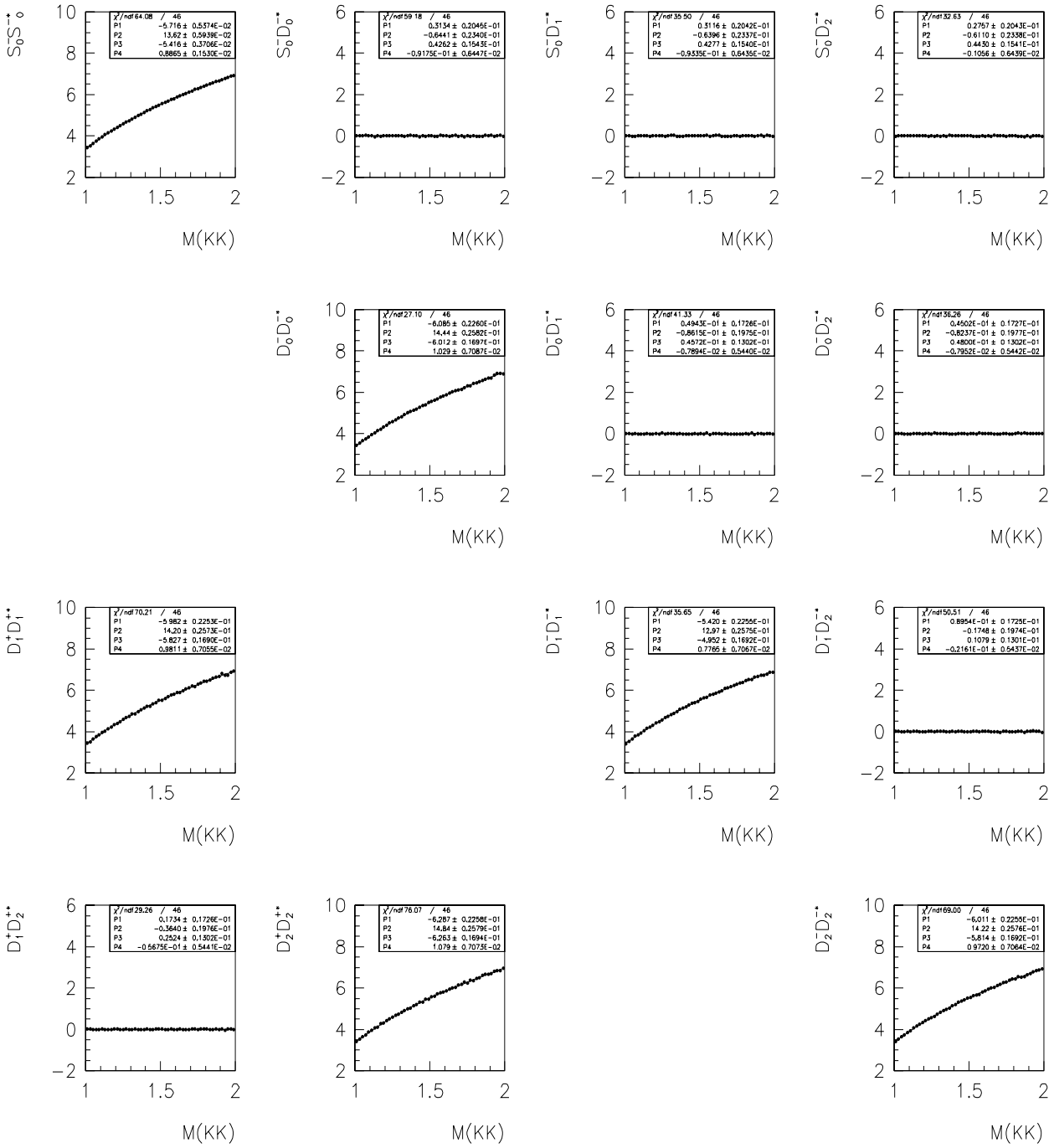


Figure 79: Amplitudes acceptance integrals for generated events. The upper triangle corresponds to negative naturality waves, and the lower triangle corresponds to positive naturality waves.

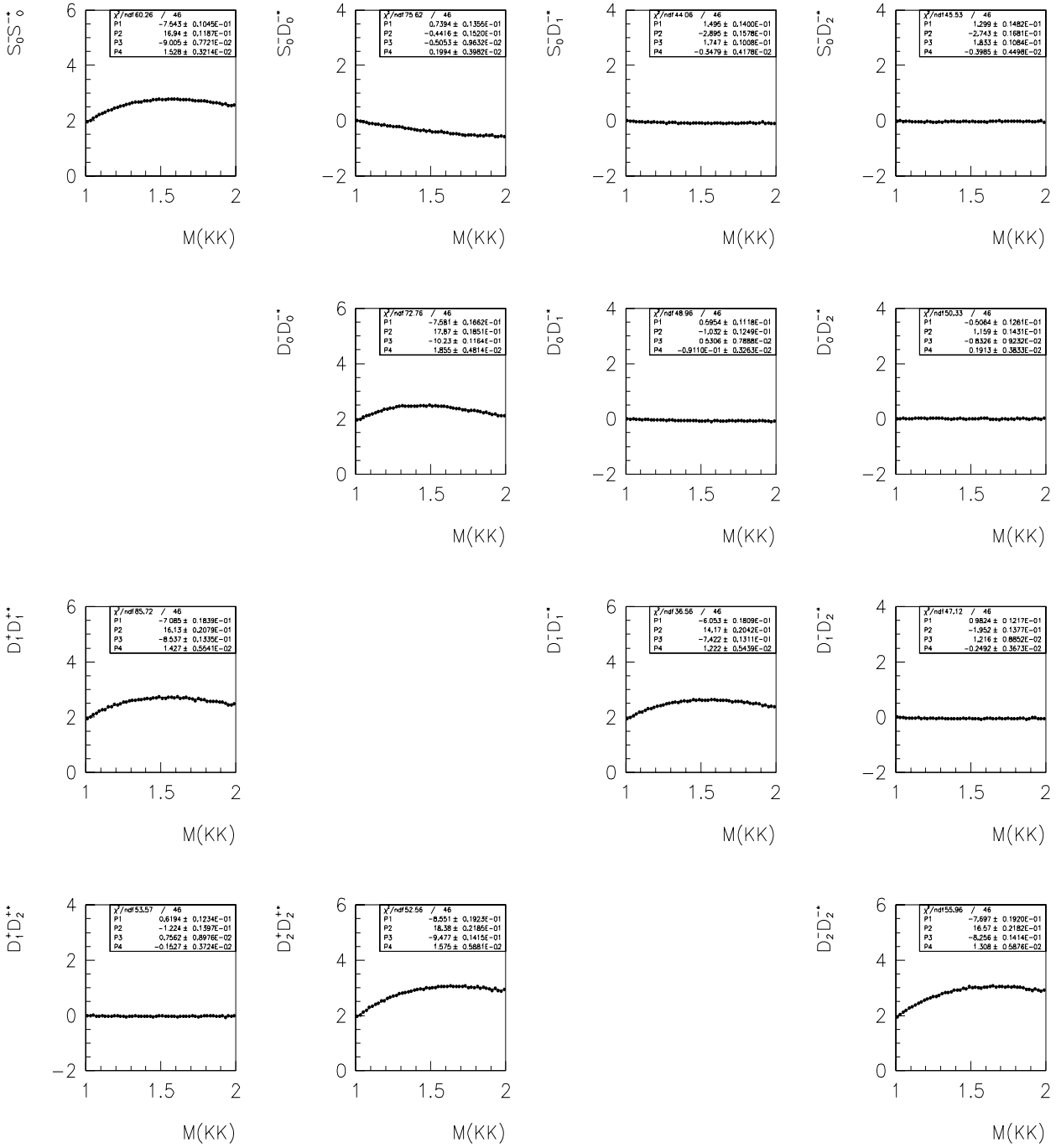


Figure 80: Amplitudes acceptance integrals for accepted events. The upper triangle corresponds to negative naturality waves, and the lower triangle corresponds to positive naturality waves.

# References


[1] S.Godfrey and N.Isgur, Phys. Rev. **D32** (1985) 189.

[2] See the paper by G.Eigen, Proceedings of the Erice School, Ed. Gastaldi Plenum Press (1989) V.37, or the Preprint CALT 68-1483 (1987), of the same author, for more references on this subject.

[3] The Particle Data Group; Review of Particle Properties, Phys. Rev. **D54**, 1996.

[4] C.N.Yang, Phys. Rev. **77**, (1950) 242.

[5] M.S.Chanowitz and S.R.Sharpe, Phys. Lett. **B132**(1983) 413.

[6] S.J.Lindenbaum *et al.*, Comm. Nucl. Part. Phys. **13** (1984) 285; A.Etkin *et al.*, Phys. Lett. **B201** (1988) 568.

[7] C.Edwards *et al.*, Phys. Rev. Lett. **48** (1982) 458.

[8] A.Etkin *et al.*, Phys. Rev. Lett. **49** (1982) 1620. A.Etkin *et al.*, Phys. Lett. **B165** (1985) 217.

[9] D.M.Coffman *et al.*, SLAC–PUB–3720 (1986).

[10] D.Alde *et al.* (GAMS Collaboration), Nucl. Phys. **B269** (1986) 485; D.Alde *et al.* (GAMS Collaboration), Phys. Lett. **B201** (1988) 160.

[11] R.M.Baltrusaitis *et al.* (Mark III Collaboration), Phys. Rev. Lett. **56** (1986) 107.

[12] See for example: G.B.West, "A theorem on the lightest glueball state", hep-ph/9603316, Mar. 14, 1996.

[13] G.Bali *et al.* (UKQCD Collaboration), Phys. Lett. **B309** (1993) 378.

[14] H.Chen, J.Sexton, A.Vaccarino and D.Weingarten, Nucl. Phys. **B34** (1994) 357.

[15] D.Weingarten, "Scalar Quarkonium and the Scalar Glueball", hep-lat/9608070, Aug. 13, 1996. W.Lee and D.Weingarten, "Scalar Quarkonium Masses", hep-lat/9608071, Aug. 13, 1996.

[16] C.Amsler *et al.* (Crystal Barrel Collaboration), Phys. Lett. **B291** (1992) 347.

[17] V.V.Anisovich *et al.* (Crystal Barrel Collaboration), Phys. Lett. **B323** (1994) 233.

[18] B.V.Bolonkin *et al.* (MSS ITEP Collaboration), Sov. J. Nucl. Phys. **43** (1986) 776.

[19] B.V.Bolonkin *et al.* (MSS ITEP Collaboration), Nucl. Phys. **B309** (1988) 426.

[20] D.Aston *et al.* (LASS Collaboration), SLAC–PUB–4340 (1987).

[21] D.Aston *et al.* (LASS Collaboration), Nucl. Phys. **B301** (1988) 525.

[22] F.Barreiro *et al.* (Amsterdam-CERN-Nijmegen-Oxford Collaboration), Nucl. Phys. **B121** (1977) 237.

[23] D.Aston *et al.* (LASS Collaboration), Phys. Lett. **B201** (1988) 573.

[24] J.Weinstein and N.Isgur, Phys. Rev. Lett. **48** (1982) 659, Phys. Rev. **D27** (1983) 588.

[25] Chen, Proc. of the Hadron '91 Conf. See also SLAC-PUB-5669.

[26] J.E.Augustine *et al.* (DM2 Collaboration), Phys. Rev. Lett. **60** (1988) 2238.

[27] M.Althoff *et al.* (TASSO Collaboration), Phys. Lett. **B121** (1983) 216; M.Althoff *et al.* (TASSO Collaboration), Z. Phys. **C29** (1985) 189.

[28] H.J.Lipkin, Nucl. Phys. **B7** (1968) 321 ; Proc. EPS Intern. Conf. on High Energy Physics (Palermo, 1975) p.609 ; D.Faiman *et al.*, Phys. Lett. **B59** (1975) 269.

[29] Ch.Berger *et al.* (PLUTO Collaboration), Z. Phys. **C37** (1988) 329.

[30] H.J.Behrend *et al.* (CELLO Collaboration), Z. Phys. **C43** (1989) 91.

[31] T.A.Armstrong *et al.* (WA76 Collaboration), Phys. Lett. **B227** (1989) 186.

[32] T.A.Armstrong *et al.* (WA76 Collaboration), Z. Phys. **C51** (1991) 351.

[33] J.Z.Bai *et al.* (BES Collaboration), Phys. Rev. Lett. **76** (1996) 3502.

[34] M.A.Sosa, "Partial Wave Analysis of the Centrally Produced $K_s^0 K^{\pm}\pi^{\mp}$ System at 800 $GeV/c$", University of Guanajuato, México (1995).

[35] K.Markianos, Ph.D. Thesis on the process $pp \to p_{missing}(\pi\pi)p_{fast}$, to be submitted to the University of Massachusetts, Amherst.

[36] M.Church, "$\Xi^-$ Production in 15–28 $GeV$ Neutron–Proton Interactions", Nevis–260. Columbia University, Nevis Laboratories (1986).

[37] B.Stern, "A Search for Charmed Particles in 15–28 $GeV$ Neutron–Proton Interactions", Nevis–266. Columbia University, Nevis Laboratories (1988).

[38] M.J.Forbush, "High Mass Diffractive Dissociation at 27.5 $GeV$ Proton–Proton Interactions in Exclusive Final States", Texas A&M University (1990).

[39] E.E.Gottschalk, "Strange Baryon Production in 27.5 $GeV/c$ Proton–Proton Interactions", Nevis–278. Columbia University, Nevis Laboratories (1992).

[40] L.R.Wiencke, "Observation of Final State Coulomb Interactions in Proton–Proton Collisions at 27.5 $GeV/c$", Nevis–280. Columbia University, Nevis Laboratories (1993).

[41] J.Uribe, "Pion Pion Correlations at Low Relative Momentum Produced in the Reactions $pp \to pp\,(\pi^+\pi^-)^n$ with $n$=2,3,4,5,6", UMAHEP–385. University of Massachusetts, Amherst (1993).

[42] S.Lee, "Lambda Polarization in Exclusive and Diffractive Inclusive Final States Produced in Proton–Proton Diffraction Dissociation at 800 $GeV/c$", UMAHEP–409. University of Massachusetts, Amherst (1994).

[43] D.C.Christian *et al.*, Nucl. Instr. Meth. **A345** (1994) 62.

[44] E.P.Hartouni *et al.*, Nucl. Instr. Meth. **A317** (1992) 161.

[45] D.C.Christian, Fermilab TM-1956 (1995).

[46] D.C.Christian, Internal Memo to BNL E766 and FNAL E690 (1987).

[47] J.A.Crittenden *et al.*, IEEE Trans. Nucl. Sci. **31** (1984) 1028.

[48] B.C.Knapp and W.Sippach, IEEE Trans. Nucl. Sci. **NS27** (1980) 578.
E.P.Hartouni *et al.*, IEEE Trans. Nucl. Sci. **36** (1989) 1480.
B.C.Knapp, Nucl. Instr. Meth. **A289** (1990) 561.

[49] S.U.Chung and T.L.Trueman, Phys. Rev. **D11** (1975) 633.

[50] Gauss, C.F.Werke, Vol. 4, Götingen (1880).

[51] R.A.Fisher, Mess. of Math. **41** (1912) 155.

[52] S.U. Chung, "Amplitude analysis of two-pseudoscalar systems", BNL–QGS–95–41 (1995).

[53] S.U. Chung, "Amplitude analysis of a system with two identical spinless particles", BNL–QGS–96–32 (1996).

[54] S.A. Sadovsky, "On the ambiguities in the partial–wave analysis of $\pi^- p \to \eta\pi^0 n$ reaction", IHEP 91–75 (1991).

[55] E. Barrelet, Nuovo Cimento **8A**, 331 (1972).

[56] S.U. Chung, "$C$– and $G$–parity, a new definition and applications –Updated Version–", BNL–QGS–95–02 (1995).